

Roland Winkler

Spin–Orbit Coupling Effects in Two-Dimensional Electron and Hole Systems

With 64 Figures and 26 Tables



Springer

Dr. Roland Winkler
Universität Erlangen-Nürnberg
Institut für Technische Physik III
Staudtstrasse 7
91058 Erlangen, Germany
E-mail: roland.winkler@physik.uni-erlangen.de

Cataloging-in-Publication Data applied for

A catalog record for this book is available from the Library of Congress.

Bibliographic information published by Die Deutsche Bibliothek

Die Deutsche Bibliothek lists this publication in the Deutsche Nationalbibliografie; detailed bibliographic data is available in the Internet at <http://dnb.ddb.de>.

Physics and Astronomy Classification Scheme (PACS):

73.21.Fg, 71.70.Ej, 73.43.Qt, 03.65.Sq

ISSN print edition: 0081-3869

ISSN electronic edition: 1615-0430

ISBN 3-540-01187-0 Springer-Verlag Berlin Heidelberg New York

This work is subject to copyright. All rights are reserved, whether the whole or part of the material is concerned, specifically the rights of translation, reprinting, reuse of illustrations, recitation, broadcasting, reproduction on microfilm or in any other way, and storage in data banks. Duplication of this publication or parts thereof is permitted only under the provisions of the German Copyright Law of September 9, 1965, in its current version, and permission for use must always be obtained from Springer-Verlag. Violations are liable for prosecution under the German Copyright Law.

Springer-Verlag Berlin Heidelberg New York
a member of BertelsmannSpringer Science+Business Media GmbH

<http://www.springer.de>

© Springer-Verlag Berlin Heidelberg 2003
Printed in Germany

The use of general descriptive names, registered names, trademarks, etc. in this publication does not imply, even in the absence of a specific statement, that such names are exempt from the relevant protective laws and regulations and therefore free for general use.

Typesetting: Camera-ready copy from the author using a Springer \LaTeX macro package

Production: LE- \TeX Jelonek, Schmidt & Vöckler GbR, Leipzig

Cover concept: eStudio Calamar Steinen

Cover production: *design & production* GmbH, Heidelberg

Printed on acid-free paper SPIN: 10864040 56/3141/YL 5 4 3 2 1 0

to Freya

Preface

Spin-orbit coupling makes the spin degree of freedom respond to its orbital environment. In solids this yields such fascinating phenomena as a spin splitting of electron states in inversion-asymmetric systems even at zero magnetic field and a Zeeman splitting that is significantly enhanced in magnitude over the Zeeman splitting of free electrons. In this book, we review spin-orbit coupling effects in quasi-two-dimensional electron and hole systems. These tailor-made systems are particularly suited to investigating these questions because an appropriate design allows one to manipulate the orbital motion of the electrons such that spin-orbit coupling becomes a “control knob” with which one can steer the spin degree of freedom.

In the present book, we omit elaborate rigorous derivations of theoretical concepts and formulas as much as possible. On the other hand, we aim at a thorough discussion of the physical ideas that underlie the concepts we use, as well as at a detailed interpretation of our results. In particular, we complement accurate numerical calculations by simple and transparent analytical models that capture the important physics.

Throughout this book we focus on a direct comparison between experiment and theory. The author thus deeply appreciates an extensive collaboration with Mansour Shayegan, Stergios J. Papadakis, Etienne P. De Poortere, and Emanuel Tutuc, in which many theoretical findings were developed together with the corresponding experimental results. The good agreement achieved between experiment and theory represents an important confirmation of the concepts and ideas presented in this book.

The author is grateful to many colleagues for stimulating discussions and exchanges of views. In particular, he had numerous discussions with Ulrich Rössler, not only about physics but also beyond. Finally, he thanks Springer-Verlag for its kind cooperation.

Erlangen, July 2003

Roland Winkler

Contents

1	Introduction	1
1.1	Spin–Orbit Coupling in Solid-State Physics	1
1.2	Spin–Orbit Coupling in Quasi-Two-Dimensional Systems	3
1.3	Overview	3
	References	6
2	Band Structure of Semiconductors	9
2.1	Bulk Band Structure and $\mathbf{k} \cdot \mathbf{p}$ Method	9
2.2	The Envelope Function Approximation	12
2.3	Band Structure in the Presence of Strain	15
2.4	The Paramagnetic Interaction in Semimagnetic Semiconductors	17
2.5	Theory of Invariants	18
	References	20
3	The Extended Kane Model	21
3.1	General Symmetry Considerations	21
3.2	Invariant Decomposition for the Point Group T_d	22
3.3	Invariant Expansion for the Extended Kane Model	23
3.4	The Spin–Orbit Gap Δ_0	26
3.5	Kane Model and Luttinger Hamiltonian	27
3.6	Symmetry Hierarchies	29
	References	33
4	Electron and Hole States in Quasi-Two-Dimensional Systems	35
4.1	The Envelope Function Approximation for Quasi-Two-Dimensional Systems	35
4.1.1	Envelope Functions	36
4.1.2	Boundary Conditions	36
4.1.3	Unphysical Solutions	37
4.1.4	General Solution of the EFA Hamiltonian Based on a Quadrature Method	39
4.1.5	Electron and Hole States for Different Crystallographic Growth Directions	41
4.2	Density of States of a Two-Dimensional System	41

4.3	Effective-Mass Approximation.....	42
4.4	Electron and Hole States in a Perpendicular Magnetic Field: Landau Levels	43
4.4.1	Creation and Annihilation Operators	43
4.4.2	Landau Levels in the Effective-Mass Approximation ..	45
4.4.3	Landau Levels in the Axial Approximation	46
4.4.4	Landau Levels Beyond the Axial Approximation	46
4.5	Example: Two-Dimensional Hole Systems.....	47
4.5.1	Heavy-Hole and Light-Hole States	47
4.5.2	Numerical Results	48
4.5.3	HH–LH Splitting and Spin–Orbit Coupling	53
4.6	Approximate Diagonalization of the Subband Hamiltonian: The Subband $\mathbf{k} \cdot \mathbf{p}$ Method	54
4.6.1	General Approach	55
4.6.2	Example: Effective Mass and g Factor of a Two-Dimensional Electron System	56
	References	58
5	Origin of Spin–Orbit Coupling Effects	61
5.1	Dirac Equation and Pauli Equation	62
5.2	Invariant Expansion for the 8×8 Kane Hamiltonian	65
	References	67
6	Inversion-Asymmetry-Induced Spin Splitting	69
6.1	$B = 0$ Spin Splitting and Spin–Orbit Interaction	70
6.2	BIA Spin Splitting in Zinc Blende Semiconductors	71
6.2.1	BIA Spin Splitting in Bulk Semiconductors	71
6.2.2	BIA Spin Splitting in Quasi-2D Systems.....	75
6.3	SIA Spin Splitting	77
6.3.1	SIA Spin Splitting in the Γ_6^c Conduction Band: the Rashba Model	77
6.3.2	Rashba Coefficient and Ehrenfest’s Theorem	83
6.3.3	The Rashba Model for the Γ_8^v Valence Band	86
6.3.4	Conceptual Analogies Between SIA Spin Splitting and Zeeman Splitting	98
6.4	Cooperation of BIA and SIA	99
6.4.1	Interference of BIA and SIA	99
6.4.2	BIA Versus SIA: Tunability of $B = 0$ Spin Splitting ...	100
6.4.3	Density Dependence of SIA Spin Splitting	104
6.5	Interface Contributions to $B = 0$ Spin Splitting	110
6.6	Spin Orientation of Electron States	114
6.6.1	General Discussion	115
6.6.2	Numerical Results	119
6.7	Measuring $B = 0$ Spin Splitting	121

6.8	Comparison with Raman Spectroscopy	122
	References	125
7	Anisotropic Zeeman Splitting in Quasi-2D Systems	131
7.1	Zeeman Splitting in 2D Electron Systems	132
7.2	Zeeman Splitting in Inversion-Asymmetric Systems	134
7.3	Zeeman Splitting in 2D Hole Systems:	
	Low-Symmetry Growth Directions	138
7.3.1	Theory	138
7.3.2	Comparison with Magnetotransport Experiments	143
7.4	Zeeman Splitting in 2D Hole Systems: Growth Direction [001]	146
	References	148
8	Landau Levels and Cyclotron Resonance	151
8.1	Cyclotron Resonance in Quasi-2D Systems	151
8.2	Spin Splitting in the Cyclotron Resonance of 2D Electron Systems	153
8.3	Cyclotron Resonance of Holes in Strained Asymmetric Ge-SiGe Quantum Wells	156
8.3.1	Self-Consistent Subband Calculations for $B = 0$	158
8.3.2	Landau Levels and Cyclotron Masses	161
8.3.3	Absorption Spectra	162
8.4	Landau Levels in Inversion-Asymmetric Systems	163
8.4.1	Landau Levels and the Rashba Term	164
8.4.2	Landau Levels and the Dresselhaus Term	165
8.4.3	Landau Levels in the Presence of Both BIA and SIA	166
	References	169
9	Anomalous Magneto-Oscillations	171
9.1	Origin of Magneto-Oscillations	173
9.2	SdH Oscillations and $B = 0$ Spin Splitting in 2D Hole Systems	174
9.2.1	Theoretical Model	174
9.2.2	Calculated Results	175
9.2.3	Experimental Findings	178
9.2.4	Anomalous Magneto-Oscillations in Other 2D Systems	179
9.3	Discussion	181
9.3.1	Magnetic Breakdown	182
9.3.2	Anomalous Magneto-Oscillations and Spin Precession	183
9.4	Outlook	192
	References	193
10	Conclusions	195

A Notation and Symbols 197
 Abbreviations 199
 References 199

B Quasi-Degenerate Perturbation Theory 201
 References 204

C The Extended Kane Model: Tables 207
 References 218

D Band Structure Parameters 219
 GaAs–Al_xGa_{1–x}As 219
 Si_{1–x}Ge_x 219
 References 219

Index 223

1 Introduction

In atomic physics, spin–orbit (SO) interaction enters into the Hamiltonian from a nonrelativistic approximation to the Dirac equation [1]. This approach gives rise to the Pauli SO term

$$H_{\text{SO}} = -\frac{\hbar}{4m_0^2c^2} \boldsymbol{\sigma} \cdot \mathbf{p} \times (\nabla V_0) , \quad (1.1)$$

where \hbar is Planck’s constant, m_0 is the mass of a free electron, c is the velocity of light, \mathbf{p} is the momentum operator, V_0 is the Coulomb potential of the atomic core, and $\boldsymbol{\sigma} = (\sigma_x, \sigma_y, \sigma_z)$ is the vector of Pauli spin matrices. It is well known that atomic spectra are strongly affected by SO coupling [2].

1.1 Spin–Orbit Coupling in Solid-State Physics

In a crystalline solid, the motion of electrons is characterized by energy bands $E_n(\mathbf{k})$ with band index n and wave vector \mathbf{k} . Here also, SO coupling has a very profound effect on the energy band structure $E_n(\mathbf{k})$. For example, in semiconductors such as GaAs, SO interaction gives rise to a splitting of the topmost valence band (Fig. 1.1). In a tight-binding picture without spin, the electron states at the valence band edge are p-like (orbital angular momentum $l = 1$). With SO coupling taken into account, we obtain electronic states with total angular momentum $j = 3/2$ and $j = 1/2$. These $j = 3/2$ and $j = 1/2$ states are split in energy by a gap Δ_0 , which is referred to as the SO gap. This example illustrates how the *orbital* motion of crystal electrons is affected by SO coupling.¹ It is less obvious in what sense the *spin* degree of freedom is affected by the SO coupling in a solid. In the present work we shall analyze both questions for quasi-two-dimensional semiconductors such as quantum wells (QWs) and heterostructures.

It was first emphasized by Elliot [3] and by Dresselhaus et al. [4] that the Pauli SO coupling (1.1) may have important consequences for the one-electron energy levels in bulk semiconductors. Subsequently, SO coupling effects in a bulk zinc blende structure were discussed in two classic papers by

¹ We use the term “orbital motion” for Bloch electrons in order to emphasize the close similarity we have here between atomic physics and solid-state physics.

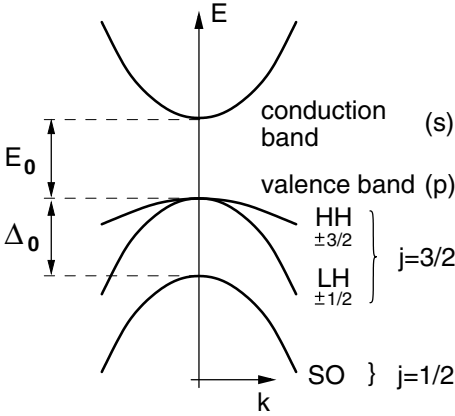


Fig. 1.1. Qualitative sketch of the band structure of GaAs close to the fundamental gap

Parmenter [5] and Dresselhaus [6]. Unlike the diamond structure of Si and Ge, the zinc blende structure does not have a center of inversion, so that we can have a spin splitting of the electron and hole states at nonzero wave vectors \mathbf{k} even for a magnetic field $B = 0$. In the inversion-symmetric Si and Ge crystals we have, on the other hand, a twofold degeneracy of the Bloch states for every wave vector \mathbf{k} . Clearly, the spin splitting of the Bloch states in the zinc blende structure must be a consequence of SO coupling, because otherwise the spin degree of freedom of the Bloch electrons would not “know” whether it was moving in an inversion-symmetric diamond structure or an inversion-asymmetric zinc blende structure (see also Sect. 6.1).

In solid-state physics, it is a considerable task to analyze a microscopic Schrödinger equation for the Bloch electrons in a lattice-periodic crystal potential.² Often, band structure calculations for electron states in the vicinity of the fundamental gap are based on the $\mathbf{k} \cdot \mathbf{p}$ method and the envelope function approximation. Here SO coupling enters solely in terms of matrix elements of the operator (1.1) between bulk band-edge Bloch states, such as the SO gap Δ_0 in Fig. 1.1. These matrix elements provide a convenient parameterization of SO coupling effects in semiconductor structures.

Besides the $B = 0$ spin splitting in inversion-asymmetric semiconductors, a second important effect of SO coupling shows up in the Zeeman splitting of electrons and holes. The Zeeman splitting is characterized by effective g factors g^* that can differ substantially from the free-electron g factor $g_0 = 2$. This was first noted by Roth et al. [7], who showed using the $\mathbf{k} \cdot \mathbf{p}$ method that g^* of electrons can be parameterized using the SO gap Δ_0 .

² We note that in a solid (as in atomic physics) the dominant contribution to the Pauli SO term (1.1) stems from the motion in the bare Coulomb potential in the innermost region of the atomic cores, see Sect. 3.4. In a pseudopotential approach the bare Coulomb potential in the core region is replaced by a smooth pseudopotential.

1.2 Spin–Orbit Coupling in Quasi-Two-Dimensional Systems

Quasi-two-dimensional (2D) semiconductor structures such as QWs and heterostructures are well suited for a systematic investigation of SO coupling effects. Increasing perfection in crystal growth techniques such as molecular-beam epitaxy (MBE) and metal-organic chemical vapor deposition (MOCVD) allows one to design and investigate tailor-made quantum structures (“do-it-yourself quantum mechanics” [8]). Moreover, the size quantization in these systems gives rise to many completely new phenomena that do not exist in three-dimensional semiconductors. We remark here that whenever we talk about 2D systems, in fact we have in mind *quasi*-2D systems with a finite spatial extension in the z direction, the growth direction of these systems.

A detailed understanding of SO-related phenomena in 2D systems is important both in fundamental research and in applications of 2D systems in electronic devices. For example, for many years it was accepted that no metallic phase could exist in a disordered 2D carrier system. This was due to the scaling arguments of Abrahams et al. [9] and the support of subsequent experiments [10]. In the past few years, however, experiments on high-quality 2D systems have provided us with reason to revisit the question of whether or not a metallic phase can exist in 2D systems [11]. At present, these new findings are controversial [12]. Following the observation that an in-plane magnetic field suppresses the metallic behavior, it was suggested by Pudalov that the metallic behavior could be a consequence of SO coupling [13]. Using samples with tunable spin splitting, it could be shown that the metallic behavior of the resistivity depends on the symmetry of the confinement potential and the resulting spin splitting of the valence band [14].

Datta and Das [15] have proposed a new type of electronic device where the current modulation arises from spin precession due to the SO coupling in a narrow-gap semiconductor, while magnetized contacts are used to preferentially inject and detect specific spin orientations. Recently, extensive research aiming at the realization of such a device has been under way [16].

1.3 Overview

In Chap. 2, we start with a general discussion of the band structure of semiconductors and its description by means of the $\mathbf{k} \cdot \mathbf{p}$ method (Sect. 2.1) [17] and its generalization, the envelope function approximation (EFA, Sect. 2.2) [18, 19]. It is an important advantage of these methods that not only can they cope with external electric and magnetic fields but they can also describe, for example, the modifications in the band structure due to strain (Sect. 2.3) [20] or to the paramagnetic interaction in semimagnetic semiconductors (Sect. 2.4) [21]. The “bare” $\mathbf{k} \cdot \mathbf{p}$ and EFA Hamiltonians are infinite-

dimensional matrices. However, quasi-degenerate perturbation theory (Appendix B) and the theory of invariants (Sect. 2.5) [20] enable one to derive a hierarchy of finite-dimensional $\mathbf{k} \cdot \mathbf{p}$ Hamiltonians for the accurate description of the band structure $E_n(\mathbf{k})$ close to an expansion point $\mathbf{k} = \mathbf{k}_0$.

In Chap. 3, we introduce the extended Kane model [22] which is the $\mathbf{k} \cdot \mathbf{p}$ model that will be used in the work described in this book. We start with some general symmetry considerations using a simple tight-binding picture (Sect. 3.1). On the basis of an invariant decomposition corresponding to the irreducible representations of the point group T_d (Sect. 3.2), we present in Sect. 3.3 the invariant expansion for the extended Kane model. Owing to the central importance of the SO gap Δ_0 in the present work, Sect. 3.4 is devoted to a discussion of this quantity. In Sect. 3.5 we discuss the relation between the 14×14 extended Kane model and simplified $\mathbf{k} \cdot \mathbf{p}$ models of reduced size, such as the 8×8 Kane model and the 4×4 Luttinger Hamiltonian. Finally, we discuss in Sect. 3.6 the symmetry hierarchies that can be obtained when the Kane model is decomposed into terms with higher and lower symmetry [23, 24]. They provide a natural language for our discussions in subsequent chapters of the relative importance of different terms. All relevant tables for the extended Kane model are summarized in Appendix C.

While Chap. 3 reviews the bulk band structure, Chap. 4 is devoted to electron and hole states in quasi-2D systems [25]. Section 4.1 discusses the EFA for quasi-2D systems. Then we review, for later reference, the density of states of a 2D system (Sect. 4.2) and the most elementary model within the EFA, the effective-mass approximation (EMA), which assumes a simple nondegenerate, isotropic band (Sect. 4.3). In subsequent chapters the EMA is often used as a starting point for developing more elaborate models. An in-plane magnetic field can be naturally included in the general concepts of Sect. 4.1, which are based on plane wave states for the in-plane motion. On the other hand, a perpendicular field leads to the formation of completely quantized Landau levels to be discussed in Sect. 4.4. As an example of the concepts introduced in Chap. 3 we discuss next the subband dispersion of quasi-2D hole systems with different crystallographic growth directions (Sect. 4.5). The numerical schemes are complemented by an approximate, fully analytical solution of the EFA multiband Hamiltonian based on Löwdin partitioning (Sect. 4.6). In subsequent chapters we see that this approach provides many insights that are difficult to obtain by means of numerical calculations.

In Chap. 5, we give a general overview of the origin of SO coupling effects in quasi-2D systems. In Sect. 5.1 we recapitulate, from relativistic quantum mechanics, the derivation of the Pauli equation from the Dirac equation [1]. In Sect. 5.2 we compare these well-known results with the effective Hamiltonians we obtain from a decoupling of conduction and valence band states starting from a simplified 8×8 Kane Hamiltonian. In analogy with the Pauli equation, we obtain a conduction band Hamiltonian that contains both an effective Zeeman term and an SO term for $B = 0$ spin splitting.

In Chap. 6, we analyze the zero-magnetic-field spin splitting in inversion-asymmetric 2D systems. The general connection between $B = 0$ spin splitting and SO interaction is discussed in Sect. 6.1. Usually we have two contributions to $B = 0$ spin splitting. The first one originates from the bulk inversion asymmetry (BIA) of the zinc blende structure (Sect. 6.2) [6]. The second one is the Rashba spin splitting due to the structure inversion asymmetry (SIA) of semiconductor quantum structures (Sect. 6.3) [26, 27]. It turns out that the Rashba spin splitting of 2D hole systems is very different from the more familiar case of Rashba spin splitting in 2D electron systems [28]. In Sect. 6.4 we focus on the interplay between BIA and SIA, as well as on the density dependence of $B = 0$ spin splitting. A third contribution to $B = 0$ spin splitting is discussed in Sect. 6.5, which can be traced back to the particular properties of the heterointerfaces in quasi-2D systems [29]. The $B = 0$ spin splitting does not lead to a magnetic moment of the 2D system. Nevertheless, we obtain a spin orientation of the single-particle states that varies as a function of the in-plane wave vector (Sect. 6.6). In Sect. 6.7 we give a brief overview of common experimental techniques for measuring $B = 0$ spin splitting. As an example, in Sect. 6.8 we compare calculated spin splittings [30] with Raman experiments by Jusserand et al. [31].

In Chap. 7, we review the anisotropic Zeeman splitting in 2D systems. First we discuss 2D electron systems (Sect. 7.1), where size quantization yields a significant difference between the effective g factor for a perpendicular and an in-plane magnetic field [32]. In inversion-asymmetric systems (growth direction [001]), we can even have an anisotropy of the Zeeman splitting with respect to different in-plane directions of the magnetic field (Sect. 7.2) [33]. Next we focus on 2D hole systems with low-symmetry growth directions (Sect. 7.3). It is shown both theoretically and experimentally that coupling the spin degree of freedom to the anisotropic orbital motion of a 2D hole system gives rise to a highly anisotropic Zeeman splitting with respect to different orientations of an in-plane magnetic field \mathbf{B} relative to the crystal axes [34]. Finally, Sect. 7.4 is devoted to 2D hole systems with a growth direction [001] where the Zeeman splitting in an in-plane magnetic field is suppressed [35].

In Chap. 8, we analyze cyclotron spectra in 2D electron and hole systems. These spectra reveal the complex nature of the Landau levels in these systems, as well as the high level of accuracy that can be achieved in the theoretical description and interpretation of the Landau-level structure of 2D systems. We start with a general introduction to cyclotron resonance in quasi-2D systems (Sect. 8.1) [23]. In Sect. 8.2 we discuss the spin splitting of the cyclotron resonance due to the energy dependence of the effective g factor g^* in narrow-gap InAs QWs [36, 37, 38]. In Sect. 8.3 we present the calculated absorption spectra for 2D hole systems in strained Ge-Si_xGe_{1-x} QWs [39] which are in good agreement with the experimental data of Engelhardt et al. [40]. Finally, we discuss Landau levels in inversion-asymmetric systems,

where the interplay between the Zeeman term and the Dresselhaus term can give rise to zero spin splitting at a finite magnetic field [41].

In Chap. 9, we discuss magneto-oscillations such as the Shubnikov–de Haas effect. The frequencies of these oscillations have long been used to measure the unequal population of spin-split 2D subbands in inversion-asymmetric systems [42]. In Sect. 9.1 we briefly explain the origin of magneto-oscillations periodic in $1/B$. Next we present some surprising results of both experimental and theoretical investigations [14, 43] demonstrating that, in general, the magneto-oscillations are not simply related to the $B = 0$ spin splitting (Sect. 9.2). It is shown in Sect. 9.3 that these anomalous oscillations reflect the nonadiabatic spin precession of a classical spin vector along the cyclotron orbit [44].

Our conclusions are presented in Chap. 10. Some notations and symbols used frequently in this book are summarized in Appendix A.

Throughout, this work we make extensive use of group-theoretical arguments. An introduction to group theory in solid-state physics can be found, for example, in [45]. A very thorough discussion of group theory and its application to semiconductor band structure is given in [20]. We denote the irreducible representations of the crystallographic point groups in the same way as Koster et al. [46]; see also Chap. 2 of [47].

References

1. J.J. Sakurai: *Advanced Quantum Mechanics* (Addison-Wesley, Reading, MA, 1967) 62, 63, 1, 4
2. J.C. Slater: *Quantum Theory of Atomic Structure*, Vol. 2 (McGraw-Hill, New York, 1960) 27, 1
3. R.J. Elliot: See E.N. Adamas, II, Phys. Rev. **92**, 1063 (1953), reference 7 1
4. G. Dresselhaus, A.F. Kip, C. Kittel: Phys. Rev. **95**, 568–569 (1954) 1
5. R.H. Parmenter: Phys. Rev. **100**(2), 573–579 (1955) 72, 119, 2
6. G. Dresselhaus: Phys. Rev. **100**(2), 580–586 (1955) 24, 69, 71, 72, 2, 5
7. L.M. Roth, B. Lax, S. Zwerdling: Phys. Rev. **114**, 90 (1959) 14, 56, 131, 141, 2
8. L. Esaki: “The evolution of semiconductor quantum structures in reduced dimensionality – do-it-yourself quantum mechanics”, in *Electronic Properties of Multilayers and Low-Dimensional Semiconductor Structures*, ed. by J.M. Chamberlain, L. Eaves, J.C. Portal (Plenum, New York, 1990), p. 1 3
9. E. Abrahams, P.W. Anderson, D.C. Licciardello, T.V. Ramkrishnan: Phys. Rev. Lett. **42**(10), 673–676 (1979) 3
10. D.J. Bishop, D.C. Tsui, R.C. Dynes: Phys. Rev. Lett. **44**(17), 1153–1156 (1980) 3
11. S.V. Kravchenko, G.V. Kravchenko, J.E. Furneaux, V.M. Pudalov, M. D’Iorio: Phys. Rev. B **50**(11), 8039–8042 (1994) 3
12. E. Abrahams, S.V. Kravchenko, M.P. Sarachik: Rev. Mod. Phys. **73**, 251–266 (2001) 3

13. V.M. Pudalov: Pis'ma Zh. Eksp. Teor. Fiz. **66**, 168–172 (1997). [JETP Lett. **66**, 175 (1997)] **70, 3**
14. S.J. Papadakis, E.P. De Poortere, H.C. Manoharan, M. Shayegan, R. Winkler: Science **283**, 2056 (1999) **77, 100, 104, 109, 143, 171, 172, 174, 177, 178, 3, 6**
15. S. Datta, B. Das: Appl. Phys. Lett. **56**(7), 665–667 (1990) **117, 118, 121, 3**
16. H. Ohno (Ed.): *Proceedings of the First International Conference on the Physics and Applications of Spin Related Phenomena in Semiconductors*, Vol. 10 of Physica E (2001) **3**
17. E.O. Kane: “The $\mathbf{k} \cdot \mathbf{p}$ method”, in *Semiconductors and Semimetals*, ed. by R.K. Willardson, A.C. Beer, Vol. 1 (Academic Press, New York, 1966), p. 75 **10, 25, 3**
18. J.M. Luttinger, W. Kohn: Phys. Rev. **97**(4), 869–883 (1955) **38, 201, 3**
19. J.M. Luttinger: Phys. Rev. **102**(4), 1030 (1956) **18, 28, 29, 88, 98, 99, 106, 131, 142, 158, 3**
20. G.L. Bir, G.E. Pikus: *Symmetry and Strain-Induced Effects in Semiconductors* (Wiley, New York, 1974) **15, 16, 18, 19, 98, 118, 201, 213, 3, 4, 6**
21. J. Kossut: “Band structure and quantum transport phenomena in narrow-gap diluted magnetic semiconductors”, in *Semiconductors and Semimetals*, ed. by R.K. Willardson, A.C. Beer, Vol. 25 (Academic Press, Boston, 1988), p. 183 **17, 3**
22. U. Rössler: Solid State Commun. **49**, 943 (1984) **21, 25, 26, 27, 29, 71, 4**
23. K. Suzuki, J.C. Hensel: Phys. Rev. B **9**(10), 4184–4218 (1974) **15, 17, 24, 31, 32, 43, 44, 151, 152, 158, 4, 5**
24. H.R. Trebin, U. Rössler, R. Ranvaud: Phys. Rev. B **20**(2), 686–700 (1979) **15, 22, 25, 31, 32, 43, 46, 48, 77, 98, 99, 151, 152, 158, 166, 209, 210, 212, 213, 214, 217, 4**
25. G. Bastard: *Wave Mechanics Applied to Semiconductor Heterostructures* (Les Editions de Physique, Les Ulis, 1988) **9, 13, 15, 4**
26. F.J. Ohkawa, Y. Uemura: J. Phys. Soc. Jpn. **37**, 1325 (1974) **35, 38, 65, 69, 78, 83, 5**
27. Y.A. Bychkov, E.I. Rashba: J. Phys. C: Solid State Phys. **17**, 6039–6045 (1984) **66, 69, 77, 78, 83, 165, 5**
28. R. Winkler: Phys. Rev. B **62**, 4245 (2000) **70, 81, 86, 96, 108, 109, 5**
29. I.L. Aleiner, E.L. Ivchenko: JETP Lett. **55**(11), 692–695 (1992) **110, 111, 112, 5**
30. L. Wissinger, U. Rössler, R. Winkler, B. Jusserand, D. Richards: Phys. Rev. B **58**, 15 375 (1998) **70, 78, 83, 122, 124, 5**
31. B. Jusserand, D. Richards, G. Allan, C. Priester, B. Etienne: Phys. Rev. B **51**, 4707 (1995) **70, 122, 123, 124, 125, 5**
32. E.L. Ivchenko, A.A. Kiselev: Sov. Phys. Semicond. **26**, 827 (1992) **58, 131, 132, 5**
33. V.K. Kalevich, V.L. Korenev: JETP Lett. **57**(9), 571–575 (1993) **134, 135, 5**
34. R. Winkler, S.J. Papadakis, E.P. De Poortere, M. Shayegan: Phys. Rev. Lett. **85**, 4574 (2000) **131, 139, 143, 145, 5**
35. H.W. van Kesteren, E.C. Cosman, W.A.J.A. van der Poel: Phys. Rev. B **41**(8), 5283–5292 (1990) **111, 112, 114, 131, 138, 141, 146, 5**
36. M.J. Yang, R.J. Wagner, B.V. Shanabrock, J.R. Waterman, W.J. Moore: Phys. Rev. B **47**, 6807 (1993) **151, 154, 155, 156, 5**
37. J. Scriba, A. Wixforth, J.P. Kotthaus, C. Bolognesi, C. Nguyen, H. Kroemer: Solid State Commun. **86**, 633 (1993) **151, 154, 155, 156, 157, 5**

- 38. R. Winkler: Surf. Sci. **361/362**, 411 (1996) [27](#), [155](#), [157](#), [5](#)
- 39. R. Winkler, M. Merkler, T. Darnhofer, U. Rössler: Phys. Rev. B **53**, 10 858 (1996) [86](#), [152](#), [158](#), [160](#), [161](#), [162](#), [163](#), [219](#), [5](#)
- 40. C.M. Engelhardt, D. Többen, M. Aschauer, F. Schäffler, G. Abstreiter, E. Gornik: Solid State Electron. **37**(4–6), 949–952 (1994) [157](#), [158](#), [159](#), [162](#), [5](#)
- 41. G. Lommer, F. Malcher, U. Rössler: Phys. Rev. Lett. **60**, 728 (1988) [78](#), [82](#), [83](#), [166](#), [6](#)
- 42. H.L. Störmer, Z. Schlesinger, A. Chang, D.C. Tsui, A.C. Gossard, W. Wiegmann: Phys. Rev. Lett. **51**, 126 (1983) [122](#), [171](#), [172](#), [6](#)
- 43. R. Winkler, S.J. Papadakis, E.P. De Poortere, M. Shayegan: Phys. Rev. Lett. **84**, 713 (2000) [172](#), [177](#), [180](#), [182](#), [188](#), [6](#)
- 44. S. Keppeler, R. Winkler: Phys. Rev. Lett. **88**, 046 401 (2002) [172](#), [183](#), [186](#), [188](#), [6](#)
- 45. W. Ludwig, C. Falter: *Symmetries in Physics* (Springer, Berlin, Heidelberg, 1988) [6](#)
- 46. G.F. Koster, J.O. Dimmock, R.G. Wheeler, H. Statz: *Properties of the Thirty-Two Point Groups* (MIT, Cambridge, MA, 1963) [21](#), [23](#), [47](#), [72](#), [166](#), [199](#), [6](#)
- 47. P.Y. Yu, M. Cardona: *Fundamentals of Semiconductors* (Springer, Berlin, Heidelberg, 1996) [21](#), [6](#)

2 Band Structure of Semiconductors

Because of its central importance for fundamental physics as well as for technological applications, the electronic structure of layered semiconductor structures has attracted much interest over the last two decades [1, 2]. In theoretical studies, methods based on the envelope function approximation are predominant [3], the reason being that the EFA allows a comprehensive description of electron- and hole-like states. It can cope with periodic or aperiodic geometries of quantum structures, as well as perturbations such as a magnetic field, strain, or a built-in or external potential. Details of the underlying crystal potential are included in terms of bulk band structure parameters.

The simplest approach within the EFA is the effective-mass approximation [3] which assumes a single, isotropic, parabolic band. It provides a basic insight into the electronic structure of inversion layers, heterojunctions, QWs and superlattices, but it fails to account for the subtleties which occur in semiconductor band structures such as nonparabolicity, spin splitting, and the coupling between heavy holes and light holes. All these details of bulk band structure can be described within the framework of $\mathbf{k} \cdot \mathbf{p}$ theory (Sect. 2.1) and its generalization in terms of the EFA (Sect. 2.2). It is an important advantage of these methods that not only can they cope with external electric and magnetic fields but also they can describe, for example, the modifications in the band structure due to strain (Sect. 2.3) or to the paramagnetic interaction in semimagnetic semiconductors (Sect. 2.4). The “bare” $\mathbf{k} \cdot \mathbf{p}$ and EFA Hamiltonians are infinite-dimensional matrices. However, quasi-degenerate perturbation theory (Appendix B) and the theory of invariants (Sect. 2.5) enable one to derive a hierarchy of finite-dimensional $\mathbf{k} \cdot \mathbf{p}$ Hamiltonians for the accurate description of the band structure $E_n(\mathbf{k})$ close to an expansion point $\mathbf{k} = \mathbf{k}_0$.

2.1 Bulk Band Structure and $\mathbf{k} \cdot \mathbf{p}$ Method

The most elementary model for the band structure of a direct semiconductor close to the fundamental energy gap is an isotropic parabolic dispersion for the conduction band ($E_c(\mathbf{k})$) and for the valence band ($E_v(\mathbf{k})$)

$$E_{c/v}(\mathbf{k}) = \pm \left(\frac{E_g}{2} + \frac{\hbar^2 k^2}{2m_{c/v}^*} \right), \quad (2.1)$$

where \mathbf{k} is the wave vector, E_g is the band gap, and m_c^* and m_v^* are the effective masses for the conduction and the valence band, respectively. In a more accurate and realistic model for the dispersion $E(\mathbf{k})$, we have to take into account details such as nonparabolicity, anisotropy, and the coupling between heavy holes (HH) and light holes (LH). A powerful and flexible approach for the investigation of these questions is the $\mathbf{k} \cdot \mathbf{p}$ method [4, 5, 6]. This method enables one to calculate with arbitrary precision the semiconductor band structure $E_\nu(\mathbf{k})$ in the vicinity of a given point \mathbf{k}_0 in reciprocal space.

The derivation of the $\mathbf{k} \cdot \mathbf{p}$ method is based on the Schrödinger equation for the Bloch functions $e^{i\mathbf{k} \cdot \mathbf{r}} u_{\nu\mathbf{k}}(\mathbf{r}) \equiv e^{i\mathbf{k} \cdot \mathbf{r}} \langle \mathbf{r} | \nu \mathbf{k} \rangle$ in the microscopic lattice-periodic crystal potential $V_0(\mathbf{r})$

$$\left[\frac{p^2}{2m_0} + V_0(\mathbf{r}) \right] e^{i\mathbf{k} \cdot \mathbf{r}} u_{\nu\mathbf{k}}(\mathbf{r}) = E_\nu(\mathbf{k}) e^{i\mathbf{k} \cdot \mathbf{r}} u_{\nu\mathbf{k}}(\mathbf{r}). \quad (2.2)$$

Here m_0 denotes the free-electron mass and ν is the band index. We can easily evaluate the effect of the kinetic-energy operator on the plane-wave part of the Bloch functions. In this way we obtain a Schrödinger equation for only the lattice-periodic parts $|\nu\mathbf{k}\rangle$ of the Bloch functions,

$$\left[\frac{p^2}{2m_0} + V_0 + \frac{\hbar^2 k^2}{2m_0} + \frac{\hbar}{m_0} \mathbf{k} \cdot \mathbf{p} \right] |\nu\mathbf{k}\rangle = E_\nu(\mathbf{k}) |\nu\mathbf{k}\rangle. \quad (2.3)$$

If we include the Pauli spin-orbit interaction (1.1) in (2.2), the lattice-periodic parts of the Bloch functions are two-component spinors $|n\mathbf{k}\rangle$ and the Schrödinger equation reads

$$\begin{aligned} \left[\frac{p^2}{2m_0} + V_0 + \frac{\hbar^2 k^2}{2m_0} + \frac{\hbar}{m_0} \mathbf{k} \cdot \boldsymbol{\pi} + \frac{\hbar}{4m_0^2 c^2} \mathbf{p} \cdot \boldsymbol{\sigma} \times (\nabla V_0) \right] |n\mathbf{k}\rangle \\ = E_n(\mathbf{k}) |n\mathbf{k}\rangle, \end{aligned} \quad (2.4)$$

where

$$\boldsymbol{\pi} := \mathbf{p} + \frac{\hbar}{4m_0 c^2} \boldsymbol{\sigma} \times \nabla V_0, \quad (2.5)$$

and $\boldsymbol{\sigma} = (\sigma_x, \sigma_y, \sigma_z)$ is the vector of Pauli spin matrices. Note that in the presence of SO interaction the spin quantum number σ is, by itself, not a good quantum number. We have only a common index n for the orbital motion and the spin degree of freedom, which classifies the bands according to the irreducible representations of the double group.

For a fixed wave vector \mathbf{k}_0 , the sets of lattice-periodic functions $\{|\nu\mathbf{k}_0\rangle\}$ and $\{|n\mathbf{k}_0\rangle\}$ provide a complete and orthonormal basis [7] for (2.3) and (2.4),

respectively. Therefore we can expand the kets $\{|n\mathbf{k}\rangle\}$ in terms of band edge¹ Bloch functions $\{|\nu\mathbf{0}\rangle\}$ times spin eigenstates $|\sigma\rangle$:

$$|n\mathbf{k}\rangle = \sum_{\substack{\nu' \\ \sigma'=\uparrow,\downarrow}} c_{n\nu'\sigma'}(\mathbf{k}) |\nu'\sigma'\rangle, \quad (2.6a)$$

where

$$|\nu'\sigma'\rangle := |\nu'\mathbf{0}\rangle \otimes |\sigma'\rangle. \quad (2.6b)$$

Here we have deliberately chosen as a basis the eigenfunctions of (2.3) *without* SO interaction, because it is often helpful to treat the SO interaction as a small perturbation (see (2.7) below). Now we multiply (2.4) from the left by $\langle\nu\sigma|$. By using the eigenvalue equation for $|\nu\sigma\rangle$, we obtain an algebraic eigenvalue problem for the dispersion $E_n(\mathbf{k})$, which depends only *explicitly* on the wave vector \mathbf{k} :

$$\sum_{\nu',\sigma'} \left\{ \left[E_{\nu'}(\mathbf{0}) + \frac{\hbar^2 k^2}{2m_0} \right] \delta_{\nu\nu'} \delta_{\sigma\sigma'} + \frac{\hbar}{m_0} \mathbf{k} \cdot \mathbf{P}_{\sigma\sigma'}^{\nu\nu'} + \Delta_{\sigma\sigma'}^{\nu\nu'} \right\} c_{n\nu'\sigma'}(\mathbf{k}) = E_n(\mathbf{k}) c_{n\nu\sigma}(\mathbf{k}), \quad (2.7)$$

where

$$\mathbf{P}_{\sigma\sigma'}^{\nu\nu'} := \langle\nu\sigma|\boldsymbol{\pi}|\nu'\sigma'\rangle, \quad (2.8a)$$

$$\Delta_{\sigma\sigma'}^{\nu\nu'} := \frac{\hbar}{4m_0^2 c^2} \langle\nu\sigma|[\mathbf{p} \cdot \boldsymbol{\sigma} \times (\nabla V_0)]|\nu'\sigma'\rangle. \quad (2.8b)$$

In the coupled equations (2.7), the off-diagonal terms $(\hbar/m_0) \mathbf{k} \cdot \mathbf{P}_{\sigma\sigma'}^{\nu\nu'}$ result in a mixing of the band edge states $|\nu\mathbf{0}\rangle$ that becomes stronger the larger \mathbf{k} is and the closer in energy the band edges $E_\nu(\mathbf{0})$ are. Often we can neglect the SO interaction in (2.5) and (2.8a) so that we have $\boldsymbol{\pi} = \mathbf{p}$ and $\mathbf{P}_{\sigma\sigma'}^{\nu\nu'} = \delta_{\sigma\sigma'} \mathbf{P}_{\nu\nu'}$.

In general, the matrix elements of the SO interaction $\Delta_{\sigma\sigma'}^{\nu\nu'}$ result in a splitting of the degenerate energy levels $E_\nu(\mathbf{k})$ even at $\mathbf{k} = \mathbf{0}$. However, a more careful analysis requires that we take into account the symmetries of the bands (see Chap. 3). For example, without spin the p-like states at the valence band edge of a semiconductor such as GaAs are threefold degenerate (orbital angular momentum $l = 1$). Including spin, the SO interaction splits the sixfold degenerate states into a fourfold degenerate subspace, with total angular momentum $j = 3/2$ for the HH and LH states (Γ_8^v) and $j = 1/2$ for the spin-orbit split-off states (Γ_7^v). For the s-like conduction band (Γ_6^c), we have $\Delta_{\sigma\sigma'}^{cc'} = 0$.

A diagonalization of (2.7) yields the exact dispersion relation $E_n(\mathbf{k})$ and expansion coefficients $c_{n\nu'\sigma'}(\mathbf{k})$ for all values of \mathbf{k} and all band indices n .

¹ In many semiconductors, the valence band maximum and the conduction band minimum are at the Γ point $\mathbf{k}_0 = \mathbf{0}$. Therefore it is advantageous to expand the band structure about this extremal point. However, it is straightforward to apply the method to any other expansion point $\mathbf{k}_0 \neq \mathbf{0}$.

However, in many applications of the $\mathbf{k} \cdot \mathbf{p}$ method we are interested only in a few adjacent bands ($n = 1, \dots, N$), for which we want to know the dispersion relation $E_n(\mathbf{k})$ only in the close vicinity of the expansion point $\mathbf{k}_0 = \mathbf{0}$ (i.e. $|\mathbf{k}| \ll 2\pi/a$ where a is the lattice constant). Therefore, the $\mathbf{k} \cdot \mathbf{p}$ interaction and SO interaction are fully taken into account only for those N bands, whereas the contributions of the remote bands are considered by means of Löwdin perturbation theory (see Appendix B) with the off-diagonal terms $(\hbar/m_0) \mathbf{k} \cdot \mathbf{P}_{\sigma\sigma'}^{\nu\nu'}$ taken as small perturbations. This approach results in an N -dimensional $\mathbf{k} \cdot \mathbf{p}$ Hamiltonian which contains extra terms of higher order in \mathbf{k} .

If we restrict ourselves to a diagonalization of (2.7) by means of second-order perturbation theory we obtain (neglecting spin)

$$E_\nu(\mathbf{k}) = E_\nu(\mathbf{0}) + \frac{\hbar^2 k^2}{2m_\nu^*}, \quad (2.9)$$

where

$$\frac{m_0}{m_\nu^*} = 1 + \frac{2}{m_0} \sum_{\nu'} \frac{P_{\nu\nu'}^2}{E_\nu(\mathbf{0}) - E_{\nu'}(\mathbf{0})}. \quad (2.10)$$

The dominant contribution in the sum stems from the coupling $\mathbf{P}_{\nu\nu'}$ of the band ν to nearby bands ν' . Thus, for the effective masses $m_{c/v}^*$ in (2.1), it is often a good approximation to use

$$\frac{m_0}{m_{c/v}^*} \approx \frac{2}{m_0} \frac{P_{cv}^2}{E_g}, \quad (2.11)$$

i.e. the effective masses $m_c^* \approx m_v^*$ are proportional to the fundamental band gap $E_g = E_c - E_v$. Here E_c denotes the minimum of the conduction band and E_v is the maximum of the valence band.²

2.2 The Envelope Function Approximation

The envelope function approximation allows one to describe electron and hole states in the presence of electric and magnetic fields that vary slowly on the length scale of the lattice constant (see, however, Sect. 4.1.2). These fields can be internal, such as the fields of crystal defects [8], or the fields can be applied externally, by means of gates and external magnets, for example.

By analogy with (2.2), we consider the Schrödinger equation

$$\left[\frac{(-i\hbar\nabla + e\mathbf{A})^2}{2m_0} + V_0(\mathbf{r}) + \frac{\hbar}{4m_0^2c^2} (-i\hbar\nabla + e\mathbf{A}) \cdot \boldsymbol{\sigma} \times (\nabla V_0) \right. \\ \left. + V(\mathbf{r}) + \frac{g_0}{2} \mu_B \boldsymbol{\sigma} \cdot \mathbf{B} \right] \Psi(\mathbf{r}) = E \Psi(\mathbf{r}), \quad (2.12)$$

² Within the Kane model discussed in Chap. 3, (2.11) can be a useful approximation for the Γ_6^c conduction band and for the LH valence band. See also (4.39a).

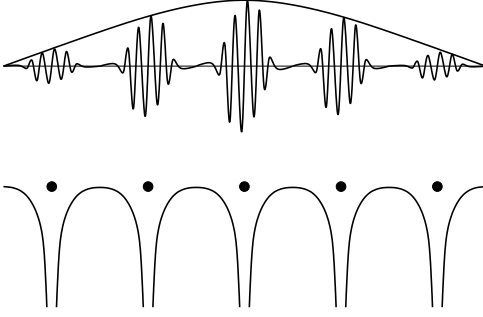


Fig. 2.1. Qualitative sketch of a wave function (2.13) in the envelope function approximation. The lower part shows the crystal potential $V_0(\mathbf{r})$. The upper part shows the slowly varying envelope function $\psi_{\nu\sigma}(\mathbf{r})$ that modulates the quickly oscillating lattice-periodic part $u_{\nu\mathbf{0}}(\mathbf{r})$ of the Bloch function

with a microscopic lattice-periodic crystal potential $V_0(\mathbf{r})$, an additional, slowly varying potential $V(\mathbf{r})$, and a vector potential $\mathbf{A} = \mathbf{A}(\mathbf{r})$, which gives rise to a magnetic field $\mathbf{B} = \nabla \times \mathbf{A}$. The symbol $\mu_B = e\hbar/(2m_0)$ denotes the Bohr magneton, e is the electron charge, and $g_0 = 2$ is the g factor of a free electron. Note that the dominant contribution to the SO interaction originates in the strong Coulomb potential $V_0(\mathbf{r})$ of the atomic core regions (see Sect. 3.4). Therefore, we need not include $V(\mathbf{r})$ in the SO interaction in (2.12).

Similarly to the derivation of the $\mathbf{k} \cdot \mathbf{p}$ method in the preceding section, we expand the wave function $\Psi(\mathbf{r})$ in terms of band-edge Bloch functions $u_{\nu'\mathbf{0}}(\mathbf{r}) \equiv \langle \mathbf{r} | \nu' \mathbf{0} \rangle$ times spin eigenstates $|\sigma'\rangle$:

$$\Psi(\mathbf{r}) = \sum_{\nu', \sigma'} \psi_{\nu'\sigma'}(\mathbf{r}) u_{\nu'\mathbf{0}}(\mathbf{r}) |\sigma'\rangle. \quad (2.13)$$

The position-dependent expansion coefficients $\psi_{\nu'\sigma'}(\mathbf{r})$ modulate the quickly oscillating Bloch functions $u_{\nu'\mathbf{0}}(\mathbf{r})$. As this modulation is slowly varying on the length scale of the lattice constant, the expansion coefficients $\psi_{\nu'\sigma'}(\mathbf{r})$ are called *envelope functions* [3]. We insert (2.13) into (2.12), multiply from the left by $\langle \sigma | u_{\nu\mathbf{0}}^*(\mathbf{r})$, and integrate over one unit cell of the lattice. If $V(\mathbf{r})$, $\mathbf{A}(\mathbf{r})$, and $\psi_{\nu'\sigma'}(\mathbf{r})$ are slowly varying within one unit cell, we can take them out of the integral as constant factors. We obtain

$$\begin{aligned} \sum_{\nu', \sigma'} \left\{ \left[E_{\nu'}(\mathbf{0}) + \frac{(-i\hbar\nabla + e\mathbf{A})^2}{2m_0} + V(\mathbf{r}) \right] \delta_{\nu\nu'} \delta_{\sigma\sigma'} \right. \\ \left. + \frac{1}{m_0} (-i\hbar\nabla + e\mathbf{A}) \cdot \mathbf{P}_{\sigma\sigma'}^{\nu\nu'} \right. \\ \left. + \Delta_{\sigma\sigma'}^{\nu\nu'} + \frac{g_0}{2} \mu_B \boldsymbol{\sigma} \cdot \mathbf{B} \delta_{\nu\nu'} \right\} \psi_{\nu'\sigma'}(\mathbf{r}) = E \psi_{\nu\sigma}(\mathbf{r}). \end{aligned} \quad (2.14)$$

This *multiband* (or *EFA*) *Hamiltonian* is a system of coupled differential equations, the eigenfunctions of which are the multicomponent envelope functions or spinors $\boldsymbol{\Psi}(\mathbf{r}) = (\psi_{\nu\sigma}(\mathbf{r}))$. A wave function (2.13) is sketched in Fig. 2.1.

Once again, we can use quasi-degenerate perturbation theory (Appendix B) to convert the infinite-dimensional eigenvalue problem (2.14) into a tractable

finite-dimensional eigenvalue problem. Apparently, we have here a close similarity between the $\mathbf{k} \cdot \mathbf{p}$ Hamiltonian (2.7) and the multiband Hamiltonian (2.14), because both Hamiltonians depend on the same set of parameters $P_{\sigma\sigma'}^{\nu\nu'}$ and $\Delta_{\sigma\sigma'}^{\nu\nu'}$. It is often argued that one can obtain the EFA Hamiltonian from the corresponding $\mathbf{k} \cdot \mathbf{p}$ Hamiltonian by setting³

$$\hbar \mathbf{k} = \mathbf{p} = -i\hbar \nabla + e\mathbf{A} \quad (2.15)$$

and adding the potential $V(\mathbf{r})$ and the Zeeman term $(g_0/2)\mu_B \boldsymbol{\sigma} \cdot \mathbf{B}$ to the diagonal. Here, $\hbar \mathbf{k} = \mathbf{p}$ is the operator of *kinetic* momentum. It must be distinguished from the operator of *canonical* momentum

$$\hbar \mathbf{k} = \mathbf{p} = -i\hbar \nabla. \quad (2.16)$$

If $\mathbf{A} = 0$ we have, of course, $\mathbf{k} = \mathbf{k}$. If also $V(\mathbf{r}) = 0$, the operator \mathbf{k} is equivalent to the vector \mathbf{k} in Sect. 2.1.

It is important to note that in the presence of a magnetic field \mathbf{B} the components of the operator \mathbf{k} no longer commute, i.e. we have

$$\mathbf{k} \times \mathbf{k} = \frac{e}{i\hbar} \mathbf{B}, \quad (2.17)$$

independent of any particular gauge for the magnetic field \mathbf{B} . Likewise, the operator \mathbf{k} and the potential $V(\mathbf{r})$ do not commute:

$$[\mathbf{k}, V(\mathbf{r})] = [\mathbf{k}, V(\mathbf{r})] = -i\nabla V(\mathbf{r}) = -ie\mathcal{E}(\mathbf{r}), \quad (2.18)$$

where $\mathcal{E}(\mathbf{r})$ is the electric field.⁴ In the finite-dimensional EFA Hamiltonian obtained by Löwdin partitioning, we thus have to distinguish between terms that are symmetric and antisymmetric in the noncommuting quantities \mathbf{k} and $V(\mathbf{r})$. While the former are present in both the finite-dimensional $\mathbf{k} \cdot \mathbf{p}$ Hamiltonian and the finite-dimensional EFA Hamiltonian, the latter are present only in the EFA Hamiltonian. The effective masses (2.10) that can be defined for the $\mathbf{k} \cdot \mathbf{p}$ Hamiltonian (2.7) become (the inverse of) the prefactors of the second-order terms symmetric in \mathbf{k} . In agreement with (2.17), the second-order terms antisymmetric in \mathbf{k} are proportional to the magnetic field \mathbf{B} like a Zeeman term, so that the corresponding prefactor can be identified with an effective g factor g^* [11]. Similarly, higher-order terms antisymmetric in the wave vector \mathbf{k} and in the potential $V(\mathbf{r})$ give rise to the Rashba term; see Sect. 6.3. Obviously, the antisymmetric terms are not present in a decomposition of the $\mathbf{k} \cdot \mathbf{p}$ Hamiltonian (2.7). Therefore, the simple substitution (2.15) is valid only for the infinite-dimensional EFA Hamiltonian (2.14). A detailed discussion of the new terms that emerge from the noncommutativity of \mathbf{k} and $V(\mathbf{r})$ will be given in subsequent chapters.

³ We follow the common practice whereby \mathbf{k} denotes both the wave vector and (apart from \hbar) the operator of kinetic momentum.

⁴ In layered structures, the effective mass m^* and the other band parameters become position-dependent (cf. Sect. 4.1.2), so that \mathbf{k} and m^* do not commute either; see [9, 10].

In second-order Löwdin perturbation theory a nondegenerate, isotropic, parabolic band (2.9) gives rise to the *effective-mass Hamiltonian* [3]

$$H = \frac{(-i\hbar\nabla + e\mathbf{A})^2}{2m_n^*} + V(\mathbf{r}) + \frac{g_n^*}{2}\mu_B \boldsymbol{\sigma} \cdot \mathbf{B} , \quad (2.19)$$

i.e. we treat the crystal electrons in the n th band like free particles with an effective mass m_n^* and an effective g factor g_n^* , which are moving in an external potential $V(\mathbf{r})$. We note that a justification of the effective-mass Hamiltonian (2.19) from a many-particle standpoint is given in [12].

In general, (2.8) provides only a formal definition of the momentum matrix elements $\mathbf{P}_{\sigma\sigma'}^{\nu\nu'}$ and SO energies $\Delta_{\sigma\sigma'}^{\nu\nu'}$. In real applications these parameters, as well as the band gaps $E_\nu(\mathbf{0})$, are usually chosen such that they give the best agreement with experimental data such as optical spectra, cyclotron resonance data [13], and the hydrogenic spectra of shallow acceptor and donor states [14]. The energy gaps $E_\nu(\mathbf{0})$ and spin-orbit gaps $\Delta_{\sigma\sigma'}^{\nu\nu'}$ can often be extracted directly from the experimental data. The appropriate numerical values of the momentum matrix elements $\mathbf{P}_{\sigma\sigma'}^{\nu\nu'}$ can be derived from relations such as (2.11) by using the measured values of m_n^* and g_n^* , which are tabulated for all important semiconductors [15]. When the Hamiltonian (2.14) is applied to semiconductor quantum structures it can be regarded as parameter-free once these quantities are known, e.g. by fitting the parameters to independent experimental data obtained for the bulk material.⁵

2.3 Band Structure in the Presence of Strain

When stress is applied to a semiconductor, the deformation of the crystal results in shifts and splittings of the energy levels. External pressure and strain are thus powerful tools to study the band structure of semiconductors [16, 17]. Another example is provided by lattice-mismatched semiconductor heterostructures, where the internal biaxial strain results in a characteristic modification of the subband levels. Here we discuss how pressure and strain can be included in $\mathbf{k} \cdot \mathbf{p}$ theory in a systematic way [18].

Application of stress to a crystal lowers the symmetry of the crystal potential V_0 . But the space group \mathcal{G}' of the strained crystal is, in general, not a subgroup of the space group \mathcal{G} of the unperturbed system. Therefore, a simple perturbation expansion is not possible [18]. However, it is possible to introduce a “deformed” coordinate system

$$r'_i = \sum_j (\delta_{ij} - \varepsilon_{ij}) r_j , \quad (2.20a)$$

which implies

⁵ Strictly speaking, in semiconductor quantum structures new parameters, which characterize the heterointerfaces, enter the multiband Hamiltonian. The most important new parameter is the band offset (see also Sect. 6.5 and [9, 10]).

$$p'_i = \sum_j (\delta_{ij} + \varepsilon_{ij}) p_j , \quad (2.20b)$$

$$k'_i = \sum_j (\delta_{ij} + \varepsilon_{ij}) k_j . \quad (2.20c)$$

Here ε denotes the strain tensor. The Bravais lattice of the strained crystal in the new coordinate system then coincides with that of the unstrained crystal in the old coordinate system. Therefore \mathcal{G}' is a subgroup of \mathcal{G} . We obtain a splitting of energy levels, which follows from the decomposition of the irreducible representations of \mathcal{G} in terms of the irreducible representations of the subgroup \mathcal{G}' [18].

Returning to the old notation, i.e. making the change $\mathbf{r}' \rightarrow \mathbf{r}$, the deformed crystal potential $V_\varepsilon[(1 + \varepsilon)\mathbf{r}]$ has the same periodicity as the unperturbed potential $V_0(\mathbf{r})$. Therefore, we can expand $V_\varepsilon(\mathbf{r})$ in a series in terms of ε ,

$$V_\varepsilon[(1 + \varepsilon)\mathbf{r}] = V_0(\mathbf{r}) + \sum_{ij} V_{ij}(\mathbf{r}) \varepsilon_{ij} + \dots , \quad (2.21a)$$

where

$$V_{ij} := \frac{1}{2 - \delta_{ij}} \lim_{\varepsilon \rightarrow 0} \frac{V_\varepsilon[(1 + \varepsilon)\mathbf{r}] - V_0(\mathbf{r})}{\varepsilon_{ij}} . \quad (2.21b)$$

Restricting ourselves to the terms linear in the strain ε , we obtain, instead of (2.4)

$$\begin{aligned} & \left\{ \frac{p^2}{2m_0} + V_0 + \frac{\hbar^2 k^2}{2m_0} + \frac{\hbar}{m_0} \mathbf{k} \cdot \boldsymbol{\pi} + \frac{\hbar}{4m_0^2 c^2} (\nabla V_0) \times \mathbf{p} \cdot \boldsymbol{\sigma} \right. \\ & + \sum_{ij} \left(-\frac{p_i p_j}{m_0} + V_{ij} \right) \varepsilon_{ij} - \frac{\hbar^2}{m_0} \mathbf{k} \varepsilon \mathbf{k} - \frac{2\hbar}{m_0} \mathbf{k} \varepsilon \boldsymbol{\pi} \\ & + \frac{\hbar}{4m_0^2 c^2} \left[\sum_{ij} \varepsilon_{ij} (\nabla V_{ij}) \times (\mathbf{p} + \hbar \mathbf{k}) \cdot \boldsymbol{\sigma} \right. \\ & \quad \left. \left. - (\varepsilon \nabla V_0) \times \mathbf{p} \cdot \boldsymbol{\sigma} - (\nabla V_0) \times (\varepsilon \mathbf{p}) \cdot \boldsymbol{\sigma} \right] \right\} |n\mathbf{k}\rangle_\varepsilon \\ & = E_n(\varepsilon, \mathbf{k}) |n\mathbf{k}\rangle_\varepsilon . \end{aligned} \quad (2.22)$$

We can solve this equation analogously to (2.4). The most important new matrix elements proportional to ε are

$$\mathcal{V}_{ij \nu \nu'} = \left\langle \nu \sigma \left| -\frac{p_i p_j}{m_0} + V_{ij} \right| \nu' \sigma' \right\rangle , \quad (2.23)$$

they are called *deformation potentials*. The elements of the strain tensor ε_{ij} are c -numbers (not operators). Accordingly, we can express the matrix elements $\langle \nu \sigma | (2\hbar/m_0) \mathbf{k} \varepsilon \boldsymbol{\pi} | \nu' \sigma' \rangle$ and $(\hbar/4m_0^2 c^2) \langle \nu \sigma | (\varepsilon \nabla V_0) \times \mathbf{p} \cdot \boldsymbol{\sigma} + (\nabla V_0) \times (\varepsilon \mathbf{p}) \cdot \boldsymbol{\sigma} | \nu' \sigma' \rangle$ in terms of the matrix elements (2.8a) and (2.8b), thus apparently reducing the number of independent parameters in the $\mathbf{k} \cdot \mathbf{p}$ model (2.22) [19, 20]. However, we would like to note that such an approach must be used with caution. First, little can be said concerning the magnitude of

the remaining strain-dependent term in the SO interaction. Second, Löwdin partitioning results in additional terms proportional to $\mathbf{k} \cdot \boldsymbol{\varepsilon}$, the magnitude of which can be estimated only unsatisfactorily [16]. In general, it is necessary to evaluate the weight factors of the strain-induced terms independently from the terms present in the absence of strain.

2.4 The Paramagnetic Interaction in Semimagnetic Semiconductors

If manganese ions Mn^{2+} are introduced into II–VI or III–V semiconductors a huge Zeeman splitting is observed for conduction and valence band electrons that cannot be explained by conventional $\mathbf{k} \cdot \mathbf{p}$ theory ($g^* \simeq 100$; as a lowest-order approximation we can often neglect the Landau-level splitting here). The enhanced Zeeman splitting stems from the exchange interaction between the extended electronic states in the conduction and valence bands and the magnetic moments of the localized Mn 3d⁵ electrons. It can be described by a Kondo-like Hamiltonian [21]

$$H_{\text{ex}} = - \sum_m J(\mathbf{r} - \mathbf{R}_m) \mathbf{S}_m \cdot \boldsymbol{\sigma} . \quad (2.24)$$

Here $\boldsymbol{\sigma}$ is the spin operator of the electrons in the conduction and valence bands, \mathbf{S}_m is the operator for the total spin of an Mn 3d shell at the position \mathbf{R}_m , the function $J(\mathbf{r} - \mathbf{R}_m)$ describes the exchange interaction, and the sum runs over all Mn atoms m . Such systems are called *semimagnetic semiconductors* or *diluted magnetic semiconductors* (DMS).

In the framework of the $\mathbf{k} \cdot \mathbf{p}$ method we can take (2.24) into account as an additional term in (2.4). Similarly to the case of (2.8), we must evaluate the matrix elements of H_{ex} with respect to band-edge Bloch functions $|\nu\sigma\rangle$. These wave functions extend over the whole crystal, so that we can assume approximately that they feel the mean magnetic moment of all Mn 3d shells (*the mean-field approximation*), oriented parallel to the external magnetic field \mathbf{B} :

$$\langle \nu\sigma | H_{\text{ex}} | \nu'\sigma' \rangle \approx - \langle \nu\sigma | \sum_m J(\mathbf{r} - \mathbf{R}_m) | \nu'\sigma' \rangle \langle \mathbf{S} \rangle \langle \nu\sigma | \boldsymbol{\sigma} | \nu'\sigma' \rangle \quad (2.25a)$$

$$\approx - \langle \nu\sigma | J | \nu'\sigma' \rangle N_0 x \langle \mathbf{S} \rangle \langle \nu\sigma | \boldsymbol{\sigma} | \nu'\sigma' \rangle \quad (2.25b)$$

$$= - \delta_{\nu\nu'} \langle \nu | J | \nu \rangle N_0 x \langle \mathbf{S} \rangle \langle \sigma | \boldsymbol{\sigma} | \sigma' \rangle . \quad (2.25c)$$

The exchange integrals $\langle \nu | J | \nu \rangle$ are material-specific parameters, N_0 is the number of unit cells per unit volume, and x is the mole fraction of Mn^{2+} ions.

The expectation value $\langle \mathbf{S} \rangle$ of the spin of the Mn 3d shells can be described by a modified Brillouin function [22] for a spin $j = 5/2$:

$$\langle \mathbf{S} \rangle = \hat{e} S_0 B_{5/2} \left(\frac{5}{2} \frac{g_0 \mu_B B}{k_B T_{\text{eff}}} \right). \quad (2.26)$$

Here μ_B is the Bohr magneton, $g_0 = 2$, k_B is Boltzmann's constant, and \hat{e} is a unit vector parallel to the direction of the external magnetic field \mathbf{B} . The effective spin S_0 and the effective temperature $T_{\text{eff}} := T + T_0$ take into account the antiferromagnetic interaction between the Mn^{2+} ions. For higher Mn concentrations x , the antiferromagnetic coupling results in a saturation of the Zeeman splitting [22]. In the paramagnetic limit of small x , we have $T_0 = 0$ and $S_0 = 5/2$. The Brillouin function $B_j(y)$ is defined as

$$B_j(y) = \frac{j + 1/2}{j} \coth \left(\frac{j + 1/2}{j} y \right) - \frac{1}{2j} \coth \left(\frac{y}{2j} \right). \quad (2.27)$$

2.5 Theory of Invariants

Using Löwdin perturbation theory, described in Appendix B, the infinite-dimensional eigenvalue problems (2.7) and (2.14) can be transformed into finite-dimensional eigenvalue problems. The $\mathbf{k} \cdot \mathbf{p}$ interaction with the remote bands that are not taken exactly into account will then result in new terms of higher order in \mathbf{k} .

A second, very systematic approach to the construction of the finite-dimensional $\mathbf{k} \cdot \mathbf{p}$ Hamiltonian is based on the *theory of invariants* [18, 23]. This approach utilizes the fact that, independent of microscopic details, the Hamiltonian must be invariant under all symmetry operations of the problem. (For example, for an unperturbed zinc blende structure, we have the point group T_d .) Solely on the basis of this rather general symmetry argument, the theory of invariants allows one to decide which terms may appear in the Hamiltonian and which terms must vanish. Moreover, we can take additional terms into account that, for example, describe the effect of strain and external electric and magnetic fields. Here we shall summarize the main results of the theory of invariants, which are important in the present context.

In the following, $\mathcal{H}(\mathcal{K})$ denotes an N -dimensional multiband Hamiltonian, where \mathcal{K} represents a general tensor operator, which can depend on the components of the wave vector \mathbf{k} , the external electric and magnetic fields \mathcal{E} and \mathbf{B} , and the strain tensor ε . The symmetry of the Hamiltonian $\mathcal{H}(\mathcal{K})$ is characterized by a point group \mathcal{G} . Assuming that the basis functions of \mathcal{H} transform according to an N -dimensional (irreducible or reducible) matrix representation $\{\mathcal{D}(g) : g \in \mathcal{G}\}$, the invariance of \mathcal{H} under the symmetry operations g reads

$$\mathcal{D}(g) \mathcal{H}(g^{-1} \mathcal{K}) \mathcal{D}^{-1}(g) = \mathcal{H}(\mathcal{K}) \quad \forall g \in \mathcal{G}. \quad (2.28)$$

Obviously, the matrix equation (2.28) represents N^2 equations for the elements $\mathcal{H}_{ij}(\mathcal{K})$ of $\mathcal{H}(\mathcal{K})$. Indeed, these constraints allow one to construct $\mathcal{H}(\mathcal{K})$ [18].

First, the general tensor operator \mathcal{K} can be decomposed into irreducible tensor operators $\mathcal{K}^{(\delta, \mu)}$ that transform according to the irreducible representation Γ_δ of \mathcal{G} . The index μ distinguishes between different irreducible tensor operators that transform according to the same irreducible representations Γ_δ . Furthermore, $\mathcal{H}(\mathcal{K})$ can be decomposed into blocks $\mathcal{H}_{\alpha\beta}(\mathcal{K})$, where α and β denote the spaces of the n_α - and n_β -fold degenerate band-edge Bloch functions, which transform according to the irreducible representations Γ_α and Γ_β , respectively, of \mathcal{G} . For each block $\mathcal{H}_{\alpha\beta}(\mathcal{K})$, one can find a complete set of linearly independent $n_\alpha \times n_\beta$ -dimensional matrices $X_l^{(\kappa, \lambda)}$ that transform according to those irreducible representations Γ_κ (of dimension L_κ) which are contained in the product representation $\Gamma_\alpha \times \Gamma_\beta^*$. The index λ distinguishes between different subsets of matrices that transform according to the same irreducible representations Γ_κ . Then each block $\mathcal{H}_{\alpha\beta}(\mathcal{K})$ can be expressed in terms of *invariants*

$$\mathcal{I}_{\kappa\lambda\mu} = \sum_{l=1}^{L_\kappa} X_l^{(\kappa, \lambda)} \mathcal{K}_l^{(\kappa, \mu)*}, \quad (2.29)$$

consisting of products of matrices $X_l^{(\kappa, \lambda)}$ and irreducible tensor components $\mathcal{K}_l^{(\kappa, \mu)*}$. One can easily show that each invariant $\mathcal{I}_{\kappa\lambda\mu}$ indeed satisfies (2.28) for all $g \in \mathcal{G}$. Equation (2.29) reflects the well-known fact that the unit representation occurs only in a product of mutually conjugate representations Γ_κ and Γ_κ^* [18]. Finally, we can expand $\mathcal{H}_{\alpha\beta}(\mathcal{K})$ in terms of the invariants $\mathcal{I}_{\kappa\lambda\mu}$:

$$\mathcal{H}_{\alpha\beta}(\mathcal{K}) = \sum_{\kappa, \lambda, \mu} \mathbf{a}_{\kappa\lambda\mu}^{\alpha\beta} \mathcal{I}_{\kappa\lambda\mu} \quad (2.30a)$$

$$= \sum_{\kappa, \lambda, \mu} \mathbf{a}_{\kappa\lambda\mu}^{\alpha\beta} \sum_{l=1}^{L_\kappa} X_l^{(\kappa, \lambda)} \mathcal{K}_l^{(\kappa, \mu)*}, \quad (2.30b)$$

where the expansion coefficients $\mathbf{a}_{\kappa\lambda\mu}^{\alpha\beta}$ are material-specific parameters.⁶ In the diagonal blocks $\mathcal{H}_{\alpha\alpha}(\mathcal{K})$, only those invariants $\mathcal{I}_{\kappa\lambda\mu}$ are allowed that are also invariant under time reversal. No such restriction exists for the off-diagonal blocks $\mathcal{H}_{\alpha\beta}(\mathcal{K})$, $\alpha \neq \beta$ [18].

If $\tilde{\mathcal{H}}$ denotes the finite-dimensional multiband Hamiltonian derived by means of Löwdin partitioning, obviously we must have $\tilde{\mathcal{H}} = \mathcal{H}(\mathcal{K})$, so that in $\tilde{\mathcal{H}}$ we have the same dependence on the general tensor operator \mathcal{K} as in the invariant expansion (2.30). Therefore, we can obtain explicit formulas for the coefficients $\mathbf{a}_{\kappa\lambda\mu}^{\alpha\beta}$ in the following way. First we derive the invariant expansion (2.30) with undetermined coefficients $\mathbf{a}_{\kappa\lambda\mu}^{\alpha\beta}$. Then we carry out the Löwdin partitioning, so that we can match $\tilde{\mathcal{H}}$ against (2.30): when we collect

⁶ In the language of group theory, the coefficients $\mathbf{a}_{\kappa\lambda\mu}^{\alpha\beta}$ are closely related to reduced matrix elements as defined by the Wigner–Eckart theorem.

all terms in $\tilde{\mathcal{H}}$ that have the structure of an invariant $\mathcal{I}_{\kappa\lambda\mu}$, the common prefactor of these terms is the coefficient $a_{\kappa\lambda\mu}^{\alpha\beta}$. We would like to note that the important advantage of the invariant expansion (2.30) lies in the fact that often it is easier to derive (2.30) than to evaluate explicitly the perturbation theory (B.15). Nevertheless, solely on the basis of the invariant expansion (2.30), it is possible to predict many qualitative features of the Hamiltonian, and numerous examples of this can be found in subsequent chapters.

References

1. T. Ando, A.B. Fowler, F. Stern: Rev. Mod. Phys. **54**, 437 (1982) 9
2. G. Bastard, J.A. Brum, R. Ferreira: Solid State Phys. **44**, 229 (1991) 9
3. G. Bastard: *Wave Mechanics Applied to Semiconductor Heterostructures* (Les Editions de Physique, Les Ulis, 1988) 4, 9, 13, 15
4. E.O. Kane: J. Phys. Chem. Solids **1**, 249 (1957) 27, 30, 56, 71, 156, 10
5. E.O. Kane: “The $\mathbf{k} \cdot \mathbf{p}$ method”, in *Semiconductors and Semimetals*, ed. by R.K. Willardson, A.C. Beer, Vol. 1 (Academic Press, New York, 1966), p. 75 3, 25, 10
6. E.O. Kane: “Energy band theory”, in *Handbook on Semiconductors*, ed. by T.S. Moss, W. Paul, Vol. 1 (North-Holland, Amsterdam, 1982), p. 193 10
7. A. Elçi, E.D. Jones: Phys. Rev. B **34**, 8611 (1986) 10
8. W. Kohn: “Shallow impurity states in silicon and germanium”, in *Solid State Phys.*, ed. by F. Seitz, D. Turnbull, Vol. 5 (Academic Press, New York, 1957), pp. 257–320 12
9. B.A. Foreman: Phys. Rev. B **48**, 4964 (1993) 37, 14, 15
10. B.A. Foreman: Phys. Rev. B **56**, R12748 (1997) 14, 15
11. L.M. Roth, B. Lax, S. Zwerdling: Phys. Rev. **114**, 90 (1959) 2, 56, 131, 141, 14
12. W. Kohn: Phys. Rev. **105**(2), 509–516 (1957) 15
13. G. Dresselhaus, A.F. Kip, C. Kittel: Phys. Rev. **98**(2), 368–384 (1955) 15
14. G.F. Koster: “Space groups and their representations”, in *Solid State Phys.*, ed. by F. Seitz, D. Turnbull, Vol. 5 (Academic Press, New York, 1957), pp. 174–256 15
15. O. Madelung (Ed.): *Semiconductors*, Vol. 17a of Landolt-Börnstein, New Series III (Springer, Berlin, Heidelberg, 1982) 74, 174, 219, 220, 221, 222, 15
16. K. Suzuki, J.C. Hensel: Phys. Rev. B **9**(10), 4184–4218 (1974) 4, 5, 24, 31, 32, 43, 44, 151, 152, 158, 15, 17
17. H.R. Trebin, U. Rössler, R. Ranvaud: Phys. Rev. B **20**(2), 686–700 (1979) 4, 22, 25, 31, 32, 43, 46, 48, 77, 98, 99, 151, 152, 158, 166, 209, 210, 212, 213, 214, 217, 15
18. G.L. Bir, G.E. Pikus: *Symmetry and Strain-Induced Effects in Semiconductors* (Wiley, New York, 1974) 3, 4, 6, 98, 118, 201, 213, 15, 16, 18, 19
19. G.E. Pikus, G.L. Bir: Sov. Phys.–Solid State **1**, 1502 (1959) 212, 213, 16
20. T.B. Bahder: Phys. Rev. B **41**, 11992 (1990) 16
21. J. Kossut: “Band structure and quantum transport phenomena in narrow-gap diluted magnetic semiconductors”, in *Semiconductors and Semimetals*, ed. by R.K. Willardson, A.C. Beer, Vol. 25 (Academic Press, Boston, 1988), p. 183 3, 17

22. J.A. Gaj, R. Panel, G. Fishman: Solid State Commun. **29**, 435 (1979) [17](#), [18](#)
23. J.M. Luttinger: Phys. Rev. **102**(4), 1030 (1956) [3](#), [28](#), [29](#), [88](#), [98](#), [99](#), [106](#), [131](#), [142](#), [158](#), [18](#)

3 The Extended Kane Model

In the present work we are interested in quantum structures made of direct semiconductors with an inversion-asymmetric zinc blende structure (point group T_d). All important semiconductors in this category, such as GaAs, InSb, and CdTe, have qualitatively a very similar band structure with the smallest gap between the valence and conduction bands occurring at the Γ point $\mathbf{k} = \mathbf{0}$. A detailed description of the band structure of these semiconductors is possible by means of the *extended Kane model* [1, 2, 3].¹

We start in Sect. 3.1 with some general symmetry considerations. Next we discuss in Sect. 3.2 the invariant decomposition for the point group T_d which allows us to give in Sect. 3.3 the invariant expansion for the extended Kane model. Section 3.4 is devoted to a brief discussion of the spin-orbit gap Δ_0 . In Sect. 3.5 we discuss the relation between the extended Kane model and smaller $\mathbf{k} \cdot \mathbf{p}$ models such as the Kane model and the Luttinger Hamiltonian. Finally, we establish in Sect. 3.6 a symmetry hierarchy for the various terms in the Kane Hamiltonian.

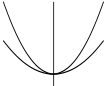
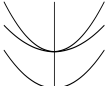
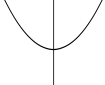
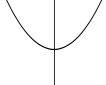
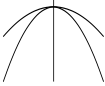



3.1 General Symmetry Considerations

In a tight-binding picture, the extended Kane model takes into account the topmost bonding p-like valence band states (X, Y, Z) and the antibonding s-like (S) and p-like ($X', Y',$ and Z') states in the lowest conduction bands. In the language of group theory,² the s-like states (orbital angular momentum $l = 0$, representation \mathcal{D}_0^- of the full rotation group $\mathcal{R} = SU(2) \times C_i$) transform according to the irreducible representation Γ_1 of the point group T_d (conduction band Γ_1^c), and the p-like states ($l = 1$) transform according to Γ_5 (valence band Γ_5^v and conduction band Γ_5^c). Note, however, that in a diamond structure the bonding p-like states in the valence band are even (\mathcal{D}_1^+ of \mathcal{R} , Γ_5^+ of O_h), whereas the antibonding p-like states in the conduc-

¹ The valence band block of this model is also appropriate for calculating hole states in Si and Ge (diamond lattice, point group O_h); see Sect. 8.3.

² We denote the irreducible representations of the crystallographic point groups in the same way as Koster et al. [4]; see also Chap. 2 of [5]. Superscripts “ \pm ” denote whether the representation is even or odd with respect to parity.

Table 3.1. Symmetry classification of the bands in the extended Kane model

Single group		Double group	
O_h/T_d	Full rotation group \mathcal{R}	O_h/T_d	
 Γ_5^-	$l = 1$ (\mathcal{D}_1^-) p antibonding	$j = 3/2$ ($\mathcal{D}_{3/2}^-$) \rightarrow Γ_8^-	
 Γ_1^-	$l = 0$ (\mathcal{D}_0^-) s antibonding	$j = 1/2$ ($\mathcal{D}_{1/2}^-$) \rightarrow Γ_7^-	
 Γ_5^+	$l = 1$ (\mathcal{D}_1^+) p bonding	$j = 1/2$ ($\mathcal{D}_{1/2}^+$) \rightarrow Γ_6^-	
		$j = 3/2$ ($\mathcal{D}_{3/2}^+$) \rightarrow Γ_8^+	
		$j = 1/2$ ($\mathcal{D}_{1/2}^+$) \rightarrow Γ_7^+	

tion band are odd (\mathcal{D}_1^- of \mathcal{R} , Γ_5^- of O_h). The symmetries of the bands are summarized in Table 3.1.

When SO coupling is taken into account, $l = 0$ becomes the total angular momentum $j = 1/2$ so that the states transform according to Γ_6 of T_d ($\mathcal{D}_{1/2}^-$ of \mathcal{R}). The Γ_5 bands split into fourfold degenerate $j = 3/2$ states, transforming according to Γ_8 of T_d ($\mathcal{D}_{3/2}^\pm$ of \mathcal{R}), and $j = 1/2$ states, transforming according to Γ_7 of T_d ($\mathcal{D}_{1/2}^\pm$ of \mathcal{R}). As the splitting between the valence bands Γ_5^v and Γ_7^v is a direct consequence of SO coupling, the band Γ_7^v is sometimes called the *spin-orbit split-off valence band* [6]. The resulting 14 basis functions are listed in Table C.1.

3.2 Invariant Decomposition for the Point Group T_d

Before discussing the details of the extended Kane model, we shall study the general features of a multiband Hamiltonian for the point group T_d according to the theory of invariants.

For the point group T_d , there are three double-group representations, denoted Γ_6 , Γ_7 , and Γ_8 . They provide the building blocks for any spin-dependent multiband Hamiltonian for T_d . For the two-dimensional representations Γ_6 and Γ_7 , we need four basis matrices. Here we can use the unit matrix $\mathbb{1}_{2 \times 2}$ and the Pauli spin matrices σ_i . For the four-dimensional representation Γ_8 , we need 16 matrices, which can be constructed from the three angular-momentum matrices J_x , J_y , and J_z for $j = 3/2$ and properly symmetrized powers thereof. The construction of basis matrices for the off-diagonal subspaces between Γ_6 , Γ_7 , and Γ_8 is described in [7]. All basis matrices are listed in Table C.3.

The wave vector \mathbf{k} and electric field \mathcal{E} transform according to the irreducible representation Γ_5 of T_d , whereas the magnetic field \mathbf{B} transforms according to Γ_4 . We remark that the wave vector \mathbf{k} and the magnetic field \mathbf{B} are odd with respect to time-reversal symmetry, while the electric field \mathcal{E} is even. We can construct irreducible tensor components $\mathcal{K}_l^{(\delta,\mu)}$ of higher order in \mathbf{k} , \mathbf{B} , and \mathcal{E} by using the Clebsch–Gordan coefficients $\langle \delta l | \alpha i, \beta j \rangle$ for the point group T_d , which are tabulated in [4]. More explicitly, from tensor components $\mathcal{K}_i^{(\alpha,\mu)}$ and $\mathcal{K}_j^{(\beta,\nu)}$ that transform according to the irreducible representations Γ_α and Γ_β we obtain new irreducible tensor components $\mathcal{K}_l^{(\delta,\lambda)}$ given by

$$\mathcal{K}_l^{(\delta,\lambda)}{}_{\text{sym}} = \sum_{i,j} \langle \delta l | \alpha i, \beta j \rangle \{ \mathcal{K}_i^{(\alpha,\mu)}, \mathcal{K}_j^{(\beta,\nu)} \}, \quad (3.1a)$$

$$\mathcal{K}_l^{(\delta,\lambda)}{}_{\text{asym}} = \sum_{i,j} \langle \delta l | \alpha i, \beta j \rangle [\mathcal{K}_i^{(\alpha,\mu)}, \mathcal{K}_j^{(\beta,\nu)}], \quad (3.1b)$$

where $\{ \dots \}$ and $[\dots]$ denote the symmetrized and antisymmetrized products, respectively, of their arguments. Up to fourth order in the wave vector \mathbf{k} and second order in \mathbf{B} and \mathcal{E} , we obtain the irreducible tensor components listed in Table C.4. Note, however, that the definition of these tensor operators is not unique, because any linear combination of sets of tensor operators that transforms according to the irreducible representation Γ_δ also transforms according to Γ_δ . As remarked at the end of Sect. 2.5, using Tables C.3 and C.4 we can derive many important features of the Hamiltonian without the need to explicitly carry out the cumbersome perturbation theory which is necessary to determine the prefactors of the invariants.

3.3 Invariant Expansion for the Extended Kane Model

The extended Kane model takes exactly into account (up to infinite order in \mathbf{k}) all $\mathbf{k} \cdot \mathbf{p}$ and SO interactions between the bands Γ_8^c , Γ_7^c , Γ_6^c , Γ_8^v , and Γ_7^v . The $\mathbf{k} \cdot \mathbf{p}$ interactions with the other bands are taken into account by second-order perturbation theory (see Fig. 3.1). The 14×14 matrix Hamiltonian of the extended Kane model falls into blocks with respect to the five bands under consideration:

$$\mathcal{H}_{14 \times 14} = \begin{pmatrix} \mathcal{H}_{8c8c} & \mathcal{H}_{8c7c} & \mathcal{H}_{8c6c} & \mathcal{H}_{8c8v} & \mathcal{H}_{8c7v} \\ \mathcal{H}_{7c8c} & \mathcal{H}_{7c7c} & \mathcal{H}_{7c6c} & \mathcal{H}_{7c8v} & \mathcal{H}_{7c7v} \\ \mathcal{H}_{6c8c} & \mathcal{H}_{6c7c} & \mathcal{H}_{6c6c} & \mathcal{H}_{6c8v} & \mathcal{H}_{6c7v} \\ \mathcal{H}_{8v8c} & \mathcal{H}_{8v7c} & \mathcal{H}_{8v6c} & \mathcal{H}_{8v8v} & \mathcal{H}_{8v7v} \\ \mathcal{H}_{7v8c} & \mathcal{H}_{7v7c} & \mathcal{H}_{7v6c} & \mathcal{H}_{7v8v} & \mathcal{H}_{7v7v} \end{pmatrix}. \quad (3.2)$$

The invariant expansion for these blocks is given in Table C.5.

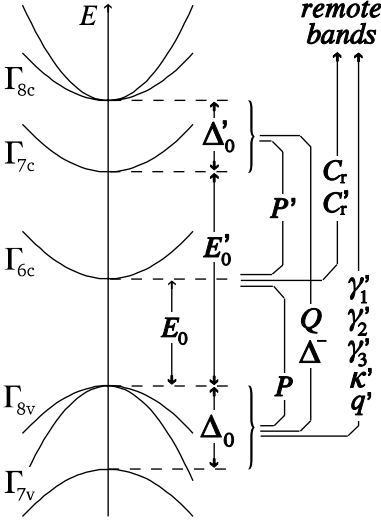


Fig. 3.1. Schematic band structure for the 14×14 extended Kane model. Besides the energy separations at the Γ point, the couplings within the model are indicated. Taken from [2]. © (1991) by the American Physical Society

The irreducible matrix elements of the momentum and the SO interaction occurring in the extended Kane model are defined as follows (see Fig. 3.1):

$$P = \frac{\hbar}{m_0} \langle S | p_x | X \rangle, \quad (3.3a)$$

$$P' = \frac{\hbar}{m_0} \langle S | p_x | X' \rangle, \quad (3.3b)$$

$$Q = \frac{\hbar}{m_0} \langle X | p_y | Z' \rangle, \quad (3.3c)$$

$$\Delta_0 = -\frac{3i\hbar}{4m_0^2c^2} \langle X | [(\nabla V_0) \times \mathbf{p}]_y | Z \rangle, \quad (3.3d)$$

$$\Delta'_0 = -\frac{3i\hbar}{4m_0^2c^2} \langle X' | [(\nabla V_0) \times \mathbf{p}]_y | Z' \rangle, \quad (3.3e)$$

$$\Delta^- = -\frac{3i\hbar}{4m_0^2c^2} \langle X | [(\nabla V_0) \times \mathbf{p}]_y | Z' \rangle. \quad (3.3f)$$

Using the phase conventions listed in Table C.1, the matrix elements P , Q , Δ_0 , and Δ'_0 are real, whereas the matrix elements P' and Δ^- are purely imaginary. Furthermore, the SO interaction is diagonal between the p-like valence and conduction band states. Thus, Δ_0 and Δ'_0 can be interpreted as the SO splittings between Γ_8^v and Γ_7^v and between Γ_8^c and Γ_7^c , respectively; see Fig. 3.1. Other phase conventions yielding off-diagonal SO matrix elements between the p-like valence band states are discussed in [8].

In subsequent chapters we shall focus on the effects of SO interaction. For this reason, we wish to point out that besides the matrix elements Δ_0 , Δ'_0 , and Δ^- , the prefactor C_k of the terms linear in \mathbf{k} in the valence band block \mathcal{H}_{8v8v} is also a direct consequence of SO interaction [9]. The main

contribution to C_k stems from the bilinear terms consisting of $\mathbf{k} \cdot \mathbf{p}$ and SO interactions, with remote Γ_3 -like intermediate states [10]. Unlike the higher-order terms for spin splitting induced by bulk inversion asymmetry (BIA, see Sect. 6.2) that can be expressed in terms of the momentum matrix elements and energy gaps (3.3), the coefficient C_k is an “elementary” parameter of the extended Kane model. In semiconductors with a diamond lattice (point group O_h) we have $P' = \Delta^- = C_k = 0$, consistent with the symmetry of the bands with respect to parity listed in Table 3.1.

The remaining parameters m^* , g^* , B_i , D , γ_i , κ , and q describe *remote-band contributions* of second order in \mathbf{k} . However, the classification of valence and conduction bands in terms of “near” and “remote” bands depends on the particular $\mathbf{k} \cdot \mathbf{p}$ model. Usually, the above parameters refer to smaller $\mathbf{k} \cdot \mathbf{p}$ models that comprise only a subspace of the five bands of the extended Kane model. Accordingly, these parameters contain the $\mathbf{k} \cdot \mathbf{p}$ interactions between this subset and the other bands of the extended Kane model in second-order perturbation theory. Therefore, in order to take these interactions into account only once, we use *reduced band parameters* m' , g' , B'_i , D' , γ'_i , κ' , and q' , where we subtract the second-order contributions from those interactions that are taken exactly into account [11, 12]; see also Sect. 3.5. The definition of the reduced band parameters is given in Table C.9.

In Table C.5 we have included in the off-diagonal blocks \mathcal{H}_{6c8v} and \mathcal{H}_{6c7v} the terms proportional to Kane’s parameter B [13] (following [14], we distinguish B_{8v}^\pm and B_{7v}). These terms contribute to the inversion-asymmetry-induced spin splitting in the conduction and valence bands (Sect. 6.2). A treatment of Zeeman splitting at the same level of accuracy requires that we take into account also the analogous terms antisymmetric in \mathbf{k} , which contribute to the anisotropic Zeeman splitting in the conduction and valence bands [14]. The prefactor of these terms has been denoted by D .

We have included in Table C.5 also the strain-induced terms that will be used in Sect. 8.3. The deformation potentials C_i , D_d , D_u , and D'_u are explained in [7]. Several common alternative notations for deformation potentials are listed in Table C.6. The paramagnetic interaction is characterized by the s-d and p-d exchange integrals

$$\alpha = -\langle S | J | S \rangle \quad \text{and} \quad \beta = -\langle X | J | X \rangle. \quad (3.4)$$

As an example, we show in Fig. 3.2 the (spin-split) dispersion $E(\mathbf{k})$ of electrons in the lowest conduction band [1] and of holes in the highest valence bands in bulk GaAs, calculated by means of the 14×14 extended Kane model. The dispersion in the valence bands is strongly nonparabolic and anisotropic. Even for electrons we have significant nonparabolic corrections, but the anisotropic terms are fairly small (see Sect. 3.6). BIA spin splitting in bulk semiconductors will be discussed in detail in Sect. 6.2.1.

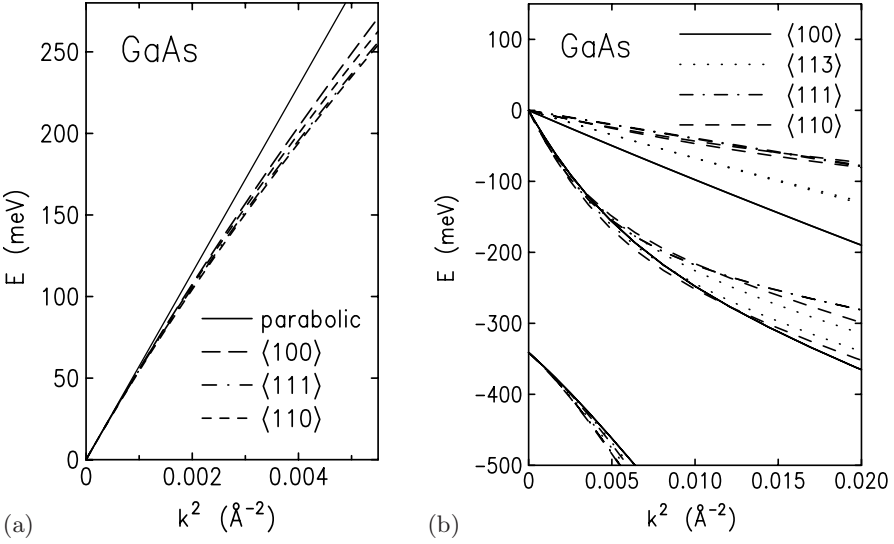


Fig. 3.2. Spin-split dispersion $E(\mathbf{k})$ (a) of electrons in the lowest conduction band and (b) of holes in the highest valence bands in bulk GaAs. The calculation was based on the 14×14 extended Kane model. Different line styles correspond to different directions in \mathbf{k} space as indicated. The *solid line* in (a) indicates the parabolic dispersion based on the effective mass at the band edge. (a) taken from [1]. © (1984), with permission by Elsevier

3.4 The Spin–Orbit Gap Δ_0

The SO gap Δ_0 (and Δ'_0) defined in (3.3) is of fundamental importance for the discussion of SO-related phenomena in subsequent chapters. Therefore, the present section is devoted to a discussion of this quantity.

The matrix element Δ_0 reflects the Pauli SO interaction (1.1) caused by the strong Coulomb potential in the innermost region of the atomic cores. Theoretical values of Δ_0 in a binary semiconductor AB can be estimated from [15]

$$\Delta_0(\text{AB}) = \frac{1}{2}(1 - f_i)\Delta_A + \frac{1}{2}(1 + f_i)\Delta_B, \quad (3.5)$$

where Δ_j is the atomic SO splitting of constituent $j = \text{A, B}$. The symbol f_i denotes the ionicity of the semiconductor AB, and we have assumed that A is the cation and B is the anion. Similar formulas have been derived by other authors [16]. In (3.5), the anions are weighted more than the cations. This reflects the general trend that the anions in a binary semiconductor contribute more strongly to the topmost valence band states than do the cations. Atomic SO splittings Δ_j are listed in Table 3.2. We see that in each row of the periodic table, the splittings Δ_j increase from left to right in much the same way.

Table 3.2. Contribution Δ_j of atom j to the SO splitting Δ_0 (in eV). Taken from [15]

Be 0.002	B 0.004	C 0.006	N 0.009	O 0.010	F 0.010
Mg 0.01	Al 0.024	Si 0.044	P 0.08	S 0.09	Cl 0.09
Zn 0.10	Ga 0.18	Ge 0.29	As 0.43	Se 0.48	Br 0.49
Cd 0.10	In 0.36	Sn 0.80	Sb 1.05	Te 1.10	I 1.11
Hg 0.5	Tl 0.9	Pb 2.0			

Likewise, they increase in each column from top to bottom.³ A comparison of experimental SO gaps Δ_0^{exp} with theoretical SO gaps Δ_0^{theo} estimated by means of (3.5) is given in Table 3.3. In the present context, it might appear trivial to achieve good agreement between experimental SO gaps and theoretical estimates based on (3.5) because, for every binary semiconductor AB, we could choose the ionicity f_i appropriately. However, in early models of semiconductor band structure the ionicity f_i was a fundamental parameter that was used to explain many different properties of binary semiconductors [15]. We see in Table 3.3 that for Si we have $\Delta_0 = 44$ meV, whereas for Ge we have $\Delta_0 = 290$ meV. Therefore, we can readily understand why SO effects in Si quantum structures are rather small [18, 19].

The SO gap Δ'_0 is typically smaller than Δ_0 . Lawaetz [20] estimates $\Delta'_0 \approx 0.64\Delta_0$.

3.5 Kane Model and Luttinger Hamiltonian

The 14×14 matrix of the extended Kane Hamiltonian provides an accurate description of the band structure of semiconductors close to the fundamental gap [1]. Nevertheless, it is often convenient to consider smaller $\mathbf{k} \cdot \mathbf{p}$ models such as the 8×8 Kane model [21],

$$\mathcal{H}_{8 \times 8} = \begin{pmatrix} \mathcal{H}_{6c6c} & \mathcal{H}_{6c8v} & \mathcal{H}_{6c7v} \\ \mathcal{H}_{8v6c} & \mathcal{H}_{8v8v} & \mathcal{H}_{8v7v} \\ \mathcal{H}_{7v6c} & \mathcal{H}_{7v8v} & \mathcal{H}_{7v7v} \end{pmatrix}. \quad (3.6)$$

³ The atomic SO splittings Δ_j are effective quantities that should not be confused with splittings of atomic energy levels. Nevertheless, the trends of Δ_j are qualitatively consistent with the results of atomic physics, where it is known that the SO coupling varies roughly as the fourth power of the (effective) atomic number [17].

Table 3.3. Comparison between experimental SO gaps Δ_0^{exp} and theoretical SO gaps Δ_0^{theo} estimated by means of (3.5) using the ionicities f_i . Taken from [15]

Compound	Δ_0^{exp} (eV)	Δ_0^{theo} (eV)	f_i
C	0.006	0.006	0
Si	0.044	0.044	0
Ge	0.29	0.29	0
α -Sn		0.80	0
AlN		0.012	0.449
AlP		0.060	0.307
AlAs		0.29	0.274
AlSb	0.75	0.80	0.250
GaN	0.011	0.095	0.500
GaP	0.127	0.11	0.327
GaAs	0.34	0.34	0.310
GaSb	0.80	0.98	0.261
InN		0.08	0.578
InP	0.11	0.16	0.421
InAs	0.38	0.40	0.357
InSb	0.82	0.80	0.321
ZnO	-0.005	0.03	0.616
ZnS	0.07	0.09	0.623
ZnSe	0.43	0.42	0.630
ZnTe	0.93	0.86	0.609
CdS	0.066	0.09	0.685
CdSe		0.42	0.699
CdTe	0.92	0.94	0.717
HgS		0.13	0.79
HgSe		0.48	0.68
HgTe		0.99	0.65

In subsequent chapters we shall often describe hole states by means of the 4×4 Luttinger Hamiltonian \mathcal{H}_{8v8v} , which is the simplest model for the fourfold degenerate topmost valence band [22].⁴ We would like to remark that even though \mathcal{H}_{8v8v} does not depend on the SO gap Δ_0 , it corresponds to the limit of strong SO interaction $\Delta_0 \rightarrow \infty$.

In fact, we can establish a *hierarchy of $\mathbf{k} \cdot \mathbf{p}$ models*, starting from the full 14×14 extended Kane Hamiltonian and going down through models with a successively reduced size. These smaller models can be derived from $\mathcal{H}_{14 \times 14}$ by means of Löwdin partitioning so that they contain terms of higher order in \mathbf{k} . Here, our definition of the reduced band parameters in Table C.9 ensures that, to leading order in \mathbf{k} , the smaller models yield the same results as the 14×14 extended Kane model. Only higher-order terms in a Taylor expansion of the dispersion $E_n(\mathbf{k})$ differ from each other if a larger or smaller model

⁴ Often the 6×6 valence band Hamiltonian containing the bands Γ_8^v and Γ_7^v is also called the Luttinger Hamiltonian [23, 24].

is used. Therefore, the higher-order terms of $E_n(\mathbf{k})$ provide a direct measure of the accuracy of different $\mathbf{k} \cdot \mathbf{p}$ models [1]. For example, the effective-mass approximation (2.9) is sometimes called parabolic approximation, because it yields the correct second-order term in a Taylor expansion of $E_n(\mathbf{k})$, but it neglects all higher-order terms. Obviously, such simplified models are most accurate if only small wave vectors \mathbf{k} are relevant.

Strictly speaking we must distinguish between, for example, the 4×4 Luttinger Hamiltonian for the Γ_8^v valence band and the block \mathcal{H}_{8v8v} in the extended Kane model (3.2) or \mathcal{H}_{8v8v} in the Kane model (3.6) because the blocks of the latter kind contain reduced band parameters as given in Table C.9; see Sect. 3.3. However, for brevity of notation we shall use the same symbols $\mathcal{H}_{\alpha\beta}$, and we assume that each block contains the appropriate reduced band parameters as given in Table C.9.

3.6 Symmetry Hierarchies

For the interpretation of the band structure of both bulk semiconductors and quasi-2D systems, it is very helpful to decompose the full Hamiltonian \mathcal{H} into terms with higher and lower symmetry. Typically, the terms with higher symmetry have larger prefactors than have the terms with lower symmetry, so that we have a *symmetry hierarchy* for the terms in \mathcal{H} .

Bulk semiconductors with a diamond structure have the point group O_h , which is the point group of a cube. Bulk semiconductors with a zinc blende structure have the point group T_d , which is the point group of a tetrahedron. We obtain O_h from T_d by adding the inversion to the latter group, i.e. T_d is a subgroup of $O_h = T_d \otimes C_i$, where C_i is the point group that contains only the identity and the inversion. It has long been known that the additional terms in the band structure of a semiconductor with a zinc blende structure are rather small when compared with the terms that are present also in semiconductors with a diamond structure [22]. (Obviously, the latter terms are symmetry-allowed also in zinc blende structures because $T_d \subset O_h$.)

Lipari and Baldareschi [25] generalized this idea by noting that O_h is a subgroup of the full rotation group \mathcal{R} :

$$\mathcal{R} \supset O_h \supset T_d. \quad (3.7)$$

Thus one can write \mathcal{H} in the form

$$\mathcal{H} = \mathcal{H}_{\text{spher}} + \mathcal{H}_{\text{cub}} + \mathcal{H}_{\text{tetra}}, \quad (3.8)$$

where $\mathcal{H}_{\text{spher}}$ is the spherical part of \mathcal{H} that transforms according to \mathcal{R} , \mathcal{H}_{cub} is the cubic part that transforms according to O_h , and $\mathcal{H}_{\text{tetra}}$ denotes the remaining terms with tetrahedral symmetry that transform according to T_d only. In the *spherical approximation*, we replace the full Hamiltonian \mathcal{H} by $\mathcal{H}_{\text{spher}}$. This implies that the eigenstates of the Hamiltonian are also eigenstates of the angular-momentum operator $\hat{\mathbf{J}}$ (both \hat{J}^2 and \hat{J}_z). Similarly,

we can define the *cubic approximation*, where the second term in (3.8) is also taken into account. It is a general property of the cubic approximation that \mathcal{H} (i.e. the operator for the kinetic energy) commutes with the parity operator.⁵ The cubic and tetrahedral terms in (3.8) reflect the fact that in a crystal structure, angular momentum is merely an “almost good” quantum number.

The symmetry hierarchy (3.7) is very general. In particular, it does not distinguish between electrons and holes. On the other hand, we saw in Fig. 3.2 that anisotropic corrections are significantly more important for holes than for electrons. The reason for this is that the dispersion of electrons basically depends on the off-diagonal $\mathbf{k} \cdot \mathbf{p}$ coupling between the lowest conduction band Γ_6^c and the topmost valence bands Γ_8^v and Γ_7^v (proportional to Kane’s momentum matrix element P) [21]. These terms have spherical symmetry. Therefore they contribute only to nonparabolicity and not to the anisotropy of $E(\mathbf{k})$. Cubic contributions to the dispersion $E(\mathbf{k})$ result from $\mathbf{k} \cdot \mathbf{p}$ coupling to the higher conduction bands Γ_8^c and Γ_7^c and to remote bands. For holes, they are proportional to $\delta = \gamma_3 - \gamma_2$ [25] and give an important contribution to $E_h(\mathbf{k})$. If Γ_8^c and Γ_7^c , as well as remote-band contributions, are neglected, both $E_c(\mathbf{k})$ and $E_h(\mathbf{k})$ become isotropic. From Tables C.3 and C.4, we find that to lowest order in \mathbf{k} the anisotropy of the conduction band Γ_6^c is caused by terms of fourth order in \mathbf{k} (Fig. 3.2a and [26]), while for the valence band Γ_8^v these terms are of second order in \mathbf{k} (Fig. 3.2b and [25]).

In semiconductor QWs the growth direction is a predefined symmetry axis, so that the point group of these systems is given by the subgroup of O_h or T_d that keeps this symmetry axis fixed. The resulting point groups for different crystallographic growth directions are listed in Table 3.4. In general, the symmetry reduction due to the subband quantization is the most important effect, i.e., instead of the full rotation group \mathcal{R} , we start the symmetry hierarchy from the axial point group $D_{\infty h}$ (if the confining potential $V(z)$ is inversion-symmetric) or from the group $C_{\infty v}$ (if the confining potential $V(z)$ is inversion-asymmetric). We obtain $D_{\infty h}$ from $C_{\infty v}$ by adding the inversion to the latter group.⁶ Analogously to (3.8), we can decompose the full Hamiltonian \mathcal{H} into

$$\mathcal{H} = \mathcal{H}_{\text{ax}} + \mathcal{H}_{\text{cub}} + \mathcal{H}_{\text{tetra}} , \quad (3.9)$$

⁵ The part $\mathcal{H}_{\text{tetra}}$ contains the effect of bulk inversion asymmetry to be discussed in Sect. 6.2. The cubic approximation to \mathcal{H} thus allows us to analyze the effect of structure inversion asymmetry (i.e. the broken inversion symmetry of the confining potential $V(z)$) independently of BIA.

⁶ The axial point group C_{∞} contains all rotations about an axis $\hat{\mathbf{n}}$. The point group $C_{\infty v}$ contains C_{∞} plus a mirror plane that includes $\hat{\mathbf{n}}$. This is the point group of an electric field. The point group $C_{\infty h}$ contains C_{∞} plus a mirror plane perpendicular to $\hat{\mathbf{n}}$. This is the point group of a magnetic field. The point group $D_{\infty h}$ contains C_{∞} plus both a mirror plane that includes $\hat{\mathbf{n}}$ and a mirror plane perpendicular to $\hat{\mathbf{n}}$. We have $D_{\infty h} = C_{\infty h} \otimes C_i = C_{\infty v} \otimes C_i$.

Table 3.4. The point group of a QW for different growth directions, starting from a bulk semiconductor with a diamond structure (point group O_h) or zinc blende structure (point group T_d), for $B = 0$ and $B = B_z > 0$. The upper and lower values correspond to a QW the geometry of which is inversion-symmetric or inversion-asymmetric, respectively. See also Sect. 6.5

		[001]	[111]	[110]	[mmn]	[0mn]	[lmn]	Axial approx.
$B = 0$	O_h	D_{4h}	D_{3d}	D_{2h}	C_{2h}	C_{2h}	C_i	$D_{\infty h}$
		C_{4v}	C_{3v}	C_{2v}	C_s	C_s	C_1	$C_{\infty v}$
	T_d	D_{2d}	C_{3v}	C_{2v}	C_s	C_2	C_1	$D_{\infty h}$
		C_{2v}	C_{3v}	C_s	C_s	C_1	C_1	$C_{\infty v}$
$B_z > 0$	O_h	C_{4h}	C_{3i}	C_{2h}	C_i	C_i	C_i	$C_{\infty h}$
		C_4	C_3	C_2	C_1	C_1	C_1	C_∞
	T_d	S_4	C_3	C_s	C_1	C_1	C_1	$C_{\infty h}$
		C_2	C_3	C_1	C_1	C_1	C_1	C_∞

where \mathcal{H}_{ax} contains the terms with axial symmetry (point group $D_{\infty h}$ or $C_{\infty v}$), \mathcal{H}_{cub} contains the terms with cubic symmetry (invariant under inversion), and $\mathcal{H}_{\text{tetra}}$ contains the remaining terms with tetrahedral symmetry (not invariant under inversion).⁷

In the *axial approximation* we replace the full Hamiltonian \mathcal{H} by \mathcal{H}_{ax} . The eigenstates of \mathcal{H}_{ax} are also eigenstates of the angular-momentum operator \hat{J}_z with the quantization axis of angular momentum parallel to the symmetry axis of the axial point group. Indeed, we can use $[\mathcal{H}_{\text{ax}}, \hat{J}_z] = 0$ as an alternative definition of the axial approximation, consistent with the fact that the irreducible representations of the axial point groups are commonly labeled by the quantum numbers of \hat{J}_z .

We can use the symmetry properties of \mathcal{H}_{ax} in order to perform the decomposition (3.9). We start by making a unitary transformation of the basis functions $\{|jm\rangle\}$ in Table C.1, such that the quantization axis of angular momentum is parallel to the growth axis (see e.g. (3.5.42) in [27]). In addition, we make a transformation of the wave vector \mathbf{k} such that the transformed component k_z is parallel to the quantization axis (see Sect. 4.1.5). We express the components k_x and k_y of the transformed wave vector in terms of $k_\pm = k_x \pm ik_y$. As we can identify k_+ and k_- with raising and lowering operators for angular momentum, we can readily decide which terms in the transformed Hamiltonian have axial symmetry:⁸ if the matrix element $\mathcal{H}_{nn'}$ of the multiband Hamiltonian \mathcal{H} connects the basis function $|n\rangle = |j_n m_n\rangle$ with $|n'\rangle = |j_{n'} m_{n'}\rangle$, only those terms which contain products $k_+^{\mu_{nn'}} k_-^{\nu_{nn'}}$ are allowed in $\mathcal{H}_{nn'}^{\text{ax}}$, where the exponents $\mu_{nn'}$ and $\nu_{nn'}$ obey the condition

⁷ The symmetry hierarchy (3.9) was developed first for bulk semiconductors in the presence of an external magnetic field and uniaxial strain [8, 7].

⁸ This decomposition is not unique. We follow footnote 35 in [8], here.

$$\mu_{nn'} - \nu_{nn'} = m_n - m_{n'}. \quad (3.10)$$

More explicitly, if we specify the direction of the symmetry axis by means of the polar angle ϕ and azimuthal angle θ with respect to the direction [001] (see Fig. C.1), we can write the axial approximation for the 8×8 Kane model as a function of ϕ and θ only. The results are given in Table C.10. Only the prefactors, not the functional form of \mathcal{H}_{ax} , change as a function of ϕ and θ , because the terms in Table C.10 represent the invariant expansion $\mathcal{H}(\mathbf{K})$ for the point groups $D_{\infty h}$ and $C_{\infty v}$. Note that the k -linear coupling between Γ_6^c and Γ_8^v , as well as the terms proportional to m^* , g^* , γ_1 , and κ , has spherical symmetry, so that these terms remain unaffected by a rotation of the coordinate system. We have restricted ourselves to a magnetic field in the z direction because any other direction of \mathbf{B} would break the axial symmetry [8, 7]. Our general formulas in Table C.10 include the results listed in Table VI of [7] for the particular cases of a growth direction parallel to [001] ($\phi = \theta = 0$), [111] ($\phi = \pi/4$, $\theta = \arccos(1/\sqrt{3})$), and [110] ($\phi = \pi/4$, $\theta = \pi/2$).

For the calculation of Landau levels described in Sect. 4.4.4, we also need a complete decomposition of $\mathcal{H}_{\text{cub}}(\phi, \theta)$ and $\mathcal{H}_{\text{tetra}}(\phi, \theta)$ with respect to powers of k_+ , k_- , and k_z , which we obtain likewise from the above analysis. The cubic part $\mathcal{H}_{\text{cub}}(\phi, \theta)$ for the most frequently needed case $\phi = \pi/4$ is given in Table C.11. However, we omit here the rather lengthy expressions for the tetrahedral terms. Note that all cubic terms in \mathcal{H}_{8v8v}^k and \mathcal{H}_{8v7v}^k depend only on the parameter $\delta = \gamma_3 - \gamma_2$ [25]. We see from Table C.11 that the axial approximation is most accurate for the high-symmetry growth directions [001] ($\phi = \theta = 0$) and [111] ($\phi = \pi/4$, $\theta = \arccos(1/\sqrt{3})$), as we have here $\mathcal{H}_{\text{cub}}(\mathbf{k}_{\parallel} = 0) = 0$, i.e. we obtain the correct subband edges from using \mathcal{H}_{ax} only.⁹ On the other hand, the cubic corrections in \mathcal{H}_{cub} are very important for low-symmetry growth directions such as [113] and [110].

The reader might ask why we present in Tables C.10 and C.11 the symmetry hierarchy for the 8×8 Hamiltonian but not for the more complete 14×14 Hamiltonian. This is because for the 14×14 extended Kane model a symmetry hierarchy is less meaningful than for the 8×8 Hamiltonian, because in the smaller model Löwdin partitioning results in a sequence of terms we can interpret and classify individually,¹⁰ whereas in the larger, more accurate model such a separation of qualitatively different terms is not possible. For example, the $\mathbf{k} \cdot \mathbf{p}$ coupling between the lowest conduction band Γ_6^c and the higher conduction bands Γ_7^c and Γ_8^c has tetrahedral symmetry, consistent with $P' = 0$ in semiconductors with a diamond structure. Accordingly, a cubic 14×14 Hamiltonian must neglect the $\mathbf{k} \cdot \mathbf{p}$ coupling between these bands. On the other hand, in the smaller Hamiltonians we can distinguish

⁹ The effect of $\mathcal{H}_{\text{tetra}}$ on the subband edges is rather small.

¹⁰ The same holds for even smaller models, such as the 2×2 Hamiltonian for electrons in the Γ_6^c conduction band, which contains terms up to fourth order in \mathbf{k} [26].

between the contribution of P' to the isotropic effective mass (Table C.9) and the contribution of P' to the tetrahedral terms of third order in k (Sect. 6.2).

References

1. U. Rössler: Solid State Commun. **49**, 943 (1984) 4, 71, 21, 25, 26, 27, 29
2. H. Mayer, U. Rössler: Phys. Rev. B **44**, 9048 (1991) 37, 74, 174, 212, 213, 214, 220, 21, 24
3. P. Pfeffer, W. Zawadzki: Phys. Rev. B **41**, 1561–1576 (1990) 21
4. G.F. Koster, J.O. Dimmock, R.G. Wheeler, H. Statz: *Properties of the Thirty-Two Point Groups* (MIT, Cambridge, MA, 1963) 6, 47, 72, 166, 199, 21, 23
5. P.Y. Yu, M. Cardona: *Fundamentals of Semiconductors* (Springer, Berlin, Heidelberg, 1996) 6, 21
6. R.A. Smith: *Semiconductors*, 2nd edn. (Cambridge University Press, Cambridge, 1978) 22
7. H.R. Trebin, U. Rössler, R. Ranvaud: Phys. Rev. B **20**(2), 686–700 (1979) 4, 15, 43, 46, 48, 77, 98, 99, 151, 152, 158, 166, 209, 210, 212, 213, 214, 217, 22, 25, 31, 32
8. K. Suzuki, J.C. Hensel: Phys. Rev. B **9**(10), 4184–4218 (1974) 4, 5, 15, 17, 43, 44, 151, 152, 158, 24, 31, 32
9. G. Dresselhaus: Phys. Rev. **100**(2), 580–586 (1955) 2, 5, 69, 71, 72, 24
10. M. Cardona, N.E. Christensen, G. Fasol: Phys. Rev. B **38**(3), 1806–1827 (1988) 71, 72, 73, 74, 220, 221, 25
11. R.C. Pidgeon, R.N. Brown: Phys. Rev. **146**, 575 (1966) 25
12. C. Hermann, C. Weisbuch: Phys. Rev. B **15**(2), 823–833 (1977) 133, 25
13. E.O. Kane: “The $\mathbf{k} \cdot \mathbf{p}$ method”, in *Semiconductors and Semimetals*, ed. by R.K. Willardson, A.C. Beer, Vol. 1 (Academic Press, New York, 1966), p. 75 3, 10, 25
14. M.H. Weiler, R.L. Aggarwal, B. Lax: Phys. Rev. B **17**, 3269 (1978) 212, 25
15. J.C. Phillips: *Bonds and Bands in Semiconductors* (Academic Press, New York, 1973) 26, 27, 28
16. D.J. Chadi: Phys. Rev. B **16**(2), 790–796 (1977) 26
17. J.C. Slater: *Quantum Theory of Atomic Structure*, Vol. 2 (McGraw-Hill, New York, 1960) 1, 27
18. R. Winkler: Surf. Sci. **361/362**, 411 (1996) 5, 155, 157, 27
19. Z. Wilamowski, W. Jantsch: Physica E **12**, 439–442 (2002) 27
20. P. Lawaetz: Phys. Rev. B **4**, 3460 (1971) 27
21. E.O. Kane: J. Phys. Chem. Solids **1**, 249 (1957) 10, 56, 71, 156, 27, 30
22. J.M. Luttinger: Phys. Rev. **102**(4), 1030 (1956) 3, 18, 88, 98, 99, 106, 131, 142, 158, 28, 29
23. E.C. Valadares: Phys. Rev. B **46**(7), 3935–3939 (1992) 38, 28
24. C.Y.P. Chao, S.L. Chuang: Phys. Rev. B **46**(7), 4110–4122 (1992) 38, 28
25. N.O. Lipari, A. Baldereschi: Phys. Rev. Lett. **25**(24), 1660–1664 (1970) 192, 29, 30, 32
26. M. Braun, U. Rössler: J. Phys. C: Solid State Phys. **18**, 3365 (1985) 37, 40, 71, 77, 166, 30, 32
27. J.J. Sakurai: *Modern Quantum Mechanics*, revised edn. (Addison-Wesley, Redwood City, 1994) 83, 151, 152, 185, 204, 208, 31

4 Electron and Hole States in Quasi-Two-Dimensional Systems

In Chaps. 2 and 3 we introduced the general concepts for characterizing the semiconductor band structure and a model for calculating it. In the present chapter we shall discuss the applications of this model to quasi-2D semiconductor quantum structures.

In Sect. 4.1 we present a general, numerical approach for solving the EFA Hamiltonian based on a quadrature method. We then review for later reference the density of states of a 2D system (Sect. 4.2) and the most elementary model within the EFA, the effective-mass approximation, which assumes a simple nondegenerate, isotropic band (Sect. 4.3). In subsequent chapters the EMA is often used as a starting point for developing more elaborate models. The case of a perpendicular magnetic field differs conceptually from the case of $B = 0$ or of an in-plane B , so it will be discussed separately in Sect. 4.4. As an example of the concepts introduced in this chapter, we discuss next the subband dispersion of quasi-2D hole systems with different crystallographic growth directions (Sect. 4.5). The results obtained by numerical calculations are usually very accurate, but sometimes less intuitive. In Sect. 4.6 we therefore complement the numerical schemes by a fully analytic approach based on Löwdin partitioning.

4.1 The Envelope Function Approximation for Quasi-Two-Dimensional Systems

The application of the EFA to semiconductor quantum structures has been discussed extensively in the literature [1,2,3,4,5,6,7,8,9,10,11,12,13,14,15,16]. In [15,16], a general approach for the numerical solution of multiband envelope function problems for a magnetic field $B = 0$ was presented which was based on a quadrature method. Here we rederive the formulas in a way that shows that this approach can include also an in-plane or perpendicular magnetic field B . In Sect. 4.1.1 we make some preliminary remarks concerning the solution of an EFA Hamiltonian for the case of $B = 0$ or of an in-plane B . In Sect. 4.1.3 we briefly discuss the general concepts and the technical problems related to a numerical solution of arbitrary multiband Hamiltonians. In Sect. 4.1.4 we show how a general solution of these eigenvalue problems, including the case of an in-plane magnetic field, can be obtained by means

of a quadrature method. Finally, we discuss in Sect. 4.1.5 how we can describe electron and hole states in QWs with different crystallographic growth directions.

4.1.1 Envelope Functions

In semiconductor heterostructures and QWs we have $V(\mathbf{r}) = V(z)$, with the z axis in the growth direction, so that for $B = 0$ the in-plane wave vector $\mathbf{k}_{\parallel} = (k_x, k_y, 0)$ is a good quantum number. Therefore, we can write the eigenfunctions (2.13) of the multiband Hamiltonian in the form

$$\Psi_{\alpha\mathbf{k}_{\parallel}}(\mathbf{r}) = \frac{e^{i\mathbf{k}_{\parallel} \cdot \mathbf{r}_{\parallel}}}{2\pi} \sum_{n'} \xi_{\alpha\mathbf{k}_{\parallel}}^{n'}(z) u_{n'\mathbf{0}}(\mathbf{r}), \quad (4.1)$$

where α is the subband index and $\mathbf{r}_{\parallel} = (x, y, 0)$. In the following, we need not consider explicitly the spin index σ of the band-edge Bloch functions. Thus for brevity, we have included the index σ in the band index n' . The energy eigenvalues that correspond to the eigenfunctions (4.1) represent the subband dispersion $E_{\alpha}(\mathbf{k}_{\parallel})$.

In order to take into account a homogeneous, in-plane magnetic field $\mathbf{B}_{\parallel} = (B_x, B_y, 0)$, we choose the asymmetric gauge

$$\mathbf{A}(z) = (zB_y, -zB_x, 0). \quad (4.2)$$

The advantage of this gauge lies in the fact that the multiband Hamiltonian \mathcal{H} depends only on the z component of the position vector \mathbf{r} and not on x and y . Thus, even for $B_{\parallel} > 0$, we have a strictly one-dimensional eigenvalue problem. The kinetic wave vector \mathbf{k} reads (see (2.15))

$$\mathbf{k} = \begin{pmatrix} \mathfrak{k}_x + (e/\hbar) z B_y \\ \mathfrak{k}_y - (e/\hbar) z B_x \\ -i\partial_z \end{pmatrix}, \quad (4.3)$$

where the c -numbers \mathfrak{k}_x and \mathfrak{k}_y are the eigenvalues of the in-plane canonical wave vector \mathfrak{k}_{\parallel} . Therefore the eigenfunctions of \mathcal{H} are still of the form (4.1), with \mathbf{k}_{\parallel} replaced by \mathfrak{k}_{\parallel} . Note that the eigenvalues $(\mathfrak{k}_x, \mathfrak{k}_y)$ depend on the gauge that is used. If we were to choose, for example, the symmetric gauge $\mathbf{A} = (1/2)\mathbf{B} \times \mathbf{r}$, we would not be able to factorize the wave functions as in (4.1), anymore.

4.1.2 Boundary Conditions

For layered semiconductor structures, we need to take into account the inhomogeneity of the system. In the EFA, this is commonly achieved by considering bulk band parameters which vary discontinuously at the interfaces [1].¹

¹ This implies that we neglect any microscopic effects of the interfaces (see, however, Sect. 6.5).

In particular, the position-dependent band edges act like effective step-like potentials for the electrons and holes. According to Sect. 2.2, discontinuous band parameters go beyond the range of validity of the EFA. Nevertheless, it has been observed that such an ansatz is capable of describing electron and hole states in QWs in very good agreement with experiment [1]. Recently, several authors have established elaborate derivations of the EFA showing that it is indeed justified to apply the EFA in cases where the potential is not slowly varying [14, 17].

In (2.14), the off-diagonal $\mathbf{k} \cdot \mathbf{p}$ coupling results in terms linear in $k_z = -i\partial_z$ while the effective-mass-like terms are of second order in k_z . The step-like position dependence of the band parameters implies that the prefactors of these differential operators vary discontinuously. Therefore, we have to use matching conditions at the interfaces for the envelope functions and their first derivatives which ensure hermiticity of the kinetic-energy operator. The question of finding the proper Hermitian formulation has been discussed in the literature [14, 18] but remains a controversial problem [19]. In the present work we use the Hermitian forms that are most frequently found in the literature [18],

$$k_z f \rightarrow -\frac{i}{2} [\partial_z f(z) + f(z) \partial_z] \quad (4.4a)$$

$$k_z^2 g \rightarrow -\partial_z g(z) \partial_z. \quad (4.4b)$$

Here, the term $k_z f$ corresponds to, e.g., an off-diagonal $\mathbf{k} \cdot \mathbf{p}$ term or a second-order term proportional to $k_x k_z$, whereas $k_z^2 g$ always represents a second-order term.

4.1.3 Unphysical Solutions

Obtaining a general solution to the multicomponent envelope function problem is a difficult problem. Several methods have been suggested, each of them suited to certain problems but always requiring additional simplifications. Hence this section is devoted to a short review of the existing approaches, outlining their underlying physical approximations, their limitations of validity, and the numerical difficulties which they entail. In the past these aspects have been mixed up to some extent.

In the bulk conduction band, the effect of nonparabolicity has been taken into account by explicitly considering terms up to fourth order in \mathbf{k} [20, 21, 22]. This yields a simple model that has proved its worth for the conduction band in large-gap semiconductors. Furthermore, it can easily be applied to the subband problem. Commonly this is done by calculating the envelope functions from a standard effective-mass Hamiltonian, and then nonparabolic corrections are taken into account by first-order perturbation theory [13, 23, 24]. However difficulties may arise when dealing with expectation values of higher order in $k_z = -i\partial_z$. In numerical calculations, these quantities can

be rather large. Using generalized Fang–Howard trial functions, appropriate for MOS structures and heterostructures, one can show analytically that the expectation values of all higher orders in k_z diverge [15]. In these cases a perturbative treatment is not possible.

Frequently, a simplified multiband $\mathbf{k} \cdot \mathbf{p}$ model is used which neglects remote-band contributions and the free-electron term [11, 1, 2, 3, 12, 25, 26]. Thus this model is mainly justified for narrow-gap systems. The corresponding subband problem is a set of coupled first-order differential equations. By eliminating the valence band envelope functions, it can be reduced to two second-order equations solely for the conduction band envelope functions (spin up and down). However, the price to be paid is a kinetic-energy operator that has singularities due to zeros of the effective mass as a function of energy and position (cf. Sect. 5.2).

White and Sham [27] and Schuurmans and ’t Hooft [10] examined the solution $k^2(E)$ of the secular equation for a multiband Hamiltonian at a fixed energy. They showed that, if the Hamiltonian contains both the conduction and the valence band, unphysical “wing band” or “spurious” solutions may occur. These are large imaginary or real \mathbf{k} vectors which, in \mathbf{k} space, lie far beyond the range of validity of the corresponding Hamiltonian. Likewise, they occur in the case of single-band Hamiltonians if the Hamiltonian contains terms of higher than second order in \mathbf{k} . In contrast to many physical problems that are characterized by differential equations we have to exclude these solutions *independently of boundary conditions*. However, the problem is that, owing to numerical instabilities, these unphysical branches prevail in the standard numerical integration schemes (e.g. the Runge-Kutta method). This makes it impossible to solve multiband Hamiltonians along these lines.

In the case of hole subbands, the degeneracy of the topmost valence band Γ_8^v must be taken into account by a multicomponent formalism. When we restrict ourselves to the Luttinger Hamiltonian [28], spurious solutions do not occur. But it is still a considerable task to solve the corresponding subband problem for the four-component spinor function $\Psi(z)$ by means of a numerical integration scheme [29], since we have to fix the energy E and the initial values for $\Psi(z_0)$, $\partial_z \Psi(z)|_{z=z_0}$ in order to determine a bound state.² Most often, variational procedures have been used with differently chosen trial functions [5, 30, 6, 7, 9].

By using the analytical solution of the bulk secular equation, Andreani et al. [31] showed that the eigenvalue problem for the 4×4 Luttinger Hamiltonian (Γ_8^v) can be solved exactly in the flat-band case. Valadares [32] and Chao and Chuang [33] extended the approach to the 6×6 valence band Hamiltonian (Γ_8^v, Γ_7^v). However, besides the restriction to a piecewise constant potential, these Hamiltonians do not include nonparabolicities beyond

² A posteriori, one of the initial values can be fixed by means of the normalization condition for the envelope functions.

the valence band mixing. These effects can be substantial even for subbands in a large-gap material [15].

A general approach to the numerical solution of multiband envelope function problems is provided by a quadrature method in reciprocal space [15]. The central idea is that a plane wave expansion in reciprocal space gives precise control over the desired, physical, and undesired, unphysical, solutions of a multiband Hamiltonian. Simultaneously, one can incorporate the Hermitian boundary conditions (4.4) in a natural way. The authors of [15] considered the case $B = 0$. Here we rederive the formulas in a way that shows that this approach can include also an in-plane or perpendicular (Sect. 4.4) magnetic field B .

4.1.4 General Solution of the EFA Hamiltonian Based on a Quadrature Method

We begin by establishing a compact notation for the coupled differential equations that is more appropriate for the numerical solution of this eigenvalue problem. We write the Schrödinger equation in the form

$$\hat{H}(z) \Psi(z) = E \Psi(z), \quad (4.5)$$

where an $N \times N$ matrix Hamiltonian \hat{H} acts on the N -component spinor Ψ . If we use (4.3), the symmetrized expressions (4.4) in the matrix elements $\hat{h}_{nn'}$ of \hat{H} can be decomposed in terms of subexpressions with equal powers of z (due to the vector potential (4.2)) and $k_z = -i\partial_z$:

$$\begin{aligned} \hat{h}_{nn'} = & \hat{h}_{nn'}^{(0,0)} + \hat{h}_{nn'}^{(0,1)} + \hat{h}_{nn'}^{(0,2)} + \dots \\ & + \hat{h}_{nn'}^{(1,0)} + \hat{h}_{nn'}^{(1,1)} + \dots \\ & + \hat{h}_{nn'}^{(2,0)} + \dots, \end{aligned} \quad (4.6)$$

where

$$\hat{h}_{nn'}^{(0,\nu)} := z^\nu g_{nn'}^{(0,\nu)}(z), \quad (4.7a)$$

$$\hat{h}_{nn'}^{(1,\nu)} := -\frac{i}{2} [\partial_z z^\nu g_{nn'}^{(1,\nu)}(z) + z^\nu g_{nn'}^{(1,\nu)}(z) \partial_z], \quad (4.7b)$$

$$\hat{h}_{nn'}^{(2,\nu)} := -\partial_z z^\nu g_{nn'}^{(2,\nu)}(z) \partial_z, \quad (4.7c)$$

i.e. the superscript μ in $\hat{h}_{nn'}^{(\mu,\nu)}$ counts the powers of $k_z = -i\partial_z$, and ν counts the powers of z . In the above equations, $g_{nn'}^{(\mu,\nu)}(z) = [g_{n'n}^{(\mu,\nu)}(z)]^*$ are complex functions which describe the position dependence of the band parameters. In general, $\hat{h}_{nn'}^{(0,0)}$ contains terms which result from the in-plane dispersion; in addition we have band edge energies and the potential $V(z)$ in the diagonal elements $\hat{h}_{nn}^{(0,0)}$. The matrix elements $\hat{h}_{nn'}^{(0,\nu)}$ with $\nu \geq 1$ stem from terms

proportional to the vector potential due to the in-plane B . The matrix elements $\hat{h}_{nn'}^{(1,0)}$ represent off-diagonal terms proportional to momentum matrix elements multiplied by $k_z = -i\partial_z$, and $\hat{h}_{nn'}^{(2,0)}$ results from remote-band contributions of second order in k_z . Note that in a $\mathbf{k} \cdot \mathbf{p}$ multiband Hamiltonian with terms up to second order in \mathbf{k} , we can restrict ourselves in (4.6) to terms $\hat{h}_{nn'}^{(\mu,\nu)}$ with $\mu + \nu \leq 2$ because, according to (4.3), the operators z and $-i\partial_z$ occur only in different Cartesian components of \mathbf{k} . It is straightforward to include in (4.6) higher orders $\hat{h}_{nn'}^{(\mu,\nu)}$, $\mu, \nu > 2$, which occur, for example, in the 2×2 Hamiltonian of [20]. Equation (4.7) corresponds to the most commonly used Hermitian formulation (4.4) of the operator \hat{H} , other formulations are given in Table I of [15].

For the numerical solution of the eigenvalue problem (4.5), we use the fact that the differential operator $-i\partial_z$ in (4.7) becomes a simple, multiplicative operator k_z in reciprocal space [15]. Therefore, a Fourier transform leads to the set of coupled integral equations

$$\begin{aligned} \hat{H}(k) \Psi(k) &= \int_{-\infty}^{\infty} dk' \sum_{\nu} \left\{ \mathcal{G}^{(0,\nu)}(k - k') + \frac{1}{2}(k + k') \mathcal{G}^{(1,\nu)}(k - k') \right. \\ &\quad \left. + kk' \mathcal{G}^{(2,\nu)}(k - k') \right\} \Psi(k') \\ &= E \Psi(k), \end{aligned} \quad (4.8)$$

where for brevity we have used $k \equiv k_z$. The symbol $\mathcal{G}^{(\mu,\nu)}(k)$ denotes the matrix of the Fourier transforms of $z^{\nu} g_{nn'}^{(\mu,\nu)}(z)$; the prefactors of these matrices $\mathcal{G}^{(\mu,\nu)}(k)$, which depend on k and k' , result from transferring the differential operators in (4.7) into reciprocal space. Strictly speaking, a Fourier transform of (4.7) turns all terms proportional to z^{ν} , $\nu > 0$, into differential operators in reciprocal space. However, if the Fourier transform of z^{ν} is implemented by means of a discrete Fourier transform on a finite, discrete mesh, this provides a sufficiently accurate approximation to the differential operator in reciprocal space. The integral kernel in (4.8) is obviously Hermitian. Integral kernels corresponding to other Hermitian formulations of \hat{H} are given in Table I of [15].

Equation (4.8) can be readily solved by means of a quadrature method [34], i.e. by discretizing the integral kernel $\hat{H}(k, k')$ in (4.8) and diagonalizing the resulting finite-dimensional matrix. This approach yields eigenfunctions $\Psi(k)$ in reciprocal space, which must be Fourier transformed into real space individually. Therefore, it turns out to be efficient to perform another discrete Fourier transform of the integral kernel $\hat{H}(k, k')$ back into real space so that a diagonalization of the resulting matrix provides the multicomponent envelope functions on a discrete mesh in real space (see [35] and the Appendix in [15]).

4.1.5 Electron and Hole States for Different Crystallographic Growth Directions

The extended Kane model described in Chap. 3 was given for a coordinate system where k_x , k_y , and k_z correspond to the principal crystallographic axes [100], [010] and [001], respectively. In order to calculate subband states for an arbitrary growth direction, it is convenient to use a symmetry-adapted rotated coordinate system $\mathbf{k}' = (k'_x, k'_y, k'_z)$, where $k'_z = -i\partial_{z'}$ (z' is the growth direction). We have $\mathbf{k}' = \mathbf{R}\mathbf{k}$, where \mathbf{R} is an orthogonal matrix. Therefore we can express the components of \mathbf{k} in terms of those of \mathbf{k}' using

$$\mathbf{k} = \mathbf{R}^{-1} \mathbf{k}' . \quad (4.9)$$

As we want to insert (4.9) into the general ansatz (4.6), we see that we have to evaluate this coordinate transformation separately for the components k'_x , k'_y , and $k'_z = -i\partial_{z'}$, as well as for the vector potential (4.2).

4.2 Density of States of a Two-Dimensional System

For use in the discussion in subsequent chapters, we shall summarize in this short section several formulas concerning the density of states of a 2D system. We consider a finite system with area \mathcal{L}^2 and a subband dispersion $E_{\alpha\sigma}(\mathbf{k}_{\parallel})$. In reciprocal space, every state occupies an area $(2\pi/\mathcal{L})^2$. Accordingly, the number \mathcal{N} of states below the energy E is

$$\mathcal{N}(E) = \sum_{\alpha, \sigma} \int \frac{d^2 k_{\parallel}}{(2\pi/\mathcal{L})^2} \theta[\pm(E - E_{\alpha\sigma}(\mathbf{k}_{\parallel}))] , \quad (4.10)$$

where the upper and lower signs stand for electrons and holes, respectively, α is the subband index, and $\sigma = \pm$ is the spin index. The density of states (DOS) $D(E)$ is the number of states per unit energy range dE and unit area \mathcal{L}^2 ,

$$D(E) = \frac{1}{\mathcal{L}^2} \frac{d}{dE} \mathcal{N}(E) = \sum_{\alpha, \sigma} \int \frac{d^2 k_{\parallel}}{(2\pi)^2} \delta[\pm(E - E_{\alpha\sigma}(\mathbf{k}_{\parallel}))] . \quad (4.11)$$

For an isotropic dispersion $E_{\alpha\sigma}(k_{\parallel})$, we can easily evaluate the angular part of the integration. We obtain

$$D(E) = \frac{1}{2\pi} \sum_{\alpha, \sigma} \frac{k_{\parallel}(E)}{|dE_{\alpha\sigma}(k_{\parallel})/dk_{\parallel}|} . \quad (4.12)$$

We define (as a generalization of (4.18) below) the DOS effective mass,

$$\frac{m_{\alpha\sigma}^*(E)}{m_0} = 4\pi \frac{\hbar^2}{2m_0} D_{\alpha\sigma}(E) = \frac{1}{\pi} \frac{\hbar^2}{2m_0} \int d^2 k_{\parallel} \delta[\pm(E - E_{\alpha\sigma}(\mathbf{k}_{\parallel}))] . \quad (4.13)$$

We shall see in subsequent chapters that $m^*(E)$ shows clearly the influence of band structure effects. Our definition of $m^*(E)$ corresponds to the cyclotron effective mass (8.5) in the limit $B \rightarrow 0$.

Finally, we note that it follows from (4.10) that the charge density $N_{\alpha\sigma}$ in the spin subband $\alpha\sigma$ is given by (assuming temperature $T = 0$)

$$N_{\alpha\sigma} = \int \frac{d^2 k_{\parallel}}{(2\pi)^2} \theta[\pm(E_F - E_{\alpha\sigma}(\mathbf{k}_{\parallel}))], \quad (4.14)$$

where E_F is the Fermi energy. For an arbitrary nonparabolic and anisotropic subband dispersion $E_{\alpha\sigma}(\mathbf{k}_{\parallel})$, one can evaluate (4.11) and (4.14) by means of analytic quadratic Brillouin zone integration [36]. The advantage of this scheme is that it fully takes into account the anisotropy of $E_{\alpha\sigma}(\mathbf{k}_{\parallel})$ as well as van Hove singularities of $D(E)$.

4.3 Effective-Mass Approximation

The simplest model for the subband structure of a quasi-2D system is based on the effective-mass Hamiltonian (2.19) for a nondegenerate, isotropic, parabolic bulk band n which becomes³

$$\left[-\frac{\hbar^2}{2m_n^*} \frac{\partial^2}{\partial z^2} + \frac{\hbar^2 k_{\parallel}^2}{2m_n^*} + E_n(z) + V(z) \right] \psi_{\alpha\mathbf{k}_{\parallel}}(\mathbf{r}) = E_{\alpha} \psi_{\alpha\mathbf{k}_{\parallel}}(\mathbf{r}), \quad (4.15)$$

where $E_n(z)$ is the position-dependent band edge of the bulk band n . The envelope functions (4.1) are fully factorized, i.e.

$$\psi_{\alpha\mathbf{k}_{\parallel}}(\mathbf{r}) = \frac{e^{i\mathbf{k}_{\parallel} \cdot \mathbf{r}_{\parallel}}}{2\pi} \xi_{\alpha}(z), \quad (4.16)$$

and we obtain a strictly parabolic subband dispersion,

$$E_{\alpha}(\mathbf{k}_{\parallel}) = E_{\alpha} + \frac{\hbar^2 k_{\parallel}^2}{2m_n^*}. \quad (4.17)$$

The density of states for every (spin-degenerate) subband is a step function

$$D_{\alpha}(E) = \frac{m_n^*}{\pi \hbar^2} \theta(E - E_{\alpha}). \quad (4.18)$$

The effective-mass approximation provides basic insight into the electronic structure of inversion layers, heterojunctions, QWs, and superlattices. For a more quantitative interpretation of experiments, we must take into account the subtleties which occur in semiconductor band structure, such as

³ In (4.15) we have neglected the position dependence of the effective mass $m_n^* = m_n^*(z)$ because, strictly speaking, this effect results in a weak coupling between the in-plane and perpendicular components of the motion so that (4.16) and (4.17) are no longer valid.

nonparabolicity, anisotropy, spin splitting, and heavy–light-hole coupling. In subsequent chapters we compare the EMA with results based on the more accurate multiband Hamiltonians introduced in Chap. 3.

4.4 Electron and Hole States in a Perpendicular Magnetic Field: Landau Levels

Electron and hole states in the presence of a perpendicular magnetic field $\mathbf{B} = (0, 0, B)$ differ conceptually from the eigenstates at $B = 0$ or for an in-plane field \mathbf{B}_{\parallel} , because the motion is fully quantized into Landau levels. Most publications on the calculation of Landau levels in 2D hole systems have restricted themselves to the axial approximation (see Sect. 3.6) to Luttinger’s $4 \times 4 \mathbf{k} \cdot \mathbf{p}$ model [7, 8, 37]. In [38], the split-off valence band Γ_7^v was taken into account with a $6 \times 6 \mathbf{k} \cdot \mathbf{p}$ model. For undoped rectangular QWs, calculations of Landau levels and matrix elements for interband optical transitions have been performed using a $6 \times 6 \mathbf{k} \cdot \mathbf{p}$ model, which includes the lowest conduction band [39, 40]. Few publications [38, 41, 42, 23] have analyzed Landau levels beyond the axial approximation. Here, we present a general scheme for calculating Landau levels, assuming an arbitrary growth direction and taking into account all cubic and tetrahedral corrections beyond the axial approximation.

4.4.1 Creation and Annihilation Operators

We want to describe Landau levels by means of an algebraic approach because this type of approach is the easiest to apply to an arbitrary multiband Hamiltonian [43, 44]. For the perpendicular field $\mathbf{B} = (0, 0, B)$, we use the symmetric gauge

$$\mathbf{A}(x, y) = \frac{B}{2}(-y, x, 0). \quad (4.19)$$

We define the operators

$$\mathcal{P}^{\pm} = -i\hbar\nabla \pm e\mathbf{A}. \quad (4.20)$$

Obviously, we have $\mathcal{P}^{+} = \mathbf{p} + \hbar\mathbf{k}$. In generalization of (2.17), the operators \mathcal{P}^{\pm} obey the commutator relations

$$[\mathcal{P}^{\pm}, \mathcal{P}^{\pm}] = \mp ie\hbar\mathbf{B}, \quad (4.21a)$$

$$[\mathcal{P}_j^{\pm}, \mathcal{P}_k^{\mp}] = 0, \quad j, k \in \{x, y, z\}. \quad (4.21b)$$

Next we define the creation and annihilation operators

$$a^\dagger = \frac{\lambda_c}{\sqrt{2}\hbar} (\mathcal{P}_x^+ + i\mathcal{P}_y^+) = \frac{\lambda_c}{\sqrt{2}} k_+ , \quad (4.22a)$$

$$a = \frac{\lambda_c}{\sqrt{2}\hbar} (\mathcal{P}_x^+ - i\mathcal{P}_y^+) = \frac{\lambda_c}{\sqrt{2}} k_- , \quad (4.22b)$$

$$b^\dagger = \frac{\lambda_c}{\sqrt{2}\hbar} (\mathcal{P}_x^- - i\mathcal{P}_y^-) , \quad (4.22c)$$

$$b = \frac{\lambda_c}{\sqrt{2}\hbar} (\mathcal{P}_x^- + i\mathcal{P}_y^-) , \quad (4.22d)$$

where the magnetic length is

$$\lambda_c = \sqrt{\frac{\hbar}{eB}} . \quad (4.23)$$

These operators obey the usual commutator relations

$$[a, a^\dagger] = [b, b^\dagger] = 1 , \quad (4.24a)$$

$$[a, b] = [a, b^\dagger] = [a^\dagger, b] = [a^\dagger, b^\dagger] = 0 . \quad (4.24b)$$

These relations show that the sets $\{a, a^\dagger\}$ and $\{b, b^\dagger\}$ define two decoupled oscillators. The operators a , a^\dagger , b , and b^\dagger form a set of four conjugate variables, just as x , y , p_x , and p_y do, so that we can express the EFA Hamiltonian \mathcal{H} in terms of the new variables. However, (4.22a) and (4.22b) show that \mathcal{H} depends on a and a^\dagger only, and not on b or b^\dagger . It follows from (4.24b) that \mathcal{H} commutes with the number operator $b^\dagger b$. Therefore, we can choose the eigenfunctions of \mathcal{H} such that they are also eigenfunctions of the oscillator associated with b (the “ b oscillator”).

As \mathcal{H} does not depend on b or b^\dagger , the b oscillator behaves like an oscillator with zero frequency. The quantum number n_b of the b oscillator can take integer values $0, 1, 2, \dots$, so that the Landau levels must be infinitely degenerate. The degeneracy per unit area of the spin-split Landau levels amounts to [45]

$$G = \frac{eB}{2\pi\hbar} . \quad (4.25)$$

Using the asymmetric gauge of the classic paper by Landau [45], it can readily be shown that (4.25) holds for an arbitrary multiband Hamiltonian. Amazingly, we are not aware of a general proof of (4.25) based on the symmetric gauge (4.19) underlying the operator formalism outlined in this section.

The operator for the component of angular momentum along the magnetic field $\hat{L}_z = xp_y - yp_x$ can be expressed in terms of the operators a and b as

$$\hat{L}_z = \hbar (a^\dagger a - b^\dagger b) . \quad (4.26)$$

As discussed by Suzuki and Hensel [43], we can visualize the system as an assembly of two types of harmonic oscillators. Each oscillator in the a system has a frequency ω_c and an angular momentum \hbar along \mathbf{B} . Each b oscillator

has zero frequency and an angular momentum $-\hbar$ along \mathbf{B} . For a system with opposite charge (holes instead of electrons), it follows readily that the role of the a and b operators must be interchanged, i.e. the a oscillators become oscillators with zero frequency, while the b oscillators have a frequency ω_c .⁴

4.4.2 Landau Levels in the Effective-Mass Approximation

Similarly to (4.15), the effective-mass Hamiltonian (2.19) for the n th bulk band acquires a particularly simple form,

$$H_\sigma = -\frac{\hbar^2}{2m_n^*} \frac{\partial^2}{\partial z^2} + E_n(z) + V(z) + \hbar\omega_c^* \left(a^\dagger a + \frac{1}{2}\right) + \frac{g_n^*}{2} \sigma \mu_B B, \quad (4.27)$$

where the cyclotron frequency is

$$\omega_c^* = \frac{eB}{m_n^*} \quad (4.28)$$

and the spin index is $\sigma = \pm 1$. The perpendicular, in-plane, and spin components of the motion are completely decoupled, so that the eigenfunctions can be written in a factorized form

$$\psi_{\alpha L \sigma} = |L\rangle |\sigma\rangle \xi^\alpha(z). \quad (4.29)$$

The kets $|L\rangle$ are eigenstates of the number operator $a^\dagger a$, where $a^\dagger a |L\rangle = L |L\rangle$ and the Landau quantum number is $L = 0, 1, \dots$, so that the eigenenergies of (4.27) read

$$E(\alpha, L, \sigma) = E_\alpha + \hbar\omega_c^* \left(L + \frac{1}{2}\right) + \frac{g^*}{2} \sigma \mu_B B. \quad (4.30)$$

Here α is the subband index for the perpendicular motion with subband edge E_α .

The general solution for the multiband EFA Hamiltonian in the presence of a perpendicular field is significantly more difficult to obtain owing to the coupling between the quantized perpendicular motion and the quantized in-plane motion. We shall achieve this goal in three steps. First, we decompose the multiband Hamiltonian \mathcal{H} into a dominant part \mathcal{H}_{ax} with axial symmetry and a second, smaller part \mathcal{H}' containing the terms of lower symmetry (see Sect. 3.6). Then we solve the problem for \mathcal{H}_{ax} . Finally, we can solve the problem for the full Hamiltonian by expanding its eigenfunctions in terms of the eigenfunctions of \mathcal{H}_{ax} .

⁴ Multiband Hamiltonians such as the extended Kane Hamiltonian yield electron and hole states simultaneously. We thus use here only the a operators and not the b operators. Strictly speaking, the states below the fundamental gap are valence band states for electrons. The corresponding hole states are obtained by complex conjugation [46].

4.4.3 Landau Levels in the Axial Approximation

In the axial approximation (Sect. 3.6), the total Hamiltonian \mathcal{H}_{ax} commutes with $\hat{F} \equiv \hbar(a^\dagger a - b^\dagger b) + \hat{J}_z$, which corresponds to the conservation of the z component of the total angular momentum [44, 47]. Here, \hat{J}_z is the operator for the z component of the angular momentum of the basis functions $u_{n\mathbf{0}}(\mathbf{r})$ in (2.13). Therefore we can write the eigenfunctions of \mathcal{H}_{ax} in the form

$$\psi_{\alpha N \sigma}(\mathbf{r}) = \sum_n |L_n = N - m_n + \frac{3}{2}\rangle \xi_{m_n}^{\alpha N \sigma}(z) u_{n\mathbf{0}}(\mathbf{r}) \quad (4.31)$$

which contains the subband index α , the Landau quantum number $N = 0, 1, \dots$, the spin index $\sigma = \pm$, and Landau oscillators $|L\rangle$. The symbol m_n denotes the z component of the angular momentum of $u_{n\mathbf{0}}(\mathbf{r})$, i.e. $\hat{J}_z u_{n\mathbf{0}}(\mathbf{r}) = m_n u_{n\mathbf{0}}(\mathbf{r})$. From a group-theoretical point of view, the index N labels the irreducible representation of the axial point group. We have no rigorous rule for choosing the quantum numbers α and σ . In general, they reflect the dominant character of the wave function (4.31) which can change as a function of B . Strictly speaking, α and σ must be replaced by one common index.

In the basis (4.31), the Schrödinger equation falls into blocks corresponding to fixed Landau quantum numbers N , for which we can readily specify the effect of a and a^\dagger . Therefore, each block can be treated in the same way as the subband problem for $B = 0$; see Sect. 4.1.4. In (4.31), we have the restriction that $L_n \geq 0$. This implies that for small Landau quantum numbers N , not all spinor components n contribute to the multicomponent wave functions (4.31) [7]. For electron systems the $N = 0$ Landau levels vanish completely, i.e., in our notation, electron Landau levels have $N \geq 1$.

4.4.4 Landau Levels Beyond the Axial Approximation

The calculation of Landau levels with inclusion of the cubic and tetrahedral terms is more difficult, in particular for low-symmetry growth directions such as [113] and [110], the reason being that the explicit expressions for \mathcal{H}_{cub} and $\mathcal{H}_{\text{tetra}}$ are very complicated for these cases. On the other hand, such a refined model is most urgently needed for the proper characterization of these low-symmetry growth directions, as here the axial model is a particularly poor approximation; see the end of Sect. 3.6.

The cubic and tetrahedral parts of the multiband Hamiltonian result in a coupling between different Landau levels $\psi_{\alpha N \sigma}(\mathbf{r})$. Thus we expand the eigenfunctions of the full Hamiltonian \mathcal{H} in terms of the eigenfunctions (4.31) of \mathcal{H}_{ax} :

$$\Psi_{\alpha N \sigma}(\mathbf{r}) = \sum_{\alpha', N, \sigma'} c_{\alpha N \sigma}^{\alpha' N \sigma'} \psi_{\alpha' N \sigma'}(\mathbf{r}) \quad (4.32a)$$

$$= \sum_{\alpha', N, \sigma'} c_{\alpha N \sigma}^{\alpha' N \sigma'} \sum_n |N - m_n + \frac{3}{2}\rangle \xi_{m_n}^{\alpha' N \sigma'}(z) u_{n\mathbf{0}}(\mathbf{r}). \quad (4.32b)$$

Here α , \mathcal{N} , and σ denote the new subband, the Landau level, and the spin index, respectively. In order to increase the variational freedom, we sum also over different subbands α' .

Strictly speaking, we should use instead of the indices α , \mathcal{N} , and σ an index β that labels the irreducible representation Γ_β according to which $|\alpha\mathcal{N}\sigma\rangle$ transforms, and a second index that counts the Landau levels that transform according to Γ_β . For pairs of Landau levels $|\alpha\mathcal{N}\sigma\rangle$ and $|\alpha'\mathcal{N}'\sigma'\rangle$ that transform according to different irreducible representations Γ_β and $\Gamma_{\beta'}$ we obtain crossings between these levels, whereas for pairs that transform according to the same irreducible representation Γ_β we obtain anticrossings (irrespective of the subband indices α and α'). According to Table 3.4, for the growth direction [001] we have (at least) the point group C_2 , with two double-group representations Γ_3 and Γ_4 [48], so that pairs of Landau levels with one level that transforms according to Γ_3 and another level that transforms according to Γ_4 cross each other. On the other hand, for low-symmetry growth directions such as [110] and [113] we obtain the trivial point group C_1 , with only one irreducible double-group representation, so that all pairs of Landau levels show anticrossings. Owing to these anticrossings between Landau levels originating in different subbands, the proper interpretation of the indices α , \mathcal{N} , and σ requires a careful analysis of the eigenfunctions $|\alpha\mathcal{N}\sigma\rangle$ with respect to the dominant expansion coefficients $c_{\alpha\mathcal{N}\sigma}^{\alpha'\mathcal{N}'\sigma'}$ as a function of the magnetic field B .

4.5 Example: Two-Dimensional Hole Systems

Electrons in bulk semiconductors (conduction band Γ_6^c) have an almost isotropic and parabolic dispersion $E(\mathbf{k})$ (Fig. 3.2a) that is passed on to the electrons in quasi-2D systems. For quasi-2D electron systems, the EMA (4.17) is thus often a useful starting point. Higher-order corrections beyond the EMA can be incorporated in a perturbative scheme [13]. The dispersion $E(\mathbf{k})$ of holes in the bulk valence band Γ_8^v , on the other hand, is highly anisotropic and nonparabolic (Fig. 3.2b). Accordingly, it is not possible to describe quasi-2D hole systems by a simple effective-mass Hamiltonian. As an example of the general concepts introduced in the previous sections, we shall therefore discuss the anisotropic and nonparabolic dispersion $E(\mathbf{k}_\parallel)$ of quasi-2D hole systems.

4.5.1 Heavy-Hole and Light-Hole States

Electrons in the Γ_6^c conduction band have a spin $j = 1/2$ that is not affected by subband quantization. Hole systems in the Γ_8^v valence band, on the other hand, have an effective spin $j = 3/2$. Size quantization in quasi-2D systems lifts the fourfold degeneracy of the $j = 3/2$ states. We obtain *heavy-hole* (HH) states with a z component of angular momentum $m = \pm 3/2$ and *light-hole*

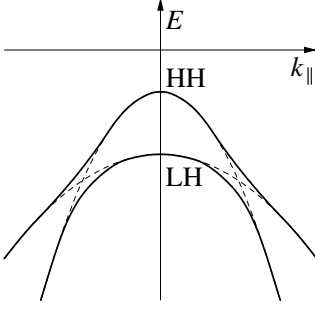


Fig. 4.1. Qualitative sketch of an HH–LH anti-crossing

(LH) states with $m = \pm 1/2$, separated in energy by the *HH–LH splitting*. The terms “heavy hole” and “light hole” refer to the large and small effective masses, respectively, of these states for the bound motion in the growth direction. However, for the in-plane motion the “heavy hole” and “light hole” characters of the HH ($m = \pm 3/2$) and LH ($m = \pm 1/2$) states is reversed, i.e. the HH states have a smaller effective mass characterizing the in-plane motion than the LH states have. If we neglect all off-diagonal terms in the Luttinger Hamiltonian, then the HH and LH states are characterized by the following effective masses for the perpendicular and in-plane motions (see Table C.10):

$$\frac{m_0}{m_z^{\text{HH}}} = \gamma_1 - 2\tilde{\gamma}, \quad \frac{m_0}{m_z^{\text{LH}}} = \gamma_1 + 2\tilde{\gamma}, \quad (4.33a)$$

$$\frac{m_0}{m_{\parallel}^{\text{HH}}} = \gamma_1 + \tilde{\gamma}, \quad \frac{m_0}{m_{\parallel}^{\text{LH}}} = \gamma_1 - \tilde{\gamma}, \quad (4.33b)$$

where

$$\tilde{\gamma} = (1 - \zeta) \gamma_2 + \zeta \gamma_3, \quad (4.33c)$$

$$\zeta = \sin^2 \theta \left\{ 3 - \frac{3}{8} \sin^2 \theta [7 + \cos(4\phi)] \right\}. \quad (4.33d)$$

The angles θ and ϕ are defined in Fig. C.1. Equation (4.33) includes the well-known results $\tilde{\gamma} = \gamma_2$ for the growth direction [001] and $\tilde{\gamma} = \gamma_3$ for [111] (Ref. [44]). According to (4.33), we obtain a steep subband dispersion $E(\mathbf{k}_{\parallel})$ for the strongly bound HH states, whereas we have a flat dispersion for the weakly bound LH states. The off-diagonal *HH–LH mixing* in the Luttinger Hamiltonian thus gives rise to HH–LH anticrossings as sketched in Fig. 4.1.

4.5.2 Numerical Results

In Fig. 4.2 we show the hole subband dispersions $E(\mathbf{k}_{\parallel})$ for symmetric 150 Å wide GaAs–Al_{0.3}Ga_{0.7}As QWs with growth directions [001], [113], [111], and [110]. For comparison, we also show $E(\mathbf{k}_{\parallel})$ in the axial approximation (dotted lines), i.e. when the in-plane anisotropy is neglected in the Hamiltonian. The

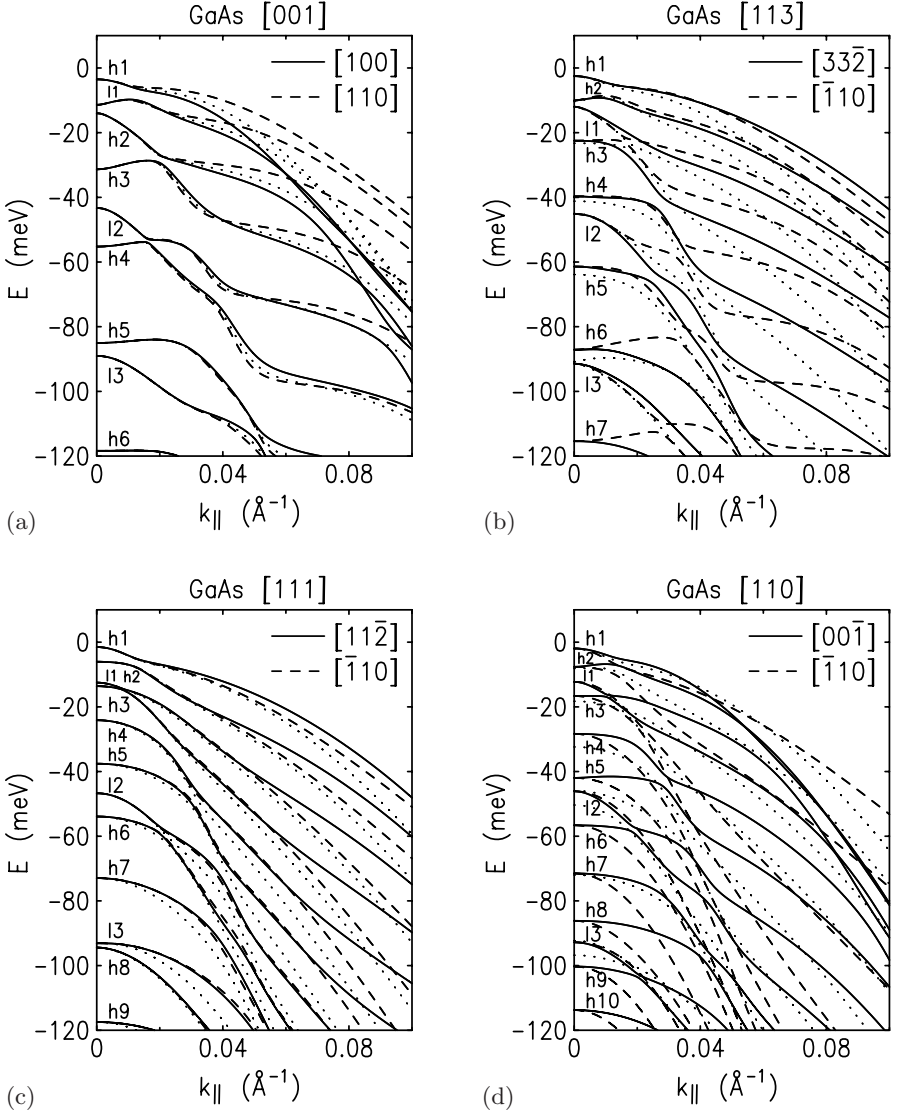


Fig. 4.2. Anisotropic hole subband dispersion $E(k_{\parallel})$ for 150 Å wide GaAs–Al_{0.3}Ga_{0.7}As QWs with growth directions (a) [001], (b) [113], (c) [111], and (d) [110], calculated by means of an 8×8 Hamiltonian (Γ_6^c , Γ_8^v , and Γ_7^v). Dotted lines correspond to the axial approximation

DOS effective mass (4.13) for the topmost subbands is displayed in Fig. 4.3. The calculations were based on the 8×8 $\mathbf{k} \cdot \mathbf{p}$ Hamiltonian (3.6) using the cubic approximation. We have neglected the tetrahedral terms, which will be discussed in detail in Sect. 6.2.

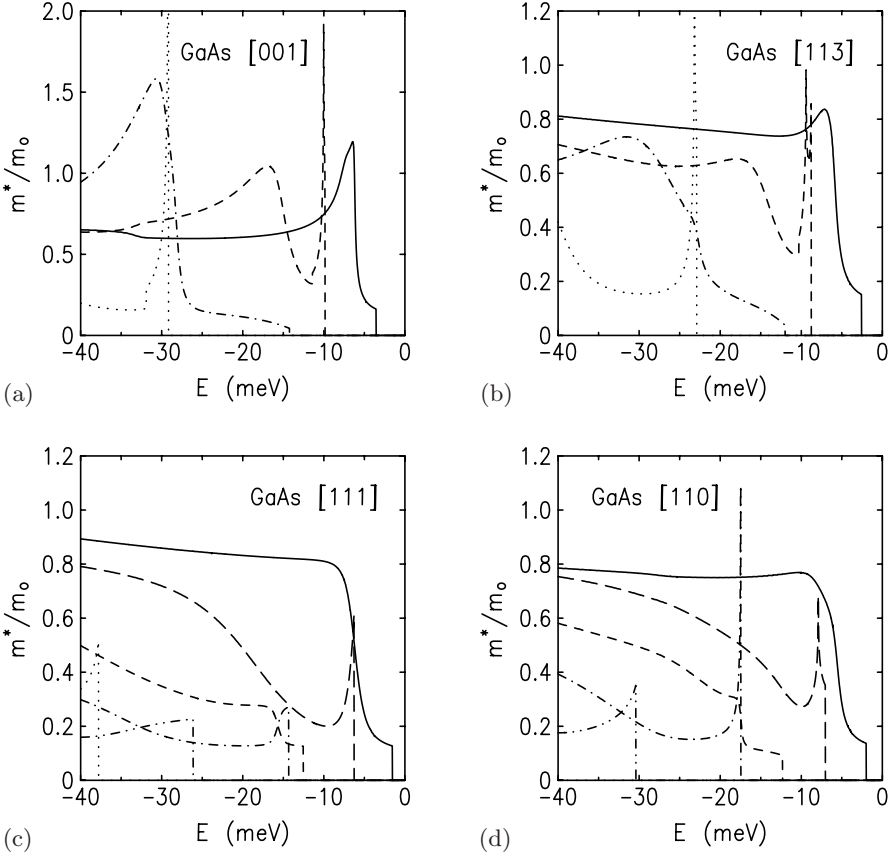


Fig. 4.3. DOS effective mass as a function of energy E for the topmost hole subbands of 150 Å wide GaAs-Al_{0.3}Ga_{0.7}As QWs with growth directions (a) [001], (b) [113], (c) [111], and (d) [110], calculated by means of an 8×8 Hamiltonian (Γ_6^c , Γ_8^v , and Γ_7^v). Note the different scale of the vertical axis in (a) as compared with (b), (c), and (d)

In Fig. 4.2 we have labeled the subband states as HH-like (h) or LH-like (l) according to their dominant spinor component at $\mathbf{k}_{\parallel} = 0$. This is an accurate scheme for the growth directions [001] and [111], where the off-diagonal coupling between HH and LH states vanishes for $\mathbf{k}_{\parallel} = 0$ (see Tables C.10 and C.11).⁵ For nonzero in-plane wave vectors, the off-diagonal terms yield a mixing of HH and LH states. This is illustrated in Fig. 4.4, where we show

⁵ For $k_{\parallel} = 0$, we have a weak coupling of HH and LH states even for the growth directions [001] and [111] due to the terms with tetrahedral symmetry that we are neglecting in this section. For a discussion of this aspect, see Sect. 6.5.

the HH character⁶ as a function of k_{\parallel} of the four topmost hole subbands for the same QWs as in Fig. 4.2. Obviously, the relevance of HH–LH mixing depends on the magnitude of the Fermi wave vector. Although the calculations were based on the 8×8 Hamiltonian (3.6), the contribution of Γ_6^c and Γ_7^v bulk band-edge states to the multicomponent wave function (4.1) is smaller than 1% for the subband states analyzed in Fig. 4.4. HH–LH anticrossings are clearly visible in Fig. 4.2. They can also be recognized in the two lowest panels of Figs. 4.4c,d, where the character of the subbands l_1 and h_3 changes abruptly at $k_{\parallel} \sim 0.007 \text{ \AA}$ and $k_{\parallel} \sim 0.01 \text{ \AA}$, respectively.

In the EMA, the density of states is a simple step function (4.18) for each subband. On the other hand, we see from Fig. 4.3 that the DOS effective mass $m^*(E)$ of a 2D hole system is a complicated function of energy, where HH–LH coupling gives rise to pronounced van Hove singularities. Furthermore, $m^*(E)$ depends sensitively on system parameters such as the crystallographic growth direction. Therefore, an effective-mass-like model such as that suggested by (4.33) is not appropriate for a quantitative interpretation of quasi-2D hole systems. Nevertheless, it can be useful for estimating qualitative trends, in particular for the h_1 subband close to the subband edge.

There are significant differences between the subband dispersion curves for the various growth directions shown in Fig. 4.2. For the growth direction [110], the anisotropy of $E(k_{\parallel})$ is the most pronounced. Moreover, the average spacing between the HH subbands is considerably smaller than for [001] and [113]. This is related to the bulk dispersion shown in Fig. 3.2b, which for the HH branch of the Γ_8^v valence band is the flattest in the [110] direction. The LH subbands depend less sensitively on the growth direction than do the HH subbands, which is again consistent with the bulk dispersion shown in Fig. 3.2b. The total number of hole subband states in a QW must be independent of the growth direction. Therefore the density of states of the few subbands in the [001] and [113] QWs is larger than the density of states of the many subbands in the [110] QW. Thus, on average, the dispersion in the [001] and [113] QWs is flatter and frequently even has a positive slope. The reciprocity between the effective masses for the perpendicular motion and for the in-plane motion can be seen also in the ζ dependence of m^* in (4.33). The axial approximation (dotted lines in Fig. 4.2) is most accurate for the high-symmetry directions [001] and [111], where at $k_{\parallel} = 0$ it yields exactly the same results as does the cubic model.

Finally, we show in Fig. 4.5 the Landau-level structure for the QWs with growth directions [001] and [113]. The left panels are based on the axial approximation. In the calculations for the right panels, both cubic and tetrahedral terms were taken into account. For the [001]-grown QW, the cubic

⁶ For the calculation of Fig. 4.4, the multicomponent envelope functions (4.1) have been expressed in a basis of band-edge Bloch functions $u_{n\mathbf{0}}(\mathbf{r})$ that are eigenstates of the z component of the angular momentum, with \hat{J}_z in the growth direction.

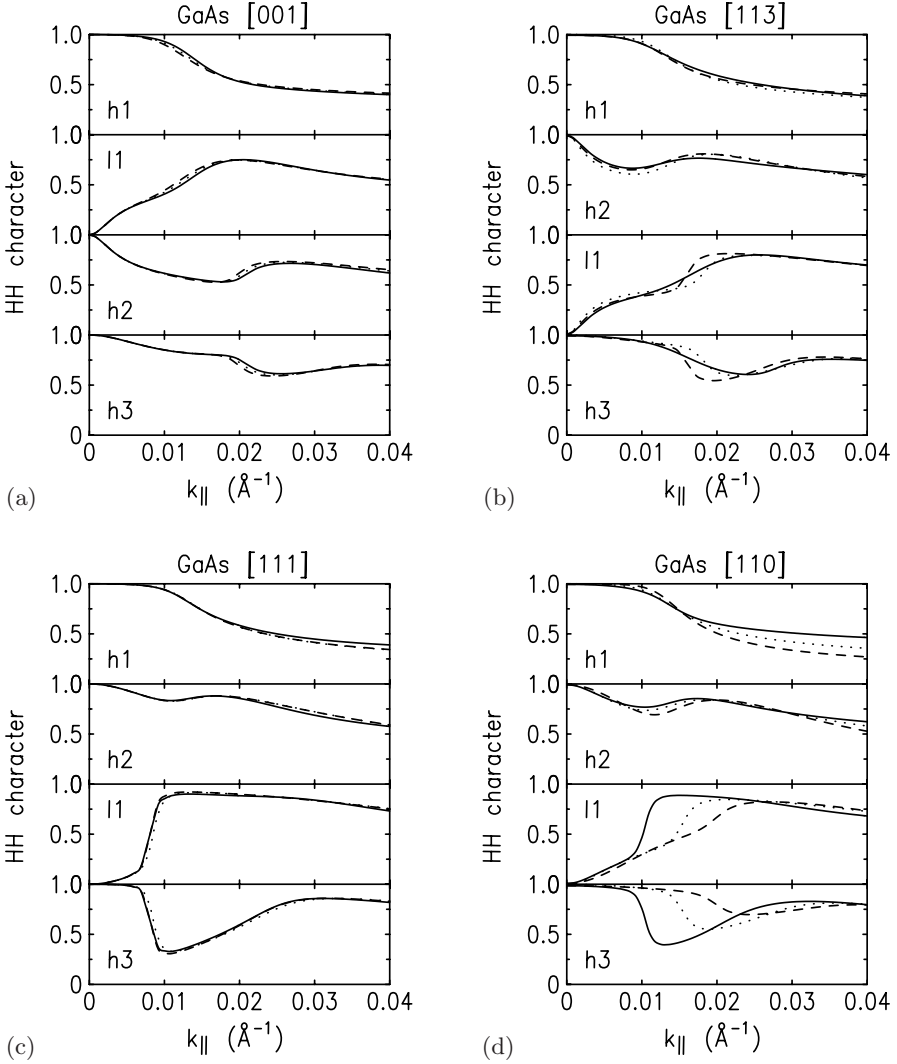


Fig. 4.4. Heavy-hole character as a function of the in-plane wave vector k_{\parallel} of the four topmost hole subbands of 150 \AA wide GaAs-Al_{0.3}Ga_{0.7}As QWs with growth directions (a) [001], (b) [113], (c) [111], and (d) [110], calculated by means of an 8×8 Hamiltonian (I_6^c , I_8^v , and I_7^v). The line styles have the same meaning as in Fig. 4.2

and tetrahedral terms are far less important than for the [113]-grown QW. Likewise, these terms are very important for the hole Landau levels in QWs grown in the [111] and [110] crystallographic directions (not shown).

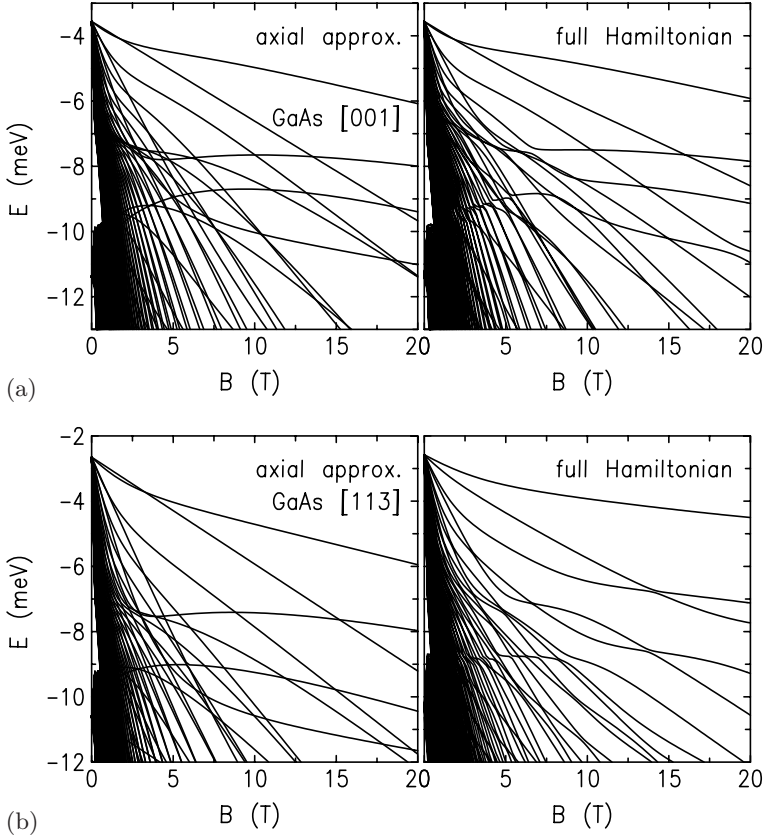


Fig. 4.5. Landau levels as a function of magnetic field B for the topmost hole subbands in 150 Å wide GaAs–Al_{0.3}Ga_{0.7}As QWs with growth directions (a) [001] and (b) [113], obtained by means of an 8×8 Hamiltonian (Γ_6^c , Γ_8^v , and Γ_7^v). The left panels are based on the axial approximation. In the calculations for the right panels, cubic and tetrahedral terms were taken into account

4.5.3 HH–LH Splitting and Spin–Orbit Coupling

In subsequent chapters, we shall discuss subtle SO coupling effects such as the $B = 0$ spin splitting in inversion-asymmetric systems and the Zeeman splitting at $B > 0$. In this brief section, we point out that in 2D hole systems these SO coupling effects are always competing with HH–LH splitting.

Electrons in the Γ_6^c conduction band have a spin $j = 1/2$ that is not affected by subband quantization. Therefore, the spin dynamics of electrons are primarily controlled by the SO terms for the $B = 0$ spin splitting and the Zeeman term. Hole systems in the Γ_8^v valence band, on the other hand, have an effective spin $j = 3/2$. Size quantization in quasi-2D systems lifts the fourfold degeneracy of the $j = 3/2$ states. As discussed above, we obtain

HH states with a z component of angular momentum $m = \pm 3/2$ and LH states with $m = \pm 1/2$, separated in energy by the HH–LH splitting. The quantization axis of angular momentum that is enforced by HH–LH splitting points in the growth direction of the quasi-2D system, even though at finite in-plane wave vectors we obtain a mixing of HH and LH states. The quantization axis perpendicular to the 2D plane is a direct consequence of the symmetry hierarchy (3.9) discussed in Sect. 3.6.

In general, the effective Hamiltonians for $B = 0$ spin splitting and Zeeman splitting tend to orient the spin vector in a direction not parallel to the growth axis of the quasi-2D system. But, of course, it is not possible to have a “second quantization axis of angular momentum” on top of the perpendicular quantization axis due to HH–LH splitting.⁷ This is the common reason why, in Chaps. 6 and 7, we shall find that in 2D HH systems both the $B = 0$ spin splitting and the Zeeman splitting for an in-plane \mathbf{B} are essentially higher-order effects.⁸ In order to overcome the quantization of angular momentum in the direction perpendicular to the 2D plane, we would need $B = 0$ spin splittings or Zeeman energies of the order of the HH–LH splitting. Note that these arguments apply only to HH states ($m = \pm 3/2$) but not to LH states ($m = \pm 1/2$). For arbitrary orientations of the quantization axis, the two LH states can always be combined such that they form eigenstates of angular momentum.

It is illuminating to discuss HH–LH splitting in a language where the bulk SO coupling is introduced as a small perturbation. Without bulk SO coupling, holes in the valence band have an orbital angular momentum $l = 1$. Size quantization splits the threefold degeneracy of the $l = 1$ states. We obtain twofold degenerate (fourfold degenerate with spin) HH states with $m = \pm 1$ and a nondegenerate (twofold degenerate with spin) LH state with $m = 0$. The quantization axis of the orbital angular momentum is perpendicular to the plane of the 2D system. The SO interaction couples the $s = 1/2$ spin vector to the quantized (“frozen”) orbital angular momentum of the 2D hole states. $B = 0$ spin splitting and Zeeman splitting of HH states are thus always competing with HH–LH splitting. They are largest in those 2D hole systems where HH–LH splitting is small [49].

4.6 Approximate Diagonalization of the Subband Hamiltonian: The Subband $\mathbf{k} \cdot \mathbf{p}$ Method

In the preceding sections, we have outlined the elaborate scheme which was used for the numerical analysis of the physical questions investigated in the

⁷ The effective Hamiltonians for $B = 0$ spin splitting can be interpreted as a Zeeman term with an effective magnetic field \mathbf{B} ; see Sect. 6.6. No such effective magnetic field can be defined that would characterize HH–LH splitting.

⁸ See the introduction of Chap. 5, which compares the importance of SO coupling effects for electron and hole states.

work described in this book. In the subsequent chapters, we give several examples of the good agreement between theory and experimental data that has been obtained along these lines. Nevertheless, it is often difficult to interpret these numerical results correctly and to derive the qualitative trends which underlie the numerically calculated results. In the context of $\mathbf{k} \cdot \mathbf{p}$ theory and the EFA, the qualitative trends can be explained by means of Löwdin perturbation theory (Appendix B) applied to the subband problem, the *subband $\mathbf{k} \cdot \mathbf{p}$ method* [7,41]. As we are interested here in subtleties such as Rashba spin splitting at zero magnetic field and anisotropic Zeeman splitting at $B > 0$, we have to evaluate the third, fourth, or even fifth order in the perturbative expansion (B.15) in order to obtain the lowest nonvanishing term.

4.6.1 General Approach

Löwdin perturbation theory can be applied not only to the bulk $\mathbf{k} \cdot \mathbf{p}$ Hamiltonian but also to the subband problem [7,41]. We note that one standard approach to the approximate diagonalization of a Hamiltonian H is based on an expansion of the eigenfunctions $|\mu\rangle$ of H in terms of some finite set of basis functions $\{|\nu\rangle : \nu = 1, \dots, N\}$. Frequently, the functions $\{|\nu\rangle\}$ are the exact eigenfunctions of some dominant part H_0 of H . We obtain approximate eigenfunctions $\{|\tilde{\mu}\rangle\}$ of the full Hamiltonian H by a numerical (exact) or perturbative (approximate) diagonalization of the matrix \tilde{H} , with matrix elements

$$\tilde{H}_{\nu\nu'} = \langle \nu | H | \nu' \rangle. \quad (4.34)$$

The eigenvalues and eigenvectors of the (finite) matrix \tilde{H} are approximate eigenvalues and eigenvectors, respectively, of the full Hamiltonian H .

We can use this approach for an approximate, fully analytical diagonalization of the EFA multiband Hamiltonian \mathcal{H} . We choose for \mathcal{H}_0 the diagonal terms of \mathcal{H} that are proportional to $k_z^2 = -\partial_z^2$, plus the confining potential $V(z)$ and the band edge energies $E_n(\mathbf{0})$:

$$(\mathcal{H}_0)_{nn'} = \delta_{nn'} \left[-\frac{\hbar^2 \partial_z^2}{2m_n^{*'}} + V(z) + E_n(\mathbf{0}) \right]. \quad (4.35)$$

Here $m_n^{*'}$ is the reduced effective mass for the n th bulk band of \mathcal{H} . The eigenfunctions of \mathcal{H}_0 are denoted $|n\alpha\rangle$, with a bulk band index n and subband index α . We expand the eigenfunctions of \mathcal{H} in terms of $\{|n\alpha\rangle\}$. We can then use Löwdin perturbation theory to diagonalize the matrix with elements

$$\tilde{\mathcal{H}}_{n\alpha, n'\alpha'} = \langle n\alpha | \mathcal{H} | n'\alpha' \rangle. \quad (4.36)$$

Often, it is reasonable to assume that we can describe the electron and hole subband states by the same set of mutually orthogonal subband wave functions

$$\langle n\alpha | n'\alpha' \rangle = \delta_{\alpha\alpha'}, \quad (4.37)$$

independent of the bulk band indices n and n' . Equation (4.37) is exactly fulfilled in a rectangular QW with infinitely deep barriers, where the subband wave functions are independent of the effective mass m_n^* . We shall often compare the analytical results for an infinitely deep rectangular QW with those for a parabolic well. Here we assume that the “width” w of the QW is given by the usual length scale of a harmonic oscillator,

$$w = \sqrt{\frac{\hbar}{m^* \omega}}. \quad (4.38)$$

For the calculation of electron states, it is often a good approximation to neglect completely the diagonal remote-band contributions of second order in \mathbf{k} [50]. In this case one might ask in what sense the unperturbed Hamiltonian \mathcal{H}_0 represents the dominant part of the total Hamiltonian \mathcal{H} . When the kinetic and potential energies in (4.35) are small, all subband states $\{|n\alpha\rangle\}$ originating in one bulk band n must be treated as quasi-degenerate, i.e. they are to be included either in Löwdin’s set A or in set B . But subband states for different bulk bands n and n' are separated by the bulk band edge energies $E_n(\mathbf{0}) - E_{n'}(\mathbf{0})$, which are large when compared with the off-diagonal $\mathbf{k} \cdot \mathbf{p}$ terms coupling the bands n and n' . Therefore, Löwdin partitioning is still well defined even if \mathcal{H} does not contain diagonal terms of second order in \mathbf{k} .

We emphasize that it is not our goal to achieve the best quantitative agreement between the numerical and analytical calculations. The main goal of the subband $\mathbf{k} \cdot \mathbf{p}$ method is a qualitative and intuitive understanding of the relative importance of competing effects and of the physical mechanisms that give rise to these effects, which, on the other hand, we can quantify by means of accurate numerical calculations.

4.6.2 Example: Effective Mass and g Factor of a Two-Dimensional Electron System

As an example of the subband $\mathbf{k} \cdot \mathbf{p}$ method, we shall compare Kane’s well-known expression for the effective mass m^* [50] and Roth’s formula for the effective g factor g^* [51] at the bulk conduction band edge,⁹

$$\frac{m_0}{m^*} = \frac{m_0}{m'} + \frac{2m_0}{\hbar^2} \frac{P^2}{3} \left(\frac{2}{E_0} + \frac{1}{E_0 + \Delta_0} \right), \quad (4.39a)$$

$$\frac{g^*}{2} = \frac{g'}{2} - \frac{2m_0}{\hbar^2} \frac{P^2}{3} \left(\frac{1}{E_0} - \frac{1}{E_0 + \Delta_0} \right), \quad (4.39b)$$

⁹ For compactness of the formulas, we do not explicitly consider the higher conduction bands Γ_8^c and Γ_7^c here. Instead, we include these bands in the remote-band contributions m' and g' (see Sect. 3.3 and Table C.9). If Γ_8^c and Γ_7^c are explicitly taken into account, these bands give rise to expressions that are similar to the contributions from the coupling to the valence bands Γ_8^v and Γ_7^v .

with the corresponding results for m^* and g^* of 2D electron states at the edge of the α th subband. We obtain the following for the in-plane effective mass and the in-plane effective g factor:

$$\frac{m_0}{m_{\alpha\parallel}} = \frac{m_0}{m'} + \frac{2m_0}{\hbar^2} \frac{P^2}{6} \left(3 \sum_{\beta} \frac{|\langle c_{\alpha} | h_{\beta} \rangle|^2}{E_{\alpha}^c - E_{\beta}^h} + \sum_{\beta} \frac{|\langle c_{\alpha} | l_{\beta} \rangle|^2}{E_{\alpha}^c - E_{\beta}^l} + 2 \sum_{\beta} \frac{|\langle c_{\alpha} | s_{\beta} \rangle|^2}{E_{\alpha}^c - E_{\beta}^s} \right), \quad (4.40a)$$

$$\frac{g_{\alpha\parallel}}{2} = \frac{g'}{2} - \frac{2m_0}{\hbar^2} \frac{iP^2}{3} \left(\sum_{\beta} \frac{\langle c_{\alpha} | k_z | l_{\beta} \rangle \langle l_{\beta} | z | c_{\alpha} \rangle - \langle c_{\alpha} | z | l_{\beta} \rangle \langle l_{\beta} | k_z | c_{\alpha} \rangle}{E_{\alpha}^c - E_{\beta}^l} - \sum_{\beta} \frac{\langle c_{\alpha} | k_z | s_{\beta} \rangle \langle s_{\beta} | z | c_{\alpha} \rangle - \langle c_{\alpha} | z | s_{\beta} \rangle \langle s_{\beta} | k_z | c_{\alpha} \rangle}{E_{\alpha}^c - E_{\beta}^s} \right). \quad (4.40b)$$

Here $\{|c_{\alpha}\rangle\}$, $\{|h_{\beta}\rangle\}$, $\{|l_{\beta}\rangle\}$, and $\{|s_{\beta}\rangle\}$ are the unperturbed electron, HH, LH, and SO subband wave functions, with eigenenergies E_{α}^c , E_{β}^h , E_{β}^l , and E_{β}^s , respectively. We can see clearly from these equations that g^* emerges from terms antisymmetric in the components of \mathbf{k} . Moreover, (4.40) shows that subband confinement increases the effective mass and decreases the effective g factor. We obtain (4.39) from (4.40) in the limiting case where the subband confinement energies are small compared with the bulk band gaps E_0 and Δ_0 .

We refer to the modifications of m^* and g^* due to subband confinement as *nonparabolic corrections*. This terminology stems from an alternative approach to the solution of the subband problem [13], where we first diagonalize the multiband Hamiltonian to obtain the bulk dispersion $E_n(\mathbf{k})$ (including nonparabolic corrections of higher order in \mathbf{k}). In a second step, we obtain the subband states by solving the one-band Hamiltonian $H_n = E_n[\mathbf{k} = (k_x, k_y, -i\partial_z)] + V(z)$. As the α th subband state is roughly a standing wave with $k_z \simeq \alpha\pi/w$, where w is the QW width, we can have significant contributions from terms in $E_n(\mathbf{k})$ of higher order in \mathbf{k} . In the subband $\mathbf{k} \cdot \mathbf{p}$ method, we perform these two steps in the opposite order: first we evaluate the subband states, and then we diagonalize the multiband Hamiltonian. Obviously, these two approaches are equivalent.

If we use the approximation (4.37), the resulting expression for the effective mass closely resembles (4.39a):

$$\frac{m_0}{m_{\alpha\parallel}} = \frac{m_0}{m'} + \frac{2m_0}{\hbar^2} \frac{P^2}{6} \left(\frac{3}{E_{\alpha}^c - E_{\alpha}^h} + \frac{1}{E_{\alpha}^c - E_{\alpha}^l} + \frac{2}{E_{\alpha}^c - E_{\alpha}^s} \right). \quad (4.41)$$

In order to further simplify (4.40b), we must choose a particular set of basis functions for which we can evaluate the matrix elements of z and $k_z = -i\partial_z$. Here the eigenfunctions of an infinitely deep rectangular well and also the eigenfunctions of a harmonic oscillator have the advantage that matrix elements of z and $k_z = -i\partial_z$ couple only subband states $|\alpha\rangle$ with $|\alpha \pm 1\rangle$. We obtain for the lowest subband ($\alpha = 1$)

$$\frac{g_{1\parallel}}{2} = \frac{g'}{2} - \frac{2m_0}{\hbar^2} P^2 a \left(\frac{1}{E_1^c - E_2^l} - \frac{1}{E_1^c - E_2^s} \right), \quad (4.42a)$$

where $a = 1/3$ for the parabolic well and $a = 256/(81\pi^2) \approx 0.320$ for the rectangular well.

A similar analysis for a perpendicular magnetic field shows that we obtain an effective g factor

$$\frac{g_{1z}}{2} = \frac{g'}{2} - \frac{2m_0}{\hbar^2} \frac{P^2}{6} \left(\frac{3}{E_1^c - E_1^h} - \frac{1}{E_1^c - E_1^l} - \frac{2}{E_1^c - E_1^s} \right). \quad (4.42b)$$

Note the different subband indices in (4.42a) and (4.42b). Equation (4.42) implies not only that subband confinement reduces the magnitude of g^* , but also that we obtain an in-plane/out-of-plane anisotropy of g^* , as first noted by Ivchenko and Kiselev [52]. A more detailed discussion of the anisotropic g factor of quasi-2D electron and hole systems will be given in Chap. 7.

References

1. G. Bastard: Phys. Rev. B **24**, 5693 (1981) [35](#), [36](#), [37](#), [38](#)
2. G.E. Marques, L.J. Sham: Surf. Sci. **113**, 131 (1982) [35](#), [38](#)
3. G.E. Marques: “The electronic properties of inversion layers in narrow-gap semiconductor compounds”, Ph.D. thesis, University of California, San Diego (1982) [35](#), [38](#)
4. W. Zawadzki: J. Phys. C: Solid State Phys. **16**, 229 (1983) [35](#)
5. M. Altarelli: “Electronic structure of semiconductor superlattices”, in *Application of High Magnetic Fields in Semiconductor Physics*, ed. by G. Landwehr (Springer, Berlin, Heidelberg, 1983), Vol. 177 of Lecture Notes in Physics, p. 174 [35](#), [38](#)
6. M. Baumgartner, G. Abstreiter, E. Bangert: J. Phys. C: Solid State Phys. **17**, 1617 (1984) [35](#), [38](#)
7. D.A. Broido, L.J. Sham: Phys. Rev. B **31**, 888 (1985) [86](#), [93](#), [161](#), [35](#), [38](#), [43](#), [46](#), [55](#)
8. U. Ekenberg, M. Altarelli: Phys. Rev. B **32**, 3712 (1985) [86](#), [93](#), [97](#), [161](#), [35](#), [43](#)
9. T. Ando: J. Phys. Soc. Jpn. **54**, 1528–1536 (1985) [86](#), [35](#), [38](#)
10. M.F.H. Schuurmans, G.W. ’t Hooft: Phys. Rev. B **31**, 8041 (1985) [35](#), [38](#)
11. F.J. Ohkawa, Y. Uemura: J. Phys. Soc. Jpn. **37**, 1325 (1974) [5](#), [65](#), [69](#), [78](#), [83](#), [35](#), [38](#)
12. R. Lassnig: Phys. Rev. B **31**, 8076 (1985) [78](#), [81](#), [83](#), [86](#), [98](#), [35](#), [38](#)
13. F. Malcher, G. Lommer, U. Rössler: Superlatt. Microstruct. **2**, 267 (1986) [72](#), [74](#), [75](#), [78](#), [83](#), [35](#), [37](#), [47](#), [57](#)
14. M.G. Burt: J. Phys.: Condens. Matter **4**, 6651–6690 (1992) [35](#), [37](#)
15. R. Winkler, U. Rössler: Phys. Rev. B **48**, 8918 (1993) [86](#), [93](#), [106](#), [108](#), [139](#), [35](#), [38](#), [39](#), [40](#)
16. R. Winkler, U. Rössler: Surf. Sci. **305**, 295 (1994) [35](#)
17. B.A. Foreman: Phys. Rev. B **48**, 4964 (1993) [14](#), [15](#), [37](#)
18. R.A. Morrow, K.R. Brownstein: Phys. Rev. B **30**, 678 (1984) [37](#)

19. B.A. Foreman: Phys. Rev. Lett. **80**(17), 3823–3826 (1998) [37](#)
20. M. Braun, U. Rössler: J. Phys. C: Solid State Phys. **18**, 3365 (1985) [30](#), [32](#), [71](#), [77](#), [166](#), [37](#), [40](#)
21. H. Mayer, U. Rössler: Phys. Rev. B **44**, 9048 (1991) [21](#), [24](#), [74](#), [174](#), [212](#), [213](#), [214](#), [220](#), [37](#)
22. U. Ekenberg: Phys. Rev. B **40**(11), 7714–7726 (1989) [37](#)
23. G. Lommer, F. Malcher, U. Rössler: Superlatt. Microstruct. **2**, 273 (1986) [37](#), [43](#)
24. R. Winkler, U. Kunze, U. Rössler: Surf. Sci. **263**, 222 (1992) [86](#), [220](#), [221](#), [37](#)
25. I. Nachev: Semicond. Sci. Technol. **3**, 29 (1988) [78](#), [83](#), [38](#)
26. P. Sobkowicz: Semicond. Sci. Technol. **5**, 183 (1990) [78](#), [83](#), [38](#)
27. S.R. White, L.J. Sham: Phys. Rev. Lett. **47**, 879 (1981) [38](#)
28. J.M. Luttinger, W. Kohn: Phys. Rev. **97**(4), 869–883 (1955) [3](#), [201](#), [38](#)
29. G. Goldoni, A. Fasolino: Phys. Rev. B **51**(15), 9903–9911 (1995) [38](#)
30. U. Ekenberg, M. Altarelli: Phys. Rev. B **30**, 3569 (1984) [93](#), [38](#)
31. L.C. Andreani, A. Pasquarello, F. Bassani: Phys. Rev. B **36**, 5887–5894 (1987) [38](#)
32. E.C. Valadares: Phys. Rev. B **46**(7), 3935–3939 (1992) [28](#), [38](#)
33. C.Y.P. Chao, S.L. Chuang: Phys. Rev. B **46**(7), 4110–4122 (1992) [28](#), [38](#)
34. C.T.H. Baker: *The Numerical Treatment of Integral Equations* (Clarendon, Oxford, 1977) [40](#)
35. C.C. Marston, G.G. Balint-Kurti: J. Chem. Phys. **91**, 3571 (1989) [40](#)
36. R. Winkler: J. Phys.: Condens. Matter **5**, 2321 (1993) [80](#), [81](#), [95](#), [142](#), [42](#)
37. E. Bangert, G. Landwehr: Surf. Sci. **170**, 593 (1986) [161](#), [43](#)
38. E. Bangert, G. Landwehr: Superlatt. Microstruct. **1**, 363 (1985) [86](#), [161](#), [43](#)
39. A. Fasolino, M. Altarelli: “Subband structure and Landau levels in heterostructures”, in *Two-Dimensional Systems, Heterostructures and Superlattices*, ed. by G. Bauer, F. Kuchar, H. Heinrich (Springer, Berlin, Heidelberg, 1984), pp. 176–182 [43](#)
40. F. Ancilotto, A. Fasolino, J.C. Maan: Phys. Rev. B **38**(3), 1788–1799 (1988) [43](#)
41. S.R. Eric Yang, D.A. Broido, L.J. Sham: Phys. Rev. B **32**(10), 6630–6633 (1985) [43](#), [55](#)
42. W. Batty, B.E. Cole, J.M. Chamberlain, J. Singleton: “Hole Landau levels in $[hkk]$ -grown GaAs/AlGaAs: exact calculations beyond the axial approximation”, in *23rd International Conference on the Physics of Semiconductors*, ed. by M. Scheffler, R. Zimmermann, Vol. 3 (World Scientific, Singapore, 1996), pp. 2143–2146 [43](#)
43. K. Suzuki, J.C. Hensel: Phys. Rev. B **9**(10), 4184–4218 (1974) [4](#), [5](#), [15](#), [17](#), [24](#), [31](#), [32](#), [151](#), [152](#), [158](#), [43](#), [44](#)
44. H.R. Trebin, U. Rössler, R. Ranvaud: Phys. Rev. B **20**(2), 686–700 (1979) [4](#), [15](#), [22](#), [25](#), [31](#), [32](#), [77](#), [98](#), [99](#), [151](#), [152](#), [158](#), [166](#), [209](#), [210](#), [212](#), [213](#), [214](#), [217](#), [43](#), [46](#), [48](#)
45. L. Landau: Z. Phys. **64**, 629–637 (1930) [44](#)
46. F. Bassani, G. Pastori Parravicini: *Electronic States and Optical Transitions in Solids* (Pergamon, Oxford, 1975) [45](#)
47. J.C. Hensel, K. Suzuki: Phys. Rev. B **9**(10), 4219–4257 (1974) [46](#)
48. G.F. Koster, J.O. Dimmock, R.G. Wheeler, H. Statz: *Properties of the Thirty-Two Point Groups* (MIT, Cambridge, MA, 1963) [6](#), [21](#), [23](#), [72](#), [166](#), [199](#), [47](#)

49. R. Winkler, H. Noh, E. Tutuc, M. Shayegan: Phys. Rev. B **65**, 155 303 (2002)
104, 106, 107, 108, 54
50. E.O. Kane: J. Phys. Chem. Solids **1**, 249 (1957) 10, 27, 30, 71, 156, 56
51. L.M. Roth, B. Lax, S. Zwerdling: Phys. Rev. **114**, 90 (1959) 2, 14, 131, 141, 56
52. E.L. Ivchenko, A.A. Kiselev: Sov. Phys. Semicond. **26**, 827 (1992) 5, 131, 132, 58

5 Origin of Spin–Orbit Coupling Effects

The microscopic driving force for spin–orbit coupling effects such as the $B = 0$ spin splitting in inversion-asymmetric systems and the Zeeman splitting at $B > 0$ is the Pauli SO interaction (1.1) due to the strong Coulomb potential of the atomic core regions, and it is illuminating to see how it affects the dynamics of the spin degree of freedom within the $\mathbf{k} \cdot \mathbf{p}$ theory and the EFA. In (2.7) and (2.14), we have expanded the eigenfunctions of the Hamiltonian in terms of the eigenfunctions of the bulk Hamiltonian *without* SO interaction. Therefore, we obtained in (2.7) and (2.14) the matrix elements $\Delta_{\sigma\sigma'}^{\nu\nu'}$ of the SO interaction explicitly. We can make a unitary transformation of the Hamiltonian \mathcal{H} so that the transformed Hamiltonian \mathcal{H}' has the 2×2 block structure

$$\mathcal{H}' = \begin{pmatrix} \mathcal{H}_{\mathbf{k} \cdot \mathbf{p}} & 0 \\ 0 & \mathcal{H}_{\mathbf{k} \cdot \mathbf{p}} \end{pmatrix} + \begin{pmatrix} \mathcal{H}_{\text{SO}}^z & \mathcal{H}_{\text{SO}}^{xy} \\ \mathcal{H}_{\text{SO}}^{xy\dagger} & -\mathcal{H}_{\text{SO}}^z \end{pmatrix} \begin{matrix} \uparrow \\ \downarrow \end{matrix}, \quad (5.1)$$

where $\mathcal{H}_{\mathbf{k} \cdot \mathbf{p}}$ is the $\mathbf{k} \cdot \mathbf{p}$ Hamiltonian without spin, i.e. the upper left block of the first term in (5.1) corresponds to spin-up, and the lower-right block corresponds to spin-down. The SO blocks \mathcal{H}_{SO} coupling spin up and spin down states contain the matrix elements $\Delta_{\sigma\sigma'}^{\nu\nu'}$, as well as those matrix elements of $\boldsymbol{\pi}$ that are nonzero only because of the SO interaction in (2.5).

For the extended Kane model, we can derive the unitary transformation $\mathcal{H} \rightarrow \mathcal{H}'$ from the Clebsch–Gordan coefficients entering into the definition of the basis functions in Table C.1. The blocks \mathcal{H}_{SO} contain the SO matrix elements Δ_0 , Δ'_0 , Δ^- , as well as the k -linear terms proportional to C_k which occur in the valence band blocks \mathcal{H}_{8v8v}^k and \mathcal{H}_{8v7v}^k . It follows from (5.1) that only these SO-interaction-induced terms control the SO coupling effects.

In general, SO coupling effects are more important for holes than for electrons. As shown in Fig. 3.1, the SO interaction acts via the gaps Δ_0 and Δ'_0 within the valence band and the higher conduction bands, respectively (subspaces of p-like atomic orbitals). But there are no matrix elements $\Delta_{\sigma\sigma'}^{\nu\nu'}$ within the lowest (s-like) conduction band. Thus one might expect that SO interaction would have a stronger effect on the hole states than on the electrons in the lowest conduction band because the latter are affected by SO interaction only as a result of the $\mathbf{k} \cdot \mathbf{p}$ coupling to neighboring bands, so that spin phenomena in the conduction band are suppressed by energy denomina-

tors of the order of the fundamental gap. The detailed analysis in subsequent chapters shows, however, an astonishing symmetry in the analytical expressions for the SO coupling terms for electrons and holes: for both electrons and holes, we need to take into account the $\mathbf{k} \cdot \mathbf{p}$ coupling of the state to its counterpart.¹ Accordingly, SO coupling effects have the same order of magnitude for electron and hole states. We must compare, however, the SO coupling energies with the kinetic energies of the particles. As holes typically have larger masses (i.e. smaller kinetic energies) than electrons, SO coupling is more important for holes than for electrons.

5.1 Dirac Equation and Pauli Equation

Before we discuss SO coupling effects in semiconductors in detail, it is helpful to recapitulate, from relativistic quantum mechanics, the derivation of the Pauli equation from the Dirac equation [1]. The Pauli equation emerges from the Dirac equation in much the same way as we derive effective Hamiltonians for the conduction or valence band from more complete multiband Hamiltonians. Furthermore, the well-known Pauli equation provides a good example for demonstrating the concepts of the theory of invariants.

Assuming a time-independent problem, the Dirac equation can be written in the form

$$(c \boldsymbol{\alpha} \cdot \mathbf{p} + \beta m_0 c^2 + V) \psi = E \psi, \quad (5.2)$$

where

$$\boldsymbol{\alpha} = \begin{pmatrix} 0 & \boldsymbol{\sigma} \\ \boldsymbol{\sigma} & 0 \end{pmatrix}, \quad (5.3a)$$

$$\beta = \begin{pmatrix} \mathbb{1}_{2 \times 2} & 0 \\ 0 & -\mathbb{1}_{2 \times 2} \end{pmatrix}, \quad (5.3b)$$

and ψ denotes a four-component spinor. We rewrite the coupled equations for the upper and lower pairs of components, ψ_A and ψ_B , as follows:

$$\boldsymbol{\sigma} \cdot \mathbf{p} \psi_B = \frac{1}{c} (\tilde{E} - V) \psi_A, \quad (5.4a)$$

$$\boldsymbol{\sigma} \cdot \mathbf{p} \psi_A = \frac{1}{c} (\tilde{E} - V + 2m_0 c^2) \psi_B, \quad (5.4b)$$

where $\tilde{E} = E - m_0 c^2$. Using the second equation, we can eliminate ψ_B in the first equation to obtain

¹ If we describe 2D holes by means of the 14×14 extended Kane Hamiltonian the energy gaps are explicitly visible in the expressions for the Zeeman and $B = 0$ spin splittings. If we use a smaller $\mathbf{k} \cdot \mathbf{p}$ Hamiltonian such as the 4×4 Luttinger Hamiltonian, the energy gaps are hidden in the definition of the Luttinger coefficients γ_i ; see Table C.9.

$$\boldsymbol{\sigma} \cdot \mathbf{p} \left[\frac{c^2}{\tilde{E} - V + 2m_0 c^2} \right] \boldsymbol{\sigma} \cdot \mathbf{p} \psi_A = (\tilde{E} - V) \psi_A . \quad (5.5)$$

Up to now, we have made no approximation. Nevertheless, we do not say that (5.5) is equivalent to (5.2), because, unlike the four-component spinors ψ , the functions ψ_A are not normalized to unity. We still need (5.4b) to obtain the solution ψ of the full problem. Furthermore, we note that (5.5) is not a conventional eigenvalue problem, because the denominator on the left-hand side of this equation depends on the energy eigenvalue \tilde{E} .

The Pauli equation emerges as a nonrelativistic approximation from the Dirac equation in the sense that we make a power expansion in the small quantity $(\tilde{E} - V)/(2m_0 c^2) \approx (v/c)^2$, where we keep only the lowest-order terms. Moreover, we want to replace the four-component spinor ψ by a two-component wave function $\tilde{\psi}$ that corresponds to the dominant part of ψ .

Equation (5.5) has already the two-component form we are looking for. Two steps are required to convert it into the Pauli equation. First we expand the energy denominator on the left-hand side of (5.5):

$$\frac{c^2}{\tilde{E} - V + 2m_0 c^2} \approx \frac{1}{2m_0} \left[1 - \frac{\tilde{E} - V}{2m_0 c^2} + \dots \right], \quad (5.6)$$

where we keep the zeroth- and first-order terms in $(v/c)^2$. The probabilistic interpretation of the Dirac theory requires that

$$\int d^3 r \psi^\dagger \psi = \int d^3 r (\psi_A^\dagger \psi_A + \psi_B^\dagger \psi_B) = 1 . \quad (5.7)$$

So, even when we keep only the first and second term in (5.6), we cannot identify ψ_A with the full wave function ψ anymore, because a fraction of the probability density

$$\int d^3 r \psi_A^\dagger \left(\frac{p^2 + e\hbar \boldsymbol{\sigma} \cdot \mathbf{B}}{4m_0^2 c^2} \right) \psi_A \propto \frac{v^2}{c^2} \quad (5.8)$$

has “escaped” into $\psi_B^\dagger \psi_B$. Therefore, in the second step we replace ψ_A in (5.5) by a new two-component wave function

$$\tilde{\psi} = \left(1 + \frac{p^2 + e\hbar \boldsymbol{\sigma} \cdot \mathbf{B}}{8m_0^2 c^2} \right) \psi_A , \quad (5.9)$$

which is correctly normalized to unity. We then obtain from (5.5), up to order $(v/c)^2$, the Pauli equation [1]

$$\begin{aligned} & \left[\frac{p^2}{2m_0} + V + \frac{e\hbar}{2m_0} \boldsymbol{\sigma} \cdot \mathbf{B} - \frac{e\hbar \boldsymbol{\sigma} \cdot \mathbf{p} \times \boldsymbol{\mathcal{E}}}{4m_0^2 c^2} - \frac{e\hbar^2}{8m_0^2 c^2} \nabla \cdot \boldsymbol{\mathcal{E}} \right. \\ & \left. - \frac{p^4}{8m_0^3 c^2} - \frac{e\hbar p^2}{4m_0^3 c^2} \boldsymbol{\sigma} \cdot \mathbf{B} - \frac{(e\hbar B)^2}{8m_0^3 c^2} \right] \tilde{\psi} = \tilde{E} \tilde{\psi}, \end{aligned} \quad (5.10)$$

where $\boldsymbol{\mathcal{E}} = (1/e) \nabla V$ is the electric field. The third term on the left-hand side of (5.10) is the Zeeman term, the fourth term is the Pauli SO coupling (1.1),

Table 5.1. Tensor operators for the point group $SU(2)$

$\mathcal{D}_0 :$	$V; \quad p^2; \quad p^4; \quad B^2; \quad \nabla \cdot \boldsymbol{\mathcal{E}}$
$\mathcal{D}_1 :$	$B_x, B_y, B_z; \quad p^2 B_x, p^2 B_y, p^2 B_z; \quad \mathcal{E}_z p_y - \mathcal{E}_y p_z, \mathcal{E}_x p_z - \mathcal{E}_z p_x, \mathcal{E}_y p_x - \mathcal{E}_x p_y$

Table 5.2. Invariants with prefactors p_{ij} for a Hamiltonian that transforms according to the irreducible representation $\mathcal{D}_{1/2}$ of $SU(2)$

$$p_{01}V + p_{02}p^2 + p_{03}p^4 + p_{04}B^2 + p_{05}\nabla \cdot \boldsymbol{\mathcal{E}} \\ + p_{11}\boldsymbol{\sigma} \cdot \boldsymbol{B} + p_{12}\boldsymbol{\sigma} \cdot (\boldsymbol{\mathcal{E}} \times \boldsymbol{p}) + p_{13}p^2\boldsymbol{\sigma} \cdot \boldsymbol{B}$$

and the fifth term is called the Darwin term. Finally, in the second line we obtain higher-order corrections to both the kinetic energy $p^2/(2m_0)$ and the Zeeman term.

We can rederive (5.10) using Löwdin partitioning (in the present context known as the Foldy–Wouthuysen transformation [2]) and the theory of invariants. The wave function $\hat{\psi}$ transforms according to the irreducible representation $\mathcal{D}_{1/2}$ of $SU(2)$. From the fact that $\mathcal{D}_{1/2} \times \mathcal{D}_{1/2} = \mathcal{D}_0 + \mathcal{D}_1$, we see that we have two sets of basis matrices, the unit matrix $\mathbb{1}_{2 \times 2}$, transforming according to \mathcal{D}_0 and the Pauli spin matrices σ_j , transforming according to \mathcal{D}_1 . The tensor operators that can be formed from the components of \boldsymbol{p} , \boldsymbol{B} and the gradient of V are listed in Table 5.1. The invariants that can be formed by combining the basis matrices and tensor operators are given in Table 5.2.

By applying fourth-order Löwdin perturbation theory to the Dirac equation (5.2), we obtain (5.10), so that we can readily identify the expansion coefficients p_{ij} appearing in Table 5.2 with the prefactors of the various terms in (5.10). More specifically, we obtain the kinetic-energy term $p^2/(2m_0)$ and the Zeeman term in second-order perturbation theory. We see here the fact, well known in $\boldsymbol{k} \cdot \boldsymbol{p}$ theory, that the terms symmetric in the components of \boldsymbol{p} are weighted by the inverse of the (effective) mass, whereas the Zeeman term stems from the terms antisymmetric in the components of \boldsymbol{p} , in accordance with $\boldsymbol{p} \times \boldsymbol{p} = -ie\hbar\boldsymbol{B}$. In third-order Löwdin perturbation theory, we obtain the Pauli SO coupling and the Darwin term. These terms reflect the non-commutativity of \boldsymbol{p} and V , i.e. $[\boldsymbol{p}, V] = -ie\hbar\boldsymbol{\mathcal{E}}$. In fourth-order perturbation theory, we finally obtain higher-order corrections to the kinetic energy and the Zeeman term (as well as corrections to the Pauli SO coupling and the Darwin term which are of second order in $(v/c)^2$).

5.2 Invariant Expansion for the 8x8 Kane Hamiltonian

In the previous section, we discussed the derivation of the Pauli equation from the Dirac equation. We shall compare these well-known results with the effective Hamiltonians we obtain from a decoupling of conduction and valence band states starting from an 8×8 Kane Hamiltonian that takes into account only the $\mathbf{k} \cdot \mathbf{p}$ coupling between the Γ_6^c conduction band and the Γ_7^v and Γ_7^v valence bands [3]. Although this is a rather simplified model for the bulk band structure, the final results capture a large part of the physics that we want to discuss in this work.

The EFA Hamiltonian reads (see Table C.5)

$$\mathcal{H}_{8 \times 8} = \begin{pmatrix} (E_c + V) \mathbb{1}_{2 \times 2} & \sqrt{3} P \mathbf{T} \cdot \mathbf{k} & -\frac{1}{\sqrt{3}} P \boldsymbol{\sigma} \cdot \mathbf{k} \\ \sqrt{3} P \mathbf{T}^\dagger \cdot \mathbf{k} & (E_v + V) \mathbb{1}_{4 \times 4} & 0 \\ -\frac{1}{\sqrt{3}} P \boldsymbol{\sigma} \cdot \mathbf{k} & 0 & (E_v - \Delta_0 + V) \mathbb{1}_{2 \times 2} \end{pmatrix} \quad (5.11a)$$

$$= \begin{pmatrix} E_c + V & 0 & \frac{-1}{\sqrt{2}} P k_+ & \sqrt{\frac{2}{3}} P k_z & \frac{1}{\sqrt{6}} P k_- & 0 & \frac{-1}{\sqrt{3}} P k_z & \frac{-1}{\sqrt{3}} P k_- \\ 0 & E_c + V & 0 & \frac{-1}{\sqrt{6}} P k_+ & \sqrt{\frac{2}{3}} P k_z & \frac{1}{\sqrt{2}} P k_- & \frac{-1}{\sqrt{3}} P k_+ & \frac{1}{\sqrt{3}} P k_z \\ \frac{-1}{\sqrt{2}} P k_- & 0 & E_v + V & 0 & 0 & 0 & 0 & 0 \\ \sqrt{\frac{2}{3}} P k_z & \frac{-1}{\sqrt{6}} P k_- & 0 & E_v + V & 0 & 0 & 0 & 0 \\ \frac{1}{\sqrt{6}} P k_+ & \sqrt{\frac{2}{3}} P k_z & 0 & 0 & E_v + V & 0 & 0 & 0 \\ 0 & \frac{1}{\sqrt{2}} P k_+ & 0 & 0 & 0 & E_v + V & 0 & 0 \\ \frac{-1}{\sqrt{3}} P k_z & \frac{-1}{\sqrt{3}} P k_- & 0 & 0 & 0 & 0 & E_v - \Delta_0 + V & 0 \\ \frac{-1}{\sqrt{3}} P k_+ & \frac{1}{\sqrt{3}} P k_z & 0 & 0 & 0 & 0 & 0 & E_v - \Delta_0 + V \end{pmatrix}. \quad (5.11b)$$

Here $\hbar \mathbf{k} = -i\hbar \nabla + e\mathbf{A}$ denotes the kinetic momentum and we have introduced the symbols E_v and E_c denoting the valence and conduction band edges, respectively. In this section we ignore the position dependence of E_v and E_c . For a detailed discussion of this aspect, see Sect. 6.3.2.

We shall transform (5.11) into an effective equation for electron states that depends only on the conduction band spinor components ψ_c of the eight-component envelope function ψ . By eliminating the valence band components from the Schrödinger equation for ψ , we obtain [4, 5]

$$\left[\mathbf{T} \cdot \mathbf{k} \frac{3P^2}{\tilde{E} - V + E_0} \mathbf{T}^\dagger \cdot \mathbf{k} + \boldsymbol{\sigma} \cdot \mathbf{k} \frac{P^2/3}{\tilde{E} - V + E_0 + \Delta_0} \boldsymbol{\sigma} \cdot \mathbf{k} \right] \psi_c = (\tilde{E} - V) \psi_c, \quad (5.12)$$

where we have used $\tilde{E} = E - E_c$ and $E_0 = E_c - E_v$. Analogously to (5.5), no approximation is involved here.

Next we expand the first and second denominators on the left-hand side of (5.12) up to first order in terms of the small quantities $(\tilde{E} - V)/E_0$ and $(\tilde{E} - V)/(E_0 + \Delta_0)$, respectively. Note, however, that as compared with the expansion (5.6), we have no strict equivalent to the order parameter $(v/c)^2$. The speed of light, c , in the Dirac Hamiltonian corresponds roughly to the quantity P/\hbar in the Kane Hamiltonian (5.11), and m_0 corresponds roughly to $\hbar^2 E_0/(2P^2)$. However, unlike the parameters P and E_0 (and Δ_0) in the Kane model, the velocity of light c appears both on the diagonal and off the diagonal. In $\mathbf{k} \cdot \mathbf{p}$ theory, we usually label different terms by the order of the energy denominators with which they appear in the decoupled Hamiltonian. This terminology is equivalent to the order of Löwdin perturbation theory that is necessary to derive a particular term.

As a second step, we choose new two-component conduction band envelope functions

$$\tilde{\psi}_c = \left[1 + \frac{P^2}{12} \left(\frac{2k^2 - (e/\hbar) \boldsymbol{\sigma} \cdot \mathbf{B}}{E_0} + \frac{k^2 + (e/\hbar) \boldsymbol{\sigma} \cdot \mathbf{B}}{E_0 + \Delta_0} \right) \right] \psi_c \quad (5.13)$$

to ensure norm conservation. This step, which is similar to (5.9), has been overlooked by several authors when deriving an effective 2×2 conduction band Hamiltonian from (5.11). After some rearrangements, we obtain

$$\begin{aligned} & \left\{ \frac{P^2}{3} \left[\frac{2}{E_0} + \frac{1}{E_0 + \Delta_0} \right] k^2 + V - \frac{P^2}{3} \left[\frac{1}{E_0} - \frac{1}{E_0 + \Delta_0} \right] \frac{e}{\hbar} \boldsymbol{\sigma} \cdot \mathbf{B} \right. \\ & + \frac{eP^2}{3} \left[\frac{1}{E_0^2} - \frac{1}{(E_0 + \Delta_0)^2} \right] \boldsymbol{\sigma} \cdot \mathbf{k} \times \boldsymbol{\mathcal{E}} \\ & \left. - \frac{eP^2}{6} \left[\frac{2}{E_0^2} + \frac{1}{(E_0 + \Delta_0)^2} \right] \nabla \cdot \boldsymbol{\mathcal{E}} \right\} \tilde{\psi}_c = \tilde{E} \tilde{\psi}_c. \end{aligned} \quad (5.14)$$

Here, the first term is the kinetic energy using Kane’s expression (4.39a) for the effective mass, the third term is the Zeeman term using Roth’s formula (4.39b) for the effective g factor, the fourth term is the Rashba term [6], analogous to the Pauli SO coupling in (5.10), and the fifth term is analogous to the Darwin term. In (5.14) we have neglected those terms that contain the fundamental gap E_0 more than twice. We shall give a more detailed discussion of the Rashba term in Sect. 6.3. The Zeeman splitting will be discussed more thoroughly in Chap. 7.

Alternatively, we can derive (5.14) using Löwdin partitioning and the theory of invariants. Here, the kinetic energy and the Zeeman term stem from second-order perturbation theory, while the SO coupling and the Darwin term require third-order perturbation theory. We remark that (5.13) is “built-in” in Löwdin perturbation theory because we have required that e^{-S} in (B.2) is a unitary operator. Note also that the invariant expansion in Table 5.2 applies

to the Pauli equation (5.10) as well as to the conduction band Hamiltonian (5.14) because the basis functions $|\uparrow\rangle$ and $|\downarrow\rangle$ of both 2×2 Hamiltonians transform according to $\mathcal{D}_{1/2}$ of $SU(2)$. In the latter case, this is due to the fact that already the simplified Kane Hamiltonian (5.11) has spherical symmetry. All invariants in the conduction band Hamiltonian (5.14), including the higher order terms not considered here, thus have a “partner” of the same functional form in the Pauli equation (5.10) (with $\mathbf{p} = \hbar\mathbf{k}$). Only the prefactors differ in these equations.

Similarly to the Pauli equation (5.10), the Zeeman splitting in (5.14) originates in the noncommutativity (2.17) of the components of \mathbf{k} , while the Rashba term can be traced back to the noncommutativity (2.18) of \mathbf{k} and V . We remark that the converse is not always correct: not every antisymmetric term gives rise to spin splitting. The Zeeman and Rashba terms are merely the lowest-order invariants that can be constructed from the antisymmetric vectors \mathbf{B} and $\mathbf{k} \times \mathcal{E}$. The spin-diagonal Darwin term also originates from (2.18). The higher-order terms include, for example, a diamagnetic shift $\propto B^2 \mathbb{1}_{2 \times 2}$ (see Tables C.3 and C.4).

In this section, we have worked out the formal similarities between relativistic quantum mechanics and the simplified Kane model. Nevertheless, there is an important difference: while the Pauli SO coupling (1.1) is an intrinsic part of the Dirac–Pauli theory, SO coupling enters into the Kane model (5.11) only via the SO gap Δ_0 of the bulk band structure. We can see in (5.14) that both the effective g factor and the Rashba term disappear in the limit $\Delta_0 \rightarrow 0$. This general result will be confirmed by the calculations presented in subsequent chapters that are based on more realistic multiband Hamiltonians. Consistently with our arguments in the preceding paragraph, antisymmetric invariants that are diagonal in the spin degree of freedom can “survive” even in the limit $\Delta_0 \rightarrow 0$.

References

1. J.J. Sakurai: *Advanced Quantum Mechanics* (Addison-Wesley, Reading, MA, 1967) 1, 4, 62, 63
2. L.L. Foldy, S.A. Wouthuysen: Phys. Rev. **78**(1), 29–36 (1950) 201, 64
3. W. Zawadzki: “‘Relativistic’ phenomena in solids, in *Optical Properties of Solids*, ed. by E.D. Haidemenakis (Gordon and Breach, New York, 1970), pp. 179–212 65
4. F.J. Ohkawa, Y. Uemura: J. Phys. Soc. Jpn. **37**, 1325 (1974) 5, 35, 38, 69, 78, 83, 65
5. T. Darnhofer, U. Rössler: Phys. Rev. B **47**(23), 16 020–16 023 (1993) 65
6. Y.A. Bychkov, E.I. Rashba: J. Phys. C: Solid State Phys. **17**, 6039–6045 (1984) 5, 69, 77, 78, 83, 165, 66

6 Inversion-Asymmetry-Induced Spin Splitting

Spin degeneracy of electron and hole states in a semiconductor is the combined effect of inversion symmetry in space and time [1]. Both symmetry operations change the wave vector \mathbf{k} into $-\mathbf{k}$, but time inversion also flips the spin, so that when we combine both we have a twofold degeneracy of the single-particle energies, $E_+(\mathbf{k}) = E_-(\mathbf{k})$; see Table 6.1. When the potential through which the carriers move is inversion-asymmetric, however, the spin degeneracy is removed even in the absence of an external magnetic field B . We then obtain two branches of the energy dispersion, $E_+(\mathbf{k})$ and $E_-(\mathbf{k})$. In quasi-2D quantum wells (QWs) and heterostructures, this spin splitting can be the consequence of a bulk inversion asymmetry (BIA) of the underlying crystal (e.g. a zinc blende structure [2]), and of a structure inversion asymmetry (SIA) of the confinement potential [3,4]. A third contribution to $B = 0$ spin splitting can be the low microscopic symmetry of the atoms at an interface [5]. We emphasize that even in inversion-asymmetric systems with $B = 0$ spin splitting we still have the Kramers degeneracy; see Table 6.1.

For a given wave vector \mathbf{k} , we can always find a spin orientation axis $\mathbf{S}(\mathbf{k})$, *local in \mathbf{k} space*, such that we have spin-up and spin-down eigenstates with respect to the axis $\mathbf{S}(\mathbf{k})$. But we do not call the branches $E_\pm(\mathbf{k})$ spin-up and spin-down, because the direction of \mathbf{S} varies as a function of \mathbf{k} such that, when averaged over all occupied states, the branches contain equal contributions of up and down spinor components. This reflects the fact that in nonmagnetic materials we have a vanishing magnetic moment at $B = 0$. While we shall focus on the effect of $B = 0$ spin splitting on the energy dispersion $E(\mathbf{k})$ and the spin degree of freedom, it has been investigated in [6] how $B = 0$ spin splitting affects also the orbital parts of the wave function.

In Sect. 6.1, we start with some general remarks on $B = 0$ spin splitting. In Sect. 6.2 we discuss BIA spin splitting in zinc blende semiconductors.

Table 6.1. $B = 0$ spin degeneracy is due to the combined effect of inversion symmetry in space and time [1]

Space inversion symmetry: $E_+(\mathbf{k}) = E_+(-\mathbf{k})$	$\left. \vphantom{\begin{matrix} \text{Space inversion symmetry: } E_+(\mathbf{k}) = E_+(-\mathbf{k}) \\ \text{Time inversion symmetry: } E_+(\mathbf{k}) = E_-(-\mathbf{k}) \end{matrix}} \right\} \Rightarrow$	$B = 0$ spin degeneracy: $E_+(\mathbf{k}) = E_-(\mathbf{k})$
Time inversion symmetry: $E_+(\mathbf{k}) = E_-(-\mathbf{k})$		
(Kramers degeneracy)		

In Sect. 6.3 we present a detailed discussion of SIA spin splitting in the conduction band Γ_6^c and in the valence bands. It turns out that Rashba spin splitting of 2D hole systems is very different from the more familiar case of Rashba spin splitting in 2D electron systems [7]. In Sect. 6.4 we focus on the interplay between BIA and SIA and on the density dependence of $B = 0$ spin splitting. A third contribution to $B = 0$ spin splitting is discussed in Sect. 6.5, which can be traced back to the particular properties of the heterointerfaces in quasi-2D systems. Next we analyze in more detail the spin orientation of the single-particle states due to $B = 0$ spin splitting (Sect. 6.6). In Sect. 6.7 we give a brief overview of common experimental techniques for measuring $B = 0$ spin splitting. As an example, we compare in Sect. 6.8 calculated spin splittings [8] with Raman experiments by Jusserand et al. [9].

6.1 $B = 0$ Spin Splitting and Spin–Orbit Interaction

How can we visualize the fact that the electron spins are “feeling” the inversion asymmetry of the spatial environment? In the EFA the full wave function (2.13) is the product of the quickly oscillating lattice-periodic part $u_{n\mathbf{0}}(\mathbf{r})$ of the Bloch functions times a slowly varying envelope function $\psi_n(\mathbf{r})$. When we have SIA spin splitting, the Bloch part “feels” the atomic fields that enter into the Pauli SO term (1.1) and the envelope function “feels” the macroscopic environment, see Fig. 2.1. Therefore, we obtain SIA spin splitting only if we have both a macroscopic electric field and a microscopic electric field from the atomic cores. This is consistent with the explicit expressions for SIA spin splitting derived in the sections below, where the splitting is always proportional to the macroscopic field times a prefactor that depends on the matrix elements $\Delta_{\sigma\sigma'}^{\nu\nu'}$ of the microscopic SO interaction. BIA spin splitting is independent of any macroscopic electric fields. It depends only on the matrix elements $\Delta_{\sigma\sigma'}^{\nu\nu'}$ of the microscopic SO interaction. Both SIA and BIA spin splitting disappear in the limit of vanishing bulk SO gaps $\Delta_{\sigma\sigma'}^{\nu\nu'} = 0$.¹

Several authors [11, 12, 13, 14] have suggested an intuitive picture for the $B = 0$ spin splitting, which is based on the idea that, for the Rashba term (6.10) discussed below, the electrons are moving with a velocity $\mathbf{v}_{\parallel} = \hbar\mathbf{k}_{\parallel}/m^*$ perpendicular to the macroscopic electric field $\mathcal{E} = (0, 0, \mathcal{E}_z)$. It was argued that in the electron’s rest frame, \mathcal{E} is Lorentz transformed into a magnetic field \mathbf{B} , so that the $B = 0$ spin splitting becomes a Zeeman splitting in the electron’s rest frame. However, this magnetic field is given by $B = (v_{\parallel}/c^2)\mathcal{E}_z$ (SI units) and for typical values of \mathcal{E}_z and v_{\parallel} we have $B \sim 2 - 20 \times 10^{-7}$ T, which would result in a spin splitting of the order of $5 \times 10^{-9} - 5 \times 10^{-5}$ meV. On the other hand, the experimentally observed spin splitting is of the order

¹ The spin degree of freedom can be affected also by exchange–correlation effects [10]. This can give rise to an exchange-induced enhancement of $B = 0$ spin splitting; see Sect. 6.4.3.

of $0.1 - 10$ meV. It is clear from the discussion above that this discrepancy is due to the fact that the idea of a Lorentz transformation neglects the contribution of the atomic cores to the SO interaction felt by a Bloch electron in a solid (see Sect. 3.4).

6.2 BIA Spin Splitting in Zinc Blende Semiconductors

Unlike Si and Ge, which have a diamond structure, the zinc blende structure of III–V and II–VI compounds such as GaAs, InSb, and $\text{Hg}_x\text{Cd}_{1-x}\text{Te}$ does not have a center of inversion.² Therefore, SO interaction gives rise to a spin splitting of the bulk energy dispersion. This BIA spin splitting is well known from early theoretical studies [2, 15, 16, 17]. It has been observed experimentally by analyzing the Shubnikov–de Haas effect in uniaxially strained bulk InSb [18] and by detecting the precession of the spin polarization of electrons photoexcited from a GaAs (110) surface [19].

6.2.1 BIA Spin Splitting in Bulk Semiconductors

We can use the theory of invariants to identify the terms in the conduction and valence band blocks of $\mathcal{H}(\mathbf{K})$ which give rise to a spin splitting of the electron and hole states. We remark that both the wave vector \mathbf{k} and the electric field \mathbf{E} are odd with respect to parity (while \mathbf{B} is even). For the symmetrized basis matrices, the transformation with respect to parity is listed in Table C.3. Only those invariants that are odd with respect to parity can contribute to BIA spin splitting. An invariant that contributes to SIA spin splitting can be either even or odd with respect to parity. Those invariants proportional to \mathbf{E} that are odd with respect to parity reflect the combined effect of BIA and SIA.

Up to third order in \mathbf{k} , we obtain the invariants listed in Table 6.2 [20, 21]. BIA spin splitting in the Γ_6^c conduction is characterized by the invariant weighted by b_{41}^{6c6c} . Using an explicit matrix notation, we have

$$\mathcal{H}_{6c6c}^b = b_{41}^{6c6c} \begin{pmatrix} \frac{1}{2}\{k_+^2 + k_-^2, k_z\} & \frac{1}{4}\{k_+^2 - k_-^2, k_- \} - \{k_z^2, k_+\} \\ \frac{1}{4}\{k_-^2 - k_+^2, k_+\} - \{k_z^2, k_- \} & -\frac{1}{2}\{k_+^2 + k_-^2, k_z\} \end{pmatrix}, \quad (6.1)$$

² Strictly speaking, the diamond structure does not have a center of inversion either. It has a nonsymmorphic space group with point group O_h , i.e. the symmetry operations in O_h must be combined with a nonprimitive translation of the translation subgroup of the diamond structure in order to map the diamond structure onto itself. Nevertheless, from all points of view we are interested in it is sufficient that the point group O_h of the diamond structure contains the inversion as a symmetry element.

Table 6.2. Invariants for the Kane model up to third order in \mathbf{k} which give rise to BIA spin splitting

$\mathcal{H}_{6c\ 6c}^b = \mathbf{b}_{41}^{6c6c} (\{k_x, k_y^2 - k_z^2\} \sigma_x + \text{cp})$
$\mathcal{H}_{8v\ 8v}^b = \frac{2}{\sqrt{3}} C_k [k_x \{J_x, J_y^2 - J_z^2\} + \text{cp}]$ $+ \mathbf{b}_{41}^{8v8v} (\{k_x, k_y^2 - k_z^2\} J_x + \text{cp}) + \mathbf{b}_{42}^{8v8v} (\{k_x, k_y^2 - k_z^2\} J_x^3 + \text{cp})$ $+ \mathbf{b}_{51}^{8v8v} (\{k_x, k_y^2 + k_z^2\} \{J_x, J_y^2 - J_z^2\} + \text{cp})$ $+ \mathbf{b}_{52}^{8v8v} (k_x^3 \{J_x, J_y^2 - J_z^2\} + \text{cp})$
$\mathcal{H}_{7v\ 7v}^b = \mathbf{b}_{41}^{7v7v} (\{k_x, k_y^2 - k_z^2\} \sigma_x + \text{cp})$
$\mathcal{H}_{8v\ 7v}^b = -i\sqrt{3} C_k (k_x U_{yz} + \text{cp}) + \mathbf{b}_{41}^{8v7v} (\{k_x, k_y^2 - k_z^2\} U_x + \text{cp})$ $+ \mathbf{b}_{51}^{8v7v} (\{k_x, k_y^2 + k_z^2\} U_{yz} + \text{cp}) + \mathbf{b}_{52}^{8v7v} (k_x^3 U_{yz} + \text{cp})$

$\mathcal{H}_{6c\ 8v}^b = iB_{8v}^+ (T_x \{k_y k_z\} + \text{cp})$ $+ \frac{1}{2} B_{8v}^- [(T_{xx} - T_{yy}) (k_z^2 - \frac{1}{3} k^2) - T_{zz} (k_x^2 - k_y^2)]$
$\mathcal{H}_{6c\ 7v}^b = -\frac{i}{\sqrt{3}} B_{7v} (\sigma_x \{k_y k_z\} + \text{cp})$

where $k_{\pm} = k_x \pm ik_y$. This invariant is often called the *Dresselhaus term* [2] or the k^3 term [22]. It is the lowest-order term that characterizes BIA spin splitting in the Γ_6^c conduction band. For \mathbf{k} parallel to [100], BIA spin splitting vanishes for both electrons and holes in all orders of \mathbf{k} (see Fig. 3.2), because here the group of the wave vector is C_{2v} , which has only one irreducible double-group representation, Γ_5 , which is two-dimensional [23, 24].³ When \mathbf{k} is parallel to [111], BIA spin splitting vanishes for electron and LH states, because these states transform according to the two-dimensional double-group representation Γ_4 of C_{3v} , whereas HH states transform according to the one-dimensional double-group representations Γ_5 and Γ_6 of C_{3v} [23, 24].

As noted in Sect. 3.3, the main contribution to the prefactor C_k of the k -linear spin splitting in the Γ_8^v valence band stems from the bilinear terms consisting of $\mathbf{k} \cdot \mathbf{p}$ and SO interactions, with remote Γ_3 -like intermediate states [17]. The coefficient C_k is thus an “elementary” parameter of the extended Kane model. We can express the remaining coefficients in Table 6.2 in terms of the parameters of the extended Kane model. We obtain, in third-order perturbation theory,

$$\mathbf{b}_{41}^{6c6c} = -\frac{4i}{3} PP'Q \left[\frac{1}{(E_0 + \Delta_0)(E_0 - E'_0 - \Delta'_0)} - \frac{1}{E_0(E_0 - E'_0)} \right], \quad (6.2a)$$

$$\mathbf{b}_{41}^{8v8v} = \frac{i}{6} PP'Q \frac{1}{E_0} \left[\frac{13}{E'_0} - \frac{5}{E'_0 + \Delta'_0} \right], \quad (6.2b)$$

$$\mathbf{b}_{42}^{8v8v} = \frac{2i}{3} PP'Q \frac{1}{E_0} \left[\frac{1}{E'_0} - \frac{1}{E'_0 + \Delta'_0} \right], \quad (6.2c)$$

³ For the same reason we have no BIA spin splitting for $\mathbf{k} \parallel [001]$ in symmetric QWs grown in the crystallographic direction [110].

$$\mathbf{b}_{51}^{8v8v} = \frac{2i}{9} PP'Q \frac{1}{E_0} \left[\frac{1}{E'_0 + \Delta'_0} - \frac{1}{E'_0} \right], \quad (6.2d)$$

$$\mathbf{b}_{52}^{8v8v} = \frac{4i}{9} PP'Q \frac{1}{E_0} \left[\frac{1}{E'_0} - \frac{1}{E'_0 + \Delta'_0} \right], \quad (6.2e)$$

$$\mathbf{b}_{41}^{7v7v} = \frac{4i}{3} PP'Q \frac{1}{(E_0 + \Delta_0)(\Delta_0 + E'_0 + \Delta'_0)}, \quad (6.2f)$$

$$\mathbf{b}_{41}^{8v7v} = i PP'Q \left[\frac{1}{E_0(E'_0 + \Delta'_0)} + \frac{1}{(E_0 + \Delta_0)(\Delta_0 + E'_0 + \Delta'_0)} \right], \quad (6.2g)$$

$$\mathbf{b}_{51}^{8v7v} = -\frac{1}{3} PP'Q \left[\frac{1}{E_0 E'_0} - \frac{1}{E_0(E'_0 + \Delta'_0)} \right] \quad (6.2h)$$

$$+ \frac{1}{(E_0 + \Delta_0)(E'_0 + \Delta_0)} - \frac{1}{(E_0 + \Delta_0)(\Delta_0 + E'_0 + \Delta'_0)} \Big], \quad (6.2i)$$

$$\mathbf{b}_{52}^{8v7v} = \mathbf{b}_{51}^{8v7v}.$$

The formulas for Kane's off-diagonal parameters B_i can be found in Table C.9.⁴ In the extended Kane model, the prefactors characterizing the BIA spin splitting are proportional to the product $PP'Q$, i.e., for both electron and hole states, BIA spin splitting originates in the $\mathbf{k} \cdot \mathbf{p}$ coupling between the valence bands Γ_8^v and Γ_7^v , the conduction band Γ_6^c , and the conduction bands Γ_8^c and Γ_7^c . Accordingly, BIA spin splitting has the same order of magnitude for electron and hole states, consistent with our general remark at the beginning of Chap. 5.

For the limiting case of zero SO splitting of the bulk bands, $\Delta_0 = \Delta'_0 = 0$, we still have nonzero coefficients \mathbf{b}_{41}^{8v8v} , \mathbf{b}_{41}^{7v7v} , and \mathbf{b}_{41}^{8v7v} . This reflects the fact that even for the valence band Γ_5^v without SO interaction we have one invariant which is cubic in \mathbf{k} , namely $(\{k_x, k_y^2 - k_z^2\}L_x + \text{cp})$. Nevertheless, $\Delta_0 = \Delta'_0 = 0$ implies that we have zero BIA spin splitting because the above cubic invariant is then acting within the block $\mathcal{H}_{\mathbf{k} \cdot \mathbf{p}}$ defined in (5.1). On the other hand, we have no cubic terms at all in materials with an inversion-symmetric diamond structure where parity conservation requires $P' = 0$.

Numerical values for the coefficients (6.2) are given in Table 6.3. The most important coefficients are C_k , \mathbf{b}_{41}^{8v8v} , \mathbf{b}_{41}^{7v7v} , and \mathbf{b}_{41}^{8v7v} , which are nonzero even if we set $\Delta_0 = \Delta'_0 = 0$. In the valence band block \mathcal{H}_{8v8v} , for typical values of k , the cubic invariant proportional to \mathbf{b}_{41}^{8v8v} has the same order of magnitude as the k -linear term proportional to C_k . It was observed by Cardona et al. [17] that when \mathbf{k} is parallel to [110] the spin splitting of the HH states in bulk

⁴ The coefficients defined in (6.2) refer to a model which does not explicitly take into account $\mathbf{k} \cdot \mathbf{p}$ coupling between the conduction and valence bands. In an 8×8 $\mathbf{k} \cdot \mathbf{p}$ Hamiltonian (3.6), Kane's off-diagonal parameters B_i as defined in Table C.9 supersede the coefficients in (6.2), i.e. we have to set the coefficients (6.2) to zero if the parameters B_i are used; see the discussion of reduced band parameters in Sect. 3.3.

Table 6.3. Expansion coefficients for the invariants in Table 6.2 evaluated for various semiconductors using (6.2) and Table C.9 (all in $\text{eV } \text{\AA}^3$, except for C_k in $\text{eV } \text{\AA}$ and B_i in $\text{eV } \text{\AA}^2$). C_k was taken from [17]. Band parameters were taken from [25, 26]

	GaAs	AlAs	InAs	InSb	CdTe	ZnSe
b_{41}^{6c6c}	27.58	18.53	27.18	760.1	43.88	14.29
C_k	-0.0034	0.0020	-0.0112	-0.0082	-0.0234	-0.0138
b_{41}^{8v8v}	-81.93	-33.51	-50.18	-934.8	-76.93	-62.33
b_{42}^{8v8v}	1.47	0.526	1.26	41.73	1.668	0.375
b_{51}^{8v8v}	0.49	0.175	0.42	13.91	0.556	0.125
b_{52}^{8v8v}	-0.98	-0.35	-0.84	-27.82	-1.11	-0.250
b_{41}^{7v7v}	-58.71	-27.27	-22.31	-146.8	-38.44	-50.71
b_{41}^{8v7v}	-101.9	-44.30	-51.29	-709.5	-82.46	-83.86
b_{51}^{8v7v}	-1.255 i	-0.474 i	-0.910 i	-23.92 i	-1.215 i	-0.335 i
B_{8v}^+	-21.32	-34.81	-3.393	-32.20	-22.41	-32.05
B_{8v}^-	-0.5175	-1.468	-0.09511	-1.662	-0.6347	-0.2704
B_{7v}	-20.24	-32.84	-3.178	-27.77	-20.47	-31.15

GaAs changes its sign, see Fig. 6.1. By means of the invariant expansion in Table 6.2 and the numerical values in Table 6.3, it can be understood that this surprising behavior is due to the fact that for $\mathbf{k} \parallel [110]$ the prefactors b_{41}^{8v8v} and C_k contribute to the HH spin splitting with opposite signs so that they cancel each other for some small value of $\mathbf{k} \parallel [110]$. In AlAs, the coefficient C_k is positive [17], so that there is no sign reversal of the HH spin splitting. For the LH states, the dominant contribution to BIA spin splitting is given by the invariant proportional to b_{41}^{8v8v} , i.e. the BIA spin splitting of LH states is essentially proportional to k^3 .

In Fig. 6.1, we show the absolute value $|\Delta E|$ of the BIA spin splitting of hole states in GaAs for \mathbf{k} parallel to $[110]$. We use a double-logarithmic plot, as it allows us to distinguish between the k -linear and the cubic splittings. The solid lines were obtained by means of a diagonalization of the extended Kane model (3.2), whereas the dashed lines are the results obtained from the 4×4 Hamiltonian \mathcal{H}_{8v8v} with terms up to third order in k . The invariant expansion is in good agreement with the more complete 14×14 Hamiltonian.

Finally, we note that the expressions (6.2) represent only the leading order terms contributing to the coefficients in Table 6.2. We obtain (rather lengthy) additional terms proportional to C_k and Δ^- . Although these two parameters are often known less accurately than the energy gaps and momentum matrix elements entering (6.2), the new terms can be significant for a quantitative analysis of BIA spin splitting. For example, the Dresselhaus coefficient b_{41}^{6c6c} of GaAs is reduced from $27.58 \text{ eV } \text{\AA}^3$ [22] to $19.55 \text{ eV } \text{\AA}^3$ [27] if the parameter Δ^- (and C_k) is taken into account in fourth-order perturbation theory. For

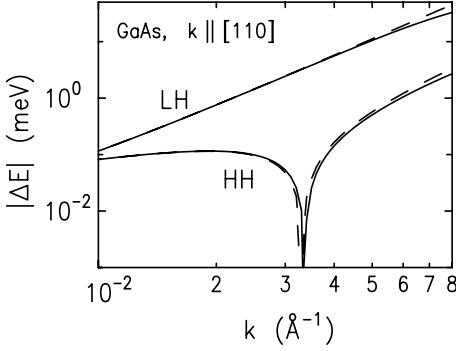


Fig. 6.1. Double-logarithmic plot of the absolute value $|\Delta E|$ of the BIA spin splitting of hole states in GaAs for $\mathbf{k} \parallel [110]$. The *solid lines* were obtained by means of a diagonalization of the full 14×14 matrix of the extended Kane model, and the *dashed lines* are the results obtained from the 4×4 Hamiltonian \mathcal{H}_{8v8v} with terms up to third order in k

consistency, all numerical values in Table 6.3 have been calculated using (6.2) and Table C.9.

6.2.2 BIA Spin Splitting in Quasi-2D Systems

For quasi-2D systems, we can readily estimate the BIA-induced spin splitting. In first-order perturbation theory, we replace the n th power of $k_z = -i\partial_z$ by the expectation value $\langle (-i\partial_z)^n \rangle$. (Note that for odd n we have $\langle (-i\partial_z)^n \rangle = 0$.) For example, for a quasi-2D electron system in a QW grown in the crystallographic direction [001], the Dresselhaus term (6.1) becomes [22, 28]

$$\mathcal{H}_{6c6c}^b = \mathbf{b}_{41}^{6c6c} \begin{pmatrix} 0 & \frac{1}{4}k_-(k_+^2 - k_-^2) - k_+\langle k_z^2 \rangle \\ \frac{1}{4}k_+(k_-^2 - k_+^2) - k_-\langle k_z^2 \rangle & 0 \end{pmatrix}. \quad (6.3)$$

This equation can easily be diagonalized. We obtain a spin splitting

$$E_{6c6c}^b(\mathbf{k}_{\parallel}) = \pm \langle \mathbf{b}_{41}^{6c6c} \rangle k_{\parallel} \sqrt{\langle k_z^2 \rangle^2 + \left(\frac{1}{4}k_{\parallel}^2 - \langle k_z^2 \rangle \right) k_{\parallel}^2 \sin^2(2\varphi)} \quad (6.4a)$$

$$\approx \pm \langle \mathbf{b}_{41}^{6c6c} \rangle \left[\langle k_z^2 \rangle k_{\parallel} - \frac{1}{2}k_{\parallel}^3 \sin^2(2\varphi) + \mathcal{O}(k_{\parallel}^5) \right], \quad (6.4b)$$

where $\mathbf{k}_{\parallel} = k_{\parallel}(\cos \varphi, \sin \varphi, 0)$. We have used angle brackets to indicate that $\langle \mathbf{b}_{41}^{6c6c} \rangle$ corresponds to an average over the coefficient \mathbf{b}_{41}^{6c6c} of the well and barrier materials. For small \mathbf{k}_{\parallel} the BIA spin splitting is linear in \mathbf{k}_{\parallel} and independent of the direction of \mathbf{k}_{\parallel} . For larger values of \mathbf{k}_{\parallel} the BIA spin splitting becomes anisotropic, with energy surfaces that have a fourfold rotational symmetry, consistent with the fact that the point group is D_{2d} . Note also that for $\varphi = 0$ ($\mathbf{k}_{\parallel} \parallel [100]$) and $\varphi = \pi/4$ ($\mathbf{k}_{\parallel} \parallel [110]$), (6.4b) is exact. Within the Dresselhaus model (6.3) we thus have zero BIA spin splitting for $\varphi = \pi/4$ and $k_{\parallel}^2 = 2\langle k_z^2 \rangle$ independent of the material specific coefficient $\langle \mathbf{b}_{41}^{6c6c} \rangle$ (see also Sect. 6.6.2).

Strictly speaking, the invariant expansion for the BIA spin splitting of quasi-2D electron systems in a QW grown in the crystallographic direction [001] (point group D_{2d}) yields

$$\begin{aligned}
\mathcal{H}_{6c6c}^b &= b_{51}^{6c6c} (k_+ \sigma_+ + k_- \sigma_-) \\
&+ \frac{1}{4} b_{52}^{6c6c} (\{k_-, k_+^2 - k_-^2\} \sigma_+ + \{k_+, k_-^2 - k_+^2\} \sigma_-) \\
&+ \frac{1}{4} b_{53}^{6c6c} [(k_-^3 + 3\{k_-, k_+^2\}) \sigma_+ + (k_+^3 + 3\{k_+, k_-^2\}) \sigma_-] \quad (6.5)
\end{aligned}$$

(see Tables 6.7 and 6.8). In this equation, we have a third invariant, weighted by b_{53}^{6c6c} , which goes beyond (6.3). We can evaluate the prefactors in (6.5) by means of the subband $\mathbf{k} \cdot \mathbf{p}$ method. For the α th electron subband, we obtain

$$\begin{aligned}
b_{51}^{6c6c} &= \frac{2i}{3} PP'Q \sum_{\beta \neq \alpha} \left[\frac{\langle c_\alpha | \mathbf{k}_z | s_\beta \rangle}{\Delta_{\alpha\beta}^{cs}} \left(\frac{\langle s_\beta | \mathbf{k}_z | H_\alpha \rangle}{\Delta_{\alpha\alpha}^{cH}} + \frac{\langle L_\beta | \mathbf{k}_z | c_\alpha \rangle}{\Delta_{\alpha\beta}^{cL}} \right) \right. \\
&\quad - \frac{\langle c_\alpha | \mathbf{k}_z | S_\beta \rangle}{\Delta_{\alpha\beta}^{cS}} \left(\frac{\langle S_\beta | \mathbf{k}_z | h_\alpha \rangle}{\Delta_{\alpha\alpha}^{ch}} + \frac{\langle l_\beta | \mathbf{k}_z | c_\alpha \rangle}{\Delta_{\alpha\beta}^{cl}} \right) \\
&\quad \left. + \frac{\langle c_\alpha | \mathbf{k}_z | L_\beta \rangle \langle L_\beta | \mathbf{k}_z | h_\alpha \rangle}{\Delta_{\alpha\beta}^{cL} \Delta_{\alpha\alpha}^{ch}} - \frac{\langle c_\alpha | \mathbf{k}_z | l_\beta \rangle \langle l_\beta | \mathbf{k}_z | H_\alpha \rangle}{\Delta_{\alpha\beta}^{cl} \Delta_{\alpha\alpha}^{cH}} \right], \quad (6.6a)
\end{aligned}$$

$$\begin{aligned}
b_{52}^{6c6c} &= i PP'Q \left[\frac{1}{\Delta_{\alpha\alpha}^{cS}} \left(\frac{1}{\Delta_{\alpha\alpha}^{cl}} + \frac{1}{3\Delta_{\alpha\alpha}^{ch}} \right) - \frac{1}{\Delta_{\alpha\alpha}^{cs}} \left(\frac{1}{\Delta_{\alpha\alpha}^{cL}} + \frac{1}{3\Delta_{\alpha\alpha}^{cH}} \right) \right. \\
&\quad \left. + \frac{1}{3\Delta_{\alpha\alpha}^{cl} \Delta_{\alpha\alpha}^{cH}} - \frac{1}{3\Delta_{\alpha\alpha}^{cL} \Delta_{\alpha\alpha}^{ch}} \right], \quad (6.6b)
\end{aligned}$$

$$\begin{aligned}
b_{53}^{6c6c} &= \frac{i}{3} PP'Q \left[\frac{1}{\Delta_{\alpha\alpha}^{cS}} \left(\frac{1}{\Delta_{\alpha\alpha}^{ch}} - \frac{1}{\Delta_{\alpha\alpha}^{cl}} \right) + \frac{1}{\Delta_{\alpha\alpha}^{cs}} \left(\frac{1}{\Delta_{\alpha\alpha}^{cL}} - \frac{1}{\Delta_{\alpha\alpha}^{cH}} \right) \right. \\
&\quad \left. + \frac{1}{\Delta_{\alpha\alpha}^{cl} \Delta_{\alpha\alpha}^{cH}} - \frac{1}{\Delta_{\alpha\alpha}^{cL} \Delta_{\alpha\alpha}^{ch}} \right]. \quad (6.6c)
\end{aligned}$$

Here we have used

$$\Delta_{\alpha\alpha'}^{nn'} \equiv E_\alpha^n - E_{\alpha'}^{n'} \quad (6.7)$$

with bulk band indices n, n' and subband indices α, α' . In (6.6), we have assumed that the subband wave functions are orthogonal, $\langle n_\alpha | n'_\beta \rangle = \delta_{\alpha\beta}$, independent of the bulk band indices n, n' . The indices $n = H, L$, and S denote subbands in the higher conduction bands Γ_8^c and Γ_7^c . In (6.6), we have used $\mathbf{k}_z = -i\partial_z$, the operator of canonical momentum (2.16), in order to emphasize that this equation is valid even for $B > 0$.

For the terms in (6.2a), we can readily identify the corresponding terms in (6.6). The remaining terms in (6.6) (the last line of (6.6a) and (6.6b) and all terms in (6.6c)) are a consequence of HH–LH splitting in the bands Γ_8^v and Γ_8^c . This is the reason why the coefficient b_{53}^{6c6c} is usually rather small, so that the corresponding invariant can be neglected [29]. Typically, the fundamental gap E_0 is smaller than the gap $E_0' - E_0$ between the band Γ_6^c and the higher conduction bands Γ_8^c and Γ_7^c . Thus it follows from (6.6) that subband confinement reduces the prefactors of BIA spin splitting as compared with the bulk formula (6.2a). Finally, we remark that similar results can be

obtained for other growth directions [20, 28] and for other systems such as HH and LH systems.

6.3 SIA Spin Splitting

In semiconductor quantum structures, the spin degeneracy can be lifted not only because of a bulk inversion asymmetry of the underlying crystal structure, but also because of a structure inversion asymmetry of the confining potential $V(\mathbf{r})$. This potential may contain a built-in or external potential, as well as the effective potential from the position-dependent band edges. Recent experiments have shown that the SIA spin splitting can even be tuned continuously by means of external gates [12, 30].

We can perform a Taylor expansion of the potential $V(\mathbf{r})$,

$$V(\mathbf{r}) = V_0 + e\mathcal{E} \cdot \mathbf{r} + \dots, \quad (6.8)$$

i.e. to lowest order the inversion asymmetry of $V(\mathbf{r})$ can be characterized by an electric field \mathcal{E} . The importance of (6.8) lies in the fact that we can include the electric field \mathcal{E} in the invariant expansion (2.30), and examples will be given below. We begin in Sect. 6.3.1 with a discussion of the Rashba model for the Γ_6^c conduction band. Then we discuss the less familiar case of SIA spin splitting in the Γ_8^v valence band. In Sect. 6.3.4 we discuss the similarities between SIA spin splitting and Zeeman splitting.

6.3.1 SIA Spin Splitting in the Γ_6^c Conduction Band: the Rashba Model

To lowest order in \mathbf{k} and \mathcal{E} , the SIA spin splitting⁵ in the Γ_6^c conduction band is given by the Rashba term [4, 31],

$$\mathcal{H}_{6c6c}^r = r_{41}^{6c6c} \boldsymbol{\sigma} \cdot \mathbf{k} \times \mathcal{E}, \quad (6.9)$$

with a material-specific prefactor r_{41}^{6c6c} [32, 33]. Both \mathbf{k} and \mathcal{E} are polar vectors (transforming according to the irreducible representation Γ_5 of T_d), and $\mathbf{k} \times \mathcal{E}$ is an axial vector (transforming according to the irreducible representation Γ_4 of T_d) [33, 34]. Likewise, the vector $\boldsymbol{\sigma} = (\sigma_x, \sigma_y, \sigma_z)$ of Pauli spin matrices is an axial vector. The dot product (6.9) of $\mathbf{k} \times \mathcal{E}$ and $\boldsymbol{\sigma}$ therefore transforms according to the unit representation Γ_1 , in accordance with the theory of invariants described in Sect. 2.5. We see from Tables C.3 and C.4 that the scalar triple product (6.9) is the only term of first order in \mathbf{k} and \mathcal{E} that is compatible with the symmetry of the band.

⁵ It has become common practice to use the term “Rashba effect” both for the Hamiltonian (6.9) and for SIA spin splitting in general, even though we can have substantial quantitative differences between (6.9) and the SIA spin splitting as determined by means of a more complete multiband Hamiltonian; see Figs. 6.3 and 6.4.

SIA spin splitting of 2D electron states has been studied theoretically for many years. Research has focused mainly on the prefactor of the Rashba term [3,35,4,31,36,37,32,22,38,39,33,40,41,42,43,44,45,46,47,48,49,8,7]. Here we shall show that an analysis of the Rashba model can be very illuminating because this model can be completely solved analytically. We then present two different approaches for calculating the prefactor of the Rashba term.

General Features of the Rashba Model. For $\mathcal{E} = (0, 0, \mathcal{E}_z)$, (6.9) becomes (using an explicit matrix notation)

$$\mathcal{H}_{6c6c}^r = r_{41}^{6c6c} \mathcal{E}_z i (k_- \sigma_+ - k_+ \sigma_-), \quad (6.10a)$$

$$= r_{41}^{6c6c} \mathcal{E}_z \begin{pmatrix} 0 & i k_- \\ -i k_+ & 0 \end{pmatrix}, \quad (6.10b)$$

where $k_{\pm} = k_x \pm i k_y$ and $\sigma_{\pm} = \frac{1}{2}(\sigma_x \pm i \sigma_y)$. In this section we shall assume that in the subband dispersion $E(\mathbf{k}_{\parallel})$, we can neglect nonparabolic corrections of higher order in \mathbf{k}_{\parallel} . Combining (6.10) with the kinetic energy $\mu_c k_{\parallel}^2 \mathbb{1}_{2 \times 2}$, where μ_c (times $2/\hbar^2$) is the reciprocal effective mass, we obtain for the spin-split subband dispersion $E_{\pm}(\mathbf{k}_{\parallel})$

$$E_{\pm}(\mathbf{k}_{\parallel}) = \langle \mu_c \rangle k_{\parallel}^2 \pm \langle r_{41}^{6c6c} \mathcal{E}_z \rangle k_{\parallel}. \quad (6.11)$$

We use angle brackets to indicate that $\langle r_{41}^{6c6c} \mathcal{E}_z \rangle$ corresponds to an average of the Rashba coefficients of the well and barrier materials. Note, however, that the details of any microscopic model for $\langle r_{41}^{6c6c} \mathcal{E}_z \rangle$ are irrelevant for the following discussion. Thus we shall use in this section the abbreviation

$$\alpha := \langle r_{41}^{6c6c} \mathcal{E}_z \rangle. \quad (6.12)$$

Equation (6.11) predicts an SIA spin splitting which is linear in k_{\parallel} . For small k_{\parallel} , the Rashba term $\pm \alpha k_{\parallel}$ thus becomes the dominant term in the energy dispersion $E_{\pm}(\mathbf{k}_{\parallel})$. In particular we obtain a ring of minima for the lower branch $E_{-}(\mathbf{k}_{\parallel})$ at finite wave vectors \mathbf{k}_m where

$$|\mathbf{k}_m| \equiv k_m = \frac{\alpha}{2 \langle \mu_c \rangle}, \quad (6.13)$$

from which we obtain

$$E_{-}(\mathbf{k}_m) = -\frac{\alpha^2}{4 \langle \mu_c \rangle}. \quad (6.14)$$

The ring of minima is sketched in Fig. 6.2. As a more quantitative example, we show in Fig. 6.3 the subband dispersion $E_{\pm}(k_{\parallel})$ for an MOS inversion layer on InSb according to (6.11). If the total density N_s is smaller than the “quantum density”

$$N_m = \frac{(2k_m)^2}{4\pi} = \frac{1}{4\pi} \frac{\alpha^2}{\langle \mu_c \rangle^2}, \quad (6.15)$$

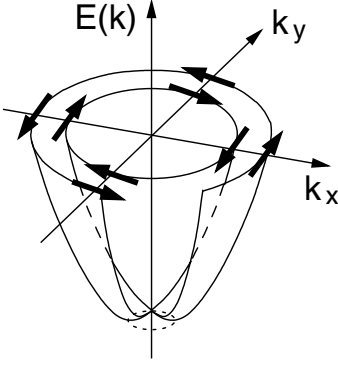


Fig. 6.2. Qualitative sketch of the spin-split dispersion $E_{\pm}(\mathbf{k}_{\parallel})$ according to (6.11). We obtain a ring of minima (dashed line at bottom) at finite wave vectors \mathbf{k}_m given by (6.13). Arrows indicate the spin orientation of the eigenstates (see Sect. 6.6.1)

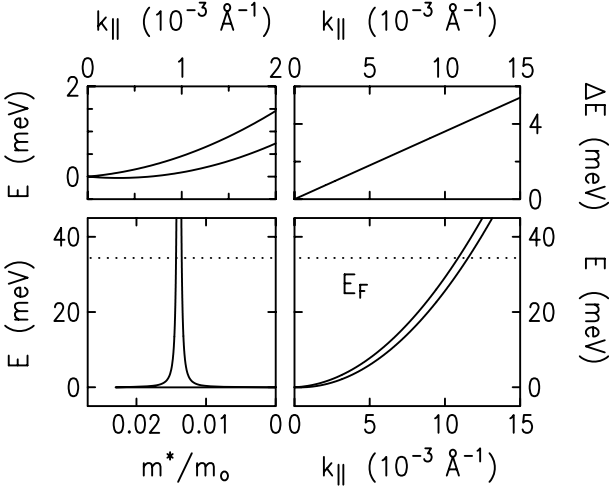


Fig. 6.3. Subband dispersion $E_{\pm}(k_{\parallel})$ (lower right) and DOS effective mass m^*/m_0 (lower left), spin splitting $E_+(k_{\parallel}) - E_-(k_{\parallel})$ (upper right), and subband dispersion $E_{\pm}(k_{\parallel})$ in the vicinity of $k_{\parallel} = 0$ (upper left) for an MOS inversion layer on InSb calculated by means of (6.11) and (6.20). We have used the same value of the electric field \mathcal{E}_z as that obtained from the self-consistent calculation shown in Fig. 6.4

only the lower spin subband is occupied. We remark that even for a large electric field $\mathcal{E}_z = 50$ kV/cm, the density N_m is fairly small. Using the numerical values for r_{41}^{6c6c} given in Table 6.6, we find that N_m is of the order $2 \times 10^6 \text{ cm}^{-2}$ (GaAs) to $8 \times 10^8 \text{ cm}^{-2}$ (InSb). The corresponding energy $E_-(\mathbf{k}_m)$ is of the order $-3 \times 10^{-5} \text{ meV}$ (GaAs) to $-6 \times 10^{-2} \text{ meV}$ (InSb).

We can determine the unequal populations N_{\pm} of the two branches $E_{\pm}(k_{\parallel})$ from the conditions

$$N_s = N_+ + N_- , \quad (6.16a)$$

$$N_{\pm} = \frac{1}{4\pi} k_{F\pm}^2 , \quad (6.16b)$$

and

$$E_F = E_{\pm}(k_{F\pm}) = \langle\mu_c\rangle k_{F\pm}^2 \pm \alpha k_{F\pm} . \quad (6.16c)$$

Here N_s is the total 2D density in the system, $k_{F\pm}$ are the Fermi wave vectors of the spin-split branches, and E_F is the Fermi energy. We obtain the following expression for the Fermi energy E_F as a function of the total density N_s :

$$E_F = 2\pi N_s \langle\mu_c\rangle - \frac{\alpha^2}{2\langle\mu_c\rangle} . \quad (6.17)$$

From these equations, we can derive the populations N_{\pm} of the spin-split branches,

$$N_{\pm} = \frac{N_s}{2} \mp \frac{\alpha}{8\pi\langle\mu_c\rangle^2} \sqrt{8\pi\langle\mu_c\rangle^2 N_s - \alpha^2} . \quad (6.18)$$

We can solve these equations for the Rashba coefficient α as a function of N_s and $\Delta N \equiv |N_+ - N_-|$

$$\alpha = \sqrt{2\pi} \langle\mu_c\rangle \left(\sqrt{N_s + \Delta N} - \sqrt{N_s - \Delta N} \right) \quad (6.19a)$$

$$= \langle\mu_c\rangle |k_{F+} - k_{F-}| , \quad (6.19b)$$

where $k_{F\pm}$ are defined in (6.16b). This equation can be used directly for the interpretation of Shubnikov-de Haas experiments [50, 51, 52, 53, 54, 55, 13, 56, 57, 58, 59]; however, see also Chap. 9.

The density of states (4.12) of the spin-split branches is given by

$$D_{\pm}(E) = \frac{1}{4\pi\langle\mu_c\rangle} \left(1 \mp \frac{\alpha}{\sqrt{4\langle\mu_c\rangle E + \alpha^2}} \right), \quad E \geq 0 , \quad (6.20a)$$

$$D_{-}(E) = \frac{1}{2\pi\langle\mu_c\rangle} \frac{\alpha}{\sqrt{4\langle\mu_c\rangle E + \alpha^2}}, \quad E < 0 , \quad (6.20b)$$

which becomes singular when $E = E_{-}(k_m)$; see Fig. 6.3. This divergent van Hove singularity of the DOS at the bottom of the subband [60] is characteristic of a k -linear spin splitting. The presence of this singularity indicates that SIA spin splitting of electron states is most important for small 2D densities (see also Sect. 6.4.2).

We can compare the results obtained from (6.11) with a more accurate, fully numerical diagonalization of an appropriate multiband Hamiltonian. As an example, we present in Fig. 6.4 the self-consistently calculated [60] subband dispersion $E_{\pm}(k_{\parallel})$, DOS effective mass m^*/m_0 , and spin splitting $\Delta E(k_{\parallel}) = E_{+}(k_{\parallel}) - E_{-}(k_{\parallel})$ for an MOS inversion layer on InSb, obtained by means of the 8×8 Kane Hamiltonian (3.6). For small k_{\parallel} , the spin splitting increases linearly as a function of k_{\parallel} , in agreement with (6.11). Owing to nonparabolicity, the spin splitting $\Delta E(k_{\parallel})$ increases sublinearly for larger k_{\parallel} [60]. Note that in Fig. 6.3 we have used the same value of the electric field \mathcal{E}_z as that which was obtained from the self-consistent calculation shown in Fig. 6.4. Therefore we can clearly see the limitations of the approximate model (6.11) as compared with the more complete Kane multiband Hamiltonian $\mathcal{H}_{8 \times 8}$.

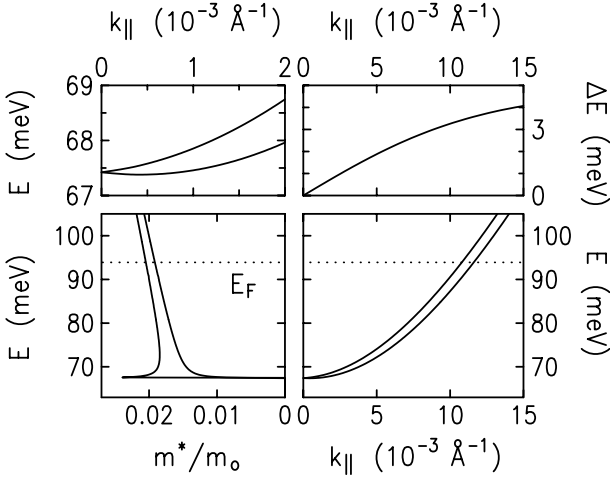


Fig. 6.4. Self-consistently calculated subband dispersion $E_{\pm}(k_{\parallel})$ (lower right), DOS effective mass m^*/m_0 (lower left), spin splitting $E_{+}(k_{\parallel}) - E_{-}(k_{\parallel})$ (upper right), and subband dispersion $E_{\pm}(k_{\parallel})$ in the vicinity of $k_{\parallel} = 0$ (upper left) for an MOS inversion layer on InSb with $N_s = 2 \times 10^{11} \text{ cm}^{-2}$ and $|N_A - N_D| = 2 \times 10^{16} \text{ cm}^{-2}$. The dotted line indicates the Fermi energy E_F . Taken from [7]. © (2000) by the American Physical Society

Calculation of the Rashba Coefficient. In the following, we present two methods for evaluating the Rashba coefficient in quasi-2D systems: (i) Löwdin partitioning for the quasi-bulk Hamiltonian, and (ii) Löwdin partitioning for the subband Hamiltonian.

Löwdin Partitioning for the Quasi-Bulk Hamiltonian. The Rashba term \mathcal{H}_{6c6c}^r in (6.9) is an *effective* Hamiltonian for the spin splitting of electron subbands, which is implicitly contained in the full EFA multiband Hamiltonian for the subband problem [60, 37]

$$\mathcal{H}_{\text{EFA}} = \mathcal{H}(\mathbf{k} \rightarrow -i\nabla) + e\mathcal{E} \cdot \mathbf{r} \mathbb{1} . \quad (6.21)$$

Here we have restricted ourselves to the lowest nontrivial order in the Taylor expansion (6.8). The effective Hamiltonian (6.9) stems from the combined effect of $\mathcal{H}(\mathbf{k})$ and the term $e\mathcal{E} \cdot \mathbf{r} \mathbb{1}$.

We can use Löwdin partitioning to separate the conduction band block \mathcal{H}_{6c6c} from all other bands. While the $\mathbf{k} \cdot \mathbf{p}$ coupling appears in the off-diagonal parts of $\mathcal{H}(\mathbf{k})$, the perturbation $e\mathcal{E} \cdot \mathbf{r}$ appears only on the diagonal of \mathcal{H}_{EFA} . We see in (B.15) that second-order Löwdin perturbation theory depends only on matrix elements that connects states from set A with states from set B . We need at least third-order perturbation theory if we are interested in effects due to matrix elements within set A or set B . It follows

that, independently of the details of $\mathcal{H}(\mathbf{k})$, SIA spin splitting requires at least third-order perturbation theory to describe it.

If we use the extended Kane model for $\mathcal{H}(\mathbf{k})$, third-order perturbation theory for the block \mathcal{H}_{6c6c} yields the Rashba term (6.9), where [61]

$$\begin{aligned} r_{41}^{6c6c} = & \frac{eP^2}{3} \left[\frac{1}{E_0^2} - \frac{1}{(E_0 + \Delta_0)^2} \right] \\ & + \frac{eP'^2}{3} \left[\frac{1}{(E_0 - E'_0)^2} - \frac{1}{(E_0 - E'_0 - \Delta'_0)^2} \right]. \end{aligned} \quad (6.22)$$

Here we have used the commutator relation $[r_\mu, k_\nu] = i\delta_{\mu\nu}$. The present approach to evaluating r_{41}^{6c6c} is similar to the derivation of Roth's formula (4.39b) for the effective g factor of electrons in a bulk semiconductor. Therefore, we call the first approach to calculating r_{41}^{6c6c} ‘‘Löwdin partitioning for the quasi-bulk Hamiltonian’’.⁶

Numerical values for r_{41}^{6c6c} obtained according to (6.22) are given in Table 6.6. Similarly to the effective g factor, the coefficient r_{41}^{6c6c} is largest for narrow-gap semiconductors, as these materials also have a large SO gap Δ_0 [39].

Rashba Coefficient for Quantum Wells. Next we calculate the Rashba coefficient of a quantum structure using the subband $\mathbf{k} \cdot \mathbf{p}$ method. Using the 8×8 Kane model (3.6) for $\mathcal{H}(\mathbf{k})$,⁷ we obtain the following for the Rashba coefficient of the α th electron subband:

$$\begin{aligned} r_{41}^{6c6c} = & \frac{2ieP^2}{3} \left[\sum_{\beta} \frac{\langle c_{\alpha}|z|l_{\beta}\rangle \langle l_{\beta}|\mathbf{k}_z|c_{\alpha}\rangle - \langle c_{\alpha}|\mathbf{k}_z|l_{\beta}\rangle \langle l_{\beta}|z|c_{\alpha}\rangle}{\Delta_{\alpha\alpha}^{cl} \Delta_{\alpha\beta}^{cl}} \right. \\ & \left. - \sum_{\beta} \frac{\langle c_{\alpha}|z|s_{\beta}\rangle \langle s_{\beta}|\mathbf{k}_z|c_{\alpha}\rangle - \langle c_{\alpha}|\mathbf{k}_z|s_{\beta}\rangle \langle s_{\beta}|z|c_{\alpha}\rangle}{\Delta_{\alpha\alpha}^{cs} \Delta_{\alpha\beta}^{cs}} \right], \end{aligned} \quad (6.23)$$

where we have used (4.37) and (6.7). We can evaluate (6.23) further using the eigenfunctions of an infinitely deep rectangular well and the eigenfunctions of a harmonic oscillator. We obtain the following for the lowest electron subband ($\alpha = 1$):

$$r_{41}^{6c6c} = eP^2 a \left[\frac{1}{\Delta_{11}^{cl} \Delta_{12}^{cl}} - \frac{1}{\Delta_{11}^{cs} \Delta_{12}^{cs}} \right], \quad (6.24)$$

where $a = 1/3$ for the parabolic well and $a = 256/(81\pi^2) \approx 0.320$ for the rectangular well, in complete analogy with (4.42a).

⁶ It might appear problematic that we assume that the electric field \mathcal{E} has an infinite range. However, this does not cause problems, because we use the multiband Hamiltonian in order to calculate bound states, the spatial dimensions of which are small compared with the dimensions of the crystal.

⁷ We obtain similar terms from the $\mathbf{k} \cdot \mathbf{p}$ coupling to the higher conduction bands Γ_8^c and Γ_7^c .

Table 6.4. Tensor operators for the conduction and valence band Hamiltonian when we explicitly take into account the position dependence of the band edges E_c and E_v

Γ_1	$V_c; \quad V_v; \quad k_z^2; \quad \{V_c - V_v, k_z^2\}; \quad \nabla \cdot \mathcal{E}_c; \quad \nabla \cdot \mathcal{E}_v$
Γ_3	$\frac{1}{\sqrt{3}}(2k_z^2 - k_x^2 - k_y^2), k_x^2 - k_y^2;$ $\frac{1}{\sqrt{3}}\{V_c - V_v, 2k_z^2 - k_x^2 - k_y^2\}, \{V_c - V_v, k_x^2 - k_y^2\};$ $\frac{1}{\sqrt{3}}[2\partial_z \mathcal{E}_c^c - \partial_x \mathcal{E}_c^c - \partial_y \mathcal{E}_c^c], \partial_x \mathcal{E}_c^c + \partial_y \mathcal{E}_c^c$
Γ_4	$B_x, B_y, B_z; \quad (V_c - V_v)B_x, (V_c - V_v)B_y, (V_c - V_v)B_z;$ $\mathcal{E}_z^c k_y - \mathcal{E}_y^c k_z, \mathcal{E}_x^c k_z - \mathcal{E}_z^c k_x, \mathcal{E}_y^c k_x - \mathcal{E}_x^c k_y;$ $\mathcal{E}_z^v k_y - \mathcal{E}_y^v k_z, \mathcal{E}_x^v k_z - \mathcal{E}_z^v k_x, \mathcal{E}_y^v k_x - \mathcal{E}_x^v k_y$
Γ_5	$\{k_y, k_z\}, \{k_z, k_x\}, \{k_x, k_y\};$ $\{V_c - V_v, k_y, k_z\}, \{V_c - V_v, k_z, k_x\}, \{V_c - V_v, k_x, k_y\};$ $\partial_y \mathcal{E}_z^c, \partial_z \mathcal{E}_x^c, \partial_x \mathcal{E}_y^c; \quad \partial_y \mathcal{E}_z^v, \partial_z \mathcal{E}_x^v, \partial_x \mathcal{E}_y^v$

6.3.2 Rashba Coefficient and Ehrenfest's Theorem

For many years, there has been an intense discussion in the literature concerning the Rashba prefactor $\langle r_{41}^{6c6c} \mathcal{E}_z \rangle$ [3, 35, 4, 31, 36, 37, 32, 22, 38, 39, 33, 40, 41, 42, 43, 44, 45, 46, 47, 48, 49, 8, 7]. Ando et al. [35] argued that Rashba spin splitting must be very small because, for a bound state, we have $\langle \mathcal{E}_z \rangle = 0$ (Ehrenfest's theorem: on average, there is no force acting on a bound state [62]).⁸ In fact, this controversy was resolved by Lassnig [37], who pointed out that Rashba spin splitting in the conduction band results from the electric field in the valence band.

Löwdin Partitioning. We can understand most easily why Rashba spin splitting of electrons is controlled by the field in the valence band by explicitly taking into account the position dependence of the band edges E_c and E_v in the simplified Kane Hamiltonian (5.11). It is convenient to define effective potentials and effective fields for the conduction and valence band

$$V_c(\mathbf{r}) = V(\mathbf{r}) + E_c(\mathbf{r}) - \langle E_c \rangle \quad \text{and} \quad \mathcal{E}_c = \frac{1}{e} \nabla V_c = \frac{1}{e} \nabla (V_c + E_c), \quad (6.25a)$$

$$V_v(\mathbf{r}) = V(\mathbf{r}) + E_v(\mathbf{r}) - \langle E_v \rangle \quad \text{and} \quad \mathcal{E}_v = \frac{1}{e} \nabla V_v = \frac{1}{e} \nabla (V_v + E_v). \quad (6.25b)$$

Here $\langle E_c \rangle$ and $\langle E_v \rangle$ denote the mean values of the position dependent conduction band and valence band edges, respectively, such that

$$E_0 = \langle E_c \rangle - \langle E_v \rangle \quad (6.25c)$$

is independent of \mathbf{r} . The relevant tensor operators are listed in Table 6.4.

⁸ Ehrenfest's theorem applies to nondegenerate states only. This is the reason why in (3.3) we have matrix elements of the Pauli SO coupling between p-like states, but not between s-like states.

We obtain, instead of (5.14), the following effective Schrödinger equation for the electron states in the conduction band:

$$\begin{aligned}
& \left\{ \frac{P^2}{3} \left[\frac{2}{E_0} + \frac{1}{E_0 + \Delta_0} \right] k^2 + V_c - \frac{P^2}{3} \left[\frac{1}{E_0} - \frac{1}{E_0 + \Delta_0} \right] \frac{e}{\hbar} \boldsymbol{\sigma} \cdot \mathbf{B} \right. \\
& + \frac{eP^2}{3} \left[\frac{1}{E_0^2} - \frac{1}{(E_0 + \Delta_0)^2} \right] \boldsymbol{\sigma} \cdot \mathbf{k} \times \boldsymbol{\mathcal{E}}_v - \frac{eP^2}{6} \left[\frac{2}{E_0^2} + \frac{1}{(E_0 + \Delta_0)^2} \right] \nabla \cdot \boldsymbol{\mathcal{E}}_v \\
& - \frac{P^2}{3} \left[\frac{2}{E_0^2} + \frac{1}{(E_0 + \Delta_0)^2} \right] \{V_c - V_v, k^2\} \\
& \left. + \frac{P^2}{3} \left[\frac{1}{E_0^2} - \frac{1}{(E_0 + \Delta_0)^2} \right] \frac{e}{\hbar} (V_c - V_v) \boldsymbol{\sigma} \cdot \mathbf{B} \right\} \tilde{\psi}_c = \tilde{E} \tilde{\psi}_c. \quad (6.26)
\end{aligned}$$

We see here that both the Rashba SO coupling and the Darwin term depend on the effective electric field $\boldsymbol{\mathcal{E}}_v = (1/e)\nabla V_v$ in the *valence band*. We obtain two additional terms in (6.26) that depend on the difference $V_c - V_v$ between the effective potentials in the conduction and valence bands. They have no equivalent in (5.14), and they yield corrections to the kinetic energy and the Zeeman term. We neglect these additional terms in the remaining discussion in this work. We note, however, that these terms were always taken into account in the numerical calculations presented in this work.

A similar analysis for the valence band states shows that the Rashba SO coupling depends only on the electric field in the conduction band. We remark that a similar analysis can also be performed for the Dirac equation. If we assume that we have different potentials for the particles and antiparticles, the Pauli SO coupling (1.1) and the Darwin term for the particles depend only on the potential for the antiparticles.

Discussion. What is the difference between the electric fields in the conduction and valence band? To illustrate this point, we show in the central part of Fig. 6.5 an electron wave function bound in a QW in the presence of an external (or built-in) field $\mathcal{E}_z^{\text{ext}} = (1/e)\partial_z V$. Within the EFA, the effective electric field \mathcal{E}_z^c in the conduction band (upper part of Fig. 6.5) is the sum of the electric field $\mathcal{E}_z^{\text{ext}}$ and the contributions due to the position dependence of the conduction band $E_c(z)$,

$$\mathcal{E}_z^c = (1/e)\partial_z(V + E_c) = \mathcal{E}_z^{\text{ext}} + (1/e)\partial_z E_c(z). \quad (6.27)$$

At the left interface, we have a large negative contribution of $(1/e)\partial_z E_c(z)$ to \mathcal{E}_z^c . This contribution is weighted with the large probability amplitude of the wave function at this interface, which cancels the remaining positive contributions to \mathcal{E}_z^c . Therefore, we indeed have

$$\langle \mathcal{E}_z^c \rangle = 0 \quad (\text{Ehrenfest's theorem}). \quad (6.28)$$

Of course, we have the same electric field $\mathcal{E}_z^{\text{ext}}$ acting in both the conduction and the valence band. However, the contributions from the interfaces to

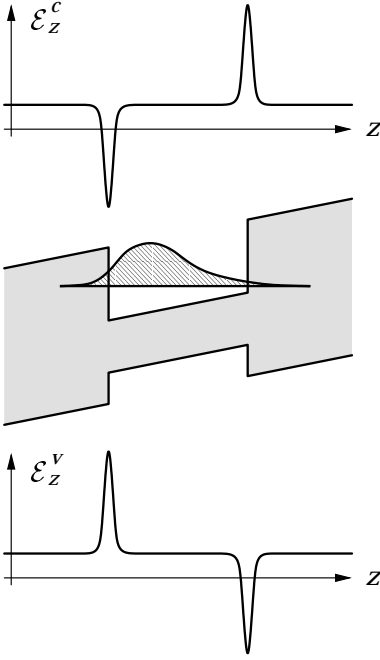


Fig. 6.5. Qualitative sketch of an electron wave function bound in a QW in the presence of an external field (*central part*). The *upper* and *lower part* show the effective electric fields \mathcal{E}_z^c and \mathcal{E}_z^v in the conduction and valence bands, respectively. While the expectation value of the wave function with respect to \mathcal{E}_z^c vanishes, i.e. $\langle \mathcal{E}_z^c \rangle = 0$ (Ehrenfest's theorem), it is indeed the electric field \mathcal{E}_z^v in the valence band that controls the Rashba spin splitting of electron states. Obviously, we have $\langle \mathcal{E}_z^v \rangle_c \neq 0$

$(1/e)\partial_z E_c(z)$ and $(1/e)\partial_z E_v(z)$ have opposite signs, compare the upper and lower parts of Fig. 6.5. Thus we have

$$\langle \mathcal{E}_z^v \rangle_c \neq 0, \quad (6.29)$$

where

$$\mathcal{E}_z^v = (1/e)\partial_z(V + E_v) = \mathcal{E}_z^{\text{ext}} + (1/e)\partial_z E_v(z). \quad (6.30)$$

In (6.29), the outer subscript c is used in order to emphasize that we evaluate the expectation value using the wave function in the conduction band.

We can readily estimate the strength of the electric field \mathcal{E}_z^v for a quasi-2D system in the presence of an external (or built-in) field $\mathcal{E}_z^{\text{ext}}$. It follows from (6.27) and (6.28) that we have

$$\langle \mathcal{E}_z^{\text{ext}} \rangle = -\langle (1/e)\partial_z E_c \rangle. \quad (6.31)$$

If the conduction and valence band offsets are Σ_c and Σ_v , respectively, we have

$$\langle (1/e)\partial_z E_v \rangle = -\frac{\Sigma_v}{\Sigma_c} \langle (1/e)\partial_z E_c \rangle = \frac{\Sigma_v}{\Sigma_c} \langle \mathcal{E}_z^{\text{ext}} \rangle. \quad (6.32)$$

Combining (6.30) and (6.32), we obtain

$$\langle \mathcal{E}_z^v \rangle_c = \langle \mathcal{E}_z^{\text{ext}} \rangle + \langle (1/e)\partial_z E_v \rangle = \frac{\Sigma_c + \Sigma_v}{\Sigma_c} \langle \mathcal{E}_z^{\text{ext}} \rangle. \quad (6.33)$$

Note that (6.26) and (6.33) imply that the SIA spin splitting is proportional to the external electric field $\mathcal{E}_z^{\text{ext}}$.

In a single heterostructure or MOS inversion layer, the electric field $\mathcal{E}_z^{\text{ext}}(z)$ due to a Hartree potential $V_H(z)$ is given by

$$\mathcal{E}_z^{\text{ext}}(z) = (1/e)\partial_z V_H(z) = \frac{e}{\epsilon\epsilon_0} \left[N_A(z_d - z) + N_s - \int_{-\infty}^z dz' \rho(z') \right], \quad (6.34)$$

where N_A is the acceptor concentration in the depletion layer, with depletion length z_d , and $\rho(z)$ is the 2D charge density [63]. By partial integration, we obtain [37]

$$\langle \mathcal{E}_z^{\text{ext}} \rangle = \frac{e}{\epsilon\epsilon_0} \left[N_A(z_d - \langle z \rangle) + \frac{N_s}{2} \right], \quad (6.35)$$

where the expectation values are evaluated using the charge density $\rho(z)$. Equations (6.33) and (6.35) are very convenient for estimating the electric field $\langle \mathcal{E}_z^v \rangle$ in quasi-2D systems.⁹

6.3.3 The Rashba Model for the Γ_8^v Valence Band

The Rashba model (6.9) for SIA spin splitting of 2D electron systems is well established in the literature. For 2D hole systems, on the other hand, the situation is more complicated because of the fourfold degeneracy of the topmost valence band Γ_8^v . Therefore, most often, hole spin splitting has been evaluated only numerically [65, 66, 67, 68, 69, 70, 71]. In the following, we show that the Rashba spin splitting of hole states is very different from the spin splitting of electron states [7].

Symmetry Analysis of Rashba Spin Splitting of Hole Systems.

By inspection of Tables C.3 and C.4, we see that for a Γ_8 band we have two sets of matrices which transform like an axial vector (representation Γ_4 of T_d), namely $\mathbf{J} = (J_x, J_y, J_z)$ and $\mathcal{J} = (J_x^3, J_y^3, J_z^3)$. These matrices can be combined with the axial vector $\mathbf{k} \times \mathcal{E}$. We can construct a third invariant from the symmetrized product of \mathbf{k} and \mathcal{E} , transforming according to Γ_5 , and the third-order product of the angular-momentum matrices \mathbf{J} , which is odd with respect to time-reversal symmetry. Finally, we can obtain an invariant proportional to \mathcal{E} , but independent of the wave vector \mathbf{k} , by combining the components of \mathcal{E} with the symmetrized products of the components of \mathbf{J} . The invariants for $\mathcal{H}_{8v\ 8v}^r$, together with those for $\mathcal{H}_{7v\ 7v}^r$ and $\mathcal{H}_{8v\ 7v}^r$, are listed in Table 6.5.¹⁰ Corresponding to these invariants, the numerical values of the Rashba coefficients for various semiconductors are listed in Table 6.6.

⁹ Combined with the well-known analytical solution for the triangular-potential approximation [63], (6.35) can be used also to obtain a simple *self-consistent* estimate of the subband structure and $\langle \mathcal{E}_z^{\text{ext}} \rangle$ in a single heterostructure [64].

¹⁰ We obtain similar expressions for the off-diagonal block \mathcal{H}_{6c8v} . However, they contribute to SIA spin splitting in higher order, so we neglect them here.

Table 6.5. Invariants for the Kane model which give rise to SIA spin splitting

$$\begin{aligned} \mathcal{H}_{6c\ 6c}^r &= r_{41}^{6c6c} [(k_y \mathcal{E}_z - k_z \mathcal{E}_y) \sigma_x + \text{cp}] \\ \mathcal{H}_{8v\ 8v}^r &= r_{41}^{8v8v} [(k_y \mathcal{E}_z - k_z \mathcal{E}_y) J_x + \text{cp}] + r_{42}^{8v8v} [(k_y \mathcal{E}_z - k_z \mathcal{E}_y) J_x^3 + \text{cp}] \\ &\quad + r_{51}^{8v8v} [\mathcal{E}_x \{J_y, J_z\} + \text{cp}] + r_{52}^{8v8v} [(k_y \mathcal{E}_z + k_z \mathcal{E}_y) \{J_x, J_y^2 - J_z^2\} + \text{cp}] \\ \mathcal{H}_{7v\ 7v}^r &= r_{41}^{7v7v} [(k_y \mathcal{E}_z - k_z \mathcal{E}_y) \sigma_x + \text{cp}] \\ \mathcal{H}_{8v\ 7v}^r &= r_{31}^{8v7v} [(k_x \mathcal{E}_x - k_y \mathcal{E}_y)(U_{xx} - U_{yy}) + (2k_z \mathcal{E}_z - k_x \mathcal{E}_x - k_y \mathcal{E}_y) U_{zz}] \\ &\quad + r_{41}^{8v7v} [(k_y \mathcal{E}_z - k_z \mathcal{E}_y) U_x + \text{cp}] \\ &\quad + r_{51}^{8v7v} [\mathcal{E}_x U_{yz} + \text{cp}] + r_{52}^{8v7v} [(k_y \mathcal{E}_z + k_z \mathcal{E}_y) U_{yz} + \text{cp}] \end{aligned}$$

Table 6.6. Rashba coefficients calculated according to (6.22) and (6.40) for the invariants in Table 6.5, evaluated for various semiconductors (all in $\text{e}\text{\AA}^2$, except for r_{51}^{8v8v} and r_{51}^{8v7v} , which are in $\text{e}\text{\AA}$)

	GaAs	AlAs	InAs	InSb	CdTe	ZnSe
r_{41}^{6c6c}	5.206	-0.243	117.1	523.0	6.930	1.057
r_{41}^{8v8v}	-14.62	-1.501	-159.9	-548.5	-10.79	-4.099
r_{42}^{8v8v}	-0.106	-0.0906	-0.162	-0.530	-0.0836	-0.0193
r_{51}^{8v8v}	0.00418			0.0362		
r_{52}^{8v8v}	-0.00005			-0.0013		
r_{41}^{7v7v}	-9.720	-1.387	-43.35	-27.07	-4.124	-3.097
r_{31}^{8v7v}	-3.87 i	-0.255 i	-87.7 i	-392.0 i	-5.16 i	-0.788 i
r_{41}^{8v7v}	-18.45	-2.336	-152.7	-432.6	-11.34	-5.433
r_{51}^{8v7v}	-0.00807			-0.0967		
r_{52}^{8v7v}	-8.15 i	-0.864 i	-175.9 i	-785.9 i	-10.84 i	-1.753 i

Similarly to the Rashba model for the conduction band Γ_6^c , the first term in $\mathcal{H}_{8v\ 8v}^r$ has axial symmetry, with the symmetry axis being the direction of the electric field \mathcal{E} . The second and fourth terms are anisotropic, i.e. they depend on the crystallographic orientations of both \mathcal{E} and \mathbf{k} . Thus it follows, without explicitly evaluating the perturbation theory, that the prefactors r_{42}^{8v8v} and r_{52}^{8v8v} are always much smaller than r_{41}^{8v8v} . This is due to the fact that the $\mathbf{k} \cdot \mathbf{p}$ coupling between Γ_8^v and Γ_6^c is isotropic, so that it can contribute to r_{41}^{8v8v} but not to r_{42}^{8v8v} or r_{52}^{8v8v} . The latter prefactors stem from $\mathbf{k} \cdot \mathbf{p}$ coupling to more remote bands, such as the higher conduction bands Γ_8^c and Γ_7^c of the extended Kane model.

For the conduction band Γ_6^c , the Rashba Hamiltonian (6.9) is the lowest-order invariant proportional to the electric field. It is linear in the wave vector \mathbf{k} . It is remarkable that, in the valence band, we have two invariants, proportional to r_{51}^{8v8v} and r_{51}^{8v7v} , that are independent of the wave vector \mathbf{k} . These invariants have the same functional form as the so-called interface terms to

be discussed in Sect. 6.5, so the discussion of r_{51}^{8v8v} and r_{51}^{8v7v} is postponed to that section.

General Features of the Rashba Model for the Valence Band Γ_8^v . For $\mathcal{E} = (0, 0, \mathcal{E}_z)$, we obtain using an explicit matrix notation,

$$\begin{aligned} \mathcal{H}_{8v8v}^r = & r_{41}^{8v8v} \mathcal{E}_z \begin{pmatrix} 0 & \frac{i\sqrt{3}}{2} k_- & 0 & 0 \\ -\frac{i\sqrt{3}}{2} k_+ & 0 & ik_- & 0 \\ 0 & -ik_+ & 0 & \frac{i\sqrt{3}}{2} k_- \\ 0 & 0 & -\frac{i\sqrt{3}}{2} k_+ & 0 \end{pmatrix} \\ & + r_{42}^{8v8v} \mathcal{E}_z \begin{pmatrix} 0 & \frac{7i\sqrt{3}}{8} k_- & 0 & -\frac{3i}{4} k_+ \\ -\frac{7i\sqrt{3}}{8} k_+ & 0 & \frac{5i}{2} k_- & 0 \\ 0 & -\frac{5i}{2} k_+ & 0 & \frac{7i\sqrt{3}}{8} k_- \\ \frac{3i}{4} k_- & 0 & -\frac{7i\sqrt{3}}{8} k_+ & 0 \end{pmatrix} \\ & + r_{52}^{8v8v} \mathcal{E}_z \begin{pmatrix} 0 & -\frac{i\sqrt{3}}{4} k_- & 0 & \frac{3i}{4} k_+ \\ \frac{i\sqrt{3}}{4} k_+ & 0 & \frac{3i}{4} k_- & 0 \\ 0 & -\frac{3i}{4} k_+ & 0 & -\frac{i\sqrt{3}}{4} k_- \\ -\frac{3i}{4} k_- & 0 & \frac{i\sqrt{3}}{4} k_+ & 0 \end{pmatrix}. \end{aligned} \quad (6.36)$$

Here the first term couples the two LH states ($m = \pm 1/2$) and the HH states ($m = \pm 3/2$) to the LH states. But there is no k -linear splitting of the HH states proportional to the dominant coefficient r_{41}^{8v8v} . Only the second and third matrices, with the small prefactors r_{42}^{8v8v} and r_{52}^{8v8v} , contain a k -linear coupling of the HH states. Assuming $r_{42}^{8v8v} = r_{52}^{8v8v} = 0$, we obtain the following for the HH spin splitting to lowest order in \mathbf{k}_{\parallel} :

$$E_{\text{HH}}^r(\mathbf{k}_{\parallel}) \propto \pm \langle r_{41}^{8v8v} \mathcal{E}_z \rangle k_{\parallel}^3. \quad (6.37a)$$

In particular, we have no k -linear splitting (and $r_{42}^{8v8v} = r_{52}^{8v8v} \equiv 0$) if we restrict ourselves to the Luttinger Hamiltonian [72], which includes Γ_8^c and Γ_7^c by means of second-order perturbation theory. Accurate numerical computations show that the dominant part of the k -linear splitting of the HH states is due to BIA. However, for typical densities and typical values of \mathcal{E}_z , this k -linear splitting is rather small (see Fig. 6.6). For the LH states, we have, to lowest order in \mathbf{k}_{\parallel} ,

$$E_{\text{LH}}^r(\mathbf{k}_{\parallel}) \propto \pm \langle r_{41}^{8v8v} \mathcal{E}_z \rangle k_{\parallel}. \quad (6.37b)$$

But even in this case it turns out that the cubic splitting often dominates over the linear term (6.37b). Thus we have a qualitative difference between the spin splitting of electrons (and LH states), which is proportional to k_{\parallel} , and the splitting of HH states, which is essentially proportional to k_{\parallel}^3 . A linear

splitting is most important in the low-density regime, whereas a splitting proportional to k_{\parallel}^3 becomes negligible for small densities. Note that for 2D hole systems the first subband is usually HH-like so that the SIA spin splitting is given by (6.37a) for low densities.

The cubic splitting of holes reflects the general fact that hole states (valence band Γ_8^v) have an angular momentum $j = 3/2$. In this case subband quantization (which is usually the dominant effect) results in HH–LH splitting, where HH states have a z component of angular momentum $m = \pm 3/2$, while LH states have $m = \pm 1/2$, with the z axis pointing in the growth direction; see Sect. 4.5.3. Therefore, subband quantization and HH–LH splitting imply that we have a predefined quantization axis for angular momentum independent of any $B = 0$ spin splitting. Similarly to the case of electrons (see Sect. 6.6.1 and Fig. 6.2), the spin quantization axis implied by the first term in (6.36) is an in-plane vector. But it is not possible to have an in-plane quantization axis for angular momentum on top of the perpendicular quantization axis due to HH–LH splitting; see Sect. 4.5.3. Therefore, Rashba spin splitting of HH states is essentially a higher-order effect. On the other hand, the small but nonzero k -linear spin splitting of HH states is due to the fact that angular momentum is merely an “almost good” quantum number; see Sect. 3.6. A more detailed discussion of the prefactors in (6.37) will be given later in this section.

From (6.37a), we obtain an HH subband dispersion $E_{\pm}(\mathbf{k}_{\parallel}) = \langle \mu_h \rangle k_{\parallel}^2 \pm \beta k_{\parallel}^3$, where μ_h (times $2/\hbar^2$) is the reciprocal effective mass and β is the effective Rashba coefficient for the cubic splitting. This dispersion implies that the densities N_{\pm} in the spin-split subbands are given by

$$N_{\pm} = \frac{N_s}{2} \mp \frac{\beta N_s}{\sqrt{2} \langle \mu_h \rangle X} \sqrt{\pi N_s (6 - 4/X)}, \quad (6.38a)$$

where

$$X = 1 + \sqrt{1 - 4\pi N_s \left(\frac{\beta}{\langle \mu_h \rangle} \right)^2}. \quad (6.38b)$$

The spin-split densities according to (6.38) are substantially different from (6.18) for a linear splitting. For electrons and a fixed electric field \mathcal{E}_z but a varying N_s the difference $\Delta N = |N_+ - N_-|$ increases like $N_s^{1/2}$, whereas for HH subbands it increases like $N_s^{3/2}$ (see also (6.51) and (6.54)). Using a fixed density N_s but a varying \mathcal{E}_z , it is more difficult to detect the difference between (6.18) and (6.38). In both cases a power expansion of ΔN gives $\Delta N = a_1 |\mathcal{E}_z| + a_3 |\mathcal{E}_z|^3 + \mathcal{O}(|\mathcal{E}_z|^5)$, where $a_3 < 0$ for electrons and $a_3 > 0$ for HH subbands.

Solving (6.38) for the Rashba coefficient β , we obtain

$$\beta = \sqrt{\frac{2}{\pi}} \langle \mu_h \rangle \frac{N_s (\tilde{N}_+ - \tilde{N}_-) + \Delta N (\tilde{N}_+ + \tilde{N}_-)}{6 N_s^2 + 2 \Delta N^2}, \quad (6.39)$$

where $\tilde{N}_\pm = \sqrt{N \pm \Delta N}$. This result should be compared with (6.19) for a linear splitting.

Löwdin Partitioning for the Quasi-Bulk Hamiltonian. Once again, we can use Löwdin partitioning to evaluate the Rashba coefficients in Table 6.5. For the quasi-bulk Hamiltonian, we obtain, in lowest order,

$$r_{41}^{8v8v} = -\frac{eP^2}{3E_0^2} + \frac{eQ^2}{9} \left[\frac{10}{E_0'^2} - \frac{7}{(E_0' + \Delta_0')^2} \right], \quad (6.40a)$$

$$r_{42}^{8v8v} = -\frac{4eQ^2}{9} \left[\frac{1}{E_0'^2} - \frac{1}{(E_0' + \Delta_0')^2} \right], \quad (6.40b)$$

$$r_{51}^{8v8v} = \frac{2i}{9} \frac{eQ\Delta^-}{(E_0' + \Delta_0')^2}, \quad (6.40c)$$

$$r_{52}^{8v8v} = \frac{2\sqrt{3}i}{9} \frac{eQ\Delta^- C_k}{(E_0' + \Delta_0')^3}, \quad (6.40d)$$

$$r_{41}^{7v7v} = -\frac{e}{3} \left[\frac{P^2}{(E_0 + \Delta_0)^2} - \frac{Q^2}{(\Delta_0 + E_0' + \Delta_0')^2} \right], \quad (6.40e)$$

$$r_{31}^{8v7v} = -\frac{ieP^2}{4} \left[\frac{1}{E_0^2} - \frac{1}{(E_0 + \Delta_0)^2} \right] + \frac{ieQ^2}{4} \left[\frac{1}{(E_0' + \Delta_0')^2} - \frac{1}{(\Delta_0 + E_0 + \Delta_0')^2} \right], \quad (6.40f)$$

$$r_{41}^{8v7v} = -\frac{eP^2}{4} \left[\frac{1}{E_0^2} + \frac{1}{(E_0 + \Delta_0)^2} \right] + \frac{eQ^2}{4} \left[\frac{1}{(E_0' + \Delta_0')^2} + \frac{1}{(\Delta_0 + E_0 + \Delta_0')^2} \right], \quad (6.40g)$$

$$r_{51}^{8v7v} = \frac{ieQ\Delta^-}{3} \left[\frac{1}{(\Delta_0 + E_0' + \Delta_0')^2} - \frac{2}{E_0'^2} \right], \quad (6.40h)$$

$$r_{52}^{8v7v} = -\frac{ieP^2}{2} \left[\frac{1}{E_0^2} - \frac{1}{(E_0 + \Delta_0)^2} \right] - \frac{ieQ^2}{2} \left[\frac{1}{(E_0' + \Delta_0')^2} - \frac{1}{(\Delta_0 + E_0 + \Delta_0')^2} \right]. \quad (6.40i)$$

These formulas have been evaluated in Table 6.6 for various semiconductors. Similarly to BIA spin splitting, we obtain the largest numerical values for those coefficients (r_{41}^{8v8v} , r_{41}^{7v7v} , and r_{41}^{8v7v}) which are nonzero even if the SO gaps of the bulk bands, Δ_0 , Δ_0' , and Δ^- , are set to zero. But we obtain SIA spin splitting only because of the nonzero matrix elements Δ_0 , Δ_0' , and Δ^- (and also C_k) of the SO interaction; see Sect. 6.1.

The formulas in (6.40) have been obtained by means of third-order perturbation theory, except for the coefficient r_{52}^{8v8v} , which requires fourth-order

perturbation theory. We can see in Table 6.6 that r_{52}^{8v8v} is several orders of magnitude smaller than all the other coefficients, so that often this term can be neglected. Our expressions for the coefficients r_{51}^{8v8v} , r_{52}^{8v8v} , and r_{51}^{8v7v} vanish for systems with a diamond structure. While the invariants weighted by r_{51}^{8v8v} and r_{51}^{8v7v} are due to the combined effect of BIA and SIA, the invariant weighted by r_{52}^{8v8v} would be symmetry-allowed even in a system with a diamond structure.

Rashba Spin Splitting of HH and LH States. Quantum confinement in a quasi-2D system (or strain applied to a bulk crystal) gives rise to a finite gap between HH and LH states. This HH–LH splitting corresponds to a quantization of angular momentum $j = 3/2$ perpendicular to the plane of the 2D system, with a z component of angular momentum $m = \pm 3/2$ for the HH states and $m = \pm 1/2$ for the LH states. The point group of the system is reduced from T_d to a subgroup of T_d that depends on the crystallographic orientation of the quantization axis. In the following we shall focus on 2D systems grown in the direction [001], so that the point group becomes D_{2d} (see Table 3.4). We remark that we obtain similar results for other growth directions.

The theory of invariants provides a natural language to describe the HH–LH splitting and the accompanying phenomena in quasi-2D systems. The 2×2 subspaces of LH states and electron states transform according to the double-group representation Γ_6 of D_{2d} , whereas the HH states transform according to Γ_7 . The symmetrized basis matrices for these bands are listed in Table 6.7. In Table 6.8, we have listed the irreducible tensor components for the point group D_{2d} . Finally, we give in Table 6.9 the invariants that characterize SIA spin splitting. Note that the invariants proportional to r_{51}^{6c6c} , r_{52}^{6c6c} , r_{53}^{6c6c} , r_{54}^{7h7h} , r_{51}^{6l6l} , r_{52}^{6l6l} , and r_{53}^{6l6l} have axial symmetry; see (3.10). As usual, we can match the results of Löwdin perturbation theory against the invariants in Table 6.9. However, it turns out that the results for the expansion coefficients depend qualitatively on the model for the bulk $\mathbf{k} \cdot \mathbf{p}$ Hamiltonian.

Rashba Coefficients of 2D Holes in the Extended Kane Model. Starting from the extended Kane Hamiltonian, we obtain the following in fifth-order perturbation theory for the coefficients of the HH and LH states listed in Table 6.9:

$$r_{51}^{7h7h} = \frac{eQ^2}{3} \left(\frac{1}{\Delta_{hL}^2} - \frac{1}{\Delta_{hS}^2} \right), \quad (6.41a)$$

$$r_{52}^{7h7h} = 0, \quad (6.41b)$$

$$r_{53}^{7h7h} = \frac{eP^2Q^2}{6\Delta_{hc}} \left(\frac{1}{\Delta_{hs}^2\Delta_{hL}} - \frac{1}{\Delta_{hl}^2\Delta_{hS}} \right) + \frac{eQ^4}{6} \left(\frac{1}{\Delta_{hs}^2\Delta_{hL}^2} - \frac{1}{\Delta_{hl}^2\Delta_{hS}^2} \right), \quad (6.41c)$$

Table 6.7. Symmetrized matrices for the matrix expansion of the blocks $\mathcal{H}_{\alpha\beta}$ for the point group D_{2d}

Block	Representations	Symmetrized matrices
\mathcal{H}_{66}	$\Gamma_6 \times \Gamma_6^*$	$\Gamma_1 : \mathbb{1}_{2 \times 2}$
	$= \Gamma_1 + \Gamma_2 + \Gamma_5$	$\Gamma_2 : \sigma_z$
		$\Gamma_5 : \sigma_x, -\sigma_y$
\mathcal{H}_{77}	$\Gamma_7 \times \Gamma_7^*$	$\Gamma_1 : \mathbb{1}_{2 \times 2}$
	$= \Gamma_1 + \Gamma_2 + \Gamma_5$	$\Gamma_2 : \sigma_z$
		$\Gamma_5 : \sigma_x, \sigma_y$

Table 6.8. Irreducible tensor components for the point group D_{2d}

Γ_1	$1; \quad k_x^2 + k_y^2; \quad k_z^2; \quad \mathcal{E}_z \{k_x, k_y\}$
Γ_2	$\{k_x^2 - k_y^2, k_z^2\}; \quad \mathcal{E}_z \{k_x + k_y, k_x - k_y\}$
Γ_4	$k_z; \quad \mathcal{E}_z$
Γ_5	$k_x, k_y; \quad \{k_z^2, k_x\}, \{k_z^2, k_y\}; \quad \{k_y^2, k_x\}, \{k_x^2, k_y\}; \quad k_x^3, k_y^3;$ $\mathcal{E}_z k_y, \mathcal{E}_z k_x; \quad \mathcal{E}_z \{k_z^2, k_y\}, \mathcal{E}_z \{k_z^2, k_x\};$ $\mathcal{E}_z \{k_y^2 + k_x^2, k_y\}, \mathcal{E}_z \{k_x^2 + k_y^2, k_x\}; \quad \mathcal{E}_z \{k_y^2 - 3k_x^2, k_y\}, \mathcal{E}_z \{k_x^2 - 3k_y^2, k_x\}$

Table 6.9. Invariants for the point group D_{2d} which give rise to SIA spin splitting

$\mathcal{H}_{6c\ 6c}^r =$	$r_{51}^{6c6c\ i} (k_- \sigma_+ - k_+ \sigma_-) \mathcal{E}_z + r_{52}^{6c6c\ i} (\{k_z^2, k_- \} \sigma_+ - \{k_z^2, k_+ \} \sigma_-) \mathcal{E}_z$ $+ r_{53}^{6c6c\ i} (\{k_+, k_-^2 \} \sigma_+ - \{k_+^2, k_- \} \sigma_-) \mathcal{E}_z + r_{54}^{6c6c\ i} (k_+^3 \sigma_+ - k_-^3 \sigma_-) \mathcal{E}_z$
$\mathcal{H}_{7h\ 7h}^r =$	$r_{51}^{7h7h\ i} (k_- \sigma_- - k_+ \sigma_+) \mathcal{E}_z + r_{52}^{7h7h\ i} (\{k_z^2, k_- \} \sigma_- - \{k_z^2, k_+ \} \sigma_+) \mathcal{E}_z$ $+ r_{53}^{7h7h\ i} (\{k_+, k_-^2 \} \sigma_- - \{k_+^2, k_- \} \sigma_+) \mathcal{E}_z + r_{54}^{7h7h\ i} (k_+^3 \sigma_- - k_-^3 \sigma_+) \mathcal{E}_z$
$\mathcal{H}_{6l\ 6l}^r =$	$r_{51}^{6l6l\ i} (k_- \sigma_+ - k_+ \sigma_-) \mathcal{E}_z + r_{52}^{6l6l\ i} (\{k_z^2, k_- \} \sigma_+ - \{k_z^2, k_+ \} \sigma_-) \mathcal{E}_z$ $+ r_{53}^{6l6l\ i} (\{k_+, k_-^2 \} \sigma_+ - \{k_+^2, k_- \} \sigma_-) \mathcal{E}_z + r_{54}^{6l6l\ i} (k_+^3 \sigma_+ - k_-^3 \sigma_-) \mathcal{E}_z$

$$r_{54}^{7h7h} = \frac{eP^4}{6\Delta_{hc}^2} \left(\frac{1}{\Delta_{hl}^2} - \frac{1}{\Delta_{hs}^2} \right) + \frac{eP^2Q^2}{6\Delta_{hc}} \left(\frac{1}{\Delta_{hl}^2\Delta_{hs}} - \frac{1}{\Delta_{hs}^2\Delta_{hl}} \right), \quad (6.41d)$$

$$r_{51}^{6l6l} = \frac{e}{3} \left(\frac{Q^2}{\Delta_{lh}^2} - \frac{P^2}{\Delta_{lc}^2} \right), \quad (6.41e)$$

$$r_{52}^{6l6l} = -\frac{eP^4}{3\Delta_{ls}^2\Delta_{lc}^2} + \frac{eQ^4}{3\Delta_{ls}^2\Delta_{lh}^2}, \quad (6.41f)$$

$$r_{53}^{6l6l} = -\frac{eP^4}{6\Delta_{lc}^2} \left(\frac{1}{\Delta_{lh}^2} + \frac{1}{\Delta_{ls}^2} \right) - \frac{eP^2Q^2}{6\Delta_{lh}^2\Delta_{lc}\Delta_{ls}} + \frac{eQ^4}{6\Delta_{ls}^2\Delta_{lh}^2}, \quad (6.41g)$$

$$r_{54}^{6l6l} = \frac{eQ^2}{6\Delta_{lh}^2\Delta_{ls}} \left(\frac{P^2}{\Delta_{lc}} + \frac{Q^2}{\Delta_{ls}} \right), \quad (6.41h)$$

where we have omitted those terms that contain the fundamental gap more than twice. We can clearly see that the SIA spin splitting of HH states is mediated by the $\mathbf{k} \cdot \mathbf{p}$ coupling to the LH (and split-off) states, as for each term of the dominant coefficient r_{54}^{7h7h} two of the energy denominators are Δ_{hl} or Δ_{hs} .

Rashba Coefficients of 2D Holes in the Luttinger Model. Frequently, subband calculations for 2D hole systems are based on the simpler 4×4 or 6×6 Luttinger Hamiltonian (see Sect. 3.5) instead of the more complete extended Kane model [65, 73, 66]. Even though the Luttinger Hamiltonian is able to describe many important features of 2D hole systems, it is known that substantial differences can occur between calculations based on \mathcal{H}_{8v8v} and on the Kane model [69]. Therefore we shall investigate the question of to what extent the Luttinger Hamiltonian can describe SIA spin splitting of 2D hole systems. We obtain the following for the Rashba coefficients in third-order perturbation theory:

$$r_{51}^{7h7h} = 0, \quad (6.42a)$$

$$r_{52}^{7h7h} = 0, \quad (6.42b)$$

$$r_{53}^{7h7h} = \frac{3}{4} \frac{e\hbar^4}{m_0^2} \gamma_3 (\gamma_2 - \gamma_3) \left(\frac{1}{\Delta_{hl}^2} - \frac{1}{\Delta_{hs}^2} \right), \quad (6.42c)$$

$$r_{54}^{7h7h} = \frac{3}{4} \frac{e\hbar^4}{m_0^2} \gamma_3 (\gamma_2 + \gamma_3) \left(\frac{1}{\Delta_{hl}^2} - \frac{1}{\Delta_{hs}^2} \right), \quad (6.42d)$$

$$r_{51}^{6l6l} = 0, \quad (6.42e)$$

$$r_{52}^{6l6l} = -3 \frac{e\hbar^4}{m_0^2} \frac{\gamma_2 \gamma_3}{\Delta_{ls}^2}, \quad (6.42f)$$

$$r_{53}^{6l6l} = \frac{3}{2} \frac{e\hbar^4}{m_0^2} \gamma_3 \left[\left(\frac{1}{2\Delta_{lh}^2} + \frac{1}{\Delta_{ls}^2} \right) \gamma_2 + \frac{\gamma_3}{2\Delta_{lh}^2} \right], \quad (6.42g)$$

$$r_{54}^{6l6l} = -\frac{3}{4} \frac{e\hbar^4}{m_0^2} \frac{\gamma_3 (\gamma_2 - \gamma_3)}{\Delta_{lh}^2}. \quad (6.42h)$$

In r_{51}^{7h7h} and r_{51}^{6l6l} , we have neglected some very small k -linear terms due to the combined effect of BIA and SIA, which are proportional to C_k^2 . These terms exist for both HH and LH states. Note that the Luttinger parameters γ_2 and γ_3 do not distinguish between H , L , and S (see Table C.9). If we subsume under E'_0 the energy gaps between h and l states on the one hand and H , L , and S states on the other hand then the coefficients (6.41) derived from the extended Kane Hamiltonian are exactly equal to those in (6.42) derived from the 6×6 Luttinger Hamiltonian. While we have $r_{51}^{6l6l} = 0$, the invariant weighted by r_{52}^{6l6l} gives rise to a k -linear spin splitting of the LH states because k_z is quantized. However, it is remarkable that, even for the LH states, there is no SIA spin splitting linear in k (i.e. $r_{52}^{6l6l} = 0$) if we

work with a 4×4 Luttinger Hamiltonian that does not take into account the split-off band Γ_7^v .

Subband-Dependent Rashba Coefficients of 2D Holes in the Luttinger Model. A more detailed understanding of SIA spin splitting of hole states requires that we explicitly take into account the subband states. In lowest-order perturbation theory, we obtain the following for the Rashba spin splitting of the HH states in a QW grown in the [001] direction:

$$r_{51}^{7h7h} = 0, \quad (6.43a)$$

$$r_{52}^{7h7h} = 0, \quad (6.43b)$$

$$r_{53}^{7h7h} = \frac{e\hbar^4}{m_0^2} \gamma_3 (\gamma_2 - \gamma_3) D_\alpha^h, \quad (6.43c)$$

$$r_{54}^{7h7h} = \frac{e\hbar^4}{m_0^2} \gamma_3 (\gamma_2 + \gamma_3) D_\alpha^h, \quad (6.43d)$$

where

$$D_\alpha^h = \frac{3i}{4} \sum_{\beta \neq \alpha} \left[\frac{\langle h_\alpha | z | h_\beta \rangle \langle l_\beta | \mathbf{k}_z | h_\alpha \rangle - \langle h_\alpha | \mathbf{k}_z | l_\beta \rangle \langle h_\beta | z | h_\alpha \rangle}{\Delta_{\alpha\beta}^{hh} \Delta_{\alpha\beta}^{hl}} \right. \\ - \frac{\langle h_\alpha | z | h_\beta \rangle \langle h_\beta | \mathbf{k}_z | l_\alpha \rangle - \langle l_\alpha | \mathbf{k}_z | h_\beta \rangle \langle h_\beta | z | h_\alpha \rangle}{\Delta_{\alpha\beta}^{hh} \Delta_{\alpha\alpha}^{hl}} \\ \left. + \frac{\langle l_\alpha | z | l_\beta \rangle \langle l_\beta | \mathbf{k}_z | h_\alpha \rangle - \langle h_\alpha | \mathbf{k}_z | l_\beta \rangle \langle l_\beta | z | h_\alpha \rangle}{\Delta_{\alpha\alpha}^{hl} \Delta_{\alpha\beta}^{hl}} \right], \quad (6.43e)$$

and we have assumed that $\langle h_\alpha | l_\beta \rangle = \delta_{\alpha\beta}$. For the lowest HH subband ($\alpha = 1$), we obtain

$$D_1^h = -\frac{3a}{4} \left[\frac{1}{\Delta_{12}^{hh} \Delta_{12}^{hl}} - \frac{1}{\Delta_{12}^{hh} \Delta_{11}^{hl}} + \frac{1}{\Delta_{11}^{hl} \Delta_{12}^{hl}} \right], \quad (6.44)$$

where $a = 1$ for a parabolic QW and $a = 256/(27\pi^2) \approx 0.96$ for an infinitely deep rectangular well. More explicitly, we have

$$D_1^h = \begin{cases} -\frac{m_0^2}{\hbar^4} \frac{256w^4}{9\pi^2 (\gamma_1 + 2\gamma_2) (3\gamma_1 - 10\gamma_2)} & \text{rectangular QW} \\ -\frac{m_0^2}{\hbar^4} \frac{6w^4}{(\gamma_1 + 2\gamma_2) (\gamma_1 - 4\gamma_2)} & \text{parabolic QW} \end{cases}, \quad (6.45)$$

where w denotes the width of the QW.

For LH subbands, we obtain

$$r_{51}^{6l6l} = 0, \quad (6.46a)$$

$$r_{52}^{6l6l} = 0, \quad (6.46b)$$

$$r_{53}^{6l6l} = \frac{e\hbar^4}{m_0^2} \gamma_3 (\gamma_2 + \gamma_3) D_\alpha^l, \quad (6.46c)$$

$$r_{54}^{6l6l} = \frac{e\hbar^4}{m_0^2} \gamma_3 (\gamma_2 - \gamma_3) D_\alpha^l, \quad (6.46d)$$

where D_α^l has the same structure as D_α^h in (6.43e) with the HH and LH indices interchanged.

In (6.43) and (6.46), we have assumed that the crystallographic growth direction is the high-symmetry direction [001]. For low-symmetry growth directions such as [113], there is a weak, anisotropic k -linear spin splitting of the HH states proportional to the small quantity $\delta = \gamma_3 - \gamma_2$ (irrespective of whether the split-off valence band Γ_7^v is taken into account or not). The LH states then have a larger k -linear spin splitting.

Example: SIA Spin Splitting in a GaAs–Al_{0.5}Ga_{0.5}As Heterostructure. As an example, we show in Fig. 6.6 the self-consistently calculated [60] anisotropic dispersion $E_\pm(\mathbf{k}_\parallel)$, DOS effective mass m^*/m_0 , and spin splitting $E_+(\mathbf{k}_\parallel) - E_-(\mathbf{k}_\parallel)$ of the topmost HH subband of a GaAs–Al_{0.5}Ga_{0.5}As heterostructure. The calculation shown in Fig. 6.6a was based on the 14×14 extended Kane Hamiltonian (3.2). It took both SIA and BIA fully into account. For comparison, we have used in Fig. 6.6b the 4×4 Luttinger Hamiltonian, which takes into account BIA spin splitting only via the k_\parallel -linear terms proportional to C_k . The weakly divergent van Hove singularity of the DOS effective mass at the subband edge indicates that, basically, the spin splitting is proportional to k_\parallel^3 , and the k_\parallel linear terms are rather small. This is clearly visible also in the upper right parts of Figs. 6.6a,b, where we show the spin splitting. As we observe essentially the same van Hove singularity in Fig. 6.6a and Fig. 6.6b, the dominant part of the k_\parallel -linear splitting must be due to BIA (i.e. C_k). This was confirmed by numerical calculations based on $\mathbf{k} \cdot \mathbf{p}$ models that take into account SIA but not BIA.

In the upper, right parts of Figs. 6.6a,b, the dotted lines show the spin splitting of the first LH subband. In Fig. 6.6a, the splitting for small k_\parallel is a linear function of k_\parallel , but for larger k_\parallel it is dominated by terms of higher order in k_\parallel owing to both HH–LH mixing and nonparabolicity. On the other hand, for the calculation shown in Fig. 6.6b, which was based on the Luttinger Hamiltonian, we obtain an LH splitting proportional to k_\parallel^3 .

Only for the crystallographic growth directions [001] and [111] are the hole subband states at $k_\parallel = 0$ pure HH and LH states. For low-symmetry growth directions such as [113] and [110], we have mixed HH–LH eigenstates even at $k_\parallel = 0$, though often the eigenstates can be labeled by their dominant spinor components (see Sect. 4.5.3).¹¹ The HH–LH mixing adds a k -linear

¹¹ In experiments with 2D hole systems, the low-symmetry growth direction [113] has recently been preferred over the the high-symmetry direction [001] because of the higher sample mobility that can be achieved with [113]-grown samples [74,75].

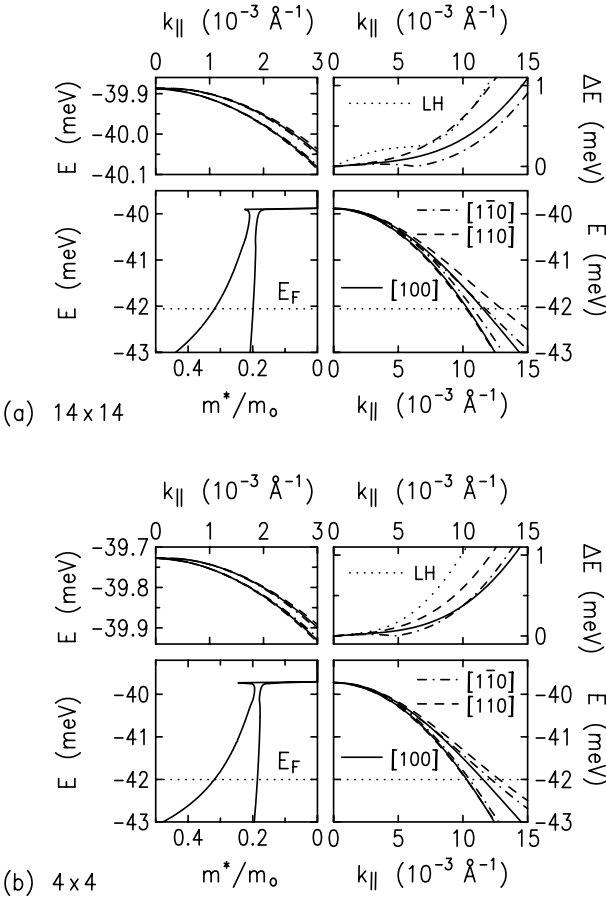


Fig. 6.6. Growth direction [001]: self-consistently calculated anisotropic dispersion $E_{\pm}(\mathbf{k}_{\parallel})$ (lower right), DOS effective mass m^*/m_0 (lower left), spin splitting $E_+(\mathbf{k}_{\parallel}) - E_-(\mathbf{k}_{\parallel})$ (upper right), and dispersion $E_{\pm}(\mathbf{k}_{\parallel})$ in the vicinity of $k_{\parallel} = 0$ (upper left), of the topmost HH subband of a [001]-grown GaAs–Al_{0.5}Ga_{0.5}As heterostructure with $N_s = 2 \times 10^{11} \text{ cm}^{-2}$ and $|N_A - N_D| = 2 \times 10^{16} \text{ cm}^{-2}$: (a) calculated by means of the 14×14 extended Kane model, and (b) calculated by means of the 4×4 Luttinger Hamiltonian. Different line styles correspond to different directions of the in-plane wave vector \mathbf{k}_{\parallel} , as indicated. In the lower parts of the figures, the dotted line indicates the Fermi energy E_F . In the upper right parts, the dotted line shows the spin splitting of the first LH subband for $\mathbf{k}_{\parallel} \parallel [100]$. (a) taken from [7]. © (2000) by the American Physical Society

term to the splitting (6.37a) of the states that are dominantly HH-like. Often this term exceeds the contribution of $\langle \mathbf{r}_{42}^{8v8v} \mathcal{E}_z \rangle$ and $\langle \mathbf{r}_{52}^{8v8v} \mathcal{E}_z \rangle$ to the k -linear splitting. However, for typical values of the Fermi wave vector, this effect

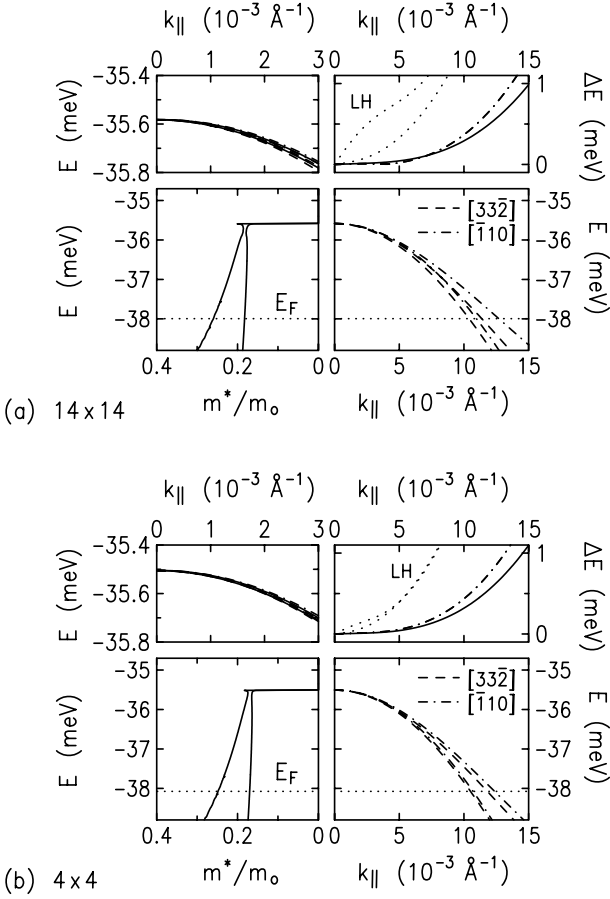


Fig. 6.7. Growth direction $[113]$: self-consistently calculated anisotropic dispersion $E_{\pm}(\mathbf{k}_{\parallel})$ (*lower right*), DOS effective mass m^*/m_0 (*lower left*), spin splitting $E_+(\mathbf{k}_{\parallel}) - E_-(\mathbf{k}_{\parallel})$ (*upper right*), and dispersion $E_{\pm}(\mathbf{k}_{\parallel})$ in the vicinity of $k_{\parallel} = 0$ (*upper left*), of the topmost HH subband of a $[113]$ -grown GaAs-Al_{0.5}Ga_{0.5}As heterostructure with $N_s = 2 \times 10^{11} \text{ cm}^{-2}$ and $|N_A - N_D| = 2 \times 10^{16} \text{ cm}^{-2}$: (a) calculated by means of the 14×14 extended Kane model, and (b) calculated by means of the 4×4 Luttinger Hamiltonian. Different line styles correspond to different directions of the in-plane wave vector \mathbf{k}_{\parallel} , as indicated. In the *lower parts* of the figures, the *dotted line* indicates the Fermi energy E_F . In the *upper right parts*, the *dotted lines* show the spin splitting of the first LH subband for $\mathbf{k}_{\parallel} \parallel [33\bar{2}]$ and $\mathbf{k}_{\parallel} \parallel [\bar{1}10]$

is still small when compared with the cubic splitting. This can be seen in Fig. 6.7, where we show the spin splitting for a quasi-2D hole system in a GaAs QW grown in the crystallographic direction $[113]$. Note that HH-LH mixing [66] at nonzero k_{\parallel} does not affect our general conclusions concerning

the HH spin splitting, because for larger k_{\parallel} the cubic term always dominates. A significant spin splitting linear in k_{\parallel} can be obtained in 2D hole systems in strained QWs, where the order of the topmost HH and LH subbands can be reversed [76].

6.3.4 Conceptual Analogies Between SIA Spin Splitting and Zeeman Splitting

Both the SIA spin splitting and the effective g factors in semiconductors are a consequence of SO interaction. Lassnig [37] pointed out that, in fact, the $B = 0$ spin splitting of electrons can be expressed in terms of a position-dependent effective g factor $g^*(z)$. A striking similarity between Zeeman splitting and Rashba spin splitting also became visible in our derivation of the Rashba coefficient in Sect. 5, as we saw that the Rashba coefficient reflects the noncommutativity of \mathbf{k} and \mathbf{r} , while the effective g factor reflects the noncommutativity (2.17) of the components of \mathbf{k} .

In the following we shall discuss the close relationship between Zeeman splitting and $B = 0$ spin splitting from a different point of view, focusing on the invariant expansion of these terms. Note that in the presence of an external magnetic field \mathbf{B} we have $\mathbf{k} \times \mathbf{k} = (-ie/\hbar)\mathbf{B}$, and the Zeeman splitting in the Γ_6^c conduction band can be expressed as

$$H_{6c}^z = \frac{i\hbar}{e} \frac{g^*}{2} \mu_B \boldsymbol{\sigma} \cdot \mathbf{k} \times \mathbf{k} = \frac{g^*}{2} \mu_B \boldsymbol{\sigma} \cdot \mathbf{B}, \quad (6.47)$$

where μ_B is the Bohr magneton. Thus, apart from a prefactor, we can obtain the Rashba term (6.9) from (6.47) by replacing one of the \mathbf{k} 's with $i\boldsymbol{\mathcal{E}}$. In the Γ_8^v valence band, we have two invariants for the Zeeman splitting [34, 72]:

$$H_{8v}^z = -2\kappa\mu_B \mathbf{J} \cdot \mathbf{B} - 2q\mu_B \boldsymbol{\mathcal{J}} \cdot \mathbf{B}, \quad (6.48)$$

where $\mathbf{J} = (J_x, J_y, J_z)$ and $\boldsymbol{\mathcal{J}} = (J_x^3, J_y^3, J_z^3)$. Once again, this equation has the same structure as the Rashba Hamiltonian for the Γ_8^v valence band; see Table 6.5. (We neglect here the third invariant, proportional to r_{52}^{8v8v} , because this coefficient is much smaller than r_{41}^{8v8v} and r_{42}^{8v8v} ; see Table 6.6.) Using the theory of invariants, we can understand that these formal similarities between Zeeman splitting and SIA spin splitting reflect the fact that both the wave vector \mathbf{k} and the electric field $\boldsymbol{\mathcal{E}}$ are polar vectors (transforming according to the irreducible representation Γ_5 of T_d), so that the higher-order tensor components of the wave vector \mathbf{k} and the mixed components containing both \mathbf{k} and $\boldsymbol{\mathcal{E}}$ must have the same structure. By inspection of Table C.4, we see that the analogue of the invariant $r_{52}^{8v8v} [(k_y \mathcal{E}_z + k_z \mathcal{E}_y) \{J_x, J_y^2 - J_z^2\} + \text{c.p.}]$ reads $[\{k_y, k_z\} \{J_x, J_y^2 - J_z^2\} + \text{c.p.}]$. However, in a diagonal block such as \mathcal{H}_{8v8v} , such an invariant is forbidden by time-reversal symmetry [77].

Finally, we would like to note that in (6.48) the first term is the isotropic part, and the second term is the anisotropic part. It is well known that for all common semiconductors for which (6.48) is applicable, the dominant

contribution to H_{8v}^z is given by the first term, proportional to κ , whereas the second term is rather small [34, 72]. Analogously to r_{41}^{8v8v} and r_{42}^{8v8v} , the isotropic $\mathbf{k} \cdot \mathbf{p}$ coupling between the bands Γ_8^v and Γ_6^c contributes to κ but not to q . The latter stems from $\mathbf{k} \cdot \mathbf{p}$ coupling to more remote bands such as Γ_8^c and Γ_7^c .

6.4 Cooperation of BIA and SIA

In the preceding two sections we discussed BIA and SIA spin splitting separately. While BIA is essentially a fixed property of a given sample, SIA can be changed, for example by external gates. However, the significance of the two terms varies depending on the material, the density, and the particular geometry of the sample under investigation. In Sect. 6.4.1 we discuss how the interference of BIA and SIA changes the $B = 0$ spin splitting qualitatively compared with the case where only BIA or SIA is present. Next we discuss in Sect. 6.4.2 how $B = 0$ spin splitting changes when the asymmetry of the sample is changed while keeping the density constant. Finally, we discuss in Sect. 6.4.3 the density dependence of SIA spin splitting.

6.4.1 Interference of BIA and SIA

In quasi-2D systems lifting of the inversion symmetry due to either BIA or SIA results in different point groups for a quantum structure; see Table 3.4. A symmetric QW with a diamond structure and growth direction [001] has the point group D_{4h} . BIA reduces the point group to D_{2d} , whereas SIA reduces the point group to C_{4v} . If we have both BIA and SIA we obtain the point group C_{2v} . These different point groups can manifest themselves in different spin splitting patterns of $B = 0$ spin splitting. However, we need to take into account the fact that the lowest-order invariants for BIA and SIA spin splitting can have higher symmetries than those we expect from Table 3.4. For example, the 2×2 Hamiltonian for a 2D electron system, up to second order in \mathbf{k} including the Rashba term, has axial symmetry $C_{\infty v}$ instead of, for example, C_{4v} as predicted by Table 3.4 for the growth direction [001].

More explicitly, the BIA and SIA spin splittings of a 2D electron system are given by (6.4) and (6.11), respectively, and it was seen that, to leading order in \mathbf{k}_{\parallel} , the spin splitting was independent of the direction of \mathbf{k}_{\parallel} . If we have both BIA and SIA then the spin splitting becomes anisotropic even in the linear term [47, 78]. Combining the Rashba term and the Dresselhaus term, we obtain

$$E_{6c6c}^{r,b}(\mathbf{k}_{\parallel}) = \pm k_{\parallel} \left\{ \alpha^2 + \alpha\eta(k_{\parallel}^2 - 2\langle k_z^2 \rangle) \sin(2\varphi) + \eta^2 \left[\langle k_z^2 \rangle^2 + \left(\frac{1}{4}k_{\parallel}^2 - \langle k_z^2 \rangle \right) k_{\parallel}^2 \sin(2\varphi)^2 \right] \right\}^{1/2} \quad (6.49a)$$

$$\approx \pm k_{\parallel} \sqrt{\alpha^2 - 2\alpha\eta\langle k_z^2 \rangle \sin(2\varphi) + \eta^2\langle k_z^2 \rangle^2} \pm \mathcal{O}(k_{\parallel}^3), \quad (6.49b)$$

where $\mathbf{k}_{\parallel} = k_{\parallel}(\cos \varphi, \sin \varphi, 0)$, and we have used for brevity $\alpha = \langle \mathbf{r}_{41}^{6c6c} \mathcal{E}_z \rangle$ and $\eta = \langle \mathbf{b}_{41}^{6c6c} \rangle$. It will become even more explicit that the interference of the Dresselhaus and Rashba terms reflects the different symmetries of these terms when we study in Sect. 6.6.1 the spin orientation due to BIA and SIA. Expressions similar to (6.49) can be derived for 2D hole systems also.

6.4.2 BIA Versus SIA: Tunability of $B = 0$ Spin Splitting

What is the relative importance of BIA and SIA for the $B = 0$ spin splitting in quasi-2D systems from a quantitative point of view? A general answer to this question is not possible, as we have to take into account both the band structure parameters of the host materials and the detailed geometry of the system under investigation.

BIA spin splitting is essentially a fixed material property, though its relevance varies with the well width and Fermi wave vector; see Sect. 6.2.2. SIA spin splitting, on the other hand, depends on the electric field \mathcal{E}_z that characterizes the inversion asymmetry of the sample. Therefore, SIA spin splitting is tunable by means of external gates that change the field \mathcal{E}_z in the sample. This was first demonstrated by Nitta et al. [12], who put a gate on the top of the sample. However, a single front or back gate changes both the asymmetry of the sample and the 2D density in the well. We can separate these effects by means of a QW with both a front and a back gate [30] so that the SIA can be tuned continuously while keeping the total density and BIA constant (Fig. 6.8).

Here we shall explore $B = 0$ spin splitting for various 2D systems assuming that the asymmetry of the sample is tuned as depicted in Fig. 6.8 while keeping the density constant. First we shall consider 2D electron systems. In Fig. 6.9, we show the self-consistently calculated spin splitting $\Delta N/N_s$ as a function of the external electric field $\mathcal{E}_z^{\text{ext}}$ in several QWs (see caption for details). The external electric field $\mathcal{E}_z^{\text{ext}}$ is defined relative to the symmetric configuration in Fig. 6.8. Different line styles in Fig. 6.9 correspond to differ-

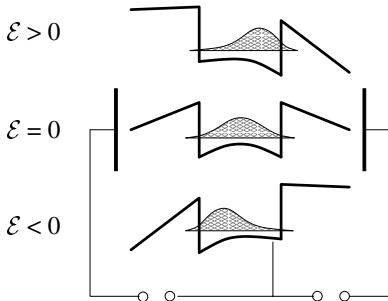


Fig. 6.8. In a QW with both a front and a back gate one can continuously tune the inversion asymmetry while keeping the total density constant [30]

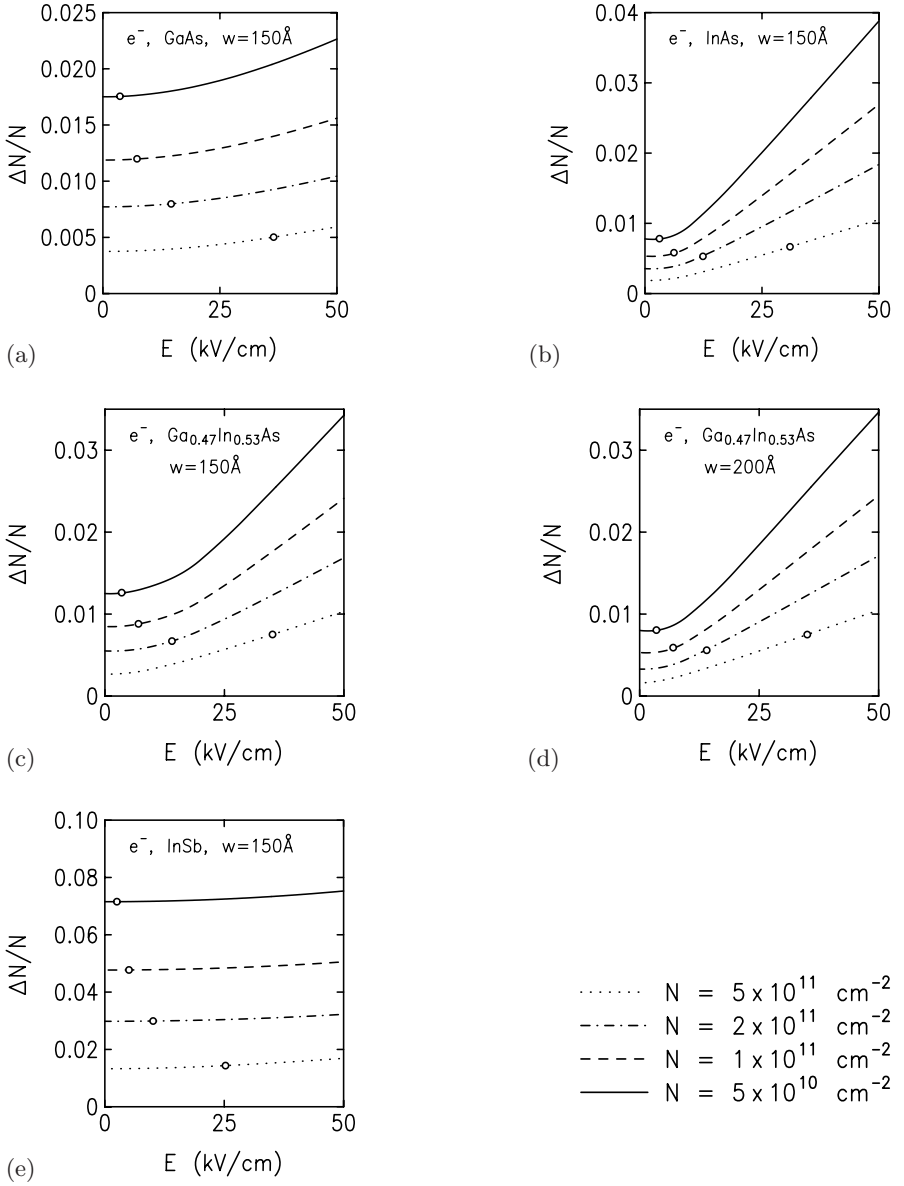


Fig. 6.9. Self-consistently calculated spin splitting $\Delta N/N_s$ of 2D electron systems as a function of the external electric field $\mathcal{E}_z^{\text{ext}}$ in (a) GaAs–Al_{0.3}Ga_{0.7}As, (b) InAs–AlSb, (c) and (d) Ga_{0.47}In_{0.53}As–Al_{0.47}In_{0.53}As, and (e) InSb QWs with well width $w = 150 \text{ \AA}$ except for (d), where $w = 200 \text{ \AA}$. Different line styles correspond to different densities N_s as indicated. Open circle indicate the spin splitting that corresponds to the self-consistent field (6.50)

ent densities N_s , as indicated. Only the lowest subband is occupied for the densities and well widths considered here.

As expected, the spin splitting increases as a function of $\mathcal{E}_z^{\text{ext}}$. Furthermore, we see that both the BIA- and SIA-induced spin splittings decrease when the density N_s is increased. This reflects the fact, discussed in Sect. 5, that a k -linear spin splitting is most important at small densities. Note that in Fig. 6.9 we have calculated $\Delta N/N_s$ up to fairly high electric fields $\mathcal{E}_z^{\text{ext}}$ in order to illustrate the general trends of the $B = 0$ spin splitting. In experiments with QWs the values of $\mathcal{E}_z^{\text{ext}}$ are typically of the order of several kV/cm (see e.g. Fig. 9.6b).

We shall compare Fig. 6.9 with the typical electric fields that can be achieved by means of asymmetric doping, which gives rise to an asymmetric self-consistent Hartree potential. If a QW is doped in only one barrier, then the Hartree potential is essentially flat in the other barrier. In this configuration, the self-consistent mean electric field is given by (6.35) with $N_A = 0$, i.e. we have

$$\langle \mathcal{E}_z \rangle \approx \frac{e}{\epsilon \epsilon_0} \frac{N_s}{2}. \quad (6.50)$$

The spin splittings that correspond to the field (6.50) have been marked by open circles in Fig. 6.9. These values are in good agreement with fully self-consistent calculations for asymmetrically doped QWs. In single heterostructures with $N_A > 0$, it is possible to achieve electric fields even larger than those given by (6.50).

In GaAs electron systems (Fig. 6.9a), we have a significant contribution to the $B = 0$ spin splitting from BIA. Only for large electric fields and high densities is there a large contribution to the $B = 0$ spin splitting from SIA. It was the latter regime that was explored by Pfeffer and Zawadzki [40] when they concluded that $B = 0$ spin splitting is typically dominated by SIA. In InAs, on the other hand (Fig. 6.9b), low densities and fairly small electric fields are sufficient to enter the regime where the $B = 0$ spin splitting is dominated by SIA. $\text{Ga}_{0.47}\text{In}_{0.53}\text{As}$ (Figs. 6.9c,d) is an intermediate system where, typically, both BIA and SIA must be taken into account. We see also that BIA is more important in narrow wells (Fig. 6.9c) than in wide wells (Fig. 6.9d), consistent with (6.4). For large electric fields $\gtrsim 30$ kV/cm the well width becomes irrelevant because the tilted QW behaves essentially like a triangular single heterostructure. In Fig. 6.9e, finally, we present for comparison the $B = 0$ spin splitting in an InSb QW. Up to now, only highly strained $\text{InSb-Al}_x\text{In}_{1-x}\text{Sb}$ QWs have been investigated experimentally [79, 80]. In Fig. 6.9e we have assumed that we have an InSb QW with infinite barriers. It is remarkable that in the narrow-gap semiconductor InSb, up to high electric fields, the dominant contribution to $B = 0$ spin splitting is from BIA.

Next we shall discuss the interplay of BIA and SIA for quasi-2D hole systems. In Fig. 6.10, we show the self-consistently calculated spin splitting

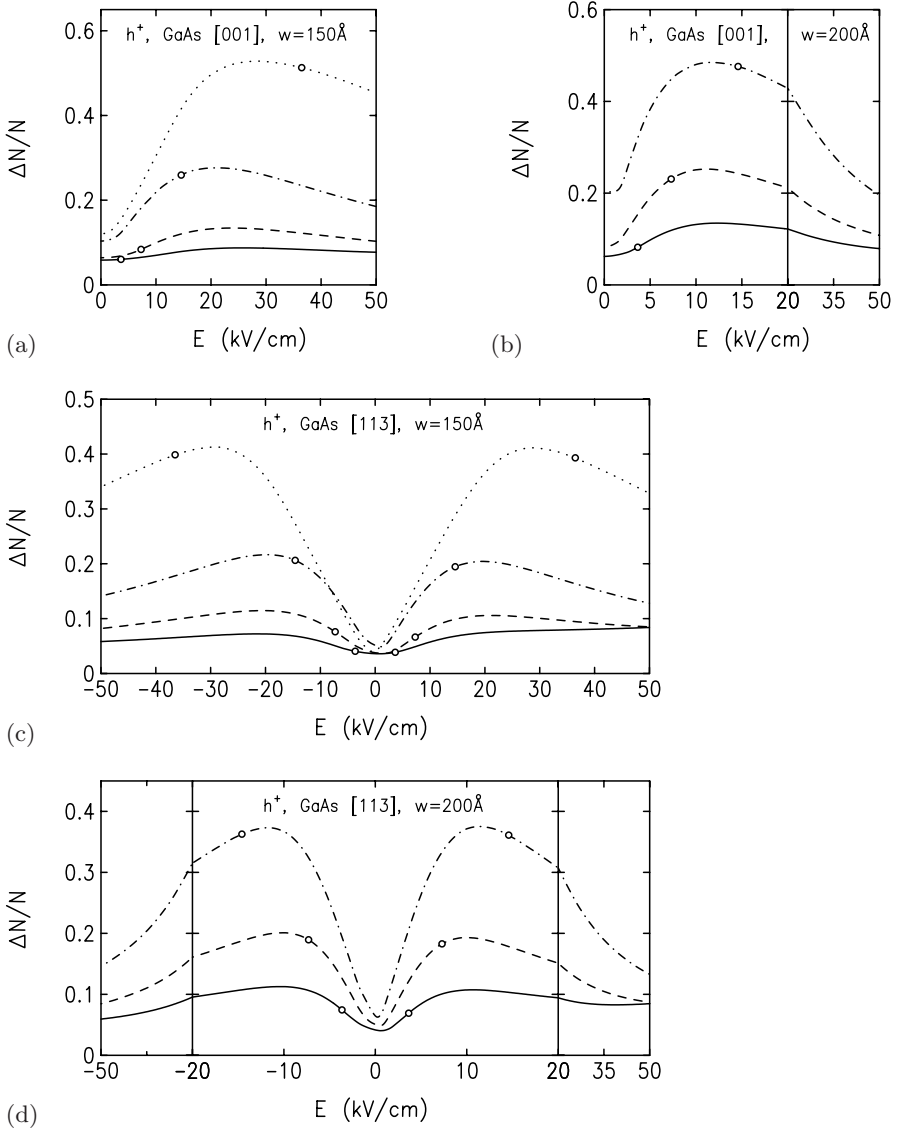


Fig. 6.10. Self-consistently calculated spin splitting $\Delta N/N_s$ of 2D hole systems in GaAs-Al_{0.3}Ga_{0.7}As QWs as a function of the external electric field $\mathcal{E}_z^{\text{ext}}$. In (a) and (b) we have considered QWs grown in the crystallographic direction [001]; in (c) and (d) we have assumed that the growth direction is [113]. In (a) and (c) we have assumed a well width $w = 150$ Å, in (b) and (d) we have used $w = 200$ Å. The different line styles have the same meaning as in Fig. 6.9. In (b) and (d), note the different scales on the horizontal axes for small and large absolute values of $\mathcal{E}_z^{\text{ext}}$. Open circles indicate the spin splitting that corresponds to the self-consistent field (6.50)

$\Delta N/N_s$ in GaAs–Al_{0.3}Ga_{0.7}As QWs as a function of the electric field $\mathcal{E}_z^{\text{ext}}$. In Figs. 6.10a,c, we have assumed a well width $w = 150$ Å; in Figs. 6.10b,d we have used $w = 200$ Å. In Figs. 6.10a,b, we have considered QWs grown in the crystallographic direction [001]; in Figs. 6.10c,d, we have assumed that the growth direction is [113]. Note that in the latter case, positive and negative values of $\mathcal{E}_z^{\text{ext}}$ are not equivalent. The different line styles have the same meaning as in Fig. 6.9. For the larger well width $w = 200$ Å, we did not consider $N_s = 5 \times 10^{11} \text{ cm}^{-2}$, because here the second subband becomes occupied. For the wide wells, we have also used different scales on the horizontal axes for small and large absolute values of $\mathcal{E}_z^{\text{ext}}$. We emphasize that $\Delta N/N_s$ is a smooth function of $\mathcal{E}_z^{\text{ext}}$. The spin splitting that corresponds to the self-consistent mean electric field (6.50) has again been marked by open circles in Fig. 6.10.

Unlike the $B = 0$ spin splitting of electrons, both the BIA and the SIA spin splittings of holes increase with density, which indicates that the dominant contributions to spin splitting are cubic in k . While the BIA-induced spin splitting increases with increasing well width, the SIA-induced spin splitting decreases. For larger values of $\mathcal{E}_z^{\text{ext}}$, the spin splitting $\Delta N/N_s$ decreases when the electric field $\mathcal{E}_z^{\text{ext}}$ is increased. This negative differential Rashba effect has the same origin as the anomalous density dependence of the Rashba effect in 2D hole systems discussed in more detail in Sect. 6.4.3: an increasing electric field increases the HH–LH splitting so that the Rashba coefficient decreases; see (6.43) and (6.44).

6.4.3 Density Dependence of SIA Spin Splitting

In the preceding section we discussed the tunability of the $B = 0$ spin splitting for the conceptually simplest (but experimentally most demanding) case of a QW where the asymmetry was changed while keeping the density constant [30]. Next we shall discuss how the $B = 0$ spin splitting changes with density. In particular, we shall study the experimentally relevant case where a single gate changes both the density and the asymmetry of the sample. It turns out that, while for a 2D electron system in a single heterostructure the Rashba coefficient and SIA spin splitting decrease when N_s and \mathcal{E}_z are reduced, a 2D hole systems can show the opposite behavior, i.e. the Rashba coefficient increases when the density is reduced [81].

2D Electron Systems. In 2D electron systems, the energy denominators in r_{41}^{6c6c} are always of the order of the fundamental gap, i.e. we have no substantial difference between (6.22) and (6.23) and the Rashba coefficient is essentially independent of the detailed geometry of the quasi-2D system. In high-quality samples, the background acceptor concentration N_A is small, so that it follows from (6.35) that $\mathcal{E}_z \propto N_s$. In this case, we obtain from (6.18)

$$\text{electron systems, } \mathcal{E}_z \propto N_s: \quad \frac{\Delta N}{N_s} \propto N_s^{1/2}. \quad (6.51a)$$

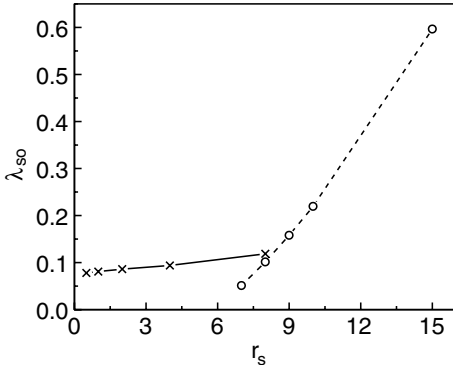


Fig. 6.11. Enhancement factor λ_{SO} of SIA spin splitting in a quasi-2D system as a function of r_s . Taken from [10]. © (1999) by the American Physical Society

For comparison, we note that in electron systems where the electric field \mathcal{E}_z is independent of N_s (see Sect. 6.4.2), we have

$$\text{electron systems, } \mathcal{E}_z = \text{const:} \quad \frac{\Delta N}{N_s} \propto N_s^{-1/2}. \quad (6.51b)$$

In the latter case, the divergence of $\Delta N/N_s$ for $N_s \rightarrow 0$ reflects the divergence of the DOS (6.20) at the subband edge.

Chen and Raikh [10] discussed the enhancement of the Rashba spin splitting ΔE due to exchange–correlation effects,

$$\frac{\Delta E^*}{\Delta E} = 1 + \lambda_{SO}. \quad (6.52)$$

Here ΔE^* denotes the renormalized spin splitting and λ_{SO} is the renormalization factor defined via (6.52). In Fig. 6.11, we show λ_{SO} as a function of the dimensionless density parameter

$$r_s = \frac{e^2}{4\pi\epsilon\epsilon_0} \frac{m^*}{\hbar^2} \frac{1}{\sqrt{\pi N_s}}, \quad (6.53)$$

which is the radius of a circle (in 2D) containing one electron, measured in units of the effective Bohr radius. One can see a significant increase in the Rashba coefficient for $r_s \gtrsim 8$. We remark that in 2D electron systems, we have the largest Rashba spin splitting for semiconductors such as InAs that have a small effective mass (i.e. small r_s). For typical densities we have $r_s \lesssim 3$, so that many-particle corrections to the $B = 0$ spin splitting can usually be neglected in 2D electron systems.¹²

2D Hole Systems. The density dependence of SIA spin splitting in 2D HH systems is qualitatively different from that for 2D electron systems because in 2D HH systems the Rashba coefficient depends on the separation between the HH and LH subbands; see (6.43) and (6.44). A decreasing separation gives

¹² For 2D electrons in GaAs, $r_s = 8$ corresponds to $N_s \approx 5.1 \times 10^9 \text{ cm}^{-2}$; in InSb, this value of $r_s = 8$ corresponds to $N_s \approx 1.1 \times 10^8 \text{ cm}^{-2}$.

rise to an increasing Rashba coefficient. The HH-LH splitting depends on the geometry of the system. We shall show now that the subband structure in accumulation-layer-like single heterostructures behaves rather differently with respect to changes of the charge density [81].

In a rectangular QW, a small density N_s and a small asymmetry imply that the properties of the system are controlled by the effective potential steps at the interfaces, i.e. changes in N_s or \mathcal{E}_z have a minor effect in such systems. In an inversion-layer-like heterostructure, we always have a band bending of the order of the fundamental gap so that, for small densities, the Hartree potential and \mathcal{E}_z are determined by the space charges due to the given concentration of ionized majority impurities in the system. For accumulation layer-like systems, on the other hand, it was shown by Stern [82] that the space charge layer is controlled by the much smaller concentration of minority impurities in the system. Thus, even for a small 2D density, the dominant contribution to the Hartree potential stems from the charges in the 2D system itself. Therefore, over a wide range of density N_s , the electric field \mathcal{E}_z is proportional to N_s . In a single heterostructure, the subband separations are approximately proportional to \mathcal{E}_z . Using the triangular-well approximation [63], we have, for the subband energies E_α^n measured from the corresponding bulk band edge, $E_\alpha^n \propto \mathcal{E}_z^{2/3}$, which implies $E_\alpha^n \propto N_s^{2/3}$. It then follows from (6.43) and (6.44) that in accumulation-layer-like 2D HH systems the most important HH Rashba coefficient r_{54}^{7h7h} (like r_{53}^{7h7h}) is proportional to $N_s^{-4/3}$. The effective HH Rashba coefficient $\beta \approx \langle r_{54}^{7h7h} \mathcal{E}_z \rangle$ thus increases in proportion to $N_s^{-1/3}$ when N_s and \mathcal{E}_z are reduced. According to (6.38), we thus have

$$\text{HH accumulation layers, } \mathcal{E}_z \propto N_s: \quad \frac{\Delta N}{N_s} \propto N_s^{1/6}. \quad (6.54a)$$

That is, in spite of the cubic spin splitting of the HH subband dispersion as compared with the linear spin splitting of the electron subbands, $\Delta N/N_s$ decreases much more slowly for HH accumulation layers than for similar quasi-2D electron systems. On the other hand, in a QW the subband separation is essentially independent of \mathcal{E}_z , so that we obtain

$$\text{HH QWs, } \mathcal{E}_z \propto N_s: \quad \frac{\Delta N}{N_s} \propto N_s^{3/2}. \quad (6.54b)$$

For comparison, we note that in HH systems where the electric field \mathcal{E}_z is independent of N_s (see Sect. 6.4.2), we have

$$\text{HH systems, } \mathcal{E}_z = \text{const}: \quad \frac{\Delta N}{N_s} \propto N_s^{1/2}. \quad (6.54c)$$

The exponents in these equations should be compared with those in (6.51).

In order to validate these qualitative arguments, we present next the results of realistic, fully self-consistent subband calculations [69]. We have used the 8×8 multiband Hamiltonian (3.6). The simpler 4×4 Luttinger Hamiltonian [72], taking into account only the band Γ_8^v , gives essentially the same

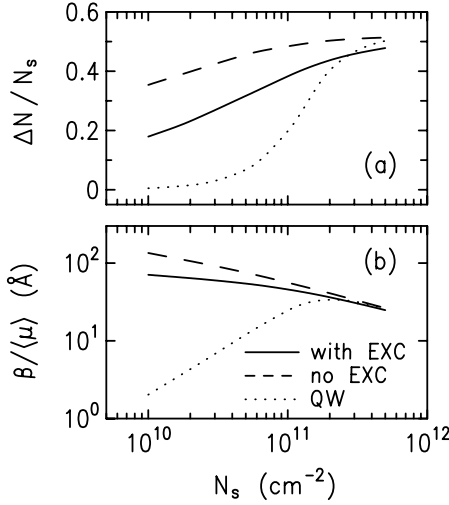


Fig. 6.12. (a) Spin splitting $\Delta N/N_s$ and (b) effective spin splitting coefficient $\beta/\langle\mu_h\rangle$, as a function of N_s , for a 2D HH system in the accumulation layer of a GaAs–Al_{0.5}Ga_{0.5}As single heterostructure on a (001) GaAs substrate, calculated including exchange–correlation (EXC, *solid lines*) and neglecting exchange–correlation (*dashed lines*). For the *dotted lines* see text. Taken from [81]. © (2002) by the American Physical Society

results. We have checked that the coupling to higher conduction bands has a minor influence. Many-particle effects have been taken into account on the basis of a density-functional approach [83]. From these calculations, we obtain the difference $\Delta N = |N_+ - N_-|$ between the spin subband densities N_{\pm} as a function of the total density $N_s = N_+ + N_-$.

In Fig. 6.12a we show $\Delta N/N_s$ calculated as a function of N_s for a 2D HH system in the accumulation layer of a GaAs–Al_{0.5}Ga_{0.5}As single heterostructure on a (001) GaAs substrate.¹³ As N_s is reduced from $5 \times 10^{11} \text{ cm}^{-2}$ to $1 \times 10^{10} \text{ cm}^{-2}$, the parameter r_s increases from 4.3 to 17. Therefore, one can expect that many-particle effects will be quite important in this regime of densities N_s . Indeed, we find that taking exchange–correlation into account (solid lines) reduces $\Delta N/N_s$ compared with a calculation without exchange–correlation (dashed lines). This behavior, which is opposite to that of 2D electron systems (Fig. 6.11), can be traced back to the fact that exchange–correlation increases the subband spacings [83] so that the dominant Rashba coefficient r_{54}^{7h7h} is reduced, in agreement with (6.44).

It is convenient to characterize the numerical results in terms of the effective Rashba coefficient $\beta \approx \langle r_{54}^{7h7h} \mathcal{E}_z \rangle$ using (6.39). Figure 6.12b shows that $\beta/\langle\mu_h\rangle$ increases when N_s is reduced. For comparison, we have also calculated $\Delta N/N_s$ for a 2D electron system in the accumulation layer of a Ga_{0.47}In_{0.53}As–Al_{0.47}In_{0.53}As single heterostructure (Fig. 6.13a). Here the spin splitting is given by (6.11), so that we can analyze the results in terms of the effective Rashba coefficient $\alpha \approx \langle r_{41}^{6c6c} \mathcal{E}_z \rangle$ using (6.19). In Fig. 6.13b it can be seen that, in contrast to Fig. 6.12b, the spin splitting coefficient $\alpha/\langle\mu_c\rangle$ decreases rapidly with decreasing N_s . We remark that, unlike the HH

¹³ For a concentration of charged minority impurities $N_{\min} \lesssim 5 \times 10^{13} \text{ cm}^{-3}$, these results are essentially independent of N_{\min} .

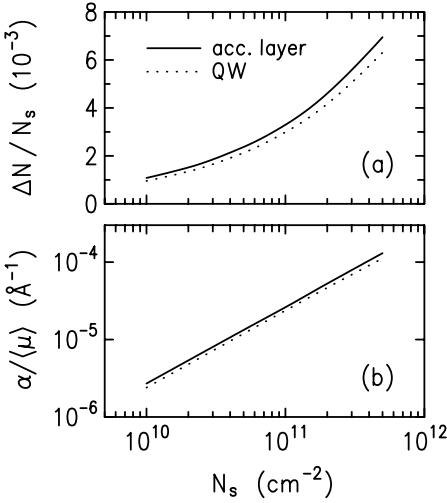


Fig. 6.13. (a) Spin splitting $\Delta N/N_s$ and (b) effective spin splitting coefficient $\alpha/\langle\mu_c\rangle$ as a function of N_s for a 2D electron system in the accumulation layer of a $\text{Ga}_{0.47}\text{In}_{0.53}\text{As}$ – $\text{Al}_{0.47}\text{In}_{0.53}\text{As}$ single heterostructure (solid lines). For the dotted lines see text. Taken from [81]. © (2002) by the American Physical Society

system in Fig. 6.12, exchange–correlation has only a weak influence on the electron system in Fig. 6.13, consistent with Fig. 6.11.

To further analyze the numerical results, we need to estimate the mean electric field $\langle\mathcal{E}_z\rangle$. In the present context, the difference between $\langle\mathcal{E}_z\rangle$ and $\langle\mathcal{E}_z^{\text{ext}}\rangle$ is unimportant because both quantities differ by a constant factor of order unity so that we can use (6.35). We note that in an accumulation layer, the contribution of the space charge layer to the Hartree potential $V_H(z)$ is very small [82]. Therefore, we can approximate (6.35) further by the mean self-consistent field (6.50). Using these values for $\langle\mathcal{E}_z\rangle$ and $\langle\mu_c\rangle = 89 \text{ eV } \text{\AA}^2$, we obtain $\langle r_{41}^{6c6c}\rangle \approx 34.3 \text{ e}\text{\AA}^2$, independent of N_s , consistent with (6.24). This implies that in Fig. 6.13b the drastic change of $\alpha/\langle\mu_c\rangle$ merely reflects the change of the electric field $\langle\mathcal{E}_z\rangle$. On the other hand, the weak variation of $\beta/\langle\mu_h\rangle$ in Fig. 6.12b indicates that the “bare” Rashba coefficient $\langle r_{54}^{7h7h}\rangle$ increases by a factor of 250 when N_s is lowered from 5×10^{11} to $1 \times 10^{10} \text{ cm}^{-2}$.¹⁴ This is in good qualitative agreement with the analytical model discussed above, which predicts an increase of r_{54}^{7h7h} by a factor of $50^{4/3} \approx 184$. Note that for very low densities the third-order perturbation approach, which underlies (6.24) and (6.44), breaks down because the subbands merge together so that higher-order corrections become important. These higher-order terms were fully taken into account in the numerical calculations [7, 69]. We remark that for an accumulation layer, the limit of a vanishing electric field implies also that the HH and LH states become degenerate. Therefore, in this limit one must go back from (6.43) to the more complex (6.36). However, for very low densities below 10^{10} cm^{-2} , the Hartree potential and spin splitting are ultimately controlled by the fixed concentration of minority impurities [82].

¹⁴ According to the present numerical calculations, $\langle\mu_h\rangle$ decreases from 19.1 to $10.7 \text{ eV } \text{\AA}$ as N_s increases from 1×10^{10} to $5 \times 10^{11} \text{ cm}^{-2}$.

It is interesting to compare the spin splittings in accumulation layers with those in QWs where \mathcal{E}_z is tuned externally, for example by means of gates [30]. The dotted lines in Figs. 6.12 and 6.13 show the calculated results for a 200 Å wide rectangular QW where the external electric field $\mathcal{E}_z^{\text{ext}}$ was chosen according to $\mathcal{E}_z^{\text{ext}}(N_s) = e/(2\epsilon\epsilon_0) N_s$ (see (6.50)). In an electron system (Fig. 6.13), we obtain spin splittings very close to the results for the accumulation layer. In particular, we have $\langle r_{41}^{6c6c} \rangle \approx 30.6 \text{ eÅ}^2$, independent of N_s . Similarly, for a 2D HH system in a QW (Fig. 6.12) and $N_s \lesssim 1 \times 10^{11} \text{ cm}^{-2}$, we obtain $\langle r_{54}^{7h7h} \rangle \approx 7.54 \times 10^6 \text{ eÅ}^4$. (For larger densities, higher-order corrections in $E_{\pm}^h(k_{\parallel})$ become important [7].) Since the subband spacings in a QW are essentially determined by the QW width (i.e. they are independent of N_s), this is consistent with (6.44). These calculations also indicate that for a 2D HH system in a QW, spin splitting becomes negligible in the regime of low density [7], which is due to the fact that the spin splitting of $E_{\pm}^h(k_{\parallel})$ is proportional to k_{\parallel}^3 . However, for 2D HH systems in single heterostructures, spin splitting can be very important in the low-density regime. A least-squares fit to the calculated $\Delta N/N_s$ for densities $N_s \leq 10^{11} \text{ cm}^{-2}$ gives $\Delta N/N_s \propto N_s^x$ with an exponent $x = 0.48$ for electrons, $x = 0.14$ and $x = 0.33$ for the HH accumulation layer without and with exchange–correlation, respectively, and $x = 1.6$ for the HH QW, in good qualitative agreement with (6.51a) and (6.54). We note that inversion layers give results similar to those for QWs, but the specific numbers depend on the details of the doping profile.

Comparison Between Experiment and Theory. In order to reinforce our conclusions, we present next a comparison between measured and calculated spin splittings in a GaAs–Al_{0.3}Ga_{0.7}As single heterostructure grown on a nominally undoped (311)A GaAs substrate with a weak p-type background doping. A back gate was used to tune the density N_s from 1.8×10^{10} to $4.2 \times 10^{10} \text{ cm}^{-2}$. To measure the spin subband densities N_{\pm} , the Shubnikov–de Haas (SdH) oscillations at low magnetic fields B were examined [12, 30] at a temperature $T \simeq 50 \text{ mK}$ (Figs. 6.14c,d). The frequencies f_{SdH} of these oscillations are a measure of the zero- B spin splitting.¹⁵ In Fig. 6.14a we present the measured and calculated spin subband densities, which exhibit remarkably close agreement. Figure 6.14b shows $\beta/\langle\mu_h\rangle$, determined by means of (6.39). On average, $\beta/\langle\mu_h\rangle$ increases as the density is reduced. Taking into account the orders-of-magnitude variations that occur for $\beta/\langle\mu_h\rangle$ in QWs and for $\alpha/\langle\mu_c\rangle$ in electron systems, the agreement between experiment and theory is quite satisfactory.¹⁶ We wish to emphasize that it is the anomalous enhancement of the Rashba coefficient in 2D HH systems in accumulation-layer-like single heterostructures that allows us to experimentally resolve the

¹⁵ This association may not be exact, i.e. f_{SdH} multiplied by (e/h) can deviate slightly from the spin subband densities; see Chap. 9.

¹⁶ We estimate that the experimental error in N_{\pm} is of the order of $\pm 4\%$, giving an error in ΔN and $\beta/\langle\mu_h\rangle$ of the order of $\pm 20\%$. The apparent increase of $\beta/\langle\mu_h\rangle$ at $N_s = 4.2 \times 10^{10} \text{ cm}^{-2}$ might be a result of experimental uncertainty.

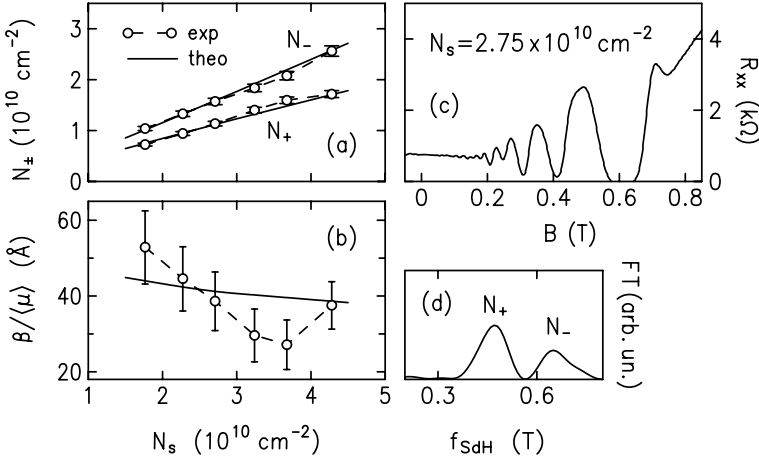


Fig. 6.14. Measured (*circles*) and calculated (*solid lines*) spin subband densities N_{\pm} (a) and effective spin splitting coefficient $\beta/\langle\mu_h\rangle$ (b) as a function of density $N_s = N_{+} + N_{-}$ for a 2D HH system in a GaAs–Al_{0.3}Ga_{0.7}As single heterostructure on a nominally undoped (311)A GaAs substrate with a weak p-type background doping. In (c) we show the measured magnetoresistance R_{xx} as a function of magnetic field B , and (d) the Fourier transform (FT) of R_{xx} for $N_s = 2.75 \times 10^{10} \text{ cm}^{-2}$

spin splitting in this density regime. Data on QW samples with comparable densities reveal no measurable spin splitting [84], consistent with the solid and dotted lines in Fig. 6.12.

6.5 Interface Contributions to $B = 0$ Spin Splitting

In Sects. 6.2 and 6.3, we discussed the contributions to $B = 0$ spin splitting due to BIA and SIA. Recently, a third mechanism for spin splitting in semiconductor quantum structures has been discussed in the literature, which can be traced back to the particular properties of the heterointerfaces in quasi-2D systems [85, 86, 87, 88, 89, 90, 91, 92, 5, 93, 94, 95]. In Table 3.4 we listed the point groups of a quasi-2D system for various crystallographic growth directions. However, a microscopic analysis of the crystal structure reveals that, at the heterointerfaces, the local symmetry can be reduced compared with that given in Table 3.4.

An ideal symmetric QW grown in the crystallographic direction [001] has the point group D_{2d} (see Table 3.4). In a quasi-2D system with this point group, the optical absorption must be independent of the crystallographic orientation of the in-plane polarization vector (Ref. [96]). The reason is that symmetry requires that two of the principal values of the tensor of the optical susceptibility must be equal and that the principal axis, which corresponds to the third value, is parallel to the growth direction of the QW. Using optically

detected magnetic resonance, van Kesteren et al. [97] observed an unexpected in-plane anisotropy in the optical absorption of [001]-grown GaAs–AlAs QWs (see also Ref. [98]). Such an optical anisotropy is compatible with the point group C_{2v} . A particularly large optical anisotropy was observed by Krebs et al. in systems without common atoms in the well and barrier materials [88, 89, 90].

In order to explain the experimental findings of van Kesteren et al. [97], it was noted by Aleĭner and Ivchenko [85] that an ideal [001] heterointerface of a GaAs–AlAs system has the microscopic point group C_{2v} ; see Fig. 6.15. To lowest order in \mathbf{k} , the point group C_{2v} is compatible with the following phenomenological interface term in the valence band block of the Kane Hamiltonian [85, 87]:

$$\mathcal{H} = \pm h_{x-y} \delta(z - z_i) \begin{pmatrix} \frac{1}{3}\{J_x, J_y\} & U_{xy} \\ U_{xy}^\dagger & 0 \end{pmatrix} \quad (6.55a)$$

$$= \pm h_{x-y} \delta(z - z_i) \begin{pmatrix} 0 & 0 & -\frac{i}{2\sqrt{3}} & 0 & 0 & \frac{i}{\sqrt{6}} \\ 0 & 0 & 0 & -\frac{i}{2\sqrt{3}} & 0 & 0 \\ \frac{i}{2\sqrt{3}} & 0 & 0 & 0 & 0 & 0 \\ 0 & \frac{i}{2\sqrt{3}} & 0 & 0 & \frac{i}{\sqrt{6}} & 0 \\ \hline 0 & 0 & 0 & -\frac{i}{\sqrt{6}} & 0 & 0 \\ -\frac{i}{\sqrt{6}} & 0 & 0 & 0 & 0 & 0 \end{pmatrix}. \quad (6.55b)$$

Here the upper and lower signs refer to a GaAs–AlAs and an AlAs–GaAs interface, respectively, and z_i is the position of the interface on the z axis. In the notation of [87] we have $h_{x-y} = \hbar^2 t_{x-y} / (m_0 a) = \sqrt{3} \hbar^2 t_{l-h} / (m_0 a)$, where a is the lattice constant. By comparing their calculations with the experimental data of van Kesteren et al. [97], Aleĭner and Ivchenko [85] estimated that $h_{x-y} = 3.3 \text{ eV } \text{\AA}$ for a GaAs–AlAs interface.

The single heterointerface in Fig. 6.15 has the point group C_{2v} . If we have a QW with two such interfaces, we must distinguish between common-atom and no-common-atom interfaces (Ref. [100]). If the interfaces share a common atom, such as the As layer in a GaAs–AlAs interface, then the point group of the QW is D_{2d} , consistent with our earlier results in Table 3.4 that did not take into account the details of the atomic structure at the interfaces. Note also that the presence of two interface terms of the form (6.55) for opposite interfaces preserves the D_{2d} symmetry. If, on the other hand, the heterointerfaces do not share a common atom, as in an InAs–GaSb interface, then the microscopic atomic structure of a symmetric QW has the point group C_{2v} . Van Kesteren et al. [97] measured the in-plane

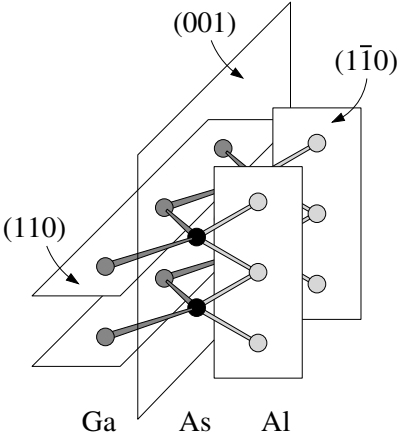


Fig. 6.15. Nearest neighbors of the As atoms at a GaAs–AlAs interface. The point group C_{2v} of a single heterojunction contains a twofold rotation axis C_2 parallel to the growth direction $[001]$ and two mirror planes (110) and $(\bar{1}\bar{1}0)$ [87,99]

optical anisotropy of GaAs–AlAs QWs. In order to explain the experimental data of these authors, we thus need an additional mechanism that gives rise to a reduction in symmetry from D_{2d} to C_{2v} , e.g. an electric field. To the best of our knowledge, the experiments of van Kesteren et al. have not been analyzed along these lines.¹⁷ Experiments by Kwok et al. (Ref. [101]) have shown explicitly that the optical anisotropy can be tuned by means of an external electric field \mathcal{E}_z (the Pockels effect).

The phenomenological interface term (6.55) describes a coupling between HH states ($m = \pm 3/2$) and LH and SO states ($m = \mp 1/2$). Such a mixing of HH and LH states that exists even for an in-plane wave vector $k_{\parallel} = 0$ was observed earlier in tight-binding calculations by Chang and Schulman [102, 103, 104]; see also the pseudopotential calculations in [105, 100]. Equation (6.55) allows us to incorporate these tight-binding results into the $\mathbf{k} \cdot \mathbf{p}$ method. In particular, we can estimate the magnitude of the weight factor h_{x-y} in (6.55) by comparing with tight-binding calculations. The results presented in Fig. 6 of [103] and Fig. 2 of [104] can be reproduced by assuming $h_{x-y} = 0.2 \text{ eV \AA}$, see Fig. 6.16 in the present book. Note that the value of h_{x-y} used here is significantly smaller than the value derived in [87]. An even smaller value is required to reproduce the results of the pseudopotential calculations in Ref. [100].

Obviously, the coupling of HH and LH states is strongest when the states are close in energy. If the QW is symmetric, only subband states of opposite parity are coupled to each other [86]. As the h_1 subband is always lowest in energy (unless the order of the subbands is reversed, for example by means of strain [76]), this subband is only weakly affected by HH–LH mixing. On the other hand, we can have a stronger mixing of the (usually unoccupied) l_1 and h_2 subbands, which is important for optical interband transitions [85, 97], for

¹⁷ We are talking here about ideal interfaces. From an experimental point of view, an important additional aspect is the morphology of the interfaces in real systems.

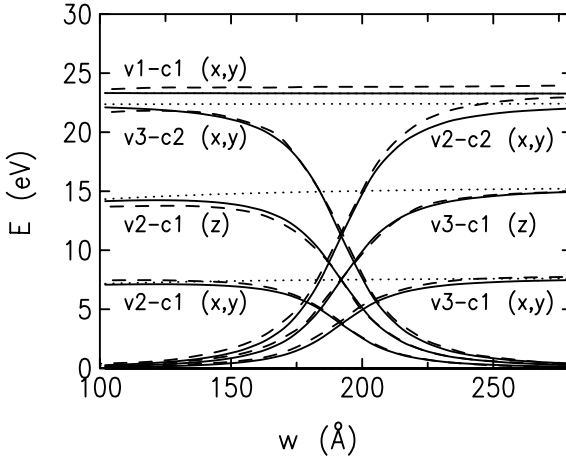


Fig. 6.16. Squared optical matrix elements at $k_{\parallel} = 0$ for a GaAs–Al_{0.3}Ga_{0.7}As superlattice with an alloy layer width of 56.5 Å, plotted as a function of the width w of the GaAs layer. The *dashed lines* are taken from Fig. 2 of [104]. The *solid lines* were calculated by means of (6.55). The *dotted lines* show the squared optical matrix elements without any HH–LH mixing. The symbols x , y , and z denote the direction of the polarization vector. In order to reproduce the results presented in Fig. 6 of [103] and Fig. 2 of [104] we have used $\gamma_1 = 7.97$, $\gamma_2 = 2.88$, valence band offset $\Sigma_v = 66.7$ meV, and $h_{x-y} = 0.2$ eV Å

example. We remark that the existence of a crossing of the unperturbed h_2 and l_1 states as a function of well width depends rather sensitively on the effective masses of the HH and LH states. Using the Luttinger coefficients listed in Appendix D, we do not obtain a crossing of the h_2 and l_1 subbands in a GaAs–AlAs QW. We note also that, to the best of our knowledge, we are not aware of experiments with (unstrained) GaAs–AlGaAs QWs showing the existence of a parameter regime that yields an (anti-)crossing of the h_2 and l_1 subbands. On the basis of tight-binding calculations for superlattices, it was observed in Ref. [103] that a crossing of the unperturbed HH and LH states can occur as a function of the superlattice miniband wave vector; see also the pseudopotential calculations in Ref. [100].

Equation (6.55) has the same structure as the lowest-order invariant for the SIA spin splitting of the valence band states in a zinc blende structure,

$$\mathcal{H} = \mathcal{E}_z \begin{pmatrix} r_{51}^{8v8v} \{J_x, J_y\} & r_{51}^{8v7v} U_{xy} \\ r_{51}^{8v7v\dagger} U_{xy}^\dagger & 0 \end{pmatrix} \quad (6.56)$$

(see Table 6.5). Clearly, (6.56) applies only if the confining potential is asymmetric ($\mathcal{E}_z \neq 0$). However, it is possible that an allegedly symmetric QW has a built-in electric field; see also Ref. [101]. We obtain a third contribution to HH–LH mixing (even for $k_{\parallel} = 0$) from the k -linear terms in the Luttinger Hamiltonian,

$$\mathcal{H} = \sqrt{3} C_k \begin{pmatrix} \frac{2}{3} [k_x \{J_x, J_y^2 - J_z^2\} + \text{cp}] & -i(k_x U_{yz} + \text{cp}) \\ i(k_x U_{yz}^\dagger + \text{cp}) & 0 \end{pmatrix} \quad (6.57)$$

(see Tables 6.2).

In a symmetric QW, (6.56) couples HH and LH subband states of the same parity. Like (6.55), the k -linear terms (6.57) couple subband states of opposite parity. Therefore, we can expect different trends in the HH–LH mixings described by (6.55), (6.56), and (6.57) if the separation of the HH and LH subbands is varied, for example by means of strain. The Rashba effect and BIA, but not (6.55), were taken into account in the numerical calculation of Zhu and Chang [78]. However, the results were not analyzed with respect to the importance of the different terms. To the best of our knowledge, a detailed investigation of the interplay of (6.55), (6.56), and (6.57) has not been performed so far [95]. Concerning the experimentally observed optical anisotropy [97, 98], we remark that exciton states can be decomposed into electron and hole states with in-plane wave vector $k_{\parallel} \geq 0$ [106], so that a proper analysis of optical anisotropy should take into account HH–LH mixing at both $k_{\parallel} = 0$ and $k_{\parallel} > 0$.

Equation (6.55) refers to the valence band only. In the zeroth order of \mathbf{k} , the electron states are not affected by the lowering of the symmetry at the interfaces. In third-order perturbation theory, the $\mathbf{k} \cdot \mathbf{p}$ coupling of the electron states to HH and LH states gives rise to the following mixed terms [5]:

$$\begin{aligned} \mathcal{H}_{6c6c} = & \pm h_{x-y} \frac{P^2}{3} \left(\frac{1}{E_0^2} + \frac{2}{E_0(E_0 + \Delta_0)} \right) \delta(z - z_i) k_x k_y \mathbb{1}_{2 \times 2} \\ & \pm h_{x-y} \frac{iP^2}{6} \left(\frac{1}{E_0^2} - \frac{1}{E_0(E_0 + \Delta_0)} \right) [k_z, \delta(z - z_i)] (k_x \sigma_x - k_y \sigma_y). \end{aligned} \quad (6.58)$$

The first term in (6.58) results in a spin-independent correction to the subband dispersion $E(\mathbf{k}_{\parallel})$. The second term contributes to the spin splitting of the subband states in a way similar to BIA. We obtain similar expressions that are quadratic and linear in the in-plane wave vector \mathbf{k}_{\parallel} , which describe spin-independent and spin-dependent contributions, respectively, to the dispersions of the HH and LH states. Recently, several authors have discussed the interface term in the context of spin relaxation [93, 94, 5].

6.6 Spin Orientation of Electron States

We have pointed out in the introductory remarks of this chapter that the $B = 0$ spin splitting in an inversion-asymmetric quasi-2D system does not give rise to a net magnetic moment. In this section we shall explore in more detail the spin orientation of electron states in the presence of $B = 0$ spin splitting.

6.6.1 General Discussion

We can always choose a suitably rotated coordinate system with basis vectors $\hat{\mathbf{e}}_1$, $\hat{\mathbf{e}}_2$, and $\hat{\mathbf{e}}_3$ such that a given spin-1/2 state $|\psi\rangle$ is oriented in the direction $\hat{\mathbf{e}}_3$ of this coordinate system. The unit vector $\hat{\mathbf{e}}_3$ is given by the expectation value

$$\hat{\mathbf{e}}_3 = \langle \psi | \boldsymbol{\sigma} | \psi \rangle, \quad (6.59)$$

where $\boldsymbol{\sigma} = (\sigma_x, \sigma_y, \sigma_z)$ is the vector of Pauli spin matrices. Using (6.59) we can readily determine the spin orientation of the spin eigenstates in the presence of BIA and SIA spin splitting. The quasi-2D eigenstates of a multiband Hamiltonian can be labeled by the in-plane wave vector \mathbf{k}_{\parallel} , see (4.1). It is important to note here that the spin orientation axis of an eigenstate $|\psi\rangle$ depends on \mathbf{k}_{\parallel} . This can be seen most easily for the Rashba Hamiltonian (6.10), for which we can evaluate (6.59) analytically. For $\mathbf{k}_{\parallel} = k_{\parallel}(\cos \varphi, \sin \varphi, 0)$, the eigenstates are

$$|\psi_{\pm}^{\text{SIA}}(\mathbf{k}_{\parallel})\rangle = \frac{e^{i\mathbf{k}_{\parallel} \cdot \mathbf{r}_{\parallel}}}{2\pi} \xi_{\mathbf{k}_{\parallel}}(z) \frac{1}{\sqrt{2}} \begin{vmatrix} 1 \\ \mp i e^{i\varphi} \end{vmatrix}, \quad (6.60)$$

so that

$$\langle \boldsymbol{\sigma}(\mathbf{k}_{\parallel}) \rangle_{\pm} = \langle \psi_{\pm}^{\text{SIA}}(\mathbf{k}_{\parallel}) | \boldsymbol{\sigma} | \psi_{\pm}^{\text{SIA}}(\mathbf{k}_{\parallel}) \rangle \quad (6.61a)$$

$$= \begin{pmatrix} \pm \sin \varphi \\ \mp \cos \varphi \\ 0 \end{pmatrix} = \pm \begin{pmatrix} \cos(\varphi - \pi/2) \\ \sin(\varphi - \pi/2) \\ 0 \end{pmatrix}, \quad (6.61b)$$

where the upper and lower signs refer to the upper and lower spin subbands, respectively, (assuming that the effective Rashba coefficient $\alpha = \langle r_{41}^{6c6c} \mathcal{E}_z \rangle$ is positive). Note that (6.61) is independent of the envelope function $\xi_{\mathbf{k}_{\parallel}}(z)$ and the magnitude k_{\parallel} of the in-plane wave vector. The spin orientation (6.61) of the eigenfunctions (6.60) as a function of the direction of the in-plane wave vector is indicated by arrows in Fig. 6.2.

We showed in (6.4) and (6.11) that both the Dresselhaus term (in the leading order of \mathbf{k}_{\parallel}) and the Rashba term give rise to apparently the same spin splitting. Nevertheless, the corresponding wave functions are qualitatively different owing to the different symmetries of the Rashba and Dresselhaus terms. If we neglect the terms cubic in \mathbf{k}_{\parallel} , the eigenfunctions in the presence of Dresselhaus spin splitting are

$$|\psi_{\pm}^{\text{BIA}}(\mathbf{k}_{\parallel})\rangle = \frac{e^{i\mathbf{k}_{\parallel} \cdot \mathbf{r}_{\parallel}}}{2\pi} \xi_{\mathbf{k}_{\parallel}}(z) \frac{1}{\sqrt{2}} \begin{vmatrix} 1 \\ \mp e^{-i\varphi} \end{vmatrix}, \quad (6.62)$$

so that

$$\langle \boldsymbol{\sigma}(\mathbf{k}_{\parallel}) \rangle_{\pm} = \mp \begin{pmatrix} \cos(-\varphi) \\ \sin(-\varphi) \\ 0 \end{pmatrix}. \quad (6.63)$$

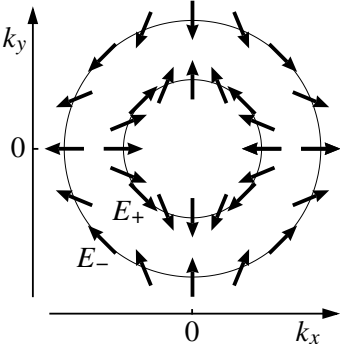


Fig. 6.17. Lowest-order spin orientation $\langle \sigma \rangle$ of the eigenstates $|\psi_{\pm}^{\text{BIA}}(\mathbf{k}_{\parallel})\rangle$ in the presence of BIA. The *inner* and *outer* circles show $\langle \sigma \rangle$ along contours of constant energy for the upper and lower branches E_+ and E_- , respectively, of the spin-split dispersion

The spin orientation (6.63) of the eigenfunctions (6.62) as a function of the direction of the in-plane wave vector is indicated by arrows in Fig. 6.17. For the Rashba spin splitting, we see in Fig. 6.2 that if we move clockwise on a contour of constant energy $E(\mathbf{k}_{\parallel})$, the spin vector rotates in the same direction, consistent with the axial symmetry of the Rashba term. On the other hand, (6.63) and Fig. 6.17 show that in the presence of BIA, the spin vector rotates counterclockwise for a clockwise motion in \mathbf{k}_{\parallel} space. The different symmetries of the Hamiltonians for BIA and SIA, which become visible in the quantity $\langle \sigma \rangle$, is also the reason for the anisotropy of the $B = 0$ spin splitting even in the leading order of \mathbf{k}_{\parallel} that was obtained in Sect. 6.4.1 for the case where both BIA and SIA are present.

In the above discussion we have assumed that the wave functions are two-component spinors. When the eigenstates $|\psi\rangle$ are multicomponent envelope functions (4.1), we must evaluate the expectation value of $\mathbf{S} = \boldsymbol{\sigma} \otimes \mathbb{1}_{\text{orb}}$ where the identity operator $\mathbb{1}_{\text{orb}}$ refers to the orbital part of $|\psi\rangle$. For the transformed Hamiltonian \mathcal{H}' in (5.1), the spin operator \mathbf{S}' has the block form

$$S'_x = \begin{pmatrix} 0 & \mathbb{1}_{\text{orb}} \\ \mathbb{1}_{\text{orb}} & 0 \end{pmatrix}, \quad S'_y = \begin{pmatrix} 0 & -i\mathbb{1}_{\text{orb}} \\ i\mathbb{1}_{\text{orb}} & 0 \end{pmatrix}, \quad S'_z = \begin{pmatrix} \mathbb{1}_{\text{orb}} & 0 \\ 0 & -\mathbb{1}_{\text{orb}} \end{pmatrix}. \quad (6.64)$$

The inverse unitary transformation that relates \mathcal{H}' to \mathcal{H} gives the spin operator in the unprimed basis. For the extended Kane model, we obtain

$$S_i = \begin{pmatrix} \frac{2}{3}J_i & -2U_i & 0 & 0 & 0 \\ -2U_i^\dagger & -\frac{1}{3}\sigma_i & 0 & 0 & 0 \\ 0 & 0 & \sigma_i & 0 & 0 \\ 0 & 0 & 0 & \frac{2}{3}J_i & -2U_i \\ 0 & 0 & 0 & -2U_i^\dagger & -\frac{1}{3}\sigma_i \end{pmatrix}, \quad i = x, y, z \quad (6.65)$$

where the matrices J_i , U_i , and σ_i are defined in Table C.2. Once again, the expectation value $\langle \psi | \mathbf{S} | \psi \rangle$ is a three-component vector that can be identified with the spin orientation of the multicomponent wave function $|\psi\rangle$. We remark that while the vector $\langle \sigma \rangle$ of a spin-1/2 system is always strictly

normalized to unity, this condition is in general not fulfilled for the spin expectation value $\langle \mathbf{S} \rangle$ of a multicomponent single-particle state (4.1). This is due to the fact that in the presence of SO interaction we cannot factorize the multicomponent wave function into an orbital part and a spin part. However, for electrons, the deviation of $|\langle \mathbf{S} \rangle|$ from unity is rather small (typically less than 1%), so it is neglected here.

For free electrons in the presence of an external magnetic field \mathbf{B} , the unit vector $\langle \boldsymbol{\sigma} \rangle$ is parallel to the vector \mathbf{B} . Following this picture, we can attribute the $B = 0$ spin splitting in quasi-2D systems to an effective magnetic field $\mathbf{B}(\mathbf{k}_{\parallel})$ parallel to $\langle \mathbf{S}(\mathbf{k}_{\parallel}) \rangle$. Obviously, the magnitude of this effective magnetic field should be related to the magnitude of the $B = 0$ spin splitting. However, depending on the particular problem of interest, it can be convenient to define the magnitude of the spin splitting in two different ways: the energy difference $\Delta E = E_+(\mathbf{k}_{\parallel}) - E_-(\mathbf{k}_{\parallel})$ characterizes the magnitude of the spin splitting for a given wave vector \mathbf{k}_{\parallel} , whereas the wave vector difference Δk characterizes the magnitude of the spin splitting at a fixed energy E . While the former is relevant for Raman experiments, for example (see Sect. 6.8), the latter quantity is an important parameter in other situations, for example for spin relaxation [107] and for the spin transistor proposed by Datta and Das [108].

In the following, we shall explore the second definition, where the effective magnetic field is given by $\mathbf{B} = \langle \mathbf{S} \rangle \Delta k$. Our precise definition of Δk is illustrated in Fig. 6.18. For a given energy E and a fixed direction φ of the in-plane wave vector $\mathbf{k}_{\parallel} = k_{\parallel}(\cos \varphi, \sin \varphi, 0)$, we determine $\mathbf{k}_{\parallel} \mp \Delta \mathbf{k}/2$ such that $E = E_+(\mathbf{k}_{\parallel} - \Delta \mathbf{k}/2) = E_-(\mathbf{k}_{\parallel} + \Delta \mathbf{k}/2)$. Here E_+ and E_- denote the upper and lower branches, respectively, of the spin-split dispersion. We then define

$$\mathbf{B} = \langle \mathbf{S} \rangle_+ \Delta k = -\langle \mathbf{S} \rangle_- \Delta k, \quad (6.66)$$

with the sign convention that the field \mathbf{B} is parallel to the effective field felt by the electrons in the upper branch $E_+(\mathbf{k}_{\parallel})$. We have used the shorthand notation

$$\langle \mathbf{S} \rangle_{\pm} = \langle \psi_{\pm}(\mathbf{k}_{\parallel} \mp \Delta \mathbf{k}/2) | \mathbf{S} | \psi_{\pm}(\mathbf{k}_{\parallel} \mp \Delta \mathbf{k}/2) \rangle. \quad (6.67)$$

We remark that for a parabolic band with an effective mass m^* plus Rashba term (6.10), the wave vector difference Δk can be evaluated analytically. It follows from (6.19) that [108]

$$\Delta k_{\text{Rashba}} = \frac{2m^*\alpha}{\hbar^2}, \quad (6.68)$$

independent of the magnitude of k_{\parallel} . From an experimental point of view, it should be kept in mind that spin splitting is often measured by analyzing Shubnikov–de Haas oscillations. Such experiments yield spin subband densities N_{\pm} which are directly related to Δk by

$$\Delta k = \sqrt{4\pi} (\sqrt{N_-} - \sqrt{N_+}), \quad (6.69)$$

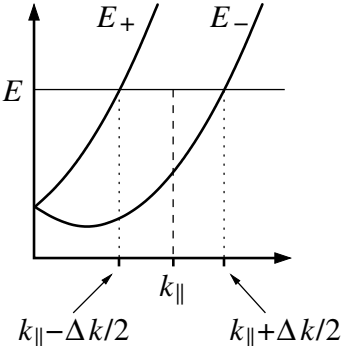


Fig. 6.18. For a given energy E and a fixed direction of the in-plane wave vector \mathbf{k}_{\parallel} , we determine $\mathbf{k}_{\parallel} \mp \Delta\mathbf{k}/2$ such that $E = E_+(\mathbf{k}_{\parallel} - \Delta\mathbf{k}/2) = E_-(\mathbf{k}_{\parallel} + \Delta\mathbf{k}/2)$. Here E_+ and E_- denotes the upper and lower branches, respectively, of the spin-split dispersion

provided we can ignore anisotropic contributions to $B = 0$ spin splitting. However, see also Chap. 9.

The definition (6.66) presupposes that the spin expectation values $\langle \mathbf{S} \rangle_+$ and $\langle \mathbf{S} \rangle_-$ are strictly antiparallel to each other. In (6.61) we saw that for the Rashba Hamiltonian, this condition is fulfilled exactly. This is closely related to the fact that for the Rashba Hamiltonian, the spin subband eigenstates $|\psi_+^{\text{SIA}}(\mathbf{k}_{\parallel})\rangle$ and $|\psi_-^{\text{SIA}}(\mathbf{k}'_{\parallel})\rangle$ are orthogonal, independent of the magnitude of \mathbf{k}_{\parallel} and \mathbf{k}'_{\parallel} as long as the wave vectors \mathbf{k}_{\parallel} and \mathbf{k}'_{\parallel} are parallel to each other.¹⁸ In general, $|\psi_+(\mathbf{k}_{\parallel} - \Delta\mathbf{k}/2)\rangle$ and $|\psi_-(\mathbf{k}_{\parallel} + \Delta\mathbf{k}/2)\rangle$ are only approximately orthogonal, so that $\langle \mathbf{S} \rangle_+$ and $\langle \mathbf{S} \rangle_-$ are only approximately antiparallel. However, we find that the angle between the vectors $\langle \mathbf{S} \rangle_+$ and $\langle \mathbf{S} \rangle_-$ is always very close to 180° , with an error $\lesssim 1^\circ$, so we neglect this point in the remaining discussion.

Even though we can evaluate the spin expectation value $\langle \mathbf{S} \rangle$ for each spin subband separately, we do not attempt to define an effective magnetic field \mathbf{B} for each spin subband. This is due to the fact that \mathbf{B} is commonly used to discuss phenomena such as spin precession [108] and spin relaxation [107], which cannot be analyzed for each spin subband individually.

The allowed directions of the effective magnetic field \mathbf{B} can be deduced from the symmetry of the QW (Table 3.4). The spin-split states for a fixed wave vector \mathbf{k}_{\parallel} are orthogonal to each other, i.e. the spin vectors of these states are antiparallel. The spin orientation of eigenstates for different wave vectors in the star of \mathbf{k}_{\parallel} are connected by the symmetry operations of the system [77]. Accordingly, only those spin orientations of the spin-split eigenstates are permissible for which every symmetry operation maps orthogonal states onto orthogonal states. In a QW grown in the crystallographic direction [001], the effective field \mathbf{B} is parallel to the plane of the quasi-2D system. Indeed, the field \mathbf{B} due to SIA is always in the plane of the well. For growth directions

¹⁸ From a group-theoretical point of view, this can be traced back to the fact that $|\psi_+(\mathbf{k}_{\parallel})\rangle$ and $|\psi_-(\mathbf{k}_{\parallel})\rangle$ transform according to different irreducible representations of the group of the wave vector \mathbf{k}_{\parallel} .

other than [001], the effective field due to BIA has also an out-of-plane component. In particular, a symmetric QW grown in the crystallographic direction [110] has the point group C_{2v} .¹⁹ Here the BIA induced field $\mathcal{B}(\mathbf{k}_{\parallel})$ must be perpendicular to the plane of the QW (to all orders in \mathbf{k}_{\parallel}). This situation is remarkable because D'yakonov-Perel' spin relaxation is suppressed if the spins are oriented perpendicular to the 2D plane (Refs. [109, 110]). Note also that in [110] grown QWs \mathcal{B} vanishes for $\mathbf{k}_{\parallel} \parallel [001]$ because here the group of \mathbf{k}_{\parallel} is C_{2v} , which has only one irreducible double-group representation, Γ_5 , which is two-dimensional [23].

6.6.2 Numerical Results

The analytically solvable models discussed in the preceding section allow one to study the qualitative trends of BIA and SIA spin splitting in quasi 2D systems. The largest spin splitting can be achieved in narrow-gap semiconductors where the subband dispersion is highly nonparabolic. Therefore, we present next numerically calculated results for $\mathcal{B}(\mathbf{k}_{\parallel})$ obtained by means of the 8×8 Kane Hamiltonian. First we analyze the BIA spin splitting, that is always present in zinc blende QWs. In Fig. 6.19a we show the effective field (6.66) along contours of constant energy for a symmetric GaAs QW grown in the crystallographic direction [001], with a well width of 100 Å. The dimensions of the arrows in Fig. 6.19 are proportional to $|\mathcal{B}| = \Delta k$. We remark that typical Fermi wave vectors of quasi 2D systems are of the order of the in-plane wave vectors covered in Fig. 6.19.

For small in-plane wave vectors \mathbf{k}_{\parallel} , the effective field in Fig. 6.19a is well described by (6.63). For larger wave vectors, the effective field becomes strongly dependent on the direction of \mathbf{k}_{\parallel} . In particular, we see that for $\mathbf{k}_{\parallel} \parallel [110]$ the effective field reverses its direction when we increase k_{\parallel} . This reversal reflects the breakdown of the linear approximation in (6.4). For wider wells, this breakdown occurs at even smaller wave vectors k_{\parallel} , consistent with (6.4).

More specifically, (6.4) predicts for $\mathbf{k}_{\parallel} \parallel [110]$ a reversal of the direction of $\mathcal{B}(\mathbf{k}_{\parallel})$ when $k_{\parallel}^2 = 2\langle k_z^2 \rangle$, independent of the material specific coefficient η that characterizes the strength of BIA spin splitting. Note, however, that $\langle k_z^2 \rangle$ depends on the material specific band offset at the interfaces. For the system in Fig. 6.19a, we find in good agreement with (6.4) that the reversal of $\mathcal{B}(\mathbf{k}_{\parallel})$ occurs for $k_{\parallel} \approx \sqrt{2\langle k_z^2 \rangle} \approx 0.029 \text{ Å}^{-1}$. For comparison, we show in Fig. 6.19b the effective field $\mathcal{B}(\mathbf{k}_{\parallel})$ for a symmetric $\text{Ga}_{0.47}\text{In}_{0.53}\text{As}$ QW with the same well width 100 Å as for Fig. 6.19a. Even though the BIA spin splitting is smaller in $\text{Ga}_{0.47}\text{In}_{0.53}\text{As}$ than in GaAs, higher-order corrections are more important in $\text{Ga}_{0.47}\text{In}_{0.53}\text{As}$ owing to the smaller fundamental gap of this material. Here we have $\langle k_z^2 \rangle \approx 3.6 \times 10^{-4} \text{ Å}^{-2}$, so that $\sqrt{2\langle k_z^2 \rangle} \approx$

¹⁹ Note that for a symmetric QW grown in the crystallographic direction [110], the symmetry axis of the point group C_{2v} is parallel to the axis [001] in the plane of the QW.

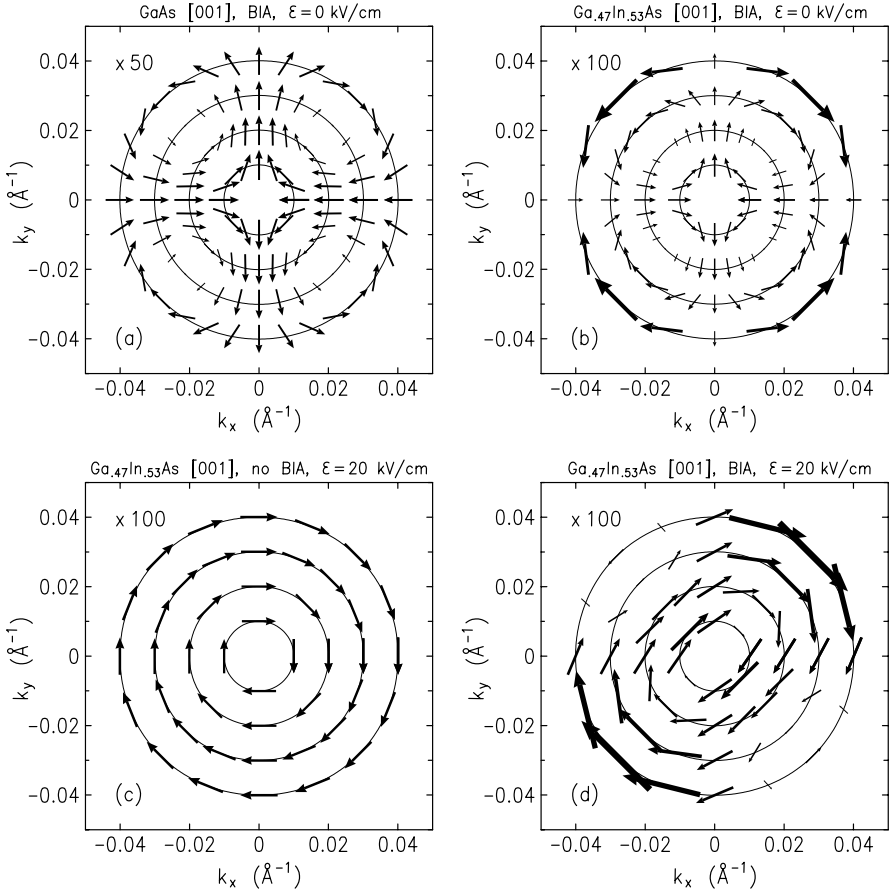


Fig. 6.19. Effective magnetic field $\mathbf{B}(\mathbf{k}_{\parallel})$ for a GaAs–Al_{0.3}Ga_{0.7}As QW (a) and a Ga_{0.47}In_{0.53}As–InP QW ((b), (c), and (c)), both with a well width of 100 Å. In (a) and (b) we have assumed that we have a symmetric well with BIA spin splitting only. (c) shows $\mathbf{B}(\mathbf{k}_{\parallel})$ due to an external field of $\mathcal{E}_z = 20$ kV/cm but neglecting BIA. Finally, (d) shows $\mathbf{B}(\mathbf{k}_{\parallel})$ when we have both BIA and SIA spin splitting (again for $\mathcal{E}_z = 20$ kV/cm). The dimensions of the *arrows* are proportional to $|\mathbf{B}| = \Delta k$. For Ga_{0.47}In_{0.53}As, we have amplified $\mathbf{B}(\mathbf{k}_{\parallel})$ by a factor of 100, for GaAs the factor is 50. All calculations were based on an 8×8 Kane Hamiltonian (Γ_6^c , Γ_8^v , and Γ_7^v) including off-diagonal remote-band contributions of second order in \mathbf{k}

0.027 \AA^{-1} . On the other hand, the reversal of the direction of $\mathbf{B}(\mathbf{k}_{\parallel})$ occurs for $k_{\parallel} \approx 0.021 \text{ \AA}^{-1}$. This illustrates the effect of the higher orders in the BIA spin splitting that were neglected in (6.3) but were fully taken into account in the numerical calculations shown in Fig. 6.19. (Note that in Fig. 6.19a the effective field \mathbf{B} has been amplified by a factor of 50, whereas in Fig. 6.19b it has been amplified by a factor of 100.)

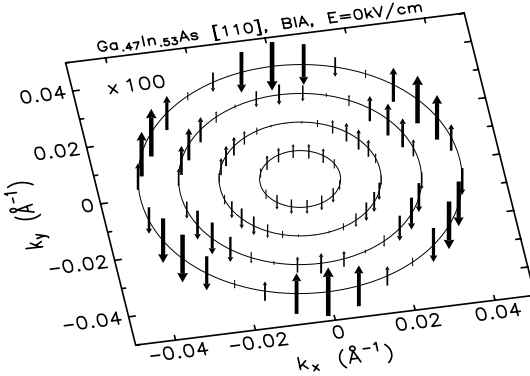


Fig. 6.20. Effective magnetic field $\mathcal{B}(\mathbf{k}_{\parallel})$ for a symmetric $\text{Ga}_{0.47}\text{In}_{0.53}\text{As}$ –InP QW with a well width of 100 Å, grown in the [110] direction. The dimensions of the *arrows* are proportional to $|\mathcal{B}| = \Delta k$, amplified by a factor of 100

$\text{Ga}_{0.47}\text{In}_{0.53}\text{As}$ QWs can have a significant Rashba spin splitting [12], so that these systems are of interest for realizing the spin transistor proposed by Datta and Das [108]. In Fig. 6.19c we show the effective field $\mathcal{B}(\mathbf{k}_{\parallel})$ for the same well as in Fig. 6.19b assuming that we have SIA spin splitting due to an electric field $\mathcal{E} = 20$ kV/cm, but here all tetrahedral terms that give rise to BIA spin splitting have been neglected. The numerical results are in good agreement with what one would expect according to (6.61) and (6.68). Finally, Figure 6.19d shows the effective field $\mathcal{B}(\mathbf{k}_{\parallel})$ for a $\text{Ga}_{0.47}\text{In}_{0.53}\text{As}$ QW when we have both BIA and SIA spin splitting. Owing to the vectorial character of \mathcal{B} , we have regions in \mathbf{k}_{\parallel} space where the contributions of BIA and SIA are additive, whereas in other regions the spin splitting decreases because of the interplay of BIA and SIA, consistent with (6.49).

In Fig. 6.19 we have considered QWs grown in the crystallographic direction [001], so that the effective field $\mathcal{B}(\mathbf{k}_{\parallel})$ is always parallel to the plane of the QW. For comparison, we show in Fig. 6.20 the effective field $\mathcal{B}(\mathbf{k}_{\parallel})$ for a symmetric $\text{Ga}_{0.47}\text{In}_{0.53}\text{As}$ QW grown in the crystallographic direction [110] with $k_x \parallel [00\bar{1}]$ and $k_y \parallel [\bar{1}10]$. Here $\mathcal{B}(\mathbf{k}_{\parallel})$ is perpendicular to the plane of the QW (Ref. [109]). For asymmetric QWs grown in the crystallographic direction [110], the effective field $\mathcal{B}(\mathbf{k}_{\parallel})$ is given by a superposition of an in-plane field as in Fig. 6.19c and a perpendicular field as in Fig. 6.20.

6.7 Measuring $B = 0$ Spin Splitting

Spin splitting has been studied by many different experimental techniques. A detailed discussion of these techniques is beyond the scope of the present work.

In an early experimental investigation, Därr et al. [35] analyzed the electron spin resonance of an electron inversion layer on InSb in a perpendicular and a tilted magnetic field (see Sect. 8.4). Wieck et al. [111] studied 2D holes in an MOS structure on Si(110). In an all-optical experiment at $B = 0$ they observed a splitting of the intersubband resonance transition that was attributed to $B = 0$ spin splitting. Gauer et al. [112, 113] studied spin-conserving and spin-flip intersubband transitions in InAs QWs. Jusserand et al. [114, 9, 115] used spin-flip Raman scattering at zero magnetic field to investigate spin splitting of 2D electrons in GaAs QWs. These experiments will be discussed in more detail in the next section. In a more indirect approach, Dresselhaus et al. [116] studied the spin precession of 2D electrons in a GaAs heterostructure using antilocalization.

Most often, spin splitting has been analyzed by measuring the longitudinal magnetoresistance oscillations in small magnetic fields perpendicular to the plane of the system, known as Shubnikov–de Haas (SdH) oscillations [50, 51, 52, 53, 54, 55, 12, 13, 56, 57, 58, 59, 117, 14, 118, 30]. The classical experiments by Störmer et al. [117] and Eisenstein et al. [14] focused on 2D hole systems in GaAs–AlGaAs heterostructures. Luo et al. [50, 53] studied SdH oscillations of 2D electrons in asymmetric InAs–GaSb QWs. Wollrab et al. [51] measured the spin splitting of electron subbands in an inversion layer on narrow-gap HgCdTe. Das et al. [52] studied the spin splitting in InGaAs–InAlAs heterostructures. In Chap. 9, we shall present a more detailed discussion of SdH oscillations in the presence of SO interaction.

6.8 Comparison with Raman Spectroscopy

Direct evidence of spin splitting of the electron subbands in QW structures comes from the detection of single-particle spin-flip transitions at the Fermi energy, which can be probed by inelastic light-scattering experiments with crossed polarizations of the incident and scattered light. Such experiments have been performed by Jusserand and coworkers [114, 9, 115] on asymmetrically n-doped GaAs–Al_xGa_{1–x}As QWs with a growth direction [001]. These experiments provide clear information about the spin splitting ΔE of the electron subbands at the Fermi energy as a function of the carrier density and about its anisotropy in \mathbf{k}_{\parallel} space. For the growth direction [001], we have the interesting situation that a symmetric QW with a diamond structure has the point group D_{4h} (see Table 3.4). BIA reduces the symmetry to C_{4v} , whereas SIA reduces the symmetry to D_{2d} . Combining both BIA and SIA, we obtain the point group C_{2v} . While for C_{4v} and D_{2d} we obtain the same splittings for $\mathbf{k}_{\parallel} \parallel [110]$ and $\mathbf{k}_{\parallel} \parallel [1\bar{1}0]$, for the point group C_{2v} these two in-plane directions are no longer equivalent (see Sect. 6.4.1). Here we compare the experimental data of Jusserand et al. [114, 9, 115] with calculated spin splittings [8] based on 8×8 and 14×14 $\mathbf{k} \cdot \mathbf{p}$ Hamiltonians and find good quantitative agreement with the Raman data.

A quantitative calculation of the subband dispersion in a QW has to take into account both the bulk band structure of the semiconductor and the geometry of the quantum structure, including the doping profile. The bulk band structure of GaAs is one of the best-known single-particle spectra in solid-state physics and is well described by the 14×14 extended Kane model introduced in Chap. 3. For GaAs, the band parameters of this model have been determined to high precision by a large number of independent experiments. An almost as accurate knowledge exists of the parameters for the barrier material $\text{Al}_x\text{Ga}_{1-x}\text{As}$ ($x \simeq 0.3$) [119]. All band parameters used in the work described here are listed in Appendix D.

The spin-splitting data obtained from inelastic light scattering [114, 115] provide sufficiently accurate and detailed information to test the different models. Here we present results from self-consistent subband calculations based on the 8×8 and 14×14 $\mathbf{k} \cdot \mathbf{p}$ models. The sample parameters were those given in Table 2 of [115]. In the experiments of [114, 9, 115], the spin splitting of the lowest electron subband at the Fermi energy and its dependence on the direction of the in-plane wave vector \mathbf{k}_{\parallel} were detected for several samples with the same nominal width of the QW of 180 Å but for different carrier concentrations.

In Fig. 6.21, we show the conduction band profile obtained from a self-consistent calculation for a 180 Å wide asymmetrically doped GaAs– $\text{Al}_x\text{Ga}_{1-x}\text{As}$ QW with a carrier concentration $N_s = 8 \times 10^{11} \text{ cm}^{-2}$, together with the lowest bound subband levels and the Fermi energy. The self-consistent potential does not depend on whether the 8×8 or 14×14 model is used. With increasing carrier density the potential asymmetry increases. According to the present self-consistent calculations, all carriers can be accommodated in the lowest subband up to $N_s = 1.2 \times 10^{12} \text{ cm}^{-2}$. These results do not change when we consider a weak unintentional acceptor concentration in the GaAs layer. (In the present calculations the depletion charge density was about 10^{10} cm^{-2} , almost independent of N_s .) The spin degeneracy of this subband is lifted at finite in-plane wave vectors owing to BIA and SIA. In Fig. 6.22, we compare the calculated spin splittings $\Delta E(\mathbf{k}_{\parallel})$ for different in-plane directions with the available experimental data. It should be noted that the experimental data points in Fig. 6.22 are those of Fig. 2 of [115] (converted from cm^{-1} to meV) divided by a factor of 2, because the latter data points are Raman spin splittings, which equal twice the subband spin splitting.

In the experiments, the electron densities were determined via the Fermi velocities $v_F = dE(k_{\parallel})/\hbar dk_{\parallel}$ obtained from the dispersion of the Raman single-particle excitation spectrum. The high-energy cutoff frequency for a Raman single-particle excitation of wave vector \mathbf{q} varies as $v_F q$ and was taken as the half-maximum point of the high-energy edge of the non-spin-flip single-particle excitation line shape, measured with the polarizations of the incident and scattered light parallel to each other. In [9, 115], the Fermi velocity was converted into k_F (and the charge carrier density) using an energy-dependent

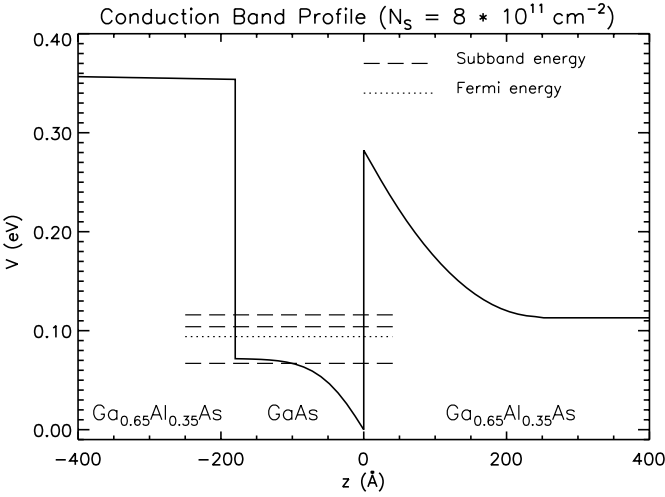


Fig. 6.21. Conduction band profile (*solid line*) of a 180 Å wide asymmetrically doped GaAs–Ga_{0.65}Al_{0.35}As QW with a carrier concentration of $N_s = 8 \times 10^{11} \text{ cm}^{-2}$. The bottom of the bound subbands (*dashed lines*) and the Fermi energy (*dotted line*) are indicated. Taken from [8]. © (1998) by the American Physical Society

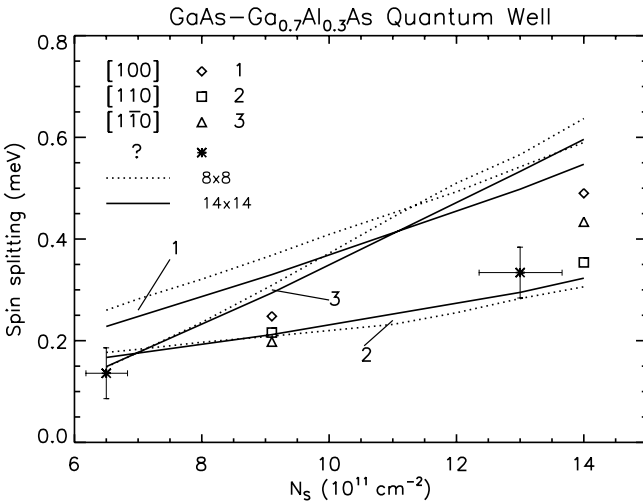


Fig. 6.22. Calculated spin splittings at the Fermi energy vs. carrier concentration for a 180 Å wide asymmetrically doped GaAs–Ga_{0.7}Al_{0.3}As QW for different directions of the in-plane wave vector, obtained from the 8×8 (*dotted lines*) and 14×14 (*solid lines*) models. Experimental data from [9, 115] are shown for comparison. For the experimental data points indicated by the *asterisks*, the direction of the in-plane wave vector was not determined. Taken from [8]. © (1998) by the American Physical Society

mass from a 2×2 model. The estimated error in the determination of these Fermi velocities of about 2.5% corresponds to an error in the densities of about 5%. Owing to the shortcomings of the 2×2 model, these densities turn out to be too large compared with those obtained from the multiband approach. Therefore, the experimental data points in Fig. 6.22 were shifted to lower density values, which, according to the present calculation, correspond to the experimentally determined Fermi velocities. The accuracy of the measured Raman spin splitting ($\pm 0.8 \text{ cm}^{-1}$) gives an error in the subband splittings of $\pm 0.05 \text{ meV}$ (see Fig. 6.22).

Considering the fact that the calculations are parameter-free, the overall agreement with the measured spin splittings is striking. While for the $[110]$ direction the results from both models (curves 2) coincide with each other and with the experimental data, there is some model dependence and deviation from the data points for the $[100]$ (curves 1) and $[\bar{1}\bar{1}0]$ (curves 3) directions, with the results from the 14×14 model (solid lines) being closer to the experiment than the results from the 8×8 model (dotted lines). For the data points denoted by the asterisks, the in-plane wave vector was not determined in the experiment. By comparison with the present calculation, they can be assigned to the $[110]$ direction. The calculated spin splittings turned out to be insensitive to changes in the Al content of the barrier in the range $x = 0.30$ to $x = 0.35$, i.e. they would be the same for $x = 0.33$, the Al content of the samples in [114, 9, 115].

Pfeffer [41] compared the Raman data [114, 9, 115] with calculations based on a 2×2 model for a single heterojunction. He used the depletion charge density N_d (which is usually not known from experimental data) as a free parameter. By changing N_d from 1.5 to $3.5 \times 10^{11} \text{ cm}^{-2}$, he increased the calculated spin splitting, for example for the $[110]$ direction by almost a factor of 2. Pfeffer compared his calculated subband splittings with the experimental data shown in Fig. 2 of [115], which are identified as the measured Raman spin splittings and thus twice the subband splittings.

References

1. C. Kittel: *Quantum Theory of Solids* (Wiley, New York, 1963) 69
2. G. Dresselhaus: Phys. Rev. **100**(2), 580–586 (1955) 2, 5, 24, 69, 71, 72
3. F.J. Ohkawa, Y. Uemura: J. Phys. Soc. Jpn. **37**, 1325 (1974) 5, 35, 38, 65, 69, 78, 83
4. Y.A. Bychkov, E.I. Rashba: J. Phys. C: Solid State Phys. **17**, 6039–6045 (1984) 5, 66, 165, 69, 77, 78, 83
5. U. Rössler, J. Kainz: Solid State Commun. **121**, 313–316 (2002) 69, 110, 114
6. G. Goldoni, A. Fasolino: Phys. Rev. Lett. **69**(17), 2567–2570 (1992) 159, 69
7. R. Winkler: Phys. Rev. B **62**, 4245 (2000) 5, 70, 81, 86, 96, 108, 109
8. L. Wissinger, U. Rössler, R. Winkler, B. Jusserand, D. Richards: Phys. Rev. B **58**, 15375 (1998) 5, 70, 78, 83, 122, 124

9. B. Jusserand, D. Richards, G. Allan, C. Priester, B. Etienne: Phys. Rev. B **51**, 4707 (1995) [5](#), [70](#), [122](#), [123](#), [124](#), [125](#)
10. G.H. Chen, M.E. Raikh: Phys. Rev. B **60**, 4826 (1999) [70](#), [105](#)
11. V.M. Pudalov: Pis'ma Zh. Eksp. Teor. Fiz. **66**, 168–172 (1997). [JETP Lett. **66**, 175 (1997)] [3](#), [70](#)
12. J. Nitta, T. Akazaki, H. Takayanagi, T. Enoki: Phys. Rev. Lett. **78**(7), 1335–1338 (1997) [171](#), [174](#), [70](#), [77](#), [100](#), [109](#), [121](#), [122](#)
13. J.P. Heida, B.J. van Wees, J.J. Kuipers, T.M. Klapwijk, G. Borghs: Phys. Rev. B **57**(19), 11 911–11 914 (1998) [171](#), [172](#), [70](#), [80](#), [122](#)
14. J.P. Eisenstein, H.L. Störmer, V. Narayanamurti, A.C. Gossard, D. Wiegmann: Phys. Rev. Lett. **53**(27), 2579–2582 (1984) [171](#), [172](#), [181](#), [70](#), [122](#)
15. E.O. Kane: J. Phys. Chem. Solids **1**, 249 (1957) [10](#), [27](#), [30](#), [56](#), [156](#), [71](#)
16. U. Rössler: Solid State Commun. **49**, 943 (1984) [4](#), [21](#), [25](#), [26](#), [27](#), [29](#), [71](#)
17. M. Cardona, N.E. Christensen, G. Fasol: Phys. Rev. B **38**(3), 1806–1827 (1988) [25](#), [220](#), [221](#), [71](#), [72](#), [73](#), [74](#)
18. D.G. Seiler, B.D. Bajaj, A.E. Stephens: Phys. Rev. B **16**(6), 2822–2833 (1977) [71](#)
19. H. Riechert, S.F. Alvarado, A.N. Titkov, V.I. Safarov: Phys. Rev. Lett. **52**(25), 2297–2300 (1984) [71](#)
20. M. Braun, U. Rössler: J. Phys. C: Solid State Phys. **18**, 3365 (1985) [30](#), [32](#), [37](#), [40](#), [166](#), [71](#), [77](#)
21. G.E. Pikus, V.A. Marushchak, A.N. Titkov: Sov. Phys. Semicond. **22**(2), 115–124 (1988) [71](#)
22. F. Malcher, G. Lommer, U. Rössler: Superlatt. Microstruct. **2**, 267 (1986) [35](#), [37](#), [47](#), [57](#), [72](#), [74](#), [75](#), [78](#), [83](#)
23. R.H. Parmenter: Phys. Rev. **100**(2), 573–579 (1955) [2](#), [72](#), [119](#)
24. G.F. Koster, J.O. Dimmock, R.G. Wheeler, H. Statz: *Properties of the Thirty-Two Point Groups* (MIT, Cambridge, MA, 1963) [6](#), [21](#), [23](#), [47](#), [166](#), [199](#), [72](#)
25. O. Madelung (Ed.): *Semiconductors*, Vol. 17a of Landolt-Börnstein, New Series III (Springer, Berlin, Heidelberg, 1982) [15](#), [174](#), [219](#), [220](#), [221](#), [222](#), [74](#)
26. O. Madelung (Ed.): *Semiconductors*, Vol. 22a of Landolt-Börnstein, New Series III (Springer, Berlin, Heidelberg, 1987) [74](#)
27. H. Mayer, U. Rössler: Phys. Rev. B **44**, 9048 (1991) [21](#), [24](#), [37](#), [174](#), [212](#), [213](#), [214](#), [220](#), [74](#)
28. R. Eppenga, M.F.H. Schuurmans: Phys. Rev. B **37**(18), 10 923–10 926 (1988) [75](#), [77](#)
29. P. von Allmen: Phys. Rev. B **46**(23), 15 382–15 386 (1992) [76](#)
30. S.J. Papadakis, E.P. De Poortere, H.C. Manoharan, M. Shayegan, R. Winkler: Science **283**, 2056 (1999) [3](#), [6](#), [143](#), [171](#), [172](#), [174](#), [177](#), [178](#), [77](#), [100](#), [104](#), [109](#)
31. Y.A. Bychkov, E.I. Rashba: JETP Lett. **39**(2), 78–81 (1984) [77](#), [78](#), [83](#)
32. G. Lommer, F. Malcher, U. Rössler: Phys. Rev. B **32**, 6965 (1985) [132](#), [77](#), [78](#), [83](#)
33. U. Rössler, F. Malcher, G. Lommer: “Spin splitting in structured semiconductors”, in *High Magnetic Fields in Semiconductor Physics II*, ed. by G. Landwehr (Springer, Berlin, Heidelberg, 1989), Vol. 87 of Solid-State Sciences, p. 376 [166](#), [181](#), [77](#), [78](#), [83](#)
34. H.R. Trebin, U. Rössler, R. Ranvaud: Phys. Rev. B **20**(2), 686–700 (1979) [4](#), [15](#), [22](#), [25](#), [31](#), [32](#), [43](#), [46](#), [48](#), [151](#), [152](#), [158](#), [166](#), [209](#), [210](#), [212](#), [213](#), [214](#), [217](#), [77](#), [98](#), [99](#)

35. A. Därr, J.P. Kotthaus, T. Ando: “Electron-spin resonance in an inversion layer on InSb”, in *Proceedings of the 13th International Conference on the Physics of Semiconductors*, ed. by F.G. Fumi (North-Holland, Amsterdam, 1976), p. 774 **78, 83, 122**
36. L.G. Gerchikov, A.V. Subashiev: *Sov. Phys. Semicond.* **26**(1), 73–78 (1992) **78, 83**
37. R. Lassnig: *Phys. Rev. B* **31**, 8076 (1985) **35, 38, 78, 81, 83, 86, 98**
38. F. Malcher, I. Nachev, A. Ziegler, U. Rössler: *Z. Phys. B: Cond. Mat.* **68**(4), 437–444 (1987) **78, 83**
39. G. Lommer, F. Malcher, U. Rössler: *Phys. Rev. Lett.* **60**, 728 (1988) **6, 166, 78, 82, 83**
40. P. Pfeffer, W. Zawadzki: *Phys. Rev. B* **52**(20), 14 332–14 335 (1995) **78, 83, 102**
41. P. Pfeffer: *Phys. Rev. B* **55**(12), R7935–R7362 (1997) **78, 83, 125**
42. T. Schäpers, G. Engels, J. Lange, T. Klocke, M. Hollfelder, H. Lüth: *J. Appl. Phys.* **83**(8), 4324–4333 (1998) **78, 83**
43. P. Pfeffer, W. Zawadzki: *Phys. Rev. B* **59**, R5312–R5315 (1999) **78, 83**
44. I. Nachev: *Semicond. Sci. Technol.* **3**, 29 (1988) **38, 78, 83**
45. P. Sobkowicz: *Semicond. Sci. Technol.* **5**, 183 (1990) **38, 78, 83**
46. P. Sobkowicz: *J. Cryst. Growth* **101**(1–4), 337–340 (1990) **78, 83**
47. E.A. de Andrada e Silva: *Phys. Rev. B* **46**, 1921 (1992) **78, 83, 99**
48. E.A. de Andrada e Silva, G.C. La Rocca, F. Bassani: *Phys. Rev. B* **50**(12), 8523–8533 (1994) **182, 189, 78, 83**
49. E.A. de Andrada e Silva, G.C. La Rocca, F. Bassani: *Phys. Rev. B* **55**(24), 16 293–16 299 (1997) **78, 83**
50. J. Luo, H. Munekata, F.F. Fang, P.J. Stiles: *Phys. Rev. B* **38**(14), 10 142–10 145 (1988) **171, 172, 80, 122**
51. R. Wollrab, R. Sizmann, F. Koch, J. Ziegler, H. Maier: *Semicond. Sci. Technol.* **4**, 491 (1989) **171, 172, 80, 122**
52. B. Das, D.C. Miller, S. Datta, R. Reifengerger, W.P. Hong, P.K. Bhat-tacharya, J. Singh, M. Jaffe: *Phys. Rev. B* **39**(2), 1411–1414 (1989) **171, 172, 174, 80, 122**
53. J. Luo, H. Munekata, F.F. Fang, P.J. Stiles: *Phys. Rev. B* **41**, 7685 (1990) **171, 172, 80, 122**
54. M. Schultz, F. Heinrichs, U. Merkt, T. Collin, T. Skauli, S. Løvold: *Semicond. Sci. Technol.* **11**, 1168–1172 (1996) **171, 172, 80, 122**
55. G. Engels, J. Lange, T. Schäpers, H. Lüth: *Phys. Rev. B* **55**(4), R1958–R1961 (1997) **171, 172, 80, 122**
56. S. Brosig, K. Ensslin, R.J. Warburton, C. Nguyen, R. Brar, M. Thomas, H. Kroemer: *Phys. Rev. B* **60**(20), R13 989–R13 992 (1999) **171, 172, 80, 122**
57. D. Grundler: *Phys. Rev. Lett.* **84**(26), 6074–6077 (2000) **171, 172, 80, 122**
58. T. Matsuyama, R. Kürsten, C. Meissner, U. Merkt: *Phys. Rev. B* **61**(23), 15 588–15 591 (2000) **171, 172, 80, 122**
59. X.C. Zhang, A. Pfeuffer-Jeschke, K. Ortner, V. Hock, H. Buhmann, C.R. Becker, G. Landwehr: *Phys. Rev. B* **63**, 245 305 (2001) **171, 172, 122**
60. R. Winkler: *J. Phys.: Condens. Matter* **5**, 2321 (1993) **42, 142, 80, 81, 95**
61. E.L. Ivchenko, G.E. Pikus: *Superlattices and Other Heterostructures*, 2nd edn., Vol. 110 of Solid-State Sciences (Springer, Berlin, Heidelberg, 1997) **82**

62. J.J. Sakurai: *Modern Quantum Mechanics*, revised edn. (Addison-Wesley, Redwood City, 1994) **31**, **151**, **152**, **185**, **204**, **208**, **83**
63. F. Stern: Phys. Rev. B **5**(12), 4891–4899 (1972) **86**, **106**
64. R. Winkler, U. Kunze, U. Rössler: Surf. Sci. **263**, 222 (1992) **37**, **220**, **221**, **86**
65. D.A. Broido, L.J. Sham: Phys. Rev. B **31**, 888 (1985) **35**, **38**, **43**, **46**, **55**, **161**, **86**, **93**
66. U. Ekenberg, M. Altarelli: Phys. Rev. B **32**, 3712 (1985) **35**, **43**, **161**, **86**, **93**, **97**
67. T. Ando: J. Phys. Soc. Jpn. **54**, 1528–1536 (1985) **35**, **38**, **86**
68. E. Bangert, G. Landwehr: Superlatt. Microstruct. **1**, 363 (1985) **43**, **161**, **86**
69. R. Winkler, U. Rössler: Phys. Rev. B **48**, 8918 (1993) **35**, **38**, **39**, **40**, **139**, **86**, **93**, **106**, **108**
70. R. Winkler, M. Merkler, T. Darnhofer, U. Rössler: Phys. Rev. B **53**, 10 858 (1996) **5**, **152**, **158**, **160**, **161**, **162**, **163**, **219**, **86**
71. O. Mauritz, U. Ekenberg: Phys. Rev. B **55**(16), 10 729–10 733 (1997) **86**
72. J.M. Luttinger: Phys. Rev. **102**(4), 1030 (1956) **3**, **18**, **28**, **29**, **131**, **142**, **158**, **88**, **98**, **99**, **106**
73. U. Ekenberg, M. Altarelli: Phys. Rev. B **30**, 3569 (1984) **38**, **93**
74. A.G. Davies, J.E.F. Frost, D.A. Ritchie, D.C. Peacock, R. Newbury, E.H. Linfield, M. Pepper, G.A.C. Jones: J. Crystal Growth **111**(1–4), 318–322 (1991) **139**, **95**
75. J.J. Heremans, M.B. Santos, K. Hirakawa, M. Shayegan: J. Appl. Phys. **76**(3), 1980–1982 (1994) **139**, **143**, **95**
76. P. Voisin, C. Delalande, M. Voos, L.L. Chang, A. Segmuller, C.A. Chang, L. Esaki: Phys. Rev. B **30**(4), 2276–2278 (1984) **98**, **112**
77. G.L. Bir, G.E. Pikus: *Symmetry and Strain-Induced Effects in Semiconductors* (Wiley, New York, 1974) **3**, **4**, **6**, **15**, **16**, **18**, **19**, **201**, **213**, **98**, **118**
78. B.F. Zhu, Y.C. Chang: Phys. Rev. B **50**(16), 11 932–11 948 (1994) **99**, **114**
79. N. Dai, G.A. Khodaparast, F. Brown, R.E. Doezema, S.J. Chung, M.B. Santos: Appl. Phys. Lett. **76**(26), 3905–3907 (2000) **102**
80. S.J. Chung, N. Dai, G.A. Khodaparast, J.L. Hicks, K.J. Goldammer, F. Brown, W.K. Liu, R.E. Doezema, S.Q. Murphy, M.B. Santos: Physica E **7**, 809–813 (2000) **102**
81. R. Winkler, H. Noh, E. Tutuc, M. Shayegan: Phys. Rev. B **65**, 155 303 (2002) **54**, **104**, **106**, **107**, **108**
82. F. Stern: Phys. Rev. Lett. **33**(16), 960–963 (1974) **106**, **108**
83. F. Stern, S. Das Sarma: Phys. Rev. B **30**(2), 840–848 (1984) **107**
84. E. Tutuc, E.P. De Poortere, S.J. Papadakis, M. Shayegan: Phys. Rev. Lett. **86**(13), 2858–2861 (2001) **110**
85. I.L. Aleñner, E.L. Ivchenko: JETP Lett. **55**(11), 692–695 (1992) **5**, **110**, **111**, **112**
86. E.L. Ivchenko, A.Y. Kaminskiĭ, I.L. Aleñner: JETP **77**(4), 609–616 (1993) **110**, **112**
87. E.L. Ivchenko, A.Y. Kaminski, U. Rössler: Phys. Rev. B **54**(8), 5852–5859 (1996) **110**, **111**, **112**
88. O. Krebs, W. Seidel, J.P. André, D. Bertho, C. Jouanin, P. Voisin: Semicond. Sci. Technol. **12**, 938–942 (1997) **110**, **111**
89. O. Krebs, D. Rondi, J.L. Gentner, L. Goldstein, P. Voisin: Phys. Rev. Lett. **80**(26), 5770–5773 (1998) **110**, **111**

90. O. Krebs, P. Voisin: Phys. Rev. B **61**(11), 7265–7268 (2000) [110](#), [111](#)
91. B. Foreman: Phys. Rev. Lett. **82**(6), 1339 (1999) [110](#)
92. O. Krebs, P. Voisin: Phys. Rev. Lett. **82**(6), 1340 (1999) [110](#)
93. L. Vervoort, R. Ferreira, P. Voisin: Phys. Rev. B **56**(20), 12 744–12 747 (1997) [110](#), [114](#)
94. L. Vervoort, R. Ferreira, P. Voisin: Semicond. Sci. Technol. **14**, 227–230 (1999) [110](#), [114](#)
95. X.L. Ye, Y.H. Chen, J.Z. Wang, Z.G. Wang, Z. Yang: Phys. Rev. B **63**, 115 317 (2001) [110](#), [114](#)
96. L.D. Landau, E.M. Lifshitz: *Electrodynamics of Continuous Media*, 2nd edn. (Pergamon, Oxford, 1984), Chaps. 13, 98, and 99 [110](#)
97. H.W. van Kesteren, E.C. Cosman, W.A.J.A. van der Poel: Phys. Rev. B **41**(8), 5283–5292 (1990) [5](#), [131](#), [138](#), [141](#), [146](#), [111](#), [112](#), [114](#)
98. C. Gourdon, P. Lavallard: Phys. Rev. B **46**(8), 4644–4650 (1992) [111](#), [114](#)
99. O. Krebs, P. Voisin: Phys. Rev. Lett. **77**(9), 1829–1832 (1996) [112](#)
100. R. Magri, A. Zunger: Phys. Rev. B **62**(15), 10 364–10 372 (2000) [111](#), [112](#), [113](#)
101. S.H. Kwok, H.T. Grahn, K. Ploog, R. Merlin: Phys. Rev. Lett. **69**(6), 973–976 (1992) [112](#), [113](#)
102. Y.C. Chang, J.N. Schulman: Appl. Phys. Lett. **43**(6), 536–538 (1983) [112](#)
103. J.N. Schulman, Y.C. Chang: Phys. Rev. B **31**(4), 2056–2068 (1985) [112](#), [113](#)
104. Y.C. Chang, J.N. Schulman: Phys. Rev. B **31**(4), 2069–2079 (1985) [112](#), [113](#)
105. G. Edwards, J.C. Inkson: Solid State Commun. **89**(7), 595–599 (1994) [112](#)
106. D.A. Broido, L.J. Sham: Phys. Rev. B **34**(6), 3917–3923 (1986) [114](#)
107. M.I. D'yakonov, V.I. Perel': Sov. Phys.–Solid State **13**(12), 3023–3026 (1972) [117](#), [118](#)
108. S. Datta, B. Das: Appl. Phys. Lett. **56**(7), 665–667 (1990) [3](#), [117](#), [118](#), [121](#)
109. M.I. D'yakonov, V.Y. Kachorovskii: Sov. Phys. Semicond. **20**(1), 110–112 (1986) [119](#), [121](#)
110. Y. Ohno, R. Terauchi, T. Adachi, F. Matsukura, H. Ohno: Phys. Rev. Lett. **83**(20), 4196–4199 (1999) [119](#)
111. A.D. Wieck, E. Batke, D. Heitmann, J.P. Kotthaus, E. Bangert: Phys. Rev. Lett. **53**(5), 493–496 (1984) [122](#)
112. C. Gauer, A. Wixforth, J.P. Kotthaus, M. Kubisa, W. Zawadzki, B. Brar, H. Kroemer: Phys. Rev. Lett. **74**(14), 2772–2775 (1995) [122](#)
113. C. Gauer, M. Hartung, A. Wixforth, J.P. Kotthaus, B. Brar, H. Kroemer: Surf. Sci. **361/362**, 472–475 (1996) [122](#)
114. B. Jusserand, D. Richards, H. Peric, B. Etienne: Phys. Rev. Lett. **69**(5), 848 (1992) [122](#), [123](#), [125](#)
115. D. Richards, B. Jusserand, G. Allan, C. Priester, B. Etienne: Solid State Electron. **40**, 127 (1992) [122](#), [123](#), [124](#), [125](#)
116. P.D. Dresselhaus, C.M.A. Papavasiliou, R.G. Wheeler: Phys. Rev. Lett. **68**(1), 106–109 (1992) [122](#)
117. H.L. Störmer, Z. Schlesinger, A. Chang, D.C. Tsui, A.C. Gossard, W. Wiegmann: Phys. Rev. Lett. **51**, 126 (1983) [6](#), [171](#), [172](#), [122](#)
118. J.P. Lu, J.B. Yau, S.P. Shukla, M. Shayegan, L. Wissinger, U. Rössler, R. Winkler: Phys. Rev. Lett. **81**, 1282 (1998) [171](#), [172](#), [174](#), [179](#), [122](#)
119. S. Adachi: *GaAs and Related Materials: Bulk Semiconducting and Superlattice Properties* (World Scientific, Singapore, 1994) [123](#)

7 Anisotropic Zeeman Splitting in Quasi-2D Systems

An external magnetic field lifts time inversion symmetry so that we can obtain a finite Zeeman energy splitting $\Delta E = g^* \mu_B B$, where g^* is the effective g factor and μ_B the Bohr magneton of the electron or hole states. It was first shown by Roth et al. [1] that electrons can have an effective g factor g^* that differs substantially from the free-electron value $g_0 = 2$. Similarly to the $B = 0$ spin splitting discussed in the preceding chapter, the effective g factor $g^* \neq 2$ results from the spin–orbit interaction, which couples the orbital motion with the spin degree of freedom. This can be understood once again by means of (5.1): without SO interaction, the motion of spin-up electrons would be completely decoupled from the motion of spin-down electrons, and there would be identical Hamiltonians $\mathcal{H}_{\mathbf{k},p}$ for spin-up and spin-down electrons except for the trivial Zeeman term $\pm(g_0/2)\mu_B B$, so that in this case Zeeman splitting would be controlled by the g factor $g_0 = 2$ of free electrons.¹

In semiconductors, the orbital motion and the effective Zeeman splitting of the electrons are closely related to each other. The inverse effective-mass tensor (times $\hbar^2/2$) is the prefactor of the quadratic terms in the dispersion $E(\mathbf{k})$ that are *symmetric* in the components of the wave vector \mathbf{k} . On the other hand, g^* (times $i\hbar\mu_B/(2e)$) is the prefactor of the *antisymmetric* quadratic terms in $E(\mathbf{k})$ [3, 1]. These antisymmetric terms reflect the non-commutativity of the components of \mathbf{k} for $B > 0$, which is expressed by the commutator relations (2.17).

Since the early days of 2D carrier systems in semiconductors, it has been commonly assumed that the Zeeman splitting is independent of the direction of the external magnetic field B [4]. Recently, however, calculations and experiments have shown that g^* can have different values for \mathbf{B} applied in the direction normal to the plane of the 2D system and for \mathbf{B} in the plane of the QW [5, 6, 7, 8, 9, 10].

¹ It was first noted by Janak [2] that exchange interactions among the carriers in a (quasi)-2D system can also modify the g factor of the particles. As we want to focus on anisotropies of g^* reflecting the anisotropy of the crystal structure, we assume that the isotropic exchange–correlation interaction is less important in this context. However, for a quantitative agreement with experimental data it can be important that the exchange–correlation interaction is taken into account, see the discussion at the end of Sect. 7.3.2.

In Sect. 7.1, we discuss the anisotropic Zeeman splitting in 2D electron systems. Next we discuss, in Sect. 7.2, Zeeman splitting in inversion-asymmetric systems. Zeeman splitting in hole systems depends strongly on the crystallographic direction in which the sample is grown. In Sect. 7.3 we discuss Zeeman splitting in 2D hole systems that have been grown in low-symmetry directions such as [113]. In Sect. 7.4 we discuss the Zeeman splitting of 2D hole systems with a growth direction [001]. For this high-symmetry direction, the results differ qualitatively from the general case discussed in Sect. 7.3.

7.1 Zeeman Splitting in 2D Electron Systems

For electrons in the conduction band Γ_6^c of a bulk semiconductor the Zeeman splitting $\Delta E = g^* \mu_B B$ is independent of the direction of the magnetic field \mathbf{B} . This can be traced back to the fact that to linear order in \mathbf{B} , the invariant expansion for the Γ_6^c band contains only one term (see Table C.5),

$$\mathcal{H}_{6c6c}^z = \frac{g^*}{2} \mu_B \mathbf{B} \cdot \boldsymbol{\sigma} . \quad (7.1)$$

In quasi-2D systems, the reduced symmetry gives rise to different invariants for the in-plane and perpendicular components $\mathbf{B}_{\parallel} = (B_x, B_y, 0)$ and B_z . We obtain

$$\mathcal{H}_{6c6c}^z = \frac{g_{\parallel}}{2} \mu_B (B_x \sigma_x + B_y \sigma_y) + \frac{g_z}{2} \mu_B B_z \sigma_z , \quad (7.2)$$

with effective g factors g_{\parallel} and g_z . This equation is fully consistent with the results in Sect. 4.6.2, where we used Löwdin partitioning to obtain the explicit analytical expressions (4.42a) and (4.42b) for g_{\parallel} and g_z , respectively.

We have noted already that (4.42) implies that the effective g factor in a quasi-2D system is reduced in magnitude owing to subband confinement [11, 5]. More specifically, we can see in these equations that g_{\parallel} for the lowest electron subband stems from $\mathbf{k} \cdot \mathbf{p}$ coupling to the l_2 and s_2 subbands, whereas g_z originates from the $\mathbf{k} \cdot \mathbf{p}$ coupling to the h_1 , l_1 , and s_1 subbands. The latter subbands are usually significantly more strongly bound than the l_2 and s_2 subbands. Therefore it follows from (4.42a) and (4.42b) that, in general, $|g_{\parallel}| < |g_z|$.² In order to check these qualitative arguments, we shall compare them with the results of accurate numerical calculations. In Fig. 7.1 we show the effective g factors g_{\parallel} and g_z , calculated as a function of the well width w , for 2D electron systems in the lowest subband of QWs made of different materials. For comparison, the effective g factor g_{bulk}^* of the corresponding bulk material is marked by arrows. The numerical calculation was based on an 8×8 multiband Hamiltonian (Γ_6^c , Γ_8^v , and Γ_7^v). This model contains g^* only implicitly. Therefore, we extracted g_{\parallel} from the Zeeman splitting ΔE calculated at $B = 1$ T using $g_{\parallel} = \Delta E / (\mu_B B)$. For g_z , we evaluated the Zeeman splitting of the lowest Landau level.

² We can have $|g_{\parallel}| > |g_z|$ if the order of the HH and LH states is reversed.

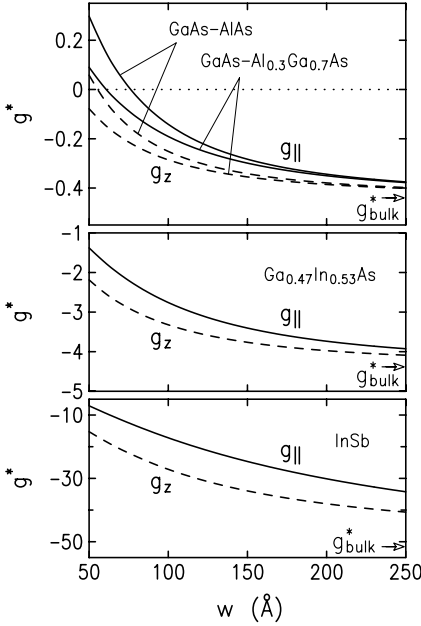


Fig. 7.1. Effective g factors g_{\parallel} and g_z as a function of well width w for a 2D electron system in the lowest subband (the results for g_z also refer to the lowest Landau level) of symmetric GaAs–Al_{0.3}Ga_{0.7}As, GaAs–AlAs, Ga_{0.47}In_{0.53}As–Al_{0.47}In_{0.53}As, and InSb QWs calculated numerically by means of an 8×8 multiband Hamiltonian (Γ_6^c , Γ_8^v , and Γ_7^v). The effective g factor g_{bulk}^* of the bulk material is marked by arrows

We see in Fig. 7.1 that we have a substantial decrease of $|g^*|$, which is strongest in narrow QWs. Moreover, the effective g factor g_{\parallel} is significantly smaller in magnitude than g_z , in good agreement with the above qualitative arguments. In GaAs, the effective g factor of the bulk material is rather small ($g^* = -0.44$). Here we have the interesting situation that nonparabolicity can give rise to a sign reversal of g^* in sufficiently narrow QWs. We remark that bulk AlAs has a positive g factor so that one can expect to find a sign reversal of g^* in sufficiently narrow QWs even without higher-order band structure effects being taken into account [12].³ However, the probability of finding an electron in the barriers is much smaller than the probability of finding an electron in the well, so that the g factor of the barrier material is less important. This can be seen in the upper part of Fig. 7.1, where we compare g^* for a GaAs–Al_{0.3}Ga_{0.7}As and a GaAs–AlAs QW. The curves for the two systems are not far from each other. Note also that an increasing Al content x in the Al _{x} Ga _{$1-x$} barriers reduces g^* both because of the larger contribution from g^* in the barriers and because of the stronger confinement of the electron and hole subband states.³ The latter implies that with increasing x , the band structure effects become more important, too.

³ Both effects originate in the fact that $g^* - g'$ is inversely proportional to the (effective) energy gap; see (4.39b) and (4.42).

7.2 Zeeman Splitting in Inversion-Asymmetric Systems

A symmetric QW grown in the crystallographic direction [001] has the point group D_{2d} (see Table 3.4), so that for an in-plane magnetic field \mathbf{B}_{\parallel} the effective g factor of electrons must be independent of the crystallographic direction of \mathbf{B}_{\parallel} . If the confining potential of the QW is inversion-asymmetric, however, the point group is reduced to C_{2v} and it is no longer required by symmetry that the effective g factor is independent of the direction of \mathbf{B}_{\parallel} [13]. By inspection of Tables C.3 and C.4, we can see that, for the Γ_6^c conduction band, we have one new invariant that will describe this effect in the lowest order in the electric field \mathcal{E} and magnetic field \mathbf{B} ,

$$\mathcal{H}_{6c6c}^{z,r,b} = z_{41}^{6c6c} [(\mathcal{E}_y B_z + \mathcal{E}_z B_y) \sigma_x + \text{cp}] . \quad (7.3)$$

For $\mathcal{E} = (0, 0, \mathcal{E}_z)$, this becomes

$$\mathcal{H}_{6c6c}^{z,r,b} = z_{41}^{6c6c} \mathcal{E}_z (B_y \sigma_x + B_x \sigma_y) . \quad (7.4)$$

Fourth-order Löwdin perturbation theory gives the following for the coefficient z_{41}^{6c6c} :

$$z_{41}^{6c6c} = \frac{ie^2}{3\hbar} PP'Q \left[\frac{1}{E_0 - E'_0 - \Delta'_0} \left(\frac{1}{(E_0 + \Delta_0)^2} - \frac{1}{E_0^2} \right) + \frac{1}{E_0} \left(\frac{1}{(E_0 - E'_0 - \Delta'_0)^2} - \frac{1}{(E_0 - E'_0)^2} \right) \right] . \quad (7.5)$$

The Zeeman term (7.4) emerges from the combined effect of bulk inversion asymmetry (BIA), an electric field \mathcal{E}_z due to structure inversion asymmetry (SIA), and an in-plane magnetic field $\mathbf{B}_{\parallel} = (B_x, B_y, 0)$. An anisotropic effective g factor in inversion-asymmetric QWs has been observed experimentally by Oestreich et al. [14] using spin quantum beat spectroscopy.

In Chap. 6, we discussed the SO terms symmetric in the components of the wave vector \mathbf{k} that give rise to a spin splitting at $B = 0$. But these terms also affect the spin splitting of electrons and holes at $B > 0$, and these terms complement the Zeeman term (7.4). Before discussing these matters in detail, we recall the effect of \mathbf{B}_{\parallel} in the framework of a simple effective-mass Hamiltonian (4.15). Using the gauge (4.2), this Hamiltonian can be evaluated perturbatively [15]. Up to second order in B_{\parallel} , we obtain for the α th subband

$$E_{\alpha}(\mathbf{k}_{\parallel}) = E_{\alpha} + \frac{\hbar^2 \tilde{\mathbf{k}}_{\parallel}^2}{2m^*} + \frac{e^2 B_{\parallel}^2}{2m^*} (\langle z^2 \rangle - \langle z \rangle^2) + \frac{e^2 \hbar^2}{m^* 2} (\mathbf{k}_x B_y - \mathbf{k}_y B_x)^2 \sum_{\beta \neq \alpha} \frac{|\langle \alpha | z | \beta \rangle|^2}{E_{\alpha} - E_{\beta}} \pm \frac{g^*}{2} \mu_B B_{\parallel} , \quad (7.6)$$

where

$$\tilde{\mathbf{k}}_{\parallel} = \begin{pmatrix} \mathbf{k}_x + (e/\hbar) \langle z \rangle B_y \\ \mathbf{k}_y - (e/\hbar) \langle z \rangle B_x \\ 0 \end{pmatrix} \quad (7.7)$$

and $\langle \dots \rangle \equiv \langle \alpha | \dots | \alpha \rangle$. Equation (7.6) allows a simple interpretation of the effect of \mathbf{B}_{\parallel} . The magnetic field shifts the energy parabolas in \mathbf{k}_{\parallel} space by $(e/\hbar)\langle z \rangle B_{\parallel}$. The third term gives rise to a diamagnetic shift of the subband edge proportional to $\langle z^2 \rangle - \langle z \rangle^2$. The fourth term results in an increased effective mass in a quasi-2D system in the presence of an in-plane magnetic field [15]. The mass increase reflects the fact that, ultimately, for large B_{\parallel} (i.e. $\lambda_c \ll w$), the electron states become dispersionless Landau levels. Note that this term, which has sometimes been overlooked, depends on \mathbf{k}_{\parallel} and not on $\tilde{\mathbf{k}}_{\parallel}$. In a QW symmetric with respect to $z = 0$, we have $\langle z \rangle = 0$ but $\langle z^2 \rangle \neq 0$ and $\langle \alpha | z | \beta \rangle \neq 0$ for $\alpha \neq \beta$.⁴

The intuitive picture underlying the above interpretation of (7.6) should be used with caution, however, because the c -numbers \mathbf{k}_{\parallel} and $\tilde{\mathbf{k}}_{\parallel}$ are not gauge-invariant quantities.⁵ This can be seen if we choose, for example, the symmetric gauge $\mathbf{A} = (1/2) \mathbf{B}_{\parallel} \times \mathbf{r}$, for which we cannot factorize the wave functions as in (4.1), anymore.

Similarly to (7.6), we obtain the following from first-order perturbation theory applied to the Dresselhaus term (neglecting the terms of third order in \mathbf{k}_{\parallel}) [13]:

$$\begin{aligned} \mathcal{H}_{6c6c}^b &= \mathbf{b}_{41}^{6c6c} \langle k_z^2 \rangle (-\tilde{\mathbf{k}}_x \sigma_x + \tilde{\mathbf{k}}_y \sigma_y) \\ &\quad + \mathbf{b}_{41}^{6c6c} (\langle k_z^2 \rangle \langle z \rangle - \langle \{k_z^2, z\} \rangle) \frac{e}{\hbar} (B_y \sigma_x + B_x \sigma_y) \end{aligned} \quad (7.8a)$$

$$= \mathbf{b}_{41,1}^{6c6c} (-\tilde{\mathbf{k}}_x \sigma_x + \tilde{\mathbf{k}}_y \sigma_y) + \mathbf{b}_{41,2}^{6c6c} (B_y \sigma_x + B_x \sigma_y), \quad (7.8b)$$

where the second equation defines the symbols $\mathbf{b}_{41,1}^{6c6c}$ and $\mathbf{b}_{41,2}^{6c6c}$. In (7.8a), the factor $\langle k_z^2 \rangle \langle z \rangle - \langle \{k_z^2, z\} \rangle$ in the second term vanishes in a symmetric QW, but it can be nonzero in an asymmetric QW. Therefore the second term emerges from the combined effect of BIA and SIA. Apparently, we have decomposed the Dresselhaus term into an “orbital” part depending on $\tilde{\mathbf{k}}_{\parallel}$ plus an anisotropic Zeeman-like term similar to (7.4). However, while in a proper Zeeman term (including (7.4)) the spin degree of freedom is decoupled from the orbital motion, no such separation of the spin and orbital degrees of freedom is possible for (7.8). We note that for any invariant $\mathcal{I}(\mathbf{k})$, gauge invariance is only achieved if a gauge transformation is applied to the full

⁴ It is illuminating to compare the approximate expression (7.6) with the exact analytical results for a parabolic QW in the presence of an in-plane magnetic field; see, for example, Sect. 1.6 of [16].

⁵ In a perturbative treatment of \mathcal{E} and \mathbf{B} , gauge invariance can be a rather tricky issue that is not automatically fulfilled; see, for example, [17,18,19] and references therein.

invariant. Accordingly, it is not possible to decompose the Dresselhaus term, which is symmetric in the components of \mathbf{k} , into a Zeeman term antisymmetric in the components of \mathbf{k} plus a “reduced” symmetric invariant. Instead we must always consider *both* terms in (7.8).

To illustrate the meaning of (7.8) we can include it in the effective-mass model (7.6). For simplicity, we shall ignore the component of \mathbf{k}_{\parallel} parallel to \mathbf{B}_{\parallel} because it remains unaffected by the magnetic field. Diagonalization of the resulting expression yields (neglecting for simplicity the coupling to other subbands)

$$E_{\alpha\pm}(\mathbf{k}_{\parallel}) = E_{\alpha} + \frac{\hbar^2 \tilde{\mathbf{k}}_{\parallel}^2}{2m^*} + \frac{e^2 B_{\parallel}^2}{2m^*} (\langle z^2 \rangle - \langle z \rangle^2) \\ \pm \left[\zeta \mathbf{b}_{41,1}^{6c6c} \tilde{\mathbf{k}}_{\parallel} + \left(\frac{g^*}{2} \mu_B - \mathbf{b}_{41,2}^{6c6c} \right) B_{\parallel} \right]. \quad (7.9)$$

Here the upper and lower signs refer to the spin-split energy branches. We have $\zeta = +1$ for $\mathbf{k}_{\parallel} \parallel [110]$ and $\mathbf{B} \parallel [\bar{1}10]$, whereas $\zeta = -1$ refers to $\mathbf{k}_{\parallel} \parallel [\bar{1}10]$ and $\mathbf{B} \parallel [110]$. While in (7.6) the spin-split parabolas were shifted in \mathbf{k}_{\parallel} space by the same amount $(e/\hbar) \langle z \rangle B_{\parallel}$ we now obtain two parabolas, the minima of which are at different points \mathbf{k}_{\pm} in \mathbf{k}_{\parallel} space,

$$\mathbf{k}_{\pm} = -\frac{e}{\hbar} \langle z \rangle B_{\parallel} \mp \zeta \mathbf{b}_{41,1}^{6c6c} \frac{m^*}{\hbar^2}. \quad (7.10)$$

Inserting (7.10) into (7.9) yields

$$E_{\alpha\pm}(\mathbf{k}_{\pm}) = E_{\alpha} - \mathbf{b}_{41,1}^{6c6c2} \frac{m^*}{2\hbar^2} \pm \left(\frac{g^*}{2} \mu_B - \zeta \mathbf{b}_{41,2}^{6c6c} \right) B_{\parallel}, \quad (7.11)$$

i.e. the “Zeeman” splitting $\pm(g^* \mu_B/2 - \zeta \mathbf{b}_{41,2}^{6c6c}) B_{\parallel}$ refers to the difference between the energies of eigenstates at different points in \mathbf{k}_{\parallel} space. This can be seen in Fig. 7.2, where we show the dispersion $E_{\pm}(\mathbf{k}_{\parallel})$ of the lowest electron subband in a 100 Å wide GaAs–AlAs QW in the presence of an in-plane magnetic field $B_{\parallel} = 1$ T and an electric field $\mathcal{E}_z = 20$ kV/cm. The solid and dashed lines refer to $\mathbf{B} \parallel [110]$ and $\mathbf{B} \parallel [\bar{1}10]$, respectively, and we have assumed $\mathbf{k}_{\parallel} \perp \mathbf{B}_{\parallel}$. The upper part was calculated by means of a 14×14 Hamiltonian (Γ_8^c , Γ_7^c , Γ_6^c , Γ_8^v , and Γ_7^v). The lower part was based on a simplified 2×2 Hamiltonian (Γ_6^c).⁶ The latter calculation results in a splitting ΔE that is substantially larger than the splitting based on the more accurate

⁶ When comparing the upper and lower parts of Fig. 7.2, the reader might wonder why nonparabolicity increases the subband energy while it is known that, for the bulk dispersion, nonparabolicity always lowers the energy of conduction band states. This can be traced back to a competition between the effect of nonparabolicity on the conduction band states inside the well – they lie above the band edge, so that nonparabolicity increases the effective mass – and the effect of nonparabolicity on the states in the barriers – they lie below the band edge, so that nonparabolicity decreases the effective mass [20].

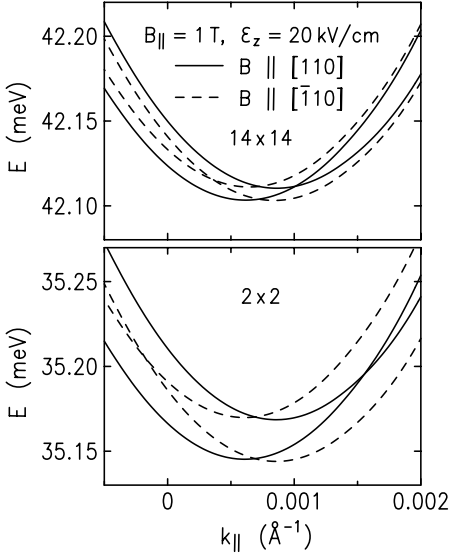


Fig. 7.2. Dispersion $E_{\pm}(\mathbf{k}_{\parallel})$ of the lowest electron subband in a 100 Å wide GaAs–AlAs QW in the presence of an in-plane magnetic field $B_{\parallel} = 1$ T and an electric field $\mathcal{E}_z = 20$ kV/cm. The *solid* and *dashed* lines refer to $\mathbf{B} \parallel [110]$ and $\mathbf{B} \parallel [\bar{1}10]$, respectively, and we have assumed $\mathbf{k}_{\parallel} \perp \mathbf{B}_{\parallel}$. The *upper part* was calculated by means of a 14×14 Hamiltonian (Γ_8^c , Γ_7^c , Γ_6^c , Γ_8^v , and Γ_7^v). The *lower part* was based on a simplified 2×2 Hamiltonian (Γ_6^c)

14×14 Hamiltonian, consistent with the results in Sect. 7.1. The minima of $E_{\pm}(\mathbf{k}_{\parallel})$ occur at finite in-plane wave vectors $\mathbf{k}_{+} \neq \mathbf{k}_{-}$, in agreement with (7.10). For $\mathbf{B} \parallel [110]$, the splitting $E_{+}(\mathbf{k}_{+}) - E_{-}(\mathbf{k}_{-})$ is roughly 10% smaller than the splitting for $\mathbf{B} \parallel [\bar{1}10]$, in agreement with (7.11). The contribution of the higher-order Zeeman term (7.4) can hardly be resolved on the scale of Fig. 7.2. The dominant effect is from the Dresselhaus term (7.8).

Figure 7.2 illustrates that in an in-plane magnetic field, the physics in the presence of the Dresselhaus term (7.8) is qualitatively different from the situation without such a term. For example, in (7.6), containing only a Zeeman term, the lowest states in the spin-split branches are connected by vertical spin-flip transitions. This does not hold anymore for spin-flip transitions in the presence of the Dresselhaus term (7.8). We remark that, similarly to (7.10) and (7.11), the Rashba term in the presence of an in-plane magnetic field also gives rise to shifted minima of the spin-split branches of the subband dispersion $E_{\alpha\pm}(\mathbf{k}_{\parallel})$. Here a nontrivial, albeit isotropic, splitting similar to (7.11) requires that we take into account the fourth term in (7.6).

Finally, we note that we derived (7.8) by first-order perturbation theory. In higher-order perturbation theory, invariants symmetric in the components of \mathbf{k} can give rise to both symmetric and antisymmetric higher-order invariants, consistent with (3.1). An example will be given in the next section.

7.3 Zeeman Splitting in 2D Hole Systems: Low-Symmetry Growth Directions

In this section, we discuss the Zeeman splitting in 2D hole systems that have been grown in low-symmetry crystallographic directions such as [113]. We shall show that the Zeeman splitting for an in-plane magnetic field in different crystallographic directions can be highly anisotropic. In Sect. 7.3.1 we present the general theoretical results, which will be compared in Sect. 7.3.2 with the results of magnetotransport experiments.

7.3.1 Theory

In Table C.5, we have two invariants in the valence band block \mathcal{H}_{8v8v}^z that give rise to a Zeeman splitting of holes. The isotropic invariant $-2\kappa\mu_B \mathbf{B} \cdot \mathbf{J}$, with an effective g factor κ , is always the dominant term. The prefactor q of the anisotropic invariant $-2q\mu_B \mathbf{B} \cdot \mathbf{J}$ with $\mathbf{J} = (J_x^3, J_y^3, J_z^3)$, is typically two orders of magnitude smaller than κ and, in the present discussion, is neglected completely. The smallness of q is in sharp contrast to the orbital motion of holes, for which we have highly anisotropic effective masses m^* reflecting the spatial anisotropy of the crystal structure (see Sect. 4.5.2).

For the Γ_8^v valence band block, the Zeeman Hamiltonian reads as follows, using an explicit matrix notation:

$$\mathcal{H}_{8v8v}^z = -2\kappa\mu_B \begin{pmatrix} \frac{3}{2}B_z & \frac{\sqrt{3}}{2}B_- & 0 & 0 \\ \frac{\sqrt{3}}{2}B_+ & \frac{1}{2}B_z & B_- & 0 \\ 0 & B_+ & -\frac{1}{2}B_z & \frac{\sqrt{3}}{2}B_- \\ 0 & 0 & \frac{\sqrt{3}}{2}B_+ & -\frac{3}{2}B_z \end{pmatrix} - 2q\mu_B \begin{pmatrix} \frac{27}{8}B_z & \frac{7\sqrt{3}}{8}B_- & 0 & \frac{3}{4}B_+ \\ \frac{7\sqrt{3}}{8}B_+ & \frac{1}{8}B_z & \frac{5}{2}B_- & 0 \\ 0 & \frac{5}{2}B_+ & -\frac{1}{8}B_z & \frac{7\sqrt{3}}{8}B_- \\ \frac{3}{4}B_- & 0 & \frac{7\sqrt{3}}{8}B_+ & -\frac{27}{8}B_z \end{pmatrix}, \quad (7.12)$$

where $B_{\pm} = B_x \pm iB_y$. Note that the first term is correct for any growth direction because it has spherical symmetry. The second term refers to the growth direction [001]. We see from (7.12) that, in the presence of an in-plane magnetic field $\mathbf{B}_{\parallel} = (B_x, B_y, 0)$, the g factor κ couples the two LH states ($m = \pm 1/2$). Furthermore it couples the HH states ($m = \pm 3/2$) to the LH states [7]. But there is no direct coupling between the HH states proportional to κ , so that the authors of [6, 7, 8, 9] concluded that the Zeeman splitting of HH states in an in-plane magnetic field is suppressed. This illustrates the general result in Sect. 4.5.3 that HH–LH splitting corresponds to a predefined quantization axis of angular momentum that points in the growth direction of

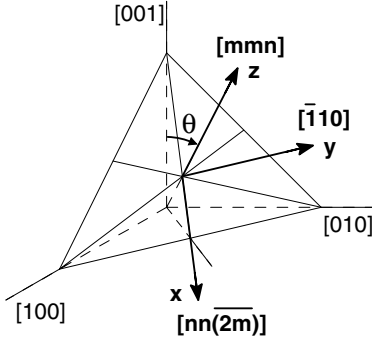


Fig. 7.3. Coordinate system for QWs grown in the $[mmn]$ direction (z direction). Here θ is the angle between $[mmn]$ and $[001]$, i.e. $\theta = \arccos(n/\sqrt{2m^2 + n^2})$. The axes for the in-plane motion are $[nn(2m)]$ (x) and $[\bar{1}10]$ (y)

the QW. An in-plane magnetic field cannot give rise to a second quantization axis of angular momentum; see also (7.19).

However, owing to the anisotropic orbital motion of holes in a crystal structure, angular momentum is merely an “almost good” quantum number. Thus, for crystallographic directions other than the high-symmetry directions $[001]$ and $[111]$ (neglecting any broken inversion symmetry) and nonzero SO interaction, it follows that g_{\parallel}^* can have significant values. In the following we show that, in agreement with these symmetry considerations, we obtain a large and highly anisotropic Zeeman splitting with respect to different orientations of the in-plane magnetic field \mathbf{B}_{\parallel} relative to the crystal axes (Ref. [10]).

We shall discuss QWs grown in the crystallographic $[mmn]$ direction (where m, n are integers). Hence we use the coordinate system shown in Fig. 7.3, where θ denotes the angle between $[mmn]$ and $[001]$. For growth directions other than $[001]$ and $[111]$, the point group of these QWs is C_{2h} (neglecting terms due to any broken inversion symmetry). We remark that QWs for 2D hole systems have often been grown in the $[113]$ direction recently, as this yields particularly high hole mobilities (Ref. [21, 22]).

In general, the dynamics of 2D holes are rather complicated owing to the nonparabolic and anisotropic terms in the Hamiltonian. Therefore, a quantitative understanding of phenomena such as the anisotropic Zeeman splitting can be obtained only by means of accurate numerical computations [23]. In particular, the Zeeman splitting of 2D hole states depends on higher orders both of the in-plane wave vector \mathbf{k}_{\parallel} and of \mathbf{B}_{\parallel} . As we shall show next, it is nevertheless very helpful for a qualitative understanding to identify analytically the relevant lowest-order terms.

We describe the hole subband states by means of the 4×4 Luttinger Hamiltonian \mathcal{H}_{8v8v} . The anisotropy of the orbital motion can be characterized by a single parameter $\delta \equiv \gamma_3 - \gamma_2$; see Table C.11. For growth directions other than $[001]$ and $[111]$, the anisotropic motion results in an off-diagonal HH–LH coupling proportional to δk^2 (see Table C.11), which complements the HH–LH coupling proportional to κB . Treating these terms by means of Löwdin

perturbation theory, we obtain the following to second order for the Zeeman term of the topmost HH subband:

$$\begin{aligned} \mathcal{H}_{[mmn]}^{\text{HH}} = & -3 [\mathcal{K} - \mathcal{G}_2 (2 - \sin^2 \theta) + \mathcal{G}_3 \cos^2 \theta] (2 - 3 \sin^2 \theta) \sin^2 \theta \mu_B B_x \sigma_x \\ & + 3 [2\mathcal{K} - \mathcal{G}_2 \sin^2 \theta - \mathcal{G}_3 (2 - \sin^2 \theta)] (2 - 3 \sin^2 \theta) \sin \theta \cos \theta \mu_B B_x \sigma_z \\ & - 3 [\mathcal{K} - \mathcal{G}_3] (2 - 3 \sin^2 \theta) \sin^2 \theta \mu_B B_y \sigma_y, \end{aligned} \quad (7.13)$$

where

$$\mathcal{K} = \frac{\hbar^2}{2m_0} \frac{\kappa \delta}{i} \sum_{\alpha} \frac{\langle h_1 | [\mathfrak{f}_z, z] | l_{\alpha} \rangle \langle l_{\alpha} | \mathfrak{f}_z^2 | h_1 \rangle + \langle h_1 | [\mathfrak{f}_z, z] | l_{\alpha} \rangle \langle l_{\alpha} | \mathfrak{f}_z^2 | h_1 \rangle}{E_1^h - E_{\alpha}^l}, \quad (7.14a)$$

$$\mathcal{G}_j = \frac{\hbar^2}{2m_0} \frac{\gamma_j \delta}{i} \sum_{\alpha} \frac{\langle h_1 | \{\mathfrak{f}_z, z\} | l_{\alpha} \rangle \langle l_{\alpha} | \mathfrak{f}_z^2 | h_1 \rangle - \langle h_1 | \mathfrak{f}_z^2 | l_{\alpha} \rangle \langle l_{\alpha} | \{\mathfrak{f}_z, z\} | h_1 \rangle}{E_1^h - E_{\alpha}^l}. \quad (7.14b)$$

Equation (7.13) is in full agreement with an invariant expansion of the Zeeman splitting for a system with the point group C_{2h} .⁷ In (7.14), we did not evaluate the commutator according to $[\mathfrak{f}_z, z] = i$, in order to show that both \mathcal{K} and \mathcal{G}_j have the antisymmetric structure we expect for a Zeeman term. Nevertheless, we have here two qualitatively very different contributions to the Zeeman spin splitting, both of which are quite remarkable. The coefficient \mathcal{K} originates from the combined effect of the bulk g factor κ and the anisotropic orbital motion characterized by $\delta = \gamma_3 - \gamma_2$. Typically we have $\langle h_1 | l_{\alpha} \rangle \approx \delta_{1\alpha}$. It follows that the dominant contribution to \mathcal{K} stems from the coupling between the subband states $|h_1\rangle$ and $|l_1\rangle$. The coefficients \mathcal{G}_j represent a contribution to the Zeeman term that is independent of the bulk g factor κ . This contribution is solely an effect of subband quantization. Using $\langle h_1 | l_{\alpha} \rangle \approx \delta_{1\alpha}$, it follows that we have $\langle h_1 | \{\mathfrak{f}_z, z\} | l_1 \rangle \approx 0$, i.e. we obtain the most important contributions to \mathcal{G}_j from a coupling to LH subbands $|h_{\alpha}\rangle$ with $\alpha > 1$. As these subbands are further away in energy, we can conclude that, typically, the dominant term in (7.14) is \mathcal{K} (with $\alpha = 1$). Note also that the coefficients \mathcal{K} and \mathcal{G}_j disappear in the axial limit $\delta = 0$.

It is convenient to diagonalize (7.13) so that we can summarize our results by an anisotropic effective g factor. We obtain

$$\begin{aligned} g_{[nn(2m)]}^{\text{HH}} = & 3 (2 - 3 \sin^2 \theta) \sin \theta \sqrt{4 - 3 \sin^2 \theta} \\ & \times \sqrt{(\mathcal{K} - \mathcal{G}_2)^2 \sin^2 \theta + (\mathcal{K} - \mathcal{G}_3)^2 \cos^2 \theta}, \end{aligned} \quad (7.15a)$$

$$g_{[\bar{1}10]}^{\text{HH}} = -3 (2 - 3 \sin^2 \theta) \sin^2 \theta |\mathcal{K} - \mathcal{G}_3|. \quad (7.15b)$$

⁷ Note that the mirror plane of C_{2h} is the $(\bar{1}10)$ plane; see Fig. 7.3.

Our sign convention for g^* corresponds to the dominant spinor component of the multicomponent eigenstates (using a basis of angular-momentum eigenfunctions with a quantization axis in the direction of \mathbf{B}_{\parallel}).

We see here that the behavior of g^* in (7.15) is fundamentally different from the in-plane/out-of-plane anisotropy of g^* of 2D hole systems visible in (7.12) (see [6, 7, 8, 9]). It is also very different from the in-plane/out-of-plane anisotropy of g^* of 2D electron systems (see Sect. 7.1), which emerges in a natural way from Roth's formula (4.39b) for the bulk electron g factor. In fact, (7.15) is a clear consequence of subband quantization.⁸

It is remarkable that though the first term in (7.14) is the dominant one, we can have a nonzero effective g factor (7.15) even in the limit $\kappa = 0$. We have stated above that the effective g factor is a consequence of SO interaction. Therefore, one might ask how it is possible to have a nonzero g^* which apparently depends only on the Luttinger parameters γ_i for the orbital motion. This can be understood as follows. The 4×4 Luttinger Hamiltonian \mathcal{H}_{8v8v} which underlies the present calculations corresponds to an infinitely large SO splitting Δ_0 between the topmost valence band Γ_8^v and the split-off band Γ_7^v . Therefore the SO interaction is not explicitly visible even though, similarly to Zeeman splitting in bulk semiconductors [1], (7.15) is a consequence of SO interaction. Equation (7.15) shows that in 2D systems, SO interaction can give rise to a Zeeman splitting even without a bulk g^* .

We can evaluate (7.14) analytically, using as unperturbed states the eigenfunctions of an infinitely deep rectangular QW and the eigenfunctions of a parabolic QW. We obtain

$$\mathcal{K} = \frac{\kappa \delta u_1}{\gamma_z^{\text{HH}} - \gamma_z^{\text{LH}}} , \quad (7.16a)$$

$$\mathcal{G}_j = \frac{2\gamma_j \delta u_2}{\gamma_z^{\text{HH}} - 5\gamma_z^{\text{LH}}} , \quad (7.16b)$$

where

$$\gamma_z^{\text{HH}} = -\gamma_1 + 2[(1 - \zeta)\gamma_2 + \zeta\gamma_3] \quad (7.17a)$$

$$\gamma_z^{\text{LH}} = -\gamma_1 - 2[(1 - \zeta)\gamma_2 + \zeta\gamma_3] \quad (7.17b)$$

$$\zeta = \sin^2 \theta \left[3 - \frac{9}{4} \sin^2 \theta \right] . \quad (7.17c)$$

⁸ In a biaxially strained bulk crystal we have a lifting of the HH–LH degeneracy, so that in an invariant expansion for the bulk Hamiltonian including strain, we find terms similar to (7.15). But in this case the resulting g^* is much smaller for the following reason: for a QW, both the numerators and the denominators in (7.14) are proportional to k_z^2 so that the k_z dependence of g^* drops out (see the discussion following (7.16)). In a biaxially strained bulk material, on the other hand, the corresponding energy denominators are proportional to the strain in the system and independent of k_z . In this case it would be difficult to probe $g^*(k_z)$ at sufficiently large values of k_z .

Here γ_z^{HH} and γ_z^{LH} are the reciprocal band-edge effective masses in the z direction in the axial approximation for the HH and LH subbands, respectively (see Table C.10). In (7.16), we have used the weights u_i to distinguish between our two model systems. The values $u_1 = u_2 = 1$ correspond to a parabolic QW. For the rectangular QW we have $u_1 = 2$ and $u_2 = 0$, i.e. for the latter geometry the coefficients \mathcal{G}_j disappear. For the parabolic well, the coefficients \mathcal{G}_j stem from a coupling to the l_3 subband. They are small corrections with respect to \mathcal{K} .

Equation (7.16) is independent of the well width w , the reason being that in (7.14) both the numerators and the energy denominators are proportional to $k_z^2 \propto 1/w^2$, so that the w dependences cancel out. However, similarly to the case of optical anisotropy in QWs [24], the effective g^* depends on w if the split-off valence band Γ_7^v is explicitly taken into account. Here, we omit the rather lengthy modifications to (7.15). They become relevant for narrow QWs with $w \lesssim 50$ Å.

Equations (7.15) and (7.16) are quite important because, in unstrained QWs, the topmost subband is an HH subband so that often only this subband is occupied. For LH subbands in an in-plane \mathbf{B} and for HH and LH subbands in a perpendicular \mathbf{B} , g^* contains terms similar to (7.15). However, the dominant contribution is given by the bulk g factor κ . We see in (7.12) that for LH subbands in an in-plane \mathbf{B} we have basically $g_{\parallel}^{\text{LH}} = 4\kappa$, while for a perpendicular \mathbf{B} we have $g_z^{\text{HH}} = 6\kappa$ and $g_z^{\text{LH}} = 2\kappa$ [9, 3].

In Fig. 7.4a we show the anisotropic g^* of the h_1 subband for a 200 Å wide GaAs–Al_{0.3}Ga_{0.7}As QW as a function of the angle θ . The analytical expressions (7.16) (dotted and dashed–dotted lines) are in very good agreement with the more accurate results obtained by means of a numerical diagonalization [7, 25] of the Luttinger Hamiltonian (solid and dashed lines). Figure 7.4 demonstrates that g^* can be very anisotropic. For example, for the growth direction [113], g^* is about a factor of four larger when $B \parallel [3\bar{3}2]$ than when $B \parallel [\bar{1}10]$. Moreover, the sign of $g_{[nn(2m)]}^{\text{HH}}$ is opposite to the sign of $g_{[\bar{1}10]}^{\text{HH}}$. For comparison, we remark that for the GaAs system considered in Fig. 7.4 we have $g_z^{\text{HH}} = 6\kappa \approx 7.2$.

Equations (7.15) and (7.16) are applicable to a wide range of cubic semiconductors with results qualitatively very similar to Fig. 7.4. For rectangular QWs ($u_1 = 2$ and $u_2 = 0$), the relative anisotropy

$$\frac{g_{[nn(2m)]}^{\text{HH}}}{g_{[\bar{1}10]}^{\text{HH}}} = -\frac{\sqrt{4 - 3 \sin^2 \theta}}{\sin \theta} \quad (7.18)$$

is independent of the material-specific parameters γ_i and κ (Fig. 7.4b). This result can be traced back to the fact that the anisotropy for different directions θ in \mathbf{k} -space is always characterized by the single parameter δ ; see Table C.11. Note that for QWs based on narrow-gap semiconductors, we have a larger κ and smaller effective masses. Thus the absolute values of g^* are significantly larger here than the g^* of GaAs shown in Fig. 7.4a, but the

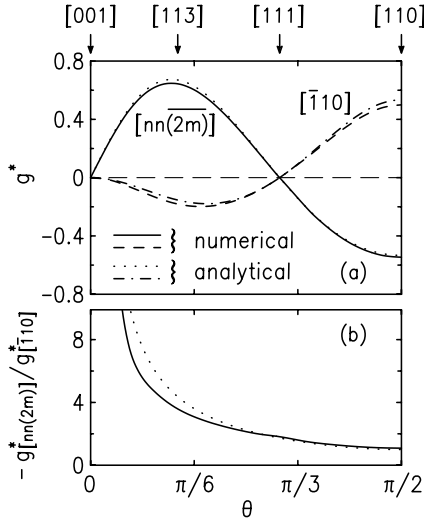


Fig. 7.4. (a) Anisotropic effective g factor g^* and (b) relative g factor anisotropy (7.18) of the h_1 subband for a 200 Å wide GaAs–Al_{0.3}Ga_{0.7}As QW as a function of θ , the angle between [001] and the growth direction. The results in (a) are shown for an in-plane \mathbf{B} along the $[nn(2m)]$ and $[\bar{1}10]$ directions. The solid and dashed lines were obtained by means of a numerical diagonalization of the Luttinger Hamiltonian. The dotted and dashed-dotted lines were obtained by means of (7.16). (a) taken from [10]. © (2000) by the American Physical Society

g^* anisotropy is still given by (7.18) and depends only on θ . The Zeeman splitting can be enhanced even further if one uses semimagnetic semiconductors containing, for example, Mn. For these materials, the structure of the Hamiltonian is identical to that of the conventional Luttinger Hamiltonian in the presence of a magnetic field, with κ replaced by the effective g factor due to the paramagnetic exchange interaction; see Table C.5 and [8, 9]. Therefore (7.15), (7.16), and the g^* anisotropy (7.18) are readily applicable to semimagnetic materials too.

7.3.2 Comparison with Magnetotransport Experiments

It has been demonstrated [10] that the in-plane anisotropy of g^* of a 2D hole systems can be probed experimentally by measuring the magnetoresistance of a high-mobility 2D hole system as a function of \mathbf{B}_{\parallel} . The samples used were 200 Å wide Si-modulation-doped GaAs QWs grown on (113)A GaAs substrates. These samples exhibit a mobility anisotropy, believed to be due to an anisotropic surface morphology [22]. They were patterned with an L-shaped Hall bar to allow simultaneous measurements of the resistivity along the $[33\bar{2}]$ and $[\bar{1}10]$ directions. Front and back gates were used to control the 2D density in the QW and the perpendicular electric field, which characterizes the asymmetry of the sample [26].

The left two panels of Fig. 7.5 show the resistivity ρ measured as a function of \mathbf{B}_{\parallel} for three different densities and for different relative orientations of \mathbf{B}_{\parallel} and the current \mathbf{I} . For easier comparison, we have plotted the fractional change $\rho(B)/\rho(B=0)$. Apart from an overall positive magnetoresistance, $\log(\rho)$ shows a change in slope at a particular value of \mathbf{B}_{\parallel} , which we call B^* . In Fig. 7.5, B^* has been marked by arrows. Similar, though sharper

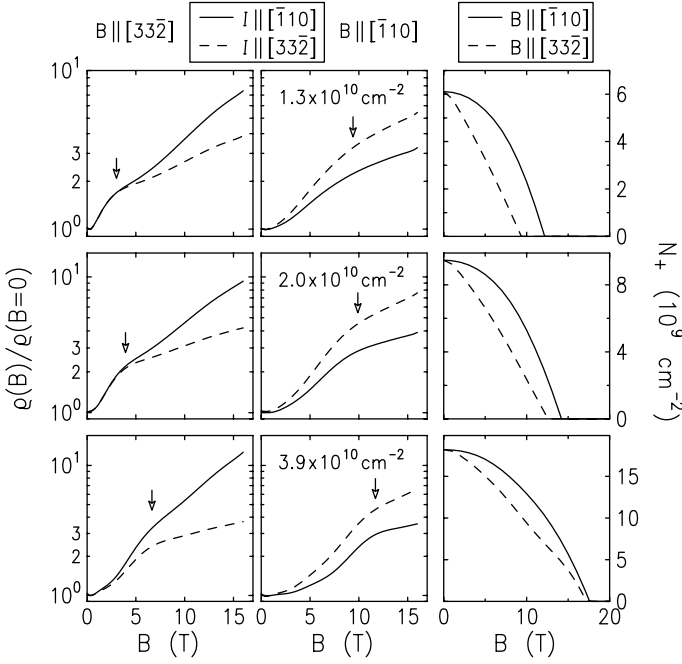


Fig. 7.5. *Left and central panels:* fractional change in resistivity $\rho(B)/\rho(0)$ due to an in-plane magnetic field B_{\parallel} , measured at $T = 0.3$ K for a GaAs 2D hole system grown on a (113) substrate, for different 2D densities as indicated. The arrows mark B^* , defined in the text. The resistivities at $B_{\parallel} = 0$ in the left panels are from top to bottom, 7.2, 2.2, and 0.55 k Ω /square. The corresponding values for the central panels are 4.9, 1.6, and 0.45 k Ω /square. *Right panels:* calculated density N_+ in the upper spin subband as a function of B . Note that the horizontal axes in the left and central panels have different scales from the right panels. Taken from [27]

features have been observed in systems with several occupied confinement subbands when a subband is depopulated by means of B_{\parallel} [28]. It has been proposed that the magnetoresistance feature at B^* in Fig. 7.5 is related to a spin-subband depopulation and the resulting changes in subband mobility and intersubband scattering as B_{\parallel} is increased. This mechanism is sketched in Fig. 7.6. At $B_{\parallel} = 0$, we have approximately equal populations of the spin subbands. Small differences are caused by the inversion-asymmetry-induced spin splitting discussed in Chap. 6. The Zeeman splitting due to an in-plane magnetic field lowers the energy of the eigenstates in one spin subband, while the energy of the eigenstates in the other subband is increased. Thus we obtain unequal populations of these subbands. For the low-density samples in Fig. 7.5, moderate magnetic fields are sufficient to completely depopulate one Zeeman-split subband. Note that in each panel of Fig. 7.5, B^* is the same for both current directions, even though the magnetoresistance is very dif-

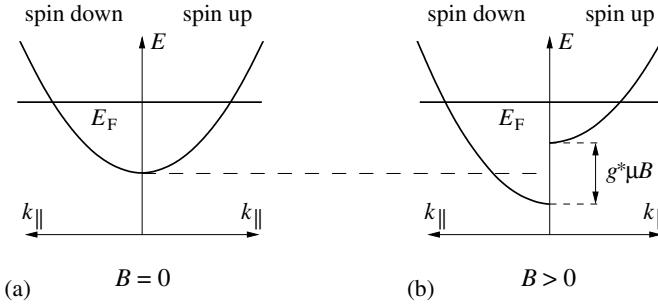


Fig. 7.6. Depopulation of one spin subband due to an in-plane magnetic field: (a) At $B_{\parallel} = 0$, we have approximately equal populations of the spin subbands. (b) Zeeman splitting at $B_{\parallel} > 0$ gives rise to a depopulation of one spin subband. We have neglected the possibility of a spin splitting at $B_{\parallel} = 0$ caused by an inversion asymmetry of the system

ferent. This implies that B^* depends on parameters which do not depend on the current direction. This supports our hypothesis, as spin-subband depopulation should not depend on the direction of the current in the sample.

Our interpretation of B^* is obviously consistent with B^* in Fig. 7.5 becoming larger with increasing density. It is remarkable that B^* for the $\mathbf{B}_{\parallel} \parallel [33\bar{2}]$ traces is about 4 T smaller than for the $\mathbf{B}_{\parallel} \parallel [\bar{1}10]$ traces, regardless of the direction of \mathbf{I} . We associate this with the anisotropy of the in-plane g^* discussed in the preceding section. This interpretation is validated by the self-consistently calculated results for the density N_+ of the upper spin subband as a function of B_{\parallel} , shown in the right panels of Fig. 7.5. The density N_+ decreases much faster for $\mathbf{B}_{\parallel} \parallel [33\bar{2}]$ than for $\mathbf{B}_{\parallel} \parallel [\bar{1}10]$, in agreement with Fig. 7.4a. We have further support for our interpretation of B^* from experiments where the asymmetry of the confining potential was increased by means of the front and back gates while keeping the 2D density fixed. We observe an increase in B^* , in agreement with the results of the self-consistent calculations.

One might ask whether the data in Fig. 7.5 could be summarized by a single value of g^* for each trace. Unfortunately, this is not possible, because, owing to the complicated band structure of holes, g^* depends on the in-plane wave vector \mathbf{k}_{\parallel} , and we are averaging over $g^*(\mathbf{k}_{\parallel})$ for \mathbf{k}_{\parallel} up to the Fermi wave vector \mathbf{k}_F . (For clarity, we have not included in (7.16) the lengthy additional terms due to the \mathbf{k}_{\parallel} dependence of g^* .) Note also that m^* depends on B ; see (7.6). The significance of these effects can be readily deduced from the right panels of Fig. 7.5, as we would have straight lines for $N_+(B)$ if g^* and the effective mass m^* were not dependent on \mathbf{k}_{\parallel} or B .

In Fig. 7.5, the measured B^* is significantly smaller than the calculated B_{\parallel} for a complete depopulation of the upper spin subband. We note that for the low-density samples used in the experiments [10], it can be expected that g^* will be enhanced in magnitude owing to the exchange interaction and

the spin polarization caused by B_{\parallel} [4, 29, 30]. This effect was not taken into account in the self-consistent calculations. The overall agreement between the experimental data and the calculations, however, implies that these many-particle effects do not qualitatively affect the anisotropy of g^* . We suggest that the anisotropic g^* given in (7.16) for an in-plane wave vector $\mathbf{k}_{\parallel} = 0$ without many-body effects could be measured using optical and microwave experiments such as those described in [14].

7.4 Zeeman Splitting in 2D Hole Systems: Growth Direction [001]

In a Taylor expansion of the Zeeman splitting $\Delta E(B)$, the g factor g^* (times μ_B) is the prefactor of the term linear in B . Often terms of higher order in B are neglected because of their relative insignificance. An interesting feature of Fig. 7.4a is the vanishing of $g^*(\theta)$ for the high-symmetry growth directions [001] and [111] (Ref. [7]).⁹ For the 2D hole system considered in Fig. 7.4, this results in a splitting ΔE which, at $B_{\parallel} = 1$ T, is more than two orders of magnitude smaller than the value of ΔE for the growth directions [113] and [110]. For the high-symmetry directions [001] and [111], the dominant contribution to ΔE is proportional to B_{\parallel}^3 . In second-order perturbation theory, we obtain the following for the h_1 subband in a QW grown in the [001] direction:

$$\begin{aligned} \mathcal{H}_{[001]}^{\text{HH}} = & \frac{3}{2}q\mu_B (B_x\sigma_x - B_y\sigma_y) \\ & + \mathcal{Z}_{[001]}^{\text{HH}} \mu_B^3 \left\{ \gamma_2 [(B_x^3 - B_x B_y^2)\sigma_x + (B_y^3 - B_y B_x^2)\sigma_y] \right. \\ & \left. + 2\gamma_3 [B_x B_y^2\sigma_x + B_y B_x^2\sigma_y] \right\}, \end{aligned} \quad (7.19a)$$

where

$$\begin{aligned} \mathcal{Z}_{[001]}^{\text{HH}} = & 6 \left(\kappa \sum_{\alpha} \frac{\langle h_1 | z^2 | l_{\alpha} \rangle \langle l_{\alpha} | [\mathbf{t}_z, z] | h_1 \rangle + \langle h_1 | [\mathbf{t}_z, z] | l_{\alpha} \rangle \langle l_{\alpha} | z^2 | h_1 \rangle}{E_1^h - E_{\alpha}^l} \right. \\ & \left. + \gamma_3 \sum_{\alpha} \frac{\langle h_1 | z^2 | l_{\alpha} \rangle \langle l_{\alpha} | \{\mathbf{t}_z, z\} | h_1 \rangle - \langle h_1 | \{\mathbf{t}_z, z\} | l_{\alpha} \rangle \langle l_{\alpha} | z^2 | h_1 \rangle}{E_1^h - E_{\alpha}^l} \right). \end{aligned} \quad (7.19b)$$

These results are fully consistent with an invariant expansion for the point group D_{4h} . For an infinitely deep rectangular QW of width w we can evaluate $\mathcal{Z}_{[001]}^{\text{HH}}$ further (neglecting the coupling to LH subbands with $\alpha > 3$ in the second sum):

⁹ The small B -linear Zeeman splitting proportional to q was discussed in [6, 31]. Note that for a 200 Å wide GaAs QW and a magnetic field $B_{\parallel} \gtrsim 4$ T the cubic splitting in (7.19) dominates over the linear splitting due to q .

$$\mathcal{Z}_{[001]}^{\text{HH}} = \left(\frac{w^2 m_0}{\pi^2 \hbar^2} \right)^2 \left[\frac{\kappa}{2\gamma_2} (6 - \pi^2) + \frac{27\gamma_3}{10\gamma_2 - 4\gamma_1} \right]. \quad (7.20)$$

The first term stems from a coupling between the subbands h_1 and l_1 , and the second term is due to a coupling between h_1 and l_3 . We can readily diagonalize (7.19) (neglecting the small q -dependent term)

$$\Delta E_{[001]}^{\text{HH}} = 2 (\mu_B B_{\parallel})^3 \sqrt{\gamma_2^2 \cos^2(2\varphi) + \gamma_3^2 \sin^2(2\varphi)} |\mathcal{Z}_{[001]}^{\text{HH}}|. \quad (7.21)$$

Here φ is the angle between \mathbf{B}_{\parallel} and the [100] axis. Unlike (7.16), $\Delta E_{[001]}^{\text{HH}}$ increases in proportion to w^4 , i.e. the Zeeman splitting is most efficiently suppressed in narrow QWs. The cubic dependence of $\Delta E_{[001]}^{\text{HH}}$ on B_{\parallel} in the approximate analytical expressions (7.19) and (7.21) is in very good agreement with more accurate numerical calculations. We obtain similar, though somewhat longer, expressions for the growth direction [111]. The Zeeman splitting of HH states in a tilted magnetic field was recently discussed with the use of similar methods by Dorozhkin [32].

Equation (7.19) characterizes the Zeeman splitting for the subband edge $k_{\parallel} = 0$. For a nonzero in-plane wave vector \mathbf{k}_{\parallel} , it is possible to achieve a significant Zeeman splitting of HH states linear in B_{\parallel} . The important invariants are (point group D_{2d})

$$\begin{aligned} \mathcal{H}_{[001]}^{\text{HH}} = & z_{51}^{7h7h} (B_x k_x^2 \sigma_x - B_y k_y^2 \sigma_y) + z_{52}^{7h7h} (B_x k_y^2 \sigma_x - B_y k_x^2 \sigma_y) \\ & + z_{53}^{7h7h} \{k_x, k_y\} (B_y \sigma_x - B_x \sigma_y), \end{aligned} \quad (7.22)$$

where

$$z_{51}^{7h7h} = -\frac{3}{2} \kappa \gamma_2 \mathcal{Z}_1 + 3\gamma_3^2 \mathcal{Z}_2, \quad (7.23a)$$

$$z_{52}^{7h7h} = \frac{3}{2} \kappa \gamma_2 \mathcal{Z}_1 - 3\gamma_2 \gamma_3 \mathcal{Z}_2, \quad (7.23b)$$

$$z_{53}^{7h7h} = \frac{3}{2} \kappa \gamma_3 \mathcal{Z}_1 - 3\gamma_3 (\gamma_2 + \gamma_3) \mathcal{Z}_2, \quad (7.23c)$$

and

$$\mathcal{Z}_1 = i \frac{\langle h_1 | [k_z, z] | l_1 \rangle \langle l_1 | h_1 \rangle}{E_1^h - E_1^l}, \quad (7.24a)$$

$$\mathcal{Z}_2 = i \sum_{\alpha} \frac{\langle h_1 | k_z | l_{\alpha} \rangle \langle l_{\alpha} | z | h_1 \rangle - \langle h_1 | z | l_{\alpha} \rangle \langle l_{\alpha} | k_z | h_1 \rangle}{E_1^h - E_{\alpha}^l}. \quad (7.24b)$$

Similarly to \mathcal{G}_j in (7.13), the terms weighted by \mathcal{Z}_2 represent contributions to the Zeeman splitting that are independent of the bulk g factor κ . For an infinitely deep rectangular QW of width w , we can evaluate \mathcal{Z}_j further:

$$\mathcal{Z}_1 = \frac{w^2 m_0}{2\pi^2 \hbar^2 \gamma_2}, \quad (7.25a)$$

$$\mathcal{Z}_2 = -\frac{512w^2 m_0}{27\pi^2 \hbar^2 (3\gamma_1 + 10\gamma_2)}. \quad (7.25b)$$

It can be seen that we obtain the largest Zeeman splitting for wide QWs where the energy denominators in (7.24) are small.

References

1. L.M. Roth, B. Lax, S. Zwerdling: Phys. Rev. **114**, 90 (1959) 2, 14, 56, 131, 141
2. J.F. Janak: Phys. Rev. **178**(3), 1416–1418 (1969) 131
3. J.M. Luttinger: Phys. Rev. **102**(4), 1030 (1956) 3, 18, 28, 29, 88, 98, 99, 106, 158, 131, 142
4. F.F. Fang, P.J. Stiles: Phys. Rev. **174**, 823 (1968) 131, 146
5. E.L. Ivchenko, A.A. Kiselev: Sov. Phys. Semicond. **26**, 827 (1992) 5, 58, 131, 132
6. H.W. van Kesteren, E.C. Cosman, W.A.J.A. van der Poel: Phys. Rev. B **41**(8), 5283–5292 (1990) 5, 111, 112, 114, 131, 138, 141, 146
7. G. Goldoni, A. Fasolino: Phys. Rev. B **48**, 4948 (1993) 131, 138, 141, 142, 146
8. P. Peyla, A. Wasiela, Y. Merle d’Aubigné, D.E. Ashenford, B. Lunn: Phys. Rev. B **47**(7), 3783–3789 (1993) 131, 138, 141, 143
9. B. Kuhn-Heinrich, W. Ossau, E. Bangert, A. Waag, G. Landwehr: Solid State Commun. **91**(6), 413–418 (1994) 131, 138, 141, 142, 143
10. R. Winkler, S.J. Papadakis, E.P. De Poortere, M. Shayegan: Phys. Rev. Lett. **85**, 4574 (2000) 5, 131, 139, 143, 145
11. G. Lommer, F. Malcher, U. Rössler: Phys. Rev. B **32**, 6965 (1985) 77, 78, 83, 132
12. C. Hermann, C. Weisbuch: Phys. Rev. B **15**(2), 823–833 (1977) 25, 133
13. V.K. Kalevich, V.L. Korenev: JETP Lett. **57**(9), 571–575 (1993) 5, 134, 135
14. M. Oestreich, S. Hallstein, W.W. Rühle: IEEE J. Sel. Top. Quantum Electron. **2**(3), 747–755 (1996) 134, 146
15. F. Stern: Phys. Rev. Lett. **21**(25), 1687–1690 (1968) 134, 135
16. S. Datta: *Electronic Transport in Mesoscopic Systems* (Cambridge University Press, Cambridge, 1995) 135
17. K.H. Yang: Ann. Phys. (N.Y.) **101**, 62–96 (1976) 135
18. D.H. Kobe: Phys. Rev. Lett. **40**(9), 538–540 (1978) 135
19. R.R. Schlicher, W. Becker, J. Bergou, M.O. Scully: “Interaction Hamiltonian in quantum optics, or: $\mathbf{p} \cdot \mathbf{A}$ vs. $\mathbf{E} \cdot \mathbf{r}$ revisited”, in *Quantum Electrodynamics and Quantum Optics*, ed. by A.O. Barut (Plenum, New York, 1984), pp. 405–441 135
20. D.F. Nelson, R.C. Miller, D.A. Kleinman: Phys. Rev. B **35**(14), 7770–7773 (1987) 136
21. A.G. Davies, J.E.F. Frost, D.A. Ritchie, D.C. Peacock, R. Newbury, E.H. Linfield, M. Pepper, G.A.C. Jones: J. Crystal Growth **111**(1–4), 318–322 (1991) 95, 139
22. J.J. Heremans, M.B. Santos, K. Hirakawa, M. Shayegan: J. Appl. Phys. **76**(3), 1980–1982 (1994) 95, 139, 143
23. R. Winkler, U. Rössler: Phys. Rev. B **48**, 8918 (1993) 35, 38, 39, 40, 86, 93, 106, 108, 139

24. R. Winkler, A.I. Nesvizhskii: Phys. Rev. B **53**, 9984 (1996) 142
25. R. Winkler: J. Phys.: Condens. Matter **5**, 2321 (1993) 42, 80, 81, 95, 142
26. S.J. Papadakis, E.P. De Poortere, H.C. Manoharan, M. Shayegan, R. Winkler: Science **283**, 2056 (1999) 3, 6, 77, 100, 104, 109, 171, 172, 174, 177, 178, 143
27. R. Winkler, S.J. Papadakis, E.P. De Poortere, M. Shayegan: “Spin–orbit coupling in two-dimensional electron and hole systems”, in *Advances in Solid State Physics*, ed. by B. Kramer, Vol. 41 (Springer, Berlin, Heidelberg, 2001), pp. 211–223 144
28. J. Jo, E.A. Garcia, K.M. Abkemeier, M.B. Santos, M. Shayegan: Phys. Rev. B **47**(7), 4056–4059 (1993) 144
29. Y. Kwon, D.M. Ceperley, R.M. Martin: Phys. Rev. B **50**, 1684 (1994) 146
30. T. Okamoto, K. Hosoya, S. Kawaji, A. Yagi: Phys. Rev. Lett. **82**(19), 3875–3878 (1999) 146
31. X. Marie, T. Amand, P. Le Jeune, M. Paillard, P. Renucci, L.E. Golub, V.D. Dymnikov, E.L. Ivchenko: Phys. Rev. B **60**(8), 5811–5817 (1999) 146
32. S.I. Dorozhkin: Phys. Rev. B **61**(11), 7803–7805 (2000) 147

8 Landau Levels and Cyclotron Resonance

Magneto-optical spectroscopy has proven to be a valuable tool for analyzing the subband structure of electrons and holes in semiconductor quantum wells [1]. We begin this chapter with a brief general discussion of cyclotron resonance in semiconductor QWs (Sect. 8.1). In Sect. 8.2 we discuss the spin-split cyclotron resonance of 2D electron systems in InAs QWs that was measured by Yang et al. [2] and Scriba et al. [3]. In Sect. 8.3 we present a detailed comparison between calculated and measured spectra of 2D hole systems in strained asymmetric Ge-SiGe QWs grown in the [001] direction. Finally, in Sect. 8.4 we discuss Landau levels in inversion-asymmetric systems.

8.1 Cyclotron Resonance in Quasi-2D Systems

Cyclotron resonance denotes the resonant absorption of light due to optical transitions between Landau levels in the presence of a quantizing magnetic field. In semiconductors, the typical frequencies of the absorbed light are in the far infrared (FIR) range. In this section we shall discuss the selection rules and the absorption coefficient for cyclotron resonance in 2D systems. We follow closely [4, 5], where these quantities were derived for bulk semiconductors (see also Sect. 5.7 of [6]).

We consider the absorption of FIR radiation with an electric dipole field $\mathcal{E} = \mathcal{E}_0 \hat{\mathbf{e}} e^{i\omega t}$, where $\hat{\mathbf{e}} = (e_x, e_y, e_z)$ denotes the polarization vector. We can associate the vector potential $\mathbf{A} = [\mathcal{E}_0/(i\omega)] \hat{\mathbf{e}} e^{i\omega t}$ with \mathcal{E} so that $\mathcal{E} = \partial_t \mathbf{A}$. If the vector potential \mathbf{A} is included in the multiband Hamiltonian \mathcal{H} , it gives rise to a perturbation

$$\mathcal{H}' = \mathcal{H}(\hbar \mathbf{k} + e\mathbf{A}) - \mathcal{H}(\hbar \mathbf{k}) \approx e\mathbf{A} \cdot \partial \mathcal{H} / \hbar \partial \mathbf{k} \equiv e\mathbf{A} \cdot \mathbf{v}, \quad (8.1)$$

where we have omitted terms of order $\mathcal{O}(A^2)$ and the last expression defines the velocity operator \mathbf{v} with matrix-valued components.

In the following, we shall use the symbols $|s\rangle$ and $|t\rangle$ as a shorthand notation for the Landau levels $|\alpha \mathcal{N} \sigma\rangle$ with subband index α , Landau quantum number \mathcal{N} , and spin index σ . The transition probability between levels $|s\rangle$

and $|t\rangle$, with eigenenergies E_s and E_t , due to the perturbation \mathcal{H}' is given by Fermi's golden rule¹ [4, 6],

$$W_{st}(\omega) = \frac{\pi e^2 \mathcal{E}_0^2}{2\hbar\omega^2} |\langle s | \hat{\mathbf{e}} \cdot \mathbf{v} | t \rangle|^2 [\delta(E_{st} - \hbar\omega) + \delta(E_{st} + \hbar\omega)] . \quad (8.2)$$

Here $E_{st} = E_s - E_t$ is the cyclotron resonance energy. Following [4], we obtain the following for the matrix elements in (8.2):

$$\langle s | \hat{\mathbf{e}} \cdot \mathbf{v} | t \rangle = \frac{\lambda_c E_{ts}}{\hbar} \langle s | e_+ a - e_- a^\dagger + e_z \lambda_c k_z | t \rangle , \quad (8.3)$$

where a^\dagger and a are the creation and annihilation operators for Landau harmonic oscillators (see (4.22)), and $e_\pm = (e_x \pm ie_y)/\sqrt{2}$. Equation (8.3) yields the selection rules

$$\Delta \mathcal{N} = \pm 1 , \quad (8.4a)$$

$$\Delta \sigma = 0 \quad (8.4b)$$

for the \pm polarizations. The first selection rule (8.4a) is rigorously valid only within the axial approximation, when $\mathcal{N} = N$. The second selection rule (8.4b) is strictly fulfilled only within the EMA, when the orbital motion is fully decoupled from the spin degree of freedom. When we take cubic and tetrahedral corrections into account we obtain weak additional transitions between the generalized Landau levels $\Psi_{\alpha\mathcal{N}\sigma}$ (see (4.32)). The hierarchy of optical transitions in bulk systems with diamond and zinc blende structures has been developed in [4] and [5], respectively. We obtain similar results for 2D systems. Note that (8.3) remains valid even in such a generalized scheme.

In accordance with (8.4a), the cyclotron effective mass is defined by

$$m_c^* = \frac{\hbar e B}{|E_{\alpha\mathcal{N}\pm 1\sigma} - E_{\alpha\mathcal{N}\sigma}|} . \quad (8.5)$$

For the effective-mass Hamiltonian (4.27) we have $m_c^* = m^*$; see (8.10) below. In the limit $B \rightarrow 0$, the cyclotron mass equals the DOS effective mass (4.13) evaluated at the Fermi edge $E = E_F$ [8].

The 2D absorption coefficient $\alpha(\omega)$ is defined as the energy absorbed per unit time and area divided by the energy flux of the radiation field, and hence it is dimensionless. If we denote the energy density of the radiation field by $U = \mathcal{E}_0^2/(8\pi)$ and the index of refraction by n , the energy flux is ncU . Thus we obtain

$$\alpha(\omega) = \frac{\hbar\omega G}{ncU} \sum_{s,t} f_s (1 - f_t) W_{st}(\omega) , \quad (8.6)$$

¹ Previously, intraband and interband transitions were discussed separately in the literature [7]. In a multiband approach, the matrix-valued velocity operator includes both the intraband and interband components of the dipole operator. Thus we can treat these two contributions on the same footing [4].

where G is the degeneracy of the Landau levels (4.25), and f_s and f_t are the occupation factors, which depend on the 2D electron or hole concentration, on the temperature, and on the magnetic field. Finally, we obtain

$$\alpha(\omega) = \frac{2\pi}{n} \frac{e^2}{4\pi\hbar c} \sum_{s,t} (f_s - f_t) E_{ts} \delta(E_{ts} - \hbar\omega) \times \left| \langle s | e_+ a - e_- a^\dagger + e_z \lambda_c k_z | t \rangle \right|^2. \quad (8.7)$$

In the calculations presented in this chapter, the δ -function in (8.7) has been replaced by a Lorentzian broadening with the same phenomenological linewidth for all transitions. As we show below, the absorption coefficient $\alpha(\omega)$ obtained can be compared directly with experimental data.

8.2 Spin Splitting in the Cyclotron Resonance of 2D Electron Systems

Within the effective-mass Hamiltonian (4.27) the energies of the Landau levels are given by the following (neglecting the subband index):

$$E_{\text{EMA}}(N, \sigma) = \hbar\omega_c^* (N + \frac{1}{2}) + \frac{g^*}{2} \sigma \mu_B B \quad (8.8)$$

where the Landau² quantum number is $N = 0, 1, \dots$, the spin index is $\sigma = \pm 1$, the cyclotron frequency is $\omega_c^* = eB/m^*$ and the effective g factor is g^* . Thus we find that the cyclotron resonance energy³

$$\Delta E(N, \sigma) = E(N + 1, \sigma) - E(N, \sigma) \quad (8.9)$$

is independent of the quantum numbers N and σ :

$$\Delta E_{\text{EMA}}(N, \sigma) = \hbar\omega_c^* = \frac{\hbar e B}{m^*}. \quad (8.10)$$

The EMA is most appropriate for electrons in the conduction band. But even for electrons, (8.10) is only approximately correct. Owing to nonparabolicity, both the effective mass m^* and the g factor g^* depend on energy, so that the Landau levels as a function of B are not straight lines, but are typically bent downwards (see Fig. 8.1). For a given value of B , we usually have three transitions that contribute simultaneously to the absorption coefficient $\alpha(\omega)$. In Fig. 8.1, these transitions are marked by arrows. Nonparabolicity thus implies that, even for electrons, the transition energies ΔE depend on both N and σ . The N dependence reflects the energy dependence of m^* . It results

² We use here the more general Landau quantum number N and not the quantum number L of a Landau harmonic oscillator (4.29) because, in order to take into account band structure effects beyond the EMA, we work with (4.31).

³ In an effective-mass-like system at a temperature $T = 0$ we have absorption for only the $+$ polarization.

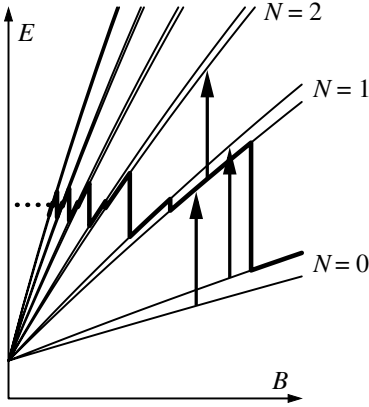


Fig. 8.1. Qualitative drawing of the Landau-level fan chart of a 2D electron system with a nonparabolic dispersion $E(k_{\parallel})$. The **bold line** marks the Fermi energy. The **arrows** indicate the three cyclotron transitions that are simultaneously possible at a given value of B (assuming a temperature $T = 0$)

in the *Landau splitting* of the cyclotron resonance [3]. The σ dependence, on the other hand, reflects the energy dependence of g^* . It gives rise to the *spin splitting* of the cyclotron resonance [3].

For a long time, attempts to observe the spin splitting of the cyclotron resonance in a nonparabolic 2D electron gas failed and various arguments were put forward to explain its suppression; see [2,3,9] and references therein. Here we show that the spin splitting of the cyclotron resonance spectra observed by Yang et al. [2] and Scriba et al. [3] can be reproduced quantitatively by using the $\mathbf{k} \cdot \mathbf{p}$ parameters known for the corresponding bulk materials. The samples investigated by Yang et al. and Scriba et al. were InAs–AlSb QWs with well widths of 149 Å and 125 Å and 2D electron densities N_s of $6.5 \times 10^{11} \text{ cm}^{-2}$ and $1.41 \times 10^{12} \text{ cm}^{-2}$, respectively. The measured cyclotron masses are reproduced in the lower right panels of Figs. 8.2a,b. We see clearly both the Landau splitting and the spin splitting of the cyclotron masses. We note that the InAs samples used by Yang et al. and Scriba et al. were good candidates for observing the spin splitting of the cyclotron resonance because InAs is a narrow-gap semiconductor with a strongly nonparabolic dispersion in the conduction band, even for moderate wave vectors \mathbf{k} .

In Fig. 8.3, we show the self-consistently calculated DOS effective mass (4.13) for the samples investigated by Yang et al. and Scriba et al. The bulk band parameters used in the calculation are listed in Appendix D. In Fig. 8.3, we see van Hove singularities of $m^*(E)$ at the subband edges that originate from the k -linear terms in $E_{\alpha}(\mathbf{k}_{\parallel})$ due to Rashba $B = 0$ spin splitting (see (6.20)). The k -linear terms are most important close to the subband edge. For larger wave vectors (higher energies), we have a strictly linear dependence of m^* on the energy E . This is due to the fact that the numerical calculations yield highly nonparabolic subband dispersion curves $E_{\alpha}(\mathbf{k}_{\parallel})$, which, basically, can be parameterized by the Kane formula

$$E_{\alpha}(\mathbf{k}_{\parallel}) = E_{\alpha}(0) + \sqrt{a_{\alpha}^2 + b_{\alpha}k_{\parallel}^2} - a_{\alpha}, \quad (8.11)$$

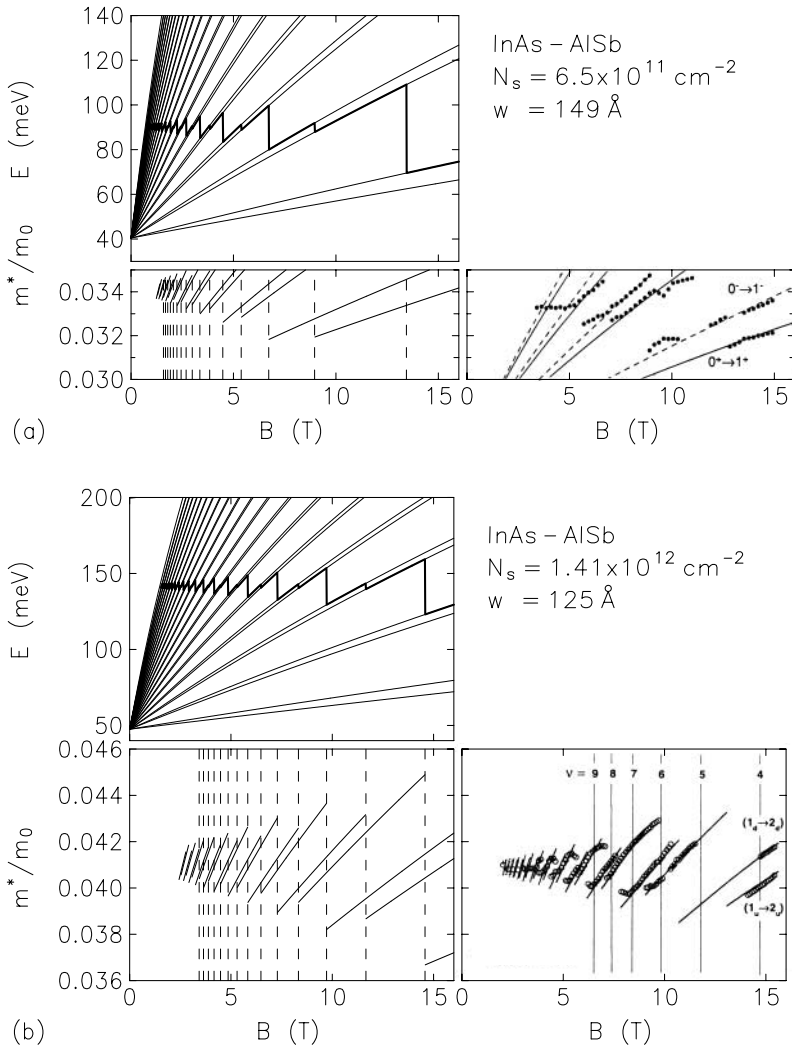


Fig. 8.2. Landau fan chart (*upper panels*) and cyclotron masses (*lower left panels*) calculated for the samples (a) of Yang et al. [2] and (b) of Scriba et al. [3]. The measured cyclotron masses are reproduced in the *lower right panels* of (a) and (b). The *bold lines* in the upper panels represent the Fermi energy. The *dashed lines* in the *lower left panels* indicate integer filling factors. *Left panels* taken from [10]. © (1996), with permission by Elsevier. *Lower right panel* of (a) taken from [2]. © (1993) by the American Physical Society. *Lower right panel* of (b) taken from [3]. © (1993), with permission by Elsevier

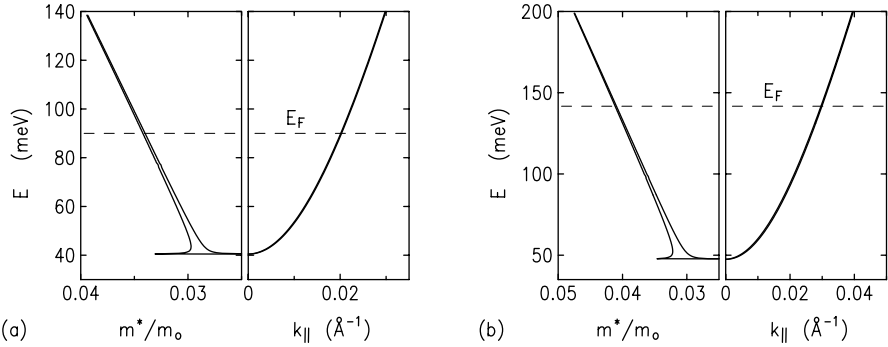


Fig. 8.3. DOS effective mass and subband dispersion calculated (a) for the 149 Å wide InAs–AlSb QW and (b) for the 125 Å wide InAs–AlSb QW, with 2D charge densities $N_s = 6.5 \times 10^{11} \text{ cm}^{-2}$ and $1.41 \times 10^{12} \text{ cm}^{-2}$, respectively, which were investigated experimentally by Yang et al. [2] and Scriba et al. [3]

where a_α and b_α are constants. Such a dispersion relation is well known for narrow-gap bulk semiconductors [11]. For a 2D dispersion (8.11), we can solve (4.13) analytically, to obtain

$$\frac{m_\alpha^*(E)}{m_0} = \frac{\hbar^2}{m_0} \frac{1}{b_\alpha} [E - E_\alpha(\mathbf{0}) + a_\alpha] \theta[E - E_\alpha(\mathbf{0})], \quad (8.12)$$

which is indeed a linear function of E .

For the calculation of Landau levels, we have used the Hartree potential obtained at $\mathbf{B} = 0$. In Figs. 8.2a,b (upper panels), we show the nonparabolic and spin-split Landau levels calculated for the samples of Yang et al. [2] and Scriba et al. [3]. The calculated cyclotron masses are displayed in the lower left panels of the same figure. The parameter-free calculations are in excellent agreement with the experimental data. In particular, we would like to note that the samples investigated by Yang et al. and Scriba et al. have very different well widths and very different 2D densities N_s . Accordingly, these samples also have very dissimilar cyclotron masses, which differ by approximately 20%. This feature is clearly reproduced by the parameter-free calculations. An FIR spectrum measured by Scriba et al. is displayed in Fig. 8.4a. The calculated absorption coefficient $\alpha(\omega)$ shown in Fig. 8.4b is in very good agreement with the measured spectrum.

8.3 Cyclotron Resonance of Holes in Strained Asymmetric Ge–SiGe Quantum Wells

Since the first successful growth of $\text{Si}_x\text{Ge}_{1-x}$ layers on a Si substrate using molecular-beam epitaxy (MBE) [12], this technique has been developed

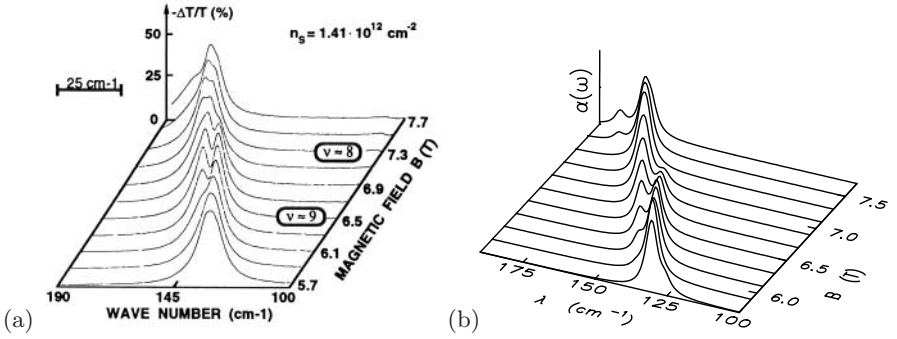


Fig. 8.4. (a) FIR spectrum measured by Scriba et al. (b) FIR spectrum calculated for the sample of Scriba et al. (a) taken from [3]. © (1993), with permission by Elsevier. (b) taken from [10]. © (1996), with permission by Elsevier

with the objective of making band structure engineering in Si-based technology possible [13, 14]. This endeavor is motivated by the fact that, compared with the metal–oxide–semiconductor (MOS) structures of the standard Si–SiO₂ technology, MBE-grown interfaces have higher perfection, allowing much higher mobilities of the confined carriers, i.e. faster devices. The price for this advantage is the lattice mismatch between Si and Ge, which limits the pseudomorphic growth of strained layers to a critical thickness of a few atomic layers for the pure materials. Using Si_xGe_{1–x} alloys, however, the critical thickness can be increased to several hundred Å [15]. The high quality of recently grown heterostructures, QWs, and superlattices using Si, Ge, and Si_xGe_{1–x} has been demonstrated in a series of optical and transport experiments [13, 16, 17, 18, 19, 20, 21].

The starting point of the present investigations is the experiments by Engelhardt et al. [18] on cyclotron resonance of holes in strained Ge layers confined between Si_xGe_{1–x} barriers of various compositions x . The lower barrier was a graded Si_xGe_{1–x} buffer layer [14] grown on a Si substrate, with a final Ge content of $(1 - x) = 0.7$. The upper Si_xGe_{1–x} barrier was δ -doped, with a spacer between the doping layer and the 2D hole gas in the Ge well. The structures were overgrown with a Si cap layer. All relevant parameters for the two samples C1072 and C1116 of [18] are given in Table 8.1. The experimental cyclotron resonance spectra for the two samples, measured at $T = 4.2$ K with a Fourier spectrometer, are reproduced in Fig. 8.5. From these spectra, one can extract the cyclotron resonance energies $\hbar\omega_c^*$ or cyclotron masses (8.5), which uncover the complex structure of the Landau-level spectrum of holes in strained QWs. The different Si contents in the two barriers and the δ -doping layer in the upper barrier result in an inversion asymmetry of the QW, which removes the spin degeneracy. Thus, even the single peak observed in the “classical” limit of low magnetic fields consists of a spin-split doublet [18]. With increasing magnetic field, the doublet splits into several

Table 8.1. Parameters of the two samples C1072 and C1116 of [18]

Sample		C1072	C1116
Upper SiGe barrier	Ge content	0.5	0.6
	δ -doping (10^{12} cm^{-2})	5	5
	spacer width (\AA)	75	100
Ge well	width (\AA)	75	168 ^a
	N_s (10^{12} cm^{-2})	1.78	1.10
Lower SiGe barrier	Ge content	0.7	0.7

^aThe well width of sample C1116 of 168 \AA was obtained by TEM measurements. It deviates from the nominal width of 125 \AA [18].

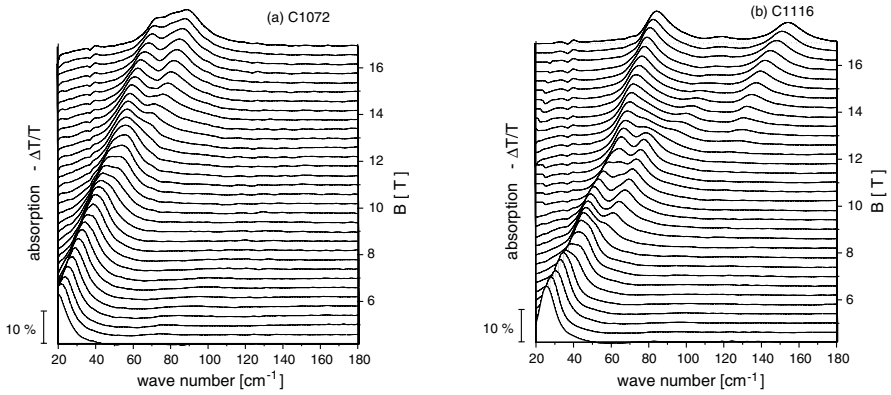


Fig. 8.5. Experimental cyclotron resonance spectra at different magnetic fields for the two samples (a) C1072 and (b) C1116, as specified in Table 8.1. Taken from [8]. © (1996) by the American Physical Society

components, whose evolution is characteristic of the sample (depending on the hole concentration and the geometry of the QW) as the Fermi energy is moved to Landau levels with lower quantum numbers. In bulk p-type semiconductors with uniaxial stress applied in the direction of \mathbf{B} , these Landau levels are known to be quite irregularly spaced as a consequence of the complex valence band structure [22, 4, 5]. The corresponding cyclotron transitions have been called “quantum resonances” [4]. The experimental data of [18] provide evidence of such quantum resonances in strained 2D hole systems.

8.3.1 Self-Consistent Subband Calculations for $B = 0$

Unlike many III–V and II–VI semiconductors, Si and Ge are indirect semiconductors, with their conduction band minima at the Δ point and L point, respectively. But the valence band maxima are located at the Γ point, so that for the description of holes in Si and Ge we can use the 6×6 Hamiltonian

$$\mathcal{H}_{6 \times 6} = \begin{pmatrix} \mathcal{H}_{8v8v} & \mathcal{H}_{8v7v} \\ \mathcal{H}_{7v8v} & \mathcal{H}_{7v7v} \end{pmatrix}, \quad (8.13)$$

with the blocks $\mathcal{H}_{\alpha\beta}$ taken from Table C.5. However, owing to the inversion symmetry of the diamond lattice, we do not have terms linear in k that are proportional to C_k . We apply the axial approximation given in Table 3.6. The lattice mismatch between Si and Ge results in a biaxial strain in the plane of the QW. Therefore, $\mathcal{H}_{6 \times 6}$ is augmented by the strain Hamiltonian listed in the lower part of Table C.5.

For $k_{\parallel} = 0$ and biaxial strain, the total Hamiltonian $\mathcal{H}_{6 \times 6}$ is diagonal in the 4×4 block \mathcal{H}_{8v8v} of the $j = 3/2$ states and in the 2×2 block \mathcal{H}_{7v7v} of the $j = 1/2$ states. But the LH and the spin-orbit split-off states have the same z component of angular momentum ($m = \pm 1/2$), so that they are coupled to each other. The z dependence of E_v and Δ_0 and the strain-induced offsets define the carrier-free potential profiles of the layered structures; these profiles are different for LH, HH and spin-orbit split-off states. The hole subbands were calculated for zero magnetic field by self-consistently solving $\mathcal{H}_{6 \times 6}$ and the Poisson equation to obtain the Hartree potential, which was superimposed on the z -dependent band edge energies.

The samples of [18] were δ -doped in the upper barrier, with a spacer between the doping layer and the 2D hole gas. Investigations on δ -doped GaAs:Si have shown that during the growth process the impurity atoms will diffuse, and widths of the actual doping layer of up to 200 Å have been reported [23]. This has been considered in the self-consistent hole subband calculations by assuming several different widths of the doping layer. It turns out that the calculated FIR spectra do not depend sensitively on this parameter.

For the hole densities of the samples in [18], only the topmost HH subband is occupied. In Fig. 8.6, we show the self-consistently calculated potential profiles for the two samples, together with the subband energies at $k_{\parallel} = 0$. We remark that for the topmost subband in the wider sample, C1116, the probability of finding a hole in the lower barrier (the barrier on the left-hand side in Fig. 8.6) is negligible. Therefore the calculations are rather insensitive to the exact value of the width of the QW, which was somewhat uncertain for sample C1116 [18]. The hole subband dispersion $E(k_{\parallel})$ is displayed in Fig. 8.7. Note the spin splitting of the subbands due to the asymmetry of the potential profile [24]. In Fig. 8.8, we show the DOS effective mass (4.13) of the topmost subband.

In the experimental work [18], it was not well known whether the well material was fully strained in accordance with the lattice mismatch between the well and the barrier material or whether the well had relaxed to some extent. We found that the calculations depended rather sensitively on this effect; the relaxation tends to increase the calculated cyclotron masses. Therefore, we have used the strain as a fitting parameter. The best agreement was obtained when the strain had 90% (sample C1072) and 80% (sample C1116) of

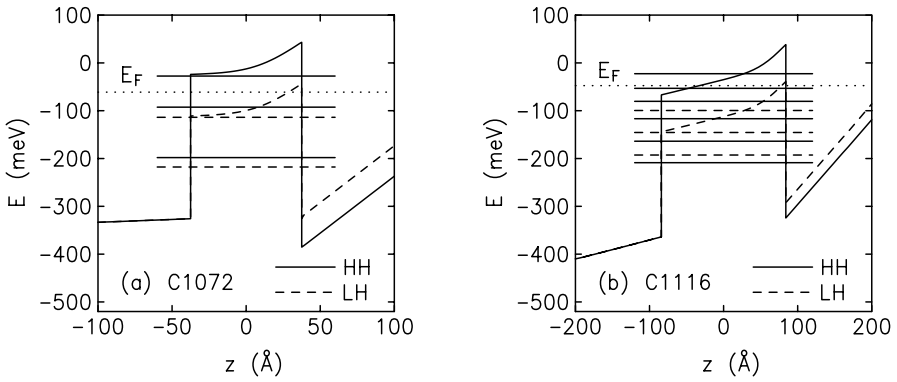


Fig. 8.6. Self-consistent potential profiles and hole subband energies at $k_{\parallel} = 0$ for the two samples (a) C1072 and (b) C1116. Owing to the biaxial strain in the QW and in the upper barrier, different potential profiles result for heavy holes (*solid lines*) and light holes (*dashed lines*). Taken from [8]. © (1996) by the American Physical Society

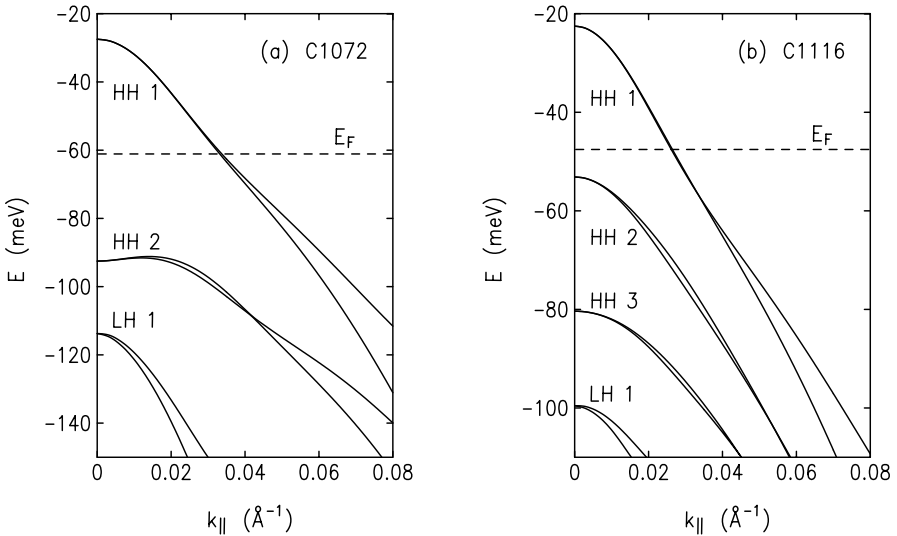


Fig. 8.7. Hole subband dispersion $E(k_{\parallel})$ for the two samples (a) C1072 and (b) C1116. Taken from [8]. © (1996) by the American Physical Society

its value in a fully strained system. We note that it is reasonable to have the larger relaxation in the wider sample.

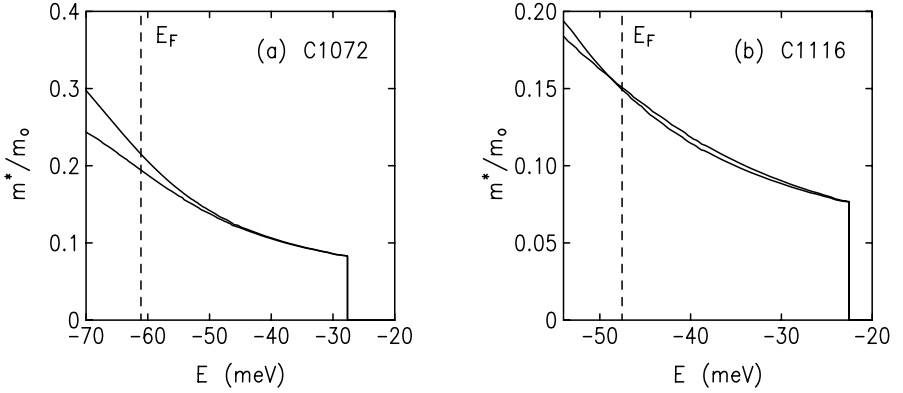


Fig. 8.8. DOS effective mass of the topmost subband for the two samples (a) C1072 and (b) C1116. Taken from [8]. © (1996) by the American Physical Society

8.3.2 Landau Levels and Cyclotron Masses

In the upper parts of Fig. 8.9, we show the fan chart of Landau levels evolving from the topmost HH subbands, together with the Fermi energy E_F obtained from the hole density, calculated for the samples C1072 and C1116. From top to bottom, the Landau levels have increasing Landau quantum numbers N , and $m = \pm 3/2$ (according to the dominant component of the eigenvectors), with $m = -3/2$ being the higher level at small magnetic fields. With increasing magnetic field, the spin-split states tend to change their order. The spin splitting of the Landau levels is a consequence of the Zeeman splitting and the Rashba SO coupling due to the asymmetry of the Hartree potential [25, 26, 27, 28]. The nonlinear dependence of the Landau levels on B corresponds to the nonparabolic dispersion $E(k_{\parallel})$ of the topmost HH subband (see Fig. 8.7).

From the fan chart in Fig. 8.9, we can obtain cyclotron masses by considering pairs of Landau levels between which dipole transitions are possible, taking account of the occupation factors and the selection rule $\Delta N = +1$ for the $+$ polarization of the circularly polarized FIR radiation. The cyclotron mass (8.5) refers to different pairs of Landau levels as the magnetic field is varied, as visualized in the lower parts of Fig. 8.9. For small magnetic fields (large filling factors), we obtain two spin-split cyclotron masses. As expected, for $B \rightarrow 0$ these masses are close to the values of m^* , which, in the classical limit of large Landau-level quantum numbers, can be read from the DOS effective mass at E_F (see Fig. 8.8). With increasing magnetic field (decreasing filling factor), the transitions take place between Landau levels with smaller N . These Landau levels show irregularities that are inherent in the top of the valence band.

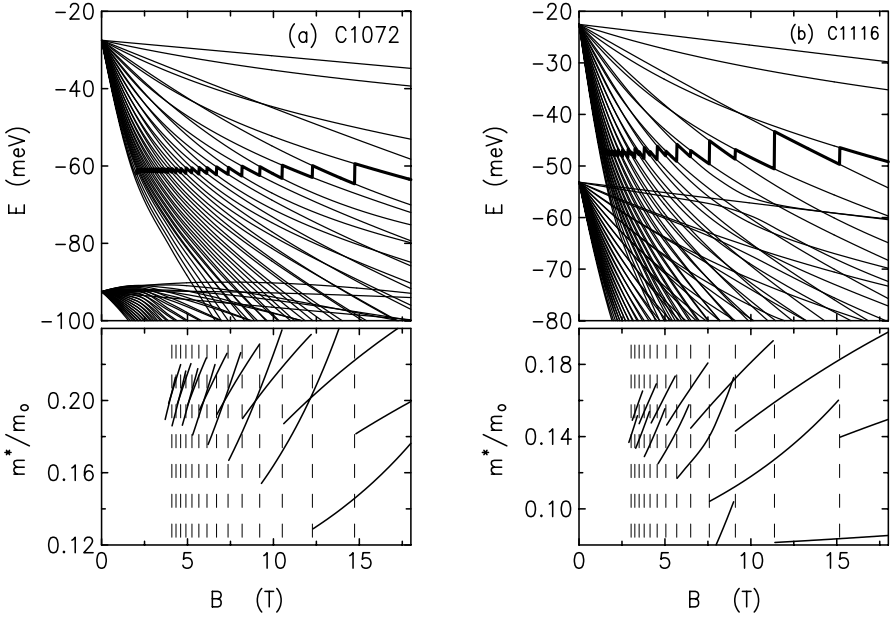


Fig. 8.9. Fan chart of Landau levels evolving from the two topmost heavy-hole subbands (*upper parts*) together with the Fermi energy (*bold line*), and the corresponding cyclotron masses (*lower parts*) for the two samples (a) C1072 and (b) C1116. Taken from [8]. © (1996) by the American Physical Society

8.3.3 Absorption Spectra

For the present case of an electric dipole field with a circular polarization in the $+$ direction, we have $e_- = e_z = 0$ in (8.3). In the calculation, the δ -function in (8.7) was replaced by a Lorentzian broadening with the same phenomenological linewidth for all transitions. The best agreement with the experimental data was obtained for a linewidth of 0.7 meV.

The calculated spectra for the two samples C1072 and C1116 are shown in Fig. 8.10 and allow direct comparison with the experimental spectra in Fig. 8.5. All essential features of the experimental data are reproduced by the calculation: the wavelength and magnetic-field dependence of the resonances, the intensities of the absorption lines, and the characteristic differences between the two samples. A striking difference between the two samples is that at high magnetic fields up to 18 T the cyclotron transition ($N = 0$) \rightarrow ($N = 1$) at wavenumbers between 140 and 180 cm^{-1} becomes possible only for the sample C1116, with the lower 2D charge density. These results are in close agreement with the experimental data (see Fig. 8.5 in the present work and Fig. 4 of [18]), although the interpretation in [18] in terms of Landau levels of bulk Ge is not correct.

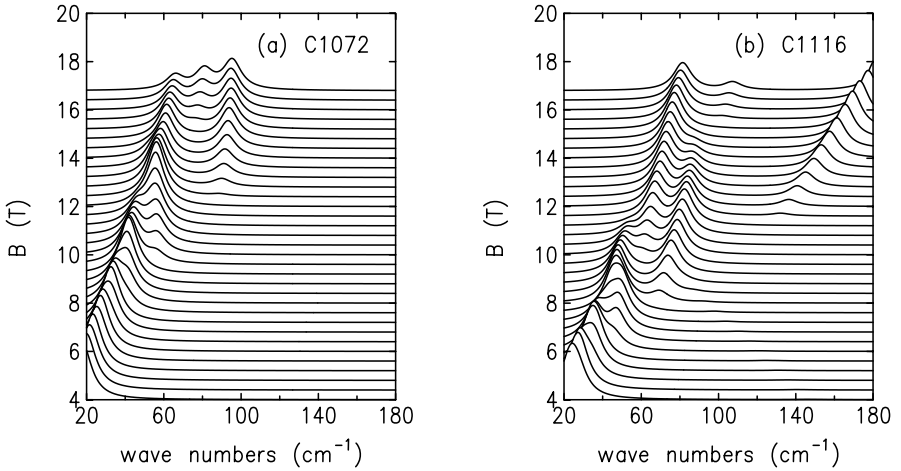


Fig. 8.10. Cyclotron absorption spectra calculated from the Landau levels of Fig. 8.9 for the two samples (a) C1072 and (b) C1116. A phenomenological broadening of 0.7 meV has been assumed for all transitions. Taken from [8]. © (1996) by the American Physical Society

As already mentioned in Section 8.3.1, the calculated FIR spectra of Fig. 8.10 are not sensitive to the position and profile of the δ -doping for a given hole concentration, and for the sample C1116 the spectra do not depend on the assumed well width either. However, as shown in Fig. 8.11, for both samples the results change dramatically if calculated on the basis of the 4×4 Luttinger Hamiltonian \mathcal{H}_{8v8v} , which neglects the spin-orbit split-off valence band Γ_7^v : the cyclotron masses decrease, the crossing of the spin-split Landau levels shifts to higher magnetic fields, and the FIR resonances move by up to 20 cm^{-1} towards higher energies. Thus, taking the coupling to the band Γ_7^v into account is essential for the agreement with the experimental data.

8.4 Landau Levels in Inversion-Asymmetric Systems

If the $B = 0$ spin splitting is dominated either by the Dresselhaus term or by the Rashba term, an analytical approach to the Landau-level structure at $B > 0$ is possible. We discuss these two cases separately. Finally, we discuss the more general and realistic case where both terms are present. Throughout this section, we assume that the crystallographic growth direction of the quasi-2D system is [001].

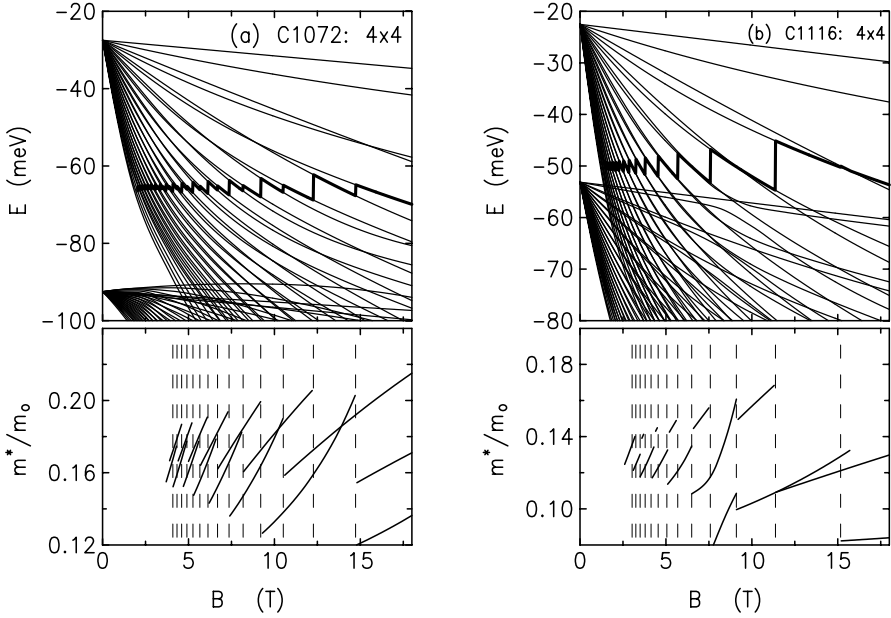


Fig. 8.11. Fan chart of Landau levels evolving from the two topmost heavy-hole subbands (*upper parts*) together with the Fermi energy (*bold line*), and corresponding cyclotron masses (*lower parts*) for the two samples (a) C1072 and (b) C1116 calculated by means of the 4×4 Luttinger Hamiltonian. Use of this simplified model results in substantial discrepancies compared with the results shown in Fig. 8.9, which were obtained by means of the more complete 6×6 Hamiltonian

8.4.1 Landau Levels and the Rashba Term

In the presence of a perpendicular magnetic field B , we replace k_{\pm} by the Landau raising and lowering operators a^{\dagger} , a defined in (4.22). We add the Rashba term to the EMA Hamiltonian (4.27), so that we obtain the following 2×2 Hamiltonian for the in-plane motion:

$$\mathcal{H} = \hbar\omega_c^* (a^{\dagger}a + \frac{1}{2}) \mathbb{1}_{2 \times 2} + \frac{g^*}{2} \mu_B B \sigma_z + \sqrt{\frac{2eB}{\hbar}} \alpha \begin{pmatrix} 0 & ia \\ -ia^{\dagger} & 0 \end{pmatrix}, \quad (8.14)$$

where $\omega_c^* = eB/m^*$, g^* is the effective g factor, μ_B is the Bohr magneton, and $\alpha = \langle \mathbf{r}_{41}^{6c6c} \mathcal{E}_z \rangle$. We can solve the problem for \mathcal{H} by expanding the eigenfunctions⁴ $|\mathcal{N}\pm\rangle$ in terms of Landau oscillator states $|L\rangle$ and spin eigenstates $|\sigma\rangle$. For the Hamiltonian (8.14), the eigenstates $|\mathcal{N}\pm\rangle$ contain only two states $|L\rangle \otimes |\sigma\rangle$:

$$|\mathcal{N}\pm\rangle = c_{1\pm} |L = \mathcal{N}\rangle \otimes |\sigma_{\pm}\rangle + c_{2\pm} |L = \mathcal{N} \pm 1\rangle \otimes |\sigma_{\mp}\rangle, \quad (8.15)$$

⁴ The Rashba Hamiltonian (8.14) (but not the Dresselhaus Hamiltonian (8.18)) has axial symmetry, so that here we have $\mathcal{N} = N$; see (4.31) and (4.32).

where $\sigma_+ = \uparrow$, $\sigma_- = \downarrow$, and $c_{i\pm}$ are expansion coefficients. Equation (8.15) illustrates that in the presence of SO coupling, the eigenstates of the Hamiltonian \mathcal{H} are not simultaneously eigenstates of the spin operator (unlike the Landau levels of a simple EMA Hamiltonian (4.27)). The energies of the Landau levels are [29]

$$E_{\mathcal{N}\pm} = \hbar\omega_c^* (\mathcal{N} + \tfrac{1}{2} \pm \tfrac{1}{2}) \mp \frac{1}{2} \sqrt{(\hbar\omega_c^* - g^* \mu_B B)^2 + 8\alpha^2 \frac{eB}{\hbar} (\mathcal{N} + \tfrac{1}{2} \pm \tfrac{1}{2})}, \quad (8.16)$$

where $\mathcal{N} = 0, 1, 2, \dots$. We can explore (8.16) in the limit of small and large magnetic fields at a fixed Fermi energy, i.e. we vary both B and \mathcal{N} such that the density $N_s \simeq [e/(\pi\hbar)] B\mathcal{N}$ is kept constant. In the limit of large magnetic fields, we obtain the following for the spin splitting at the Fermi energy:

$$\Delta E = E_{\mathcal{N}+} - E_{\mathcal{N}-} = g^* \mu_B B. \quad (8.17a)$$

In the opposite limit $B \rightarrow 0$ we have, consistent with (6.11),

$$\Delta E = -2 |\alpha| k_F, \quad (8.17b)$$

where $k_F = \sqrt{2\pi N_s}$ is the Fermi wave vector. We see here that, within the model (8.14), we have a smooth transition from the Rashba spin splitting (8.17b), which dominates in the limit $B \rightarrow 0$, to the opposite limit (8.17a), where the spin splitting ΔE is controlled by the Zeeman term. It can be shown that, consistent with (8.17), the eigenvectors (8.15) converge to (6.60) for $B \rightarrow 0$ and to $|L = \mathcal{N}\rangle \otimes |\sigma_{\pm}\rangle$ at large B .

8.4.2 Landau Levels and the Dresselhaus Term

In the preceding section, the Rashba model could be solved exactly in the presence of a quantizing magnetic field B . An analytical model for the Landau levels in the presence of the Dresselhaus term is possible only if we neglect the terms cubic in the in-plane wave vector k_{\parallel} (see (6.3)).⁵ This results in a Hamiltonian similar to (8.14),

$$\mathcal{H} = \hbar\omega_c^* (a^\dagger a + \tfrac{1}{2}) \mathbb{1}_{2 \times 2} + \frac{g^*}{2} \mu_B B \sigma_z + \sqrt{\frac{2eB}{\hbar}} \tilde{\eta} \begin{pmatrix} 0 & a^\dagger \\ a & 0 \end{pmatrix}, \quad (8.18)$$

where $\tilde{\eta} = \langle b_{41}^{6c6c} k_z^2 \rangle$. The energies of the Landau levels are

$$E_{\mathcal{N}\pm} = \hbar\omega_c^* (\mathcal{N} + \tfrac{1}{2} \mp \tfrac{1}{2}) \pm \frac{1}{2} \sqrt{(\hbar\omega_c^* + g^* \mu_B B)^2 + 8\tilde{\eta}^2 \frac{eB}{\hbar} (\mathcal{N} + \tfrac{1}{2} \mp \tfrac{1}{2})}, \quad (8.19)$$

where $\mathcal{N} = 0, 1, 2, \dots$. In the limit of large magnetic fields, we again obtain

⁵ For the anomalous Shubnikov–de Haas oscillations discussed in Chap. 9, the higher-order terms are of crucial importance.

$$\Delta E = g^* \mu_B B, \quad (8.20a)$$

whereas in the opposite limit $B \rightarrow 0$, we now have

$$\Delta E = 2 |\tilde{\eta}| k_F. \quad (8.20b)$$

Similarly to (8.17), we obtain a smooth transition from the pure Dresselhaus spin splitting (8.20b), which dominates (8.18) in the limit $B \rightarrow 0$, to the opposite limit (8.20a), where the spin splitting ΔE is controlled by the Zeeman term. However, as the effective g factor g^* is often negative, (8.20) implies that we can have a zero of the spin splitting ΔE at some intermediate magnetic field B_0 [30, 31]. For a 2D system with a Fermi wave vector k_F and $g^* < 0$, the spin splitting at the Fermi energy vanishes at

$$B_0 \approx \frac{m^*}{e\hbar} \frac{2\tilde{\eta}k_F}{\sqrt{1 - \left(1 + \frac{g^*m^*}{2m_0}\right)^2}}. \quad (8.21)$$

8.4.3 Landau Levels in the Presence of Both BIA and SIA

We can understand the different results in the two preceding sections by means of Fig. 8.12, where we have sketched the off-diagonal couplings between spin-split Landau oscillators $|L\rangle \otimes |\sigma\rangle$ due to the Dresselhaus term (D) and the Rashba term (R). In Fig. 8.12, we have assumed a negative effective g factor, consistent with many common semiconductors. In this case, because of level repulsion, the off-diagonal Rashba term increases the splitting between levels $|L\rangle \otimes |\downarrow\rangle$ and $|L\rangle \otimes |\uparrow\rangle$, whereas the Dresselhaus term competes against the Zeeman splitting. As the Zeeman term dominates the spin splitting for large B , whereas (without the Rashba term) the Dresselhaus term dominates for $B \rightarrow 0$, we obtain a zero of the spin splitting ΔE at some intermediate value of B [30, 31].

In a typical experiment with, for example, a GaAs–AlGaAs QW, we have contributions to ΔE from both the Rashba and Dresselhaus terms (see Sect. 6.4.1). Nevertheless, it is possible to have a true zero of ΔE at some finite value of B even with a more realistic multiband Hamiltonian [5, 32] that includes both BIA- and SIA-induced higher-order couplings, not shown in Fig. 8.12. This is due to the fact that for the growth direction [001] and $B > 0$, the point group of the system is C_2 (see Table 3.4), which has two irreducible double-group representations [5, 33], and for fixed \mathcal{N} the Landau levels $|\mathcal{N}+\rangle$ and $|\mathcal{N}-\rangle$ transform according to different irreducible representations. Accordingly, we have no mixing between $|L\rangle \otimes |\downarrow\rangle$ and $|L\rangle \otimes |\uparrow\rangle$ for fixed L .

As an example, we show in Fig. 8.13 the Landau levels $E_{\mathcal{N}\pm}$ and the positive energy difference $\Delta E = |E_{\mathcal{N}+} - E_{\mathcal{N}-}|$ between the Landau levels at the Fermi energy in a 150 Å wide GaAs–Al_{0.3}Ga_{0.7}As QW with $N_s = 2 \times 10^{11} \text{ cm}^{-2}$ in the presence of an external electric field $\mathcal{E}_z = 50 \text{ kV/cm}$.

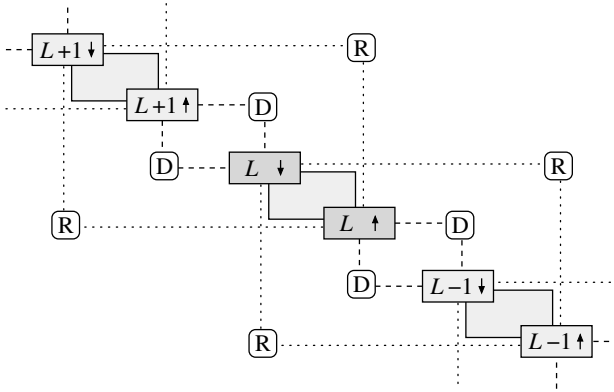


Fig. 8.12. Off-diagonal couplings between spin-split Landau harmonic oscillators $|L\rangle \otimes |\sigma\rangle$ ($\sigma = \uparrow, \downarrow$) in an inversion-asymmetric electron system. Matrix elements due to the Dresselhaus and Rashba terms are marked by the letters D and R, respectively

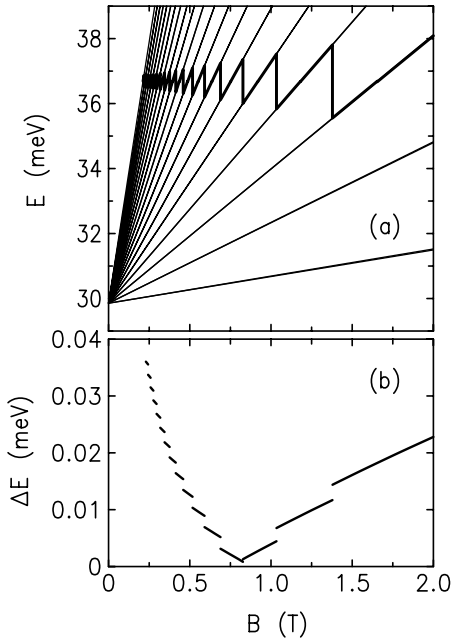


Fig. 8.13. (a) Landau levels $E_{N\pm}$ and (b) positive energy difference $\Delta E = |E_{N+} - E_{N-}|$ between the Landau levels at the Fermi energy in a 150 Å wide GaAs–Al_{0.3}Ga_{0.7}As QW with $N_s = 2 \times 10^{11} \text{ cm}^{-2}$ in the presence of an external electric field $\mathcal{E}_z = 50 \text{ kV/cm}$, calculated by means of an 8×8 Hamiltonian. In (a), the highest filled Landau level is marked by a bold line

For this calculation, we used an 8×8 Hamiltonian that takes BIA and SIA into account fully. We see that the spin splitting vanishes at about $B = 0.8 \text{ T}$, consistent with the results in Sect. 6.4.1, where it was shown that in GaAs QWs the spin splitting is usually dominated by the Dresselhaus term.

Table 8.2. Selection rules at temperature $T = 0$ for the spin-flip transition $|\mathcal{N}-\rangle \leftrightarrow |\mathcal{N}+\rangle$ due to the Dresselhaus and Rashba terms. The entries \pm indicate that the transitions induced by the Dresselhaus or the Rashba term are visible in the \pm polarization

	Dresselhaus	Rashba
$E_{\mathcal{N}-} > E_{\mathcal{N}+}$	+	–
$E_{\mathcal{N}-} < E_{\mathcal{N}+}$	–	+

In the presence of the Rashba or Dresselhaus term, the dipole operator can probe the spin-flip transition $|\mathcal{N}-\rangle \leftrightarrow |\mathcal{N}+\rangle$ because the mixing sketched in Fig. 8.12 gives rise to a finite transition amplitude (8.3) between these eigenstates [34].⁶ Indeed, it follows from (8.3) and Fig. 8.12 that, for the spin-flip transition $|\mathcal{N}-\rangle \leftrightarrow |\mathcal{N}+\rangle$, we have the selection rules listed in Table 8.2. As we usually have $g^* < 0$, the spin-flip transitions for large B are characterized by the selection rules in the upper row of Table 8.2. For small B , the lower row is relevant if the $B = 0$ spin splitting is dominated by the Dresselhaus term, and the upper row is relevant if it is dominated by the Rashba term. In general, both the Dresselhaus and the Rashba term contribute to the spin splitting at $B > 0$, so that the ratio between the oscillator strengths for + and – polarizations reflects the relative importance of these terms.

For the system considered in Fig. 8.13, we show in Fig. 8.14 the calculated

⁶ These transitions are often called electric-dipole spin resonances [34].

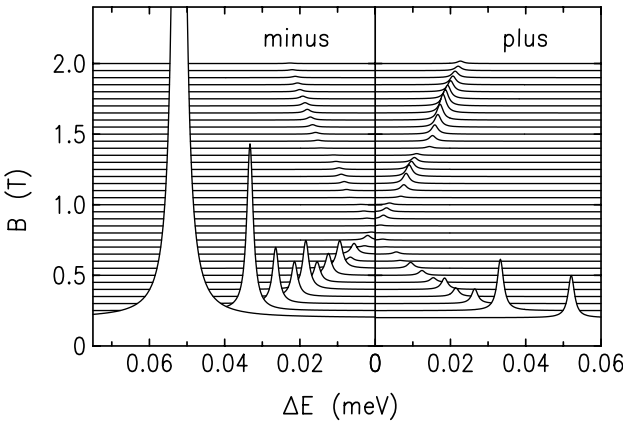


Fig. 8.14. Absorption spectrum for the spin-flip transitions due to BIA and SIA in a 150 Å wide GaAs–Al_{0.3}Ga_{0.7}As QW with $N_s = 2 \times 10^{11} \text{ cm}^{-2}$ in the presence of an external electric field $\mathcal{E}_z = 50 \text{ kV/cm}$, calculated by means of an 8×8 Hamiltonian. The left and right parts show the absorption of – and + polarized light, respectively

absorption spectrum for the spin-flip transitions. We see that above $B = 0.8$ T the dominant absorption line has the + polarization, whereas below $B = 0.8$ T the dominant line has the – polarization, in agreement with the above arguments. Note that the peak positions are the same for the two polarizations; only the intensities change.

References

1. J.C. Maan: “Magneto-optical properties of heterojunctions, quantum wells and superlattices”, in *Physics and Applications of Quantum Wells and Superlattices*, ed. by E.E. Mendez, K. von Klitzing (Plenum, New York, 1987), pp. 347–375 [151](#)
2. M.J. Yang, R.J. Wagner, B.V. Shanabrock, J.R. Waterman, W.J. Moore: Phys. Rev. B **47**, 6807 (1993) [5](#), [151](#), [154](#), [155](#), [156](#)
3. J. Scriba, A. Wixforth, J.P. Kotthaus, C. Bolognesi, C. Nguyen, H. Kroemer: Solid State Commun. **86**, 633 (1993) [5](#), [151](#), [154](#), [155](#), [156](#), [157](#)
4. K. Suzuki, J.C. Hensel: Phys. Rev. B **9**(10), 4184–4218 (1974) [4](#), [5](#), [15](#), [17](#), [24](#), [31](#), [32](#), [43](#), [44](#), [151](#), [152](#), [158](#)
5. H.R. Trebin, U. Rössler, R. Ranvaud: Phys. Rev. B **20**(2), 686–700 (1979) [4](#), [15](#), [22](#), [25](#), [31](#), [32](#), [43](#), [46](#), [48](#), [77](#), [98](#), [99](#), [209](#), [210](#), [212](#), [213](#), [214](#), [217](#), [151](#), [152](#), [158](#), [166](#)
6. J.J. Sakurai: *Modern Quantum Mechanics*, revised edn. (Addison-Wesley, Redwood City, 1994) [31](#), [83](#), [185](#), [204](#), [208](#), [151](#), [152](#)
7. C.R. Pidgeon: “Free carrier optical properties of semiconductors”, in *Handbook on Semiconductors*, ed. by M. Balkanski, Vol. 2 (North-Holland, Amsterdam, 1980), pp. 223–328 [152](#)
8. R. Winkler, M. Merkle, T. Darnhofer, U. Rössler: Phys. Rev. B **53**, 10 858 (1996) [5](#), [86](#), [219](#), [152](#), [158](#), [160](#), [161](#), [162](#), [163](#)
9. N.R. Cooper, J.T. Chalker: Phys. Rev. Lett. **72**, 2057 (1994) [154](#)
10. R. Winkler: Surf. Sci. **361/362**, 411 (1996) [5](#), [27](#), [155](#), [157](#)
11. E.O. Kane: J. Phys. Chem. Solids **1**, 249 (1957) [10](#), [27](#), [30](#), [56](#), [71](#), [156](#)
12. E. Kasper, H.J. Herzog: Appl. Phys. **8**(3), 199–205 (1975) [156](#)
13. G. Abstreiter: Phys. Scr. **T49A**, 42–45 (1993) [157](#)
14. U. König: “Electronic Si/SiGe devices: basics, technology, performance”, in *Festkörperprobleme (Advances in Solid State Physics)*, ed. by U. Rössler, Vol. 32 (Pergamon-Vieweg, Braunschweig, 1992), p. 199 [157](#)
15. J. Brunner, U. Menczgar, M. Gail, E. Friess, G. Abstreiter: Thin Solid Films **222**(1–2), 27–29 (1992) [157](#)
16. G. Abstreiter: Solid State Commun. **92**(1–2), 5–10 (1994) [157](#)
17. J.P. Cheng, V.P. Kesan, D.A. Grutzmacher, T.O. Sedgwick, J.A. Ott: Appl. Phys. Lett. **62**(13), 1522–1524 (1993) [157](#)
18. C.M. Engelhardt, D. Többen, M. Aschauer, F. Schäffler, G. Abstreiter, E. Gornik: Solid State Electron. **37**(4–6), 949–952 (1994) [5](#), [157](#), [158](#), [159](#), [162](#)
19. V.I. Gavrilenko, I.N. Kozlov, O.A. Kuznetsov, M.D. Moldavskaya, V.V. Nikonorov, L.K. Orlov, A.L. Chernov: JETP Lett. **59**(5), 348–352 (1994) [157](#)

20. V.I. Gavrilenko, I.N. Kozlov, M.D. Moldavskaya, V.V. Nikonorov, L.K. Orlov, O.A. Kuznetsov, A.L. Chernov: Jpn. J. Appl. Phys. **33**(4B), 2386–2387 (1994) [157](#)
21. S.L. Wong, D. Kinder, R.J. Nicholas, T.E. Whall, R. Kubiak: Phys. Rev. B **51**(19), 13 499–13 502 (1995) [157](#)
22. J.M. Luttinger: Phys. Rev. **102**(4), 1030 (1956) [3](#), [18](#), [28](#), [29](#), [88](#), [98](#), [99](#), [106](#), [131](#), [142](#), [158](#)
23. A. Zrenner: Appl. Phys. Lett. **55**(2), 156–158 (1989) [159](#)
24. G. Goldoni, A. Fasolino: Phys. Rev. Lett. **69**(17), 2567–2570 (1992) [69](#), [159](#)
25. D.A. Broido, L.J. Sham: Phys. Rev. B **31**, 888 (1985) [35](#), [38](#), [43](#), [46](#), [55](#), [86](#), [93](#), [161](#)
26. U. Ekenberg, M. Altarelli: Phys. Rev. B **32**, 3712 (1985) [35](#), [43](#), [86](#), [93](#), [97](#), [161](#)
27. E. Bangert, G. Landwehr: Superlatt. Microstruct. **1**, 363 (1985) [43](#), [86](#), [161](#)
28. E. Bangert, G. Landwehr: Surf. Sci. **170**, 593 (1986) [43](#), [161](#)
29. Y.A. Bychkov, E.I. Rashba: J. Phys. C: Solid State Phys. **17**, 6039–6045 (1984) [5](#), [66](#), [69](#), [77](#), [78](#), [83](#), [165](#)
30. G. Lommer, F. Malcher, U. Rössler: Phys. Rev. Lett. **60**, 728 (1988) [6](#), [78](#), [82](#), [83](#), [166](#)
31. U. Rössler, F. Malcher, G. Lommer: “Spin splitting in structured semiconductors”, in *High Magnetic Fields in Semiconductor Physics II*, ed. by G. Landwehr (Springer, Berlin, Heidelberg, 1989), Vol. 87 of Solid-State Sciences, p. 376 [77](#), [78](#), [83](#), [181](#), [166](#)
32. M. Braun, U. Rössler: J. Phys. C: Solid State Phys. **18**, 3365 (1985) [30](#), [32](#), [37](#), [40](#), [71](#), [77](#), [166](#)
33. G.F. Koster, J.O. Dimmock, R.G. Wheeler, H. Statz: *Properties of the Thirty-Two Point Groups* (MIT, Cambridge, MA, 1963) [6](#), [21](#), [23](#), [47](#), [72](#), [199](#), [166](#)
34. E.I. Rashba, V.I. Sheka: “Electric-dipole spin resonance”, in *Landau Level Spectroscopy*, ed. by G. Landwehr, E.I. Rashba (Elsevier, Amsterdam, 1991), pp. 131–206 [168](#)

9 Anomalous Magneto-Oscillations

In the year 1930, an oscillatory magnetic-field dependence was first observed in the electrical resistance of bismuth (the Shubnikov–de Haas effect [1]) and in the magnetization (the de Haas–van Alphen effect [2]). Since then, magneto-oscillations have been found in a large number of other observables, including the sample temperature, the velocity of sound, and the thermoelectric power [3]. These phenomena became of great interest and importance when Onsager showed, by means of a semiclassical argument [4], that the frequencies of the magneto-oscillations for $B > 0$ are related to extremal cross sections of the Fermi surface at $B = 0$. Since then, magneto-oscillations have proven to be a powerful tool for analyzing the Fermi surface of various materials, for example metals, semiconductors, and heavy-fermion systems.

For 2D systems, Onsager’s argument predicts a simple relation between the frequency f_{SdH} of magneto-oscillations and the 2D charge density N_s in the system,¹

$$N_s = \frac{e}{\pi\hbar} f_{\text{SdH}} . \quad (9.1)$$

Here e is the electron charge and \hbar is Planck’s constant. Following (9.1), longitudinal magnetoresistance oscillations in small magnetic fields perpendicular to the plane of the system are frequently used to measure the charge density N_s in 2D systems [5].

In Chap. 6, we have discussed the fact that inversion-asymmetry-induced spin splitting results in unequal populations N_{\pm} of the spin subbands at zero magnetic field, so that $N_s = N_+ + N_-$. For such systems, it has been observed by many groups studying different materials [6, 7, 8, 9, 10, 11, 12, 13, 14, 15, 16, 17, 18, 19, 20, 21] that the SdH oscillations exhibit a pronounced beating pattern, indicating that we have a superposition of two frequencies f_{\pm}^{SdH} . One can assume [7] that the Landau levels at $B > 0$ can be partitioned into two independent sets that correspond to the two spin subbands at $B = 0$.

¹ In this chapter, we shall always assume that only the lowest confinement subband is occupied. Otherwise we obtain a superposition of SdH frequencies according to the occupation of each confinement subband. We use the term “confinement subband” in order to distinguish it from the spin subbands discussed in this chapter.

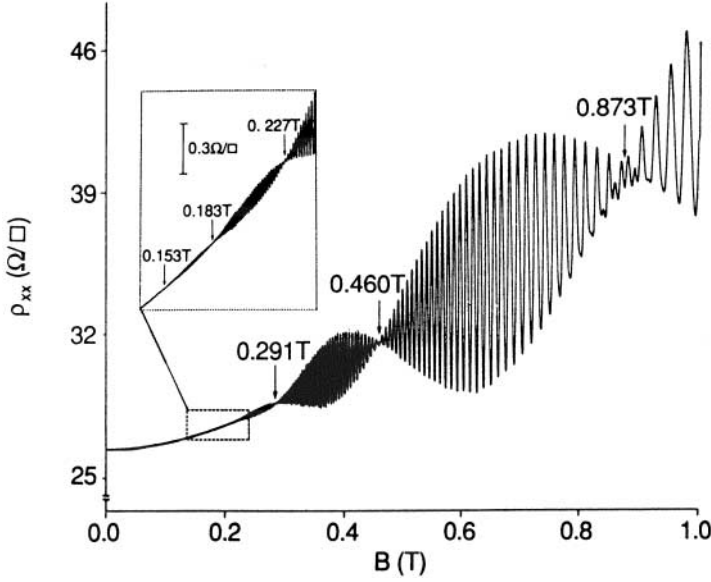


Fig. 9.1. Magnetoresistance oscillations of a 2D electron system in an asymmetric $\text{In}_{0.52}\text{Ga}_{0.48}\text{As}-\text{In}_{0.52}\text{Al}_{0.48}\text{As}$ QW measured by Das et al. [10]. Node positions in the SdH oscillations are marked by arrows. The magnetoresistance oscillations for $B < 0.25$ T are shown in the *inset*. The total 2D density according to Hall experiments was $N_s = 16.5 \times 10^{11} \text{ cm}^{-2}$. Taken from [10]. © (1989) by the American Physical Society

Each set gives rise to SdH oscillations so that, by analogy with (9.1), the spin subband densities N_{\pm} are given by

$$N_{\pm} = \frac{e}{2\pi\hbar} f_{\pm}^{\text{SdH}}. \quad (9.2)$$

This relation has often been used to analyze $B = 0$ spin splitting in 2D systems [6,7,8,9,10,11,12,13,14,15,16,17,18,19,20]. As an example, we show in Fig. 9.1 the SdH oscillations measured by Das et al. [10] for a 2D electron system in an asymmetric $\text{In}_{0.52}\text{Ga}_{0.48}\text{As}-\text{In}_{0.52}\text{Al}_{0.48}\text{As}$ QW. From (9.2), we obtain $N_+ = 8.9 \times 10^{11} \text{ cm}^{-2}$ and $N_- = 7.6 \times 10^{11} \text{ cm}^{-2}$, in good agreement with $N_s = 16.5 \times 10^{11} \text{ cm}^{-2}$ obtained from independent Hall experiments.

In this chapter, we shall present the results of a detailed analysis, where we have tested both theoretically and experimentally the validity of (9.2). We obtain good agreement between the experimental and calculated SdH oscillations. On the other hand, the calculated $B = 0$ spin splitting differs substantially from the predictions of (9.2) [22]. Using a semiclassical trace formula for particles with spin, we shall show that the anomalous magneto-oscillations reflect the nonadiabatic spin precession along the cyclotron orbits [23].

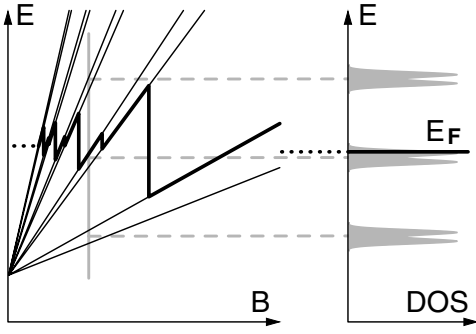


Fig. 9.2. Qualitative sketch of the Landau levels (*left*) and DOS (*right*) in the presence of a magnetic field B . The bold line indicates the Fermi energy E_F

9.1 Origin of Magneto-Oscillations

In this section, we shall briefly review the origin of magneto-oscillations periodic in $1/B$. First we shall use a quantum mechanical approach. Then we shall use a semiclassical point of view. Note that the two approaches complement each other by focusing on different aspects of this phenomenon.

We saw in Sect. 4.4 that in the presence of a magnetic field perpendicular to the plane of a 2D system, the electrons or holes condense into highly degenerate Landau levels, i.e. each Landau level corresponds to a peak in the density of states, as sketched in Fig. 9.2. The degeneracy G of each Landau level is proportional to the magnetic field B (see (4.25)), so that with increasing field B , the Landau levels are pushed through the Fermi surface. Magneto-oscillations thus reflect the oscillating DOS at the Fermi energy E_F . As many observables, such as the conductance, are proportional to the DOS at E_F , we can examine magneto-oscillations by measuring the magnetoresistance of the sample, for example.

While the above approach gives us, in general, a precise explanation of the origin of magneto-oscillations, the intuitive semiclassical approach due to Onsager [4] allows us to relate the frequencies of the magneto-oscillations to the Fermi surface at $B = 0$. This approach is based on the semiclassical model of the dynamics of Bloch electrons in a solid [24]. In the presence of a perpendicular magnetic field, the 2D electrons move on (classical) cyclotron orbits. In \mathbf{k}_{\parallel} space, these orbits follow contours of constant energy, consistent with the fact that the Lorentz force does not change the energy of a particle. Semiclassically, the electrons are forced onto quantized orbits given by the Bohr–Sommerfeld quantization condition (Fig. 9.3). The area enclosed by the Fermi contour is proportional to the 2D density N_s of electrons. As discussed above, with increasing magnetic field, the quantized cyclotron orbits are pushed one by one through the Fermi contour, which gives rise to magneto-oscillations. Thus it can be shown [4] that, semiclassically, we obtain the relation (9.1) between the density N_s and the frequency f_{SH} of the magneto-oscillations *irrespective of the detailed shape of the Fermi contour*.

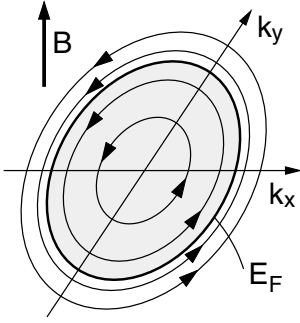


Fig. 9.3. Qualitative sketch of the quantized cyclotron orbits (*thin lines*) in the presence of a perpendicular magnetic field B . The *bold line* indicates the Fermi contour. The *shaded area* enclosed by the Fermi contour is proportional to the density N_s

9.2 SdH Oscillations and $B = 0$ Spin Splitting in 2D Hole Systems

The subject of our investigation was 2D hole systems in modulation-doped GaAs QWs. We have used GaAs because the band-structure parameters are well known [25,26], so that accurate numerical calculations can be performed, and because high-quality samples can be grown which allow the observation of many SdH oscillations [15]. As discussed in Chap. 6, the crystal structure of GaAs is zinc blende, which is inversion-asymmetric. This bulk inversion asymmetry provides a fixed contribution to spin splitting that cannot be altered in the experiments. In the classic experiment by Das et al. [10], the results of which are reproduced in Fig. 9.1, the structure inversion asymmetry of the sample was determined by an asymmetrically grown sequence of layers. Therefore the SIA spin splitting was fixed too. Recently, it has been shown that one can tune SIA spin splitting by means of one [21] or two [16] external gates. The $B = 0$ spin splitting in these systems thus has a fixed part due to BIA, and a tunable part due to SIA.

A single front or back gate changes both the asymmetry of the sample and the 2D density in the well. Such an experiment will be discussed in Sect. 9.2.4. First we shall focus on the conceptually simpler (but experimentally more demanding) case of a sample with both a front and a back gate so that one can continuously tune the inversion asymmetry while keeping the total density constant. The setup of such a system was sketched in Fig. 6.8.

9.2.1 Theoretical Model

Our calculations of magneto-oscillations were based on the methods discussed in Chap. 4. First, the 8×8 Kane Hamiltonian containing the bands Γ_6^c , Γ_8^v , and Γ_7^v was used to self-consistently calculate hole states in the QW at zero magnetic field. The Hamiltonian fully takes into account the spin splitting due to BIA and SIA. From this calculation, we obtained the spin subband densities (4.14) at $B = 0$.

We compare these results for the $B = 0$ spin splitting with a fully quantum mechanical calculation of magneto-oscillations at $B > 0$. For (9.2), we are interested only in the frequencies of these magneto-oscillations. Therefore we have analyzed directly the oscillatory DOS at E_F as a function of the magnetic field, instead of, for example, the magnetoresistance in a 2D system, which could be obtained from Kubo's formula. In [27] it was explicitly shown that the magnetoresistance in a 2D system is directly related to the oscillatory DOS at E_F . We assume that the positions of the peaks in the Fourier spectrum of the SdH oscillations are not affected by details of magnetotransport that go beyond the scope of the present work.

For the calculations at $B > 0$, we used the very same Hamiltonian as that discussed above, so that the results for $B = 0$ and $B > 0$ are directly comparable. In particular, for $B > 0$ we used the Hartree potential that was calculated self-consistently for $B = 0$. We introduced the magnetic field by replacing the in-plane wave-vector components with Landau raising and lowering operators (see Sect. 4.4). From the Landau levels $E_{N\sigma}(B)$, we obtained the Fermi energy $E_F(B)$ by an iterative solution of the equation for the (fixed) total density N_s of the system

$$N_s = \int dE D(E, B) \frac{1}{1 + \exp[(E - E_F(B))/(k_B T)]}, \quad (9.3)$$

where $D(E, B)$ is the DOS, for which we assumed a phenomenological Gaussian broadening

$$D(E, B) = G \sum_{N, \sigma} \frac{1}{\sqrt{2\pi}\Gamma} \exp\left(-\frac{[E - E_{N\sigma}(B)]^2}{2\Gamma^2}\right) \quad (9.4)$$

with linewidth Γ . The prefactor G in (9.4) is the degeneracy per unit area (4.25). From the Fermi energy $E_F(B)$, we obtained the DOS at E_F , for which we shall use the shorthand notation $D_F(B) \equiv D[E_F(B), B]$. Finally, we obtained the frequency f_{SdH} by means of a Fourier transform of $D_F(B)$ as a function of the reciprocal magnetic field.

As we were interested only in the frequencies of $D_F(B)$, we usually assumed temperature $T = 0$ in (9.3), because in the present context a finite, phenomenological broadening Γ and a finite temperature T have essentially the same effect [3]. The results depend neither on the width Γ nor on the functional form of the broadening in (9.4) (a Gaussian versus a Lorentzian, for example).

9.2.2 Calculated Results

We have considered a 200 Å wide GaAs-Al_{0.3}Ga_{0.7}As QW grown in the crystallographic direction [113] with a 2D hole density $N_s = 3.3 \times 10^{11} \text{ cm}^{-2}$. In Fig. 9.4, we show the self-consistently calculated $B = 0$ spin splitting $\Delta N = |N_+ - N_-|$ as a function of the electric field \mathcal{E}_z in the growth direction.

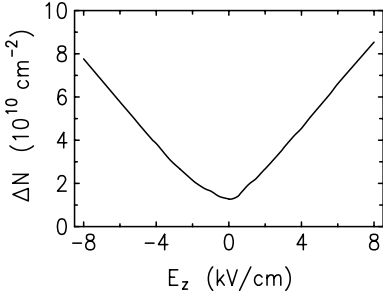


Fig. 9.4. Self-consistently calculated $B = 0$ spin splitting $\Delta N = |N_+ - N_-|$ as a function of the electric field \mathcal{E}_z in the growth direction for a 200 Å wide GaAs–Al_{0.3}Ga_{0.7}As QW grown in the crystallographic direction [113] with a 2D hole density $N_s = 3.3 \times 10^{11} \text{ cm}^{-2}$

Even around $\mathcal{E}_z = 0$, we have a significant spin splitting due to BIA. We obtain slightly different spin splittings for $\mathcal{E}_z < 0$ and $\mathcal{E}_z > 0$ because these directions of \mathcal{E}_z are not equivalent for a QW grown in the low-symmetry direction [113].

As an example, we present in Fig. 9.5 the Landau fan chart for the symmetric configuration ($\mathcal{E}_z = 0$). In Fig. 9.5a we show the fan chart obtained by means of the axial approximation; in Fig. 9.5b we show the fan chart obtained by including cubic corrections and BIA. We see that these terms are very important for a proper calculation of Landau levels for the low-symmetry growth direction [113].

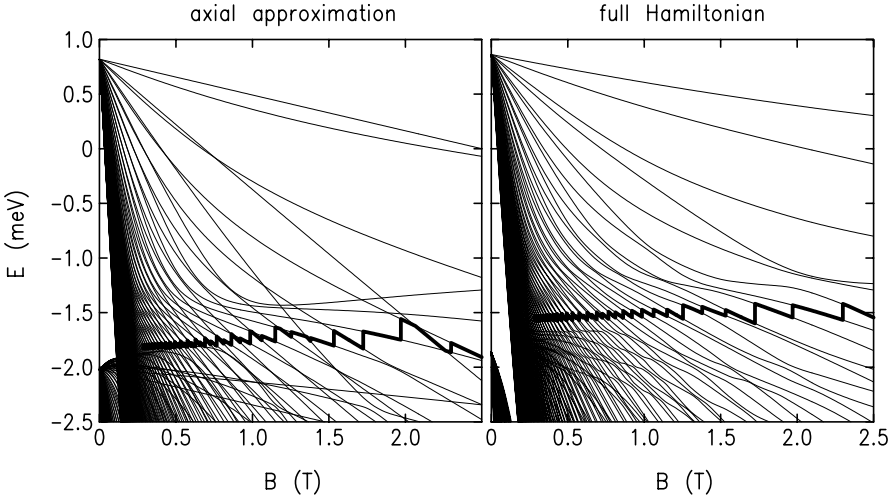


Fig. 9.5. Landau fan chart of a symmetric, 200 Å wide GaAs–Al_{0.3}Ga_{0.7}As QW grown in the crystallographic direction [113] with $N_s = 3.3 \times 10^{11} \text{ cm}^{-2}$: (a) calculated by means of the axial approximation, and (b) calculated using the full Hamiltonian, including cubic corrections and BIA. The *bold lines* indicate the Fermi energy

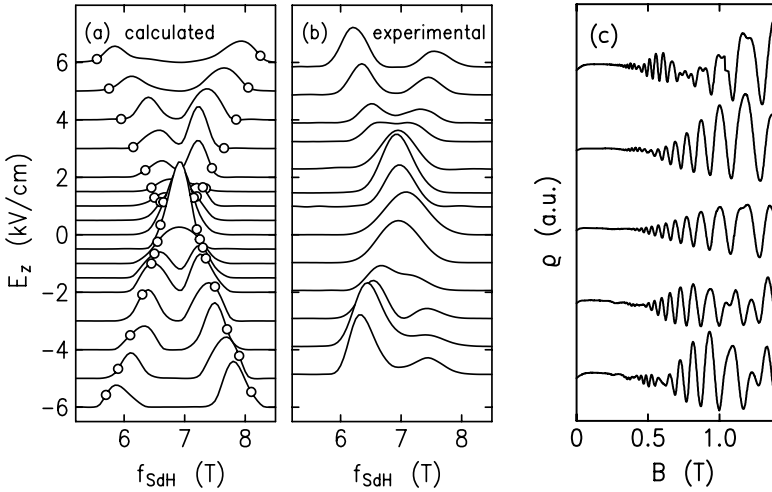


Fig. 9.6. Fourier spectra of the (a) calculated and (b) measured magneto-oscillations versus magnetic field B for different values of the electric field E_z for a 200 Å wide GaAs–Al_{0.3}Ga_{0.7}As QW with growth direction [113] and 2D hole density $N_s = 3.3 \times 10^{11} \text{ cm}^{-2}$. The open circles show the expected Fourier transform peak positions $(2\pi\hbar/e)N_{\pm}$ according to the calculated spin splitting N_{\pm} at $B = 0$. In (c) we show several measured magnetoresistance traces [16]. (a) and (b) taken from [22]. © (2000) by the American Physical Society

In Fig. 9.6a, we show the Fourier spectra of $D_F(B)$, the oscillating DOS at E_F . In order to match the experimental situation discussed below, the Fourier spectra were calculated for B between 0.20 and 0.85 T (B^{-1} between 1.17 and 5.0 T^{-1}). The expected peak positions according to the calculated $B = 0$ spin splittings (Fig. 9.4) are marked by open circles. It is very surprising that the calculated splittings of the magneto-oscillations are significantly smaller than the splittings expected from the calculation for $B = 0$. In particular, we obtain only one peak for the symmetric case $E_z = 0$, whereas we would expect two peaks from Fig. 9.4 owing to the BIA spin splitting that is present even for $E_z = 0$. We would like to emphasize once again that the calculations for $B = 0$ and $B > 0$ were based on the very same Hamiltonian.

So far, we have neglected completely in our discussion the Zeeman splitting of the Landau levels (though it is present in the numerical calculations). In fact, Zeeman splitting affects only the amplitude and phase, but not the frequency, of the oscillating DOS, because (in a perpendicular field) both the Landau-level splitting $\hbar\omega_c^*$ and the Zeeman splitting $g^*\mu_B B$ depend linearly on the magnetic field B . Accordingly, Zeeman splitting modifies the height but not the position of the peaks in the Fourier spectra in

Fig. 9.6.² On the other hand, an amplitude- and phase-sensitive modeling of the magneto-oscillations allows one to extract both the $B = 0$ spin splitting and the Zeeman splitting from the measured magneto-oscillations. However, the magneto-oscillations measured in most experiments are magnetoresistance oscillations. The amplitude and phase of these oscillations depend not only on the oscillating DOS but also on the details of the magnetotransport [27].

9.2.3 Experimental Findings

Shubnikov-de Haas oscillations for the system investigated theoretically in Figs. 9.4 and 9.6a were measured by Papadakis et al. [16]. These authors used Si-modulation-doped GaAs QWs grown by MBE on the (113)A surface of an undoped GaAs substrate. The well width was 200 Å. Photolithography was used to pattern Hall bars for resistivity measurements. The samples had metal front and back gates, which controlled both the 2D hole density and \mathcal{E}_z (see Fig. 6.8). Measurements were done at a temperature of 25 mK. In order to vary \mathcal{E}_z while maintaining a constant density, Papadakis et al. first set the front-gate (V_{fg}) and back-gate (V_{bg}) biases and measured the resistivity as a function of B . The total 2D hole density N_s was then deduced from the Hall coefficient. Then, at small B , V_{fg} was increased and the change in the hole density was measured. V_{bg} was then reduced to recover the original density. This procedure changes \mathcal{E}_z while maintaining the same density to within 3%, and allows calculation of the change in \mathcal{E}_z from the way the gates affect the density. These steps were repeated until the whole range of V_{fg} and V_{bg} that was accessible without causing gate leakage had been probed.

The Fourier spectra of the measured SdH oscillations are shown in Fig. 9.6b. Several measured magnetoresistance traces are reproduced in Fig. 9.6c. Keeping in mind that we may not expect a strict one-to-one correspondence between the oscillatory DOS at the Fermi energy (Fig. 9.6a) and the magnetoresistance oscillations (Fig. 9.6b), the agreement is quite satisfactory. However, the measured peaks confirm the result that the peaks in the spectra of the magneto-oscillations deviate substantially from the expected peak positions according to the zero- B spin splitting: for nearly all values of \mathcal{E}_z the splitting $(2\pi\hbar/e)\Delta N$ is significantly larger than $\Delta f = f_+^{\text{SdH}} - f_-^{\text{SdH}}$. In particular, near $\mathcal{E}_z = 0$ only one SdH frequency is visible in both the measured and the calculated spectra, whereas we would expect to obtain two frequencies. Note that the calculated values of ΔN near $\mathcal{E}_z = 0$ would imply a beating pattern of the SdH oscillations with two nodes within the range of B investigated. No indication of a beating pattern was observed near $\mathcal{E}_z = 0$, neither in the calculated nor in the measured SdH oscillations.

² In the particular case where the Zeeman splitting equals half the Landau-level splitting, all intensity in the Fourier spectra is shifted to the total-density peak at $f = (2\pi\hbar/e)N_s$.

It is interesting that, in spite of this anomalous behavior of the magneto-oscillations, we always find, in both the calculations and the experiments, that the sum of the two SdH frequencies correctly gives the total density, i.e. $N_s = [e/(2\pi\hbar)](f_+^{\text{SdH}} + f_-^{\text{SdH}})$. We remark that, experimentally, the total density can be measured independently by means of the quantum Hall effect.

9.2.4 Anomalous Magneto-Oscillations in Other 2D Systems

We have performed extensive calculations and further experiments which have confirmed that the results in Fig. 9.6 are typical for 2D hole systems. In Fig. 9.7, we show the results for 150 Å wide QWs which have only a front gate [15]. Here the gate voltage changes both the total density $N_s = N_+ + N_-$ in the well and the asymmetry in the sample. Therefore we have plotted Δf and ΔN versus N_s . For $N_s = 3.8 \times 10^{11} \text{ cm}^{-2}$, the QW becomes symmetric, which corresponds to a minimum of ΔN . Again we have good agreement between the measured and calculated differences Δf . However, there is a significant difference between Δf and the predicted splittings based on ΔN .

For different crystallographic growth directions, the spin splitting and SdH oscillations behave rather differently. Moreover, these quantities depend

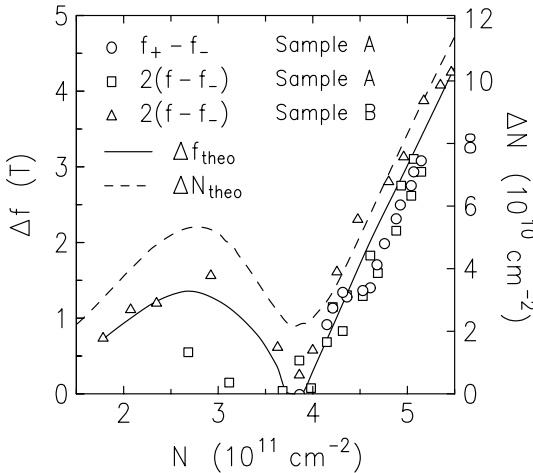


Fig. 9.7. The difference Δf between the two frequencies of the magneto-oscillations (left) and the difference ΔN between the two spin-subband densities (right), plotted against the total hole density N_s . The symbols represent experimental data and the curves the results of calculations. The frequencies $f = (\pi\hbar/e)N_s$ used to determine the values of Δf , marked by squares and triangles were measured by means of the quantum Hall effect observed at higher fields [15]. The samples were two 150 Å wide GaAs–Al_{0.3}Ga_{0.7}As QWs whose charge distribution was symmetric at $N_s = 3.8 \times 10^{11} \text{ cm}^{-2}$. The right and left vertical axes are scaled according to $\Delta N = [e/(2\pi\hbar)]\Delta f$, so that ΔN and Δf can be directly compared. Taken from [28]. © (2001), with permission by Elsevier

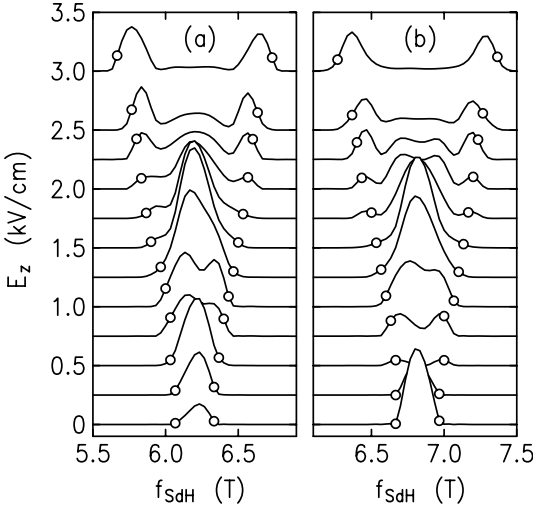


Fig. 9.8. Calculated Fourier spectra of magneto-oscillations versus magnetic field B for different values of the electric field \mathcal{E}_z for a 150 Å wide GaAs–Al_{0.5}Ga_{0.5}As QW with crystallographic growth direction [110] and 2D hole densities (a) $N_s = 3.0 \times 10^{11} \text{ cm}^{-2}$ and (b) $N_s = 3.3 \times 10^{11} \text{ cm}^{-2}$. The open circles show the expected Fourier transform peak positions $(2\pi\hbar/e)N_{\pm}$ according to the calculated spin splitting N_{\pm} at $B = 0$. Taken from [22]. © (2000) by the American Physical Society

sensitively on the total 2D hole density $N_s = N_+ + N_-$ in the well. In Fig. 9.8, we have plotted the calculated SdH Fourier spectra versus \mathcal{E}_z for a GaAs QW with a growth direction [110] and $N_s = 3.0 \times 10^{11} \text{ cm}^{-2}$ (Fig. 9.8a) and $N_s = 3.3 \times 10^{11} \text{ cm}^{-2}$ (Fig. 9.8b). Open circles mark the expected peak positions $(2\pi\hbar/e)N_{\pm}$ according to the spin splitting N_{\pm} at $B = 0$. Again, the peak positions in the Fourier spectra differ considerably from the expected positions $(2\pi\hbar/e)N_{\pm}$. Close to $\mathcal{E}_z = 0$, there is only one peak at $(\pi\hbar/e)N_s$. Around $\mathcal{E}_z = 1.0 \text{ kV/cm}$ we have two peaks, but at even larger fields \mathcal{E}_z the central peak at $(\pi\hbar/e)N_s$ shows up again. At $\mathcal{E}_z \approx 2.25 \text{ kV/cm}$ we have a triple-peak structure, consisting of a broad central peak at $(\pi\hbar/e)N_s$ and two side peaks at approximately $(2\pi\hbar/e)N_{\pm}$. In Fig. 9.8, we have a significantly smaller linewidth than in Fig. 9.6. Basically, this is due to the fact that for the Fourier transforms shown in Fig. 9.8 we used a significantly larger interval of B^{-1} (10.0 T^{-1} as compared with 3.83 T^{-1}) in order to resolve the much smaller splitting for the growth direction [110]. We note that for $\mathcal{E}_z = 0$ the SdH oscillations are perfectly regular over this large range of B^{-1} , with just *one* frequency, which makes it rather unlikely that the discrepancies between Δf and $(2\pi\hbar/e)\Delta N$ could be caused by a B -dependent rearrangement of holes between the Landau levels.

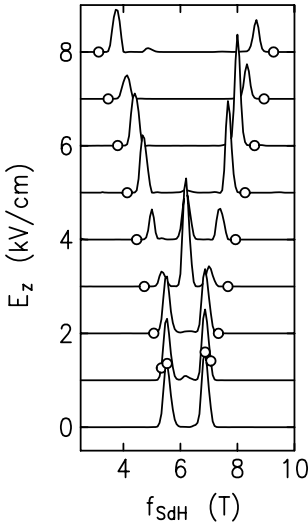


Fig. 9.9. Calculated Fourier spectra of magneto-oscillations versus magnetic field B for different values of the electric field \mathcal{E}_z for a 200 Å wide GaAs–Al_{0.3}Ga_{0.3}As QW with crystallographic growth direction [001] and 2D hole density $N_s = 3.0 \times 10^{11} \text{ cm}^{-2}$. The open circles show the expected peak positions $(2\pi\hbar/e)N_{\pm}$ according to the calculated spin splitting N_{\pm} at $B = 0$. Taken from [28]. © (2001), with permission by Elsevier

In Fig. 9.9, we have plotted the calculated SdH Fourier spectra versus \mathcal{E}_z for a GaAs QW with a growth direction [001] and $N_s = 3.0 \times 10^{11} \text{ cm}^{-2}$. Open circles mark the expected peak positions $(2\pi\hbar/e)N_{\pm}$ according to the spin splitting N_{\pm} at $B = 0$.³ For $\mathcal{E}_z = 0$, we have two peaks in the Fourier spectra that match exactly the positions expected according to the $B = 0$ spin splitting. However, for small $\mathcal{E}_z > 0$ the $B = 0$ spin splitting increases continuously, whereas the separation of the SdH frequencies stays constant. For larger \mathcal{E}_z , the separation of the side peaks is significantly smaller than $(2\pi\hbar/e)\Delta N$. Around $\mathcal{E}_z = 3 \text{ kV/cm}$ we have a triple-peak structure, consisting of a dominant central peak at $(\pi\hbar/e)N_s$ and two smaller side peaks at approximately $(2\pi\hbar/e)N_{\pm}$. For larger \mathcal{E}_z , the central peak disappears again.

Our calculations for holes were based on the fairly complex multiband Hamiltonian $\mathcal{H}_{8 \times 8}$. In Sect. 9.3.2 below, we show that qualitatively the same results can be obtained by analyzing the simpler 2×2 conduction band Hamiltonian of [29] that contains nonparabolic corrections up to fourth order in \mathbf{k} . However, this model is appropriate for electrons in large-gap semiconductors, where the spin splitting is rather small, so that it is more difficult to observe these effects experimentally.

9.3 Discussion

The common interpretation [7] of SdH oscillations in the presence of inversion asymmetry is based on the intuitive idea that for small B , the Landau

³ In Fig. 9.6 (growth direction [113]), we have distinguished between $\mathcal{E}_z < 0$ and $\mathcal{E}_z > 0$. For the growth directions [110] (Fig. 9.8) and [001] (Fig. 9.9,) $\mathcal{E}_z < 0$ and $\mathcal{E}_z > 0$ are equivalent.

levels can be partitioned into two sets which can be labeled by the two spin subbands. Each set gives rise to an SdH frequency which is related to the population of the respective spin subband according to (9.2). However, a comparison between the (partially) spin-polarized eigenstates at $B > 0$ and the unpolarized eigenstates at $B = 0$ shows that in general such a partitioning of the Landau levels is not possible. This reflects the fact that the orbital motions of the up and down spinor components are coupled in the presence of SO interaction, i.e. they cannot be analyzed separately.

9.3.1 Magnetic Breakdown

For many years, anomalous magneto-oscillations have been explained by means of magnetic breakdown [3]. In a sufficiently strong magnetic field B electrons can tunnel from an orbit on one part of the Fermi surface to an orbit on another, separated from the first by a small energy gap. The tunneling probability was found to be proportional to $\exp(-B_0/B)$, with a breakdown field B_0 , similar to Zener tunneling [3]. This brings into existence new orbits which, when quantized, correspond to *additional* peaks in the Fourier spectrum of the SdH oscillations. However, if the anomaly in the SdH oscillations reported in Fig. 9.6 were due to magnetic breakdown, for $\mathcal{E}_z = 0$ we would expect several frequencies f^{SdH} with different values rather than the observed *single* frequency. In a simple, semiclassical picture a single frequency could be explained by two *equivalent* orbits in \mathbf{k}_{\parallel} space, as sketched in Fig. 9.10. This would imply that the tunneling probabilities at the junctions j_1 and j_2 were equal to one (and thus independent of B). We remark that de Andrada e Silva et al. [30] studied anomalous magneto-oscillations for spin-split electrons in a 2D system. Their semiclassical analysis based on magnetic breakdown could not predict the breakdown field B_0 satisfactorily (see Table III in [30]).

In order to understand the deviation from (9.2) visible in Fig. 9.6, we need to look more closely at Onsager's semiclassical argument [4], which underlies (9.2). This argument is based on Bohr–Sommerfeld quantization of the semiclassical motion of Bloch electrons, which is valid for large quantum numbers. However, spin is an inherently quantum mechanical effect, for

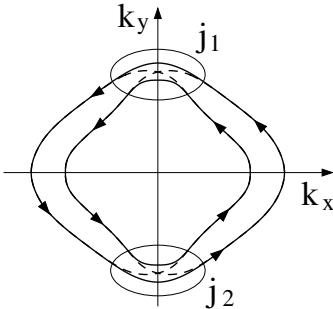


Fig. 9.10. Qualitative sketch of the spin-split Fermi contours in \mathbf{k}_{\parallel} space for a QW with growth direction [113] (*solid lines*). In a simple semiclassical picture, the observation of a single peak near $\mathcal{E}_z = 0$ in the Fourier spectra of Fig. 9.6 can be explained by two equivalent trajectories in \mathbf{k}_{\parallel} space, a left one and a right one, which follow the *dashed lines* at the breakdown junctions j_1 and j_2 . Taken from [22]. © (2000) by the American Physical Society

which the semiclassical regime of large quantum numbers is not meaningful. Therefore Bohr–Sommerfeld quantization cannot be carried through in the usual way for systems with SO interaction. In a semiclassical analysis of such a system, we have to keep spin as a discrete degree of freedom so that the motion in phase space becomes a multicomponent vector field [31], i.e. the motions along the spin-split branches of the energy surface are coupled to each other and cannot be analyzed separately.

One may ask whether we can combine the older idea of magnetic breakdown with the more recent ideas on Bohr–Sommerfeld quantization in the presence of SO interaction. Within the semiclassical theory of [31], spin-flip transitions may occur at the so-called mode-conversion points, which are points of spin degeneracy in phase space. Clearly, these points are related to magnetic breakdown. However, mode-conversion points introduce additional complications into the theory of [31], so that it was noted by the authors of that paper that their theory is not applicable in the vicinity of such points. Nevertheless, a semiclassical analysis of a particular model has shown [32] that spin flips are possible at these points for certain trajectories. However, we cannot expect that the probability for spin-flip transitions can be expressed as a conventional tunneling probability which does not take into account the spin degree of freedom for the two bands participating in the breakdown process. In the following section we shall discuss an alternative semiclassical approach based on a trace formula for particles with SO interaction.

9.3.2 Anomalous Magneto-Oscillations and Spin Precession

In this section, we shall use a semiclassical trace formula for particles with spin, which has only recently been developed [33, 34] in the context of quantum chaos, in order to show that the anomalous magneto-oscillations reflect the nonadiabatic spin precession along the cyclotron orbits [23]. While spin is a purely quantum mechanical property with no immediate analogue in classical physics, the present analysis reveals that our understanding of spin phenomena can be greatly improved by investigating equations of motion for a classical spin vector.

General Theory. Onsager’s semiclassical analysis of magneto-oscillations was based on a Bohr–Sommerfeld quantization of cyclotron orbits [4]. However, for systems with spin, there is no straightforward generalization of Bohr–Sommerfeld quantization [35, 36]. The Gutzwiller trace formula [37, 38] provides an alternative and particularly transparent semiclassical interpretation of magneto-oscillations that is applicable even in the presence of SO interaction. Rather than giving individual quantum energies, the trace formula relates the DOS $D(E)$ of a quantum mechanical system to a sum over all topologically distinct primitive periodic orbits Γ of the corresponding classical system. We decompose $D(E)$ into a smooth average DOS $\bar{D}(E)$ and an

oscillating part $\delta D(E)$. We then have, in the semiclassical (SC) asymptotic limit $\hbar \rightarrow 0$,

$$D(E) = \bar{D}(E) + \delta D(E) \quad (9.5a)$$

$$\stackrel{(\text{SC})}{\simeq} \bar{D}(E) + \sum_{\Gamma} \sum_{k=1}^{\infty} A_{\Gamma k}(E) \cos \left[\frac{k}{\hbar} S_{\Gamma}(E) - \frac{\pi}{2} \varphi_{\Gamma k} \right]. \quad (9.5b)$$

Here $S_{\Gamma}(E)$ is the classical action of the orbit Γ , k counts the number of revolutions around Γ , and the Maslov index $\varphi_{\Gamma k}$ is a phase that depends on the topology of Γ . The amplitudes $A_{\Gamma k}(E)$ depend on the energy, time period and stability of the orbit, as well as on whether the orbit is isolated or nonisolated.

We now briefly reformulate the theory of magneto-oscillations of 2D electrons without SO interaction using the language of periodic-orbit theory [38]. Here, the sum over k -fold repetitions of the classical periodic cyclotron orbits corresponds to a Fourier decomposition of the DOS as a function of the energy E . Within the EMA, we have (see (4.30))

$$D(E) = G \left\{ \sum_{L=0}^{\infty} \delta \left[E - \hbar \omega_c^* \left(L + \frac{1}{2} \right) \right] \right\} \quad (9.6a)$$

$$= G \left\{ \frac{1}{\hbar \omega_c^*} + \frac{2}{\hbar \omega_c^*} \sum_{k=1}^{\infty} (-1)^k \cos \left(\frac{k}{\hbar} \frac{2\pi E}{\omega_c^*} \right) \right\}, \quad (9.6b)$$

where G denotes the degeneracy per unit area (4.25) and $\omega_c^* = eB/m^*$ is the cyclotron frequency. The first term in (9.6b) is the average DOS, and the second term is the oscillating part. Equation (9.6b) can be derived in two ways. Starting from (9.6a), it can be obtained by purely algebraic transformations using the Poisson summation formula. Alternatively, we can evaluate (9.5b) for the periodic cyclotron orbits. Both methods yield identical results, i.e., in the particular case of a harmonic oscillator, the trace formula (9.5) is an identity.

We see in (9.6) that the action of a k -fold revolution corresponds to the k th harmonic $(k/\hbar) 2\pi E/\omega_c^* = 2\pi k m^* E/(\hbar e B)$ of the DOS. The DOS, for a fixed energy E , thus oscillates as a function of the reciprocal magnetic field $1/B$, which is the origin of magneto-oscillations. In an SdH experiment we have $E = E_F \simeq \hbar^2 k_F^2/(2m^*)$, where $k_F^2 = 2\pi N_s$. Thus we obtain Onsager's formula (9.1) from the first harmonic $k = 1$. Longer orbits $k > 1$, which give rise to higher harmonics in the oscillating DOS, are exponentially damped for small but nonzero temperatures [39], so that in the present analysis it suffices to consider $k = 1$.

Trace Formula for Systems with SO Interaction. In order to incorporate the effect of SO interaction into the trace formula (9.5), we follow the recent analysis by Bolte and Keppeler [33, 34]. We decompose the full Hamiltonian H into an orbital part H_{orb} plus the SO interaction H_{SO} :

$$H = H_{\text{orb}} + H_{\text{SO}} . \quad (9.7)$$

For simplicity, we shall restrict ourselves to spin-1/2 systems so that H_{SO} is a 2×2 matrix. The orbital part H_{orb} yields the classical orbits Γ that enter into the trace formula (9.5). Bolte and Keppeler showed that, to leading order in \hbar , the SO interaction H_{SO} results in weight factors

$$\text{tr } d_{\Gamma}(kT) \quad (9.8)$$

for the orbits in the trace formula (9.5). These factors can be determined by integrating the spin transport equation

$$i\hbar \dot{d}_{\Gamma}(t) = H_{\text{SO}}(\mathbf{r}, \mathbf{p}) d_{\Gamma}(t) \quad (9.9)$$

using the initial condition $d_{\Gamma}(0) = \mathbb{1}$. Here $d_{\Gamma}(t)$ is a 2×2 matrix in $SU(2)$, $\text{tr } d$ denotes the trace of d , T denotes the period of Γ , k counts the number of revolutions around Γ , \dot{d} is the time derivative of d , and $H_{\text{SO}}(\mathbf{r}, \mathbf{p})$ is the SO interaction along the orbit $\Gamma = [\mathbf{r}(t), \mathbf{p}(t)]$. Combining (9.5) and (9.8) we obtain

$$\delta D_{\text{SC}}(E) = \sum_{\Gamma} \sum_{k=1}^{\infty} A_{\Gamma k}(E) \text{tr } d_{\Gamma}(kT) \cos \left[\frac{k}{\hbar} S_{\Gamma}(E) - \frac{\pi}{2} \varphi_{\Gamma k} \right] . \quad (9.10)$$

It follows that the spin degree of freedom is determined by the orbital motion. On the other hand, in the lowest order of \hbar , the orbital motion remains unaffected by the motion of the spin [33, 34].

The weight factors $\text{tr } d_{\Gamma}(kT)$ allow an intuitive, classical interpretation. We write the SO interaction in the form

$$H_{\text{SO}}(\mathbf{r}, \mathbf{p}) = \frac{\hbar}{2} \boldsymbol{\sigma} \cdot \mathcal{B}(\mathbf{r}, \mathbf{p}) , \quad (9.11)$$

where $\mathcal{B}(\mathbf{r}, \mathbf{p})$ is an effective magnetic field. Here we use the same symbol as for the effective field \mathcal{B} in Sect. 6.6 because, in the present analysis, \mathcal{B} represents a classical analogue of the previously defined \mathcal{B} . The spin transport equation (9.9) for the matrix $d \in SU(2)$ is locally isomorphic to the motion of a trihedron $\mathcal{T} \in SO(3)$ attached to a classical spin vector \mathbf{s} , where \mathbf{s} obeys the equation of motion of a classical precessing spin,

$$\dot{\mathbf{s}} = \mathbf{s} \times \mathcal{B}(\mathbf{r}, \mathbf{p}) , \quad (9.12)$$

and $\mathcal{B}(\mathbf{r}, \mathbf{p})$ is the effective field along the orbit $\Gamma = [\mathbf{r}(t), \mathbf{p}(t)]$. After k periods of the orbital motion, the spin vector \mathbf{s} has been rotated by an angle $k\rho$ about an axis \mathbf{n} ; see Fig. 9.11. We remark that the axis \mathbf{n} (but not ρ) depends on the starting point of the periodic orbit. The angle ρ contains both a dynamical phase and a geometric phase similar to Berry's phase [40]. Finally we have (see e.g. (3.2.45) in [41])⁴

$$\text{tr } d_{\Gamma}(kT) = 2 \cos(k\rho/2) , \quad (9.13)$$

⁴ The relation between the angle ρ and the previously [34] defined angles θ and η is given by $\cos(\rho/2) = \cos(\theta/2) \cos \eta$.

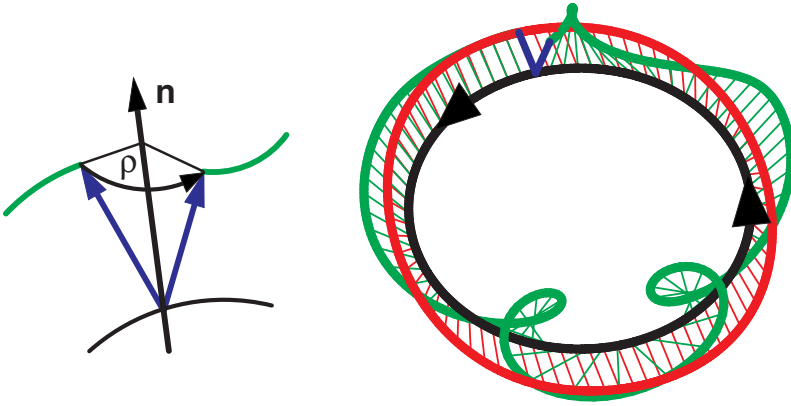


Fig. 9.11. Classical spin precession (*bold green line*) about the effective field \mathcal{B} (*bold red line*) along a cyclotron orbit (*black*) for a GaAs QW. The *thin lines* represent the momentary vectors of the effective field \mathcal{B} (*red*) and the spin s (*green*) along the cyclotron orbit. The momentary vectors for \mathcal{B} are normalized with respect to the maximum of $|\mathcal{B}|$ along the orbit. At the starting point, we have chosen $s \parallel \mathcal{B}$. After one cycle the motion of the spin vector can be identified with a rotation by an angle ρ about an axis \mathbf{n} , as shown in the blow-up on the *left*. The initial and final directions of the spin vector s are marked in *blue*. The system considered is a 100 Å wide GaAs–Al_{0.5}Ga_{0.5}As QW grown in the crystallographic direction [113] with a 2D density $N_s = 5 \times 10^{11} \text{ cm}^{-2}$ in the presence of an electric field $\mathcal{E}_z = 100 \text{ kV/cm}$ and a magnetic field $B = 0.05 \text{ T}$. Taken from [23]. © (2002) by the American Physical Society

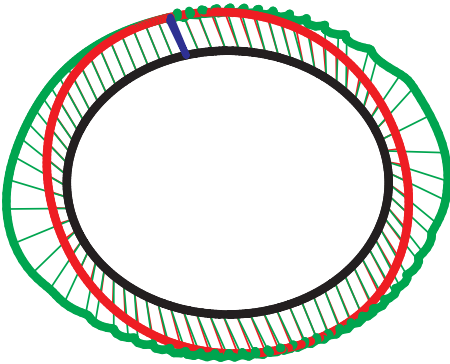


Fig. 9.12. Classical spin precession for the same system as in Fig. 9.11 but assuming an external magnetic field $B = 0.004 \text{ T}$. Here the spin precession is adiabatic

i.e. for evaluating the trace, the two-to-one correspondence between $d \in SU(2)$ and $T \in SO(3)$ is unimportant.

Example: 2D Electrons in a GaAs QW. We have analyzed magneto-oscillations for quasi-2D electron systems in semiconductors such as GaAs where we have two contributions to the SO coupling. The Dresselhaus term (6.1) reflects the bulk inversion asymmetry of the zinc blende structure of

GaAs. If the inversion symmetry of the confining potential of the quasi-2D system is broken, we obtain an additional SO coupling given by the Rashba term (6.10). While the Dresselhaus term is fixed, the Rashba SO coupling can be tuned by applying an electric field \mathcal{E}_z perpendicular to the plane of the quasi-2D system (Fig. 6.8).

We shall investigate a 2D system grown in the crystallographic direction [113] where the effective field \mathbf{B} has an out-of-plane component B_z . Using the rotated coordinate system defined in Fig 7.3, the Dresselhaus term (6.1) reads

$$\mathcal{H}_{6c6c}^b = \mathbf{b}_{41}^{6c6c} \begin{pmatrix} \mathcal{H}_z^b & \mathcal{H}_-^b \\ \mathcal{H}_-^{b\dagger} & -\mathcal{H}_z^b \end{pmatrix}, \quad (9.14a)$$

where

$$\mathcal{H}_-^b = \frac{\sqrt{2}i}{4} [c(3c^2 - 1)(k_-^3 + \{k_+k_-k_+\} - 2k_+k_z^2) - 6cs^2(\{k_-k_+k_-\} - 2k_-k_z^2)], \quad (9.14b)$$

$$\mathcal{H}_z^b = \frac{\sqrt{2}i}{4} [\frac{3}{2}s(c^2 + 1)(k_-^3 - k_+^3) + \frac{1}{2}s(3c^2 - 1)(\{k_-k_+k_-\} - \{k_+k_-k_+\})], \quad (9.14c)$$

where $s \equiv \sin \theta$ and $c \equiv \cos \theta$. For the growth direction [113], we have $\theta = \arccos(3/\sqrt{11})$. Note that we have neglected all terms containing odd powers of k_z because we have $\langle k_z^n \rangle = 0$ for n odd. The Rashba term (6.10) remains unaffected by the change of the coordinate system.

In the quantum mechanical calculation, we added the Dresselhaus term (9.14) and the Rashba term (6.10) to the EMA Hamiltonian (4.27), which then was diagonalized numerically. In the semiclassical calculation, we inserted the Dresselhaus term (9.14) and the Rashba term (6.10) into the spin transport equation (9.9). The operator of the in-plane momentum $\hbar \mathbf{k}_{\parallel}$ was replaced by the classical kinetic momentum $\mathbf{p}(t)$ along the cyclotron orbit:

$$\hbar \mathbf{k}_{\parallel} \rightarrow \mathbf{p}(t) = \sqrt{2m^*E} \begin{pmatrix} \cos \omega_c^* t \\ \sin \omega_c^* t \\ 0 \end{pmatrix}, \quad (9.15)$$

where E is the energy of the classical orbit. We then integrated the classical equations of motion (9.9) in order to evaluate (9.13). It follows from (9.6) and (9.13) that in the semiclassical calculation, apart from higher harmonics $k > 1$, the oscillating part of the DOS at the Fermi energy E_F is proportional to

$$\cos(\rho/2) \cos[2\pi m^* E_F / (\hbar e B)]. \quad (9.16)$$

Both in the quantum mechanical calculation and in the semiclassical calculation, we replaced k_z^2 by its expectation value $\langle k_z^2 \rangle$, i.e. we have assumed that the perpendicular component of the motion is completely decoupled from the in-plane component.

In Fig. 9.13, we compare the Fourier spectra of the magneto-oscillations of the DOS calculated quantum mechanically and semiclassically as outlined

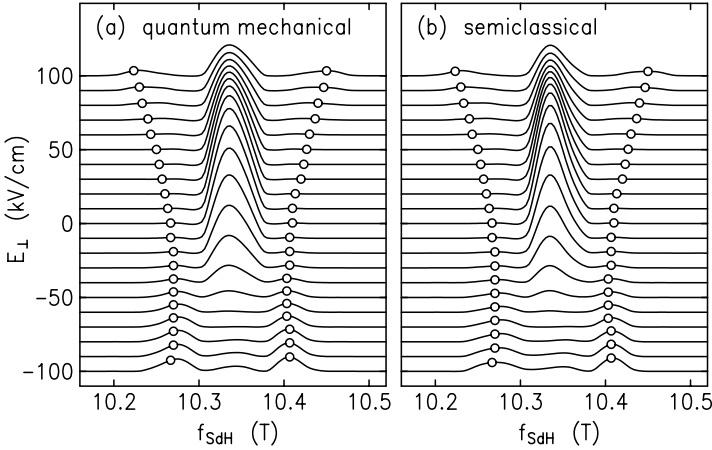


Fig. 9.13. (a) Quantum mechanical and (b) semiclassical Fourier spectra for different values of the electric field \mathcal{E}_z for a 2D electron system in a 100 Å wide GaAs–Al_{0.5}Ga_{0.5}As QW grown in the crystallographic direction [113] with constant total density $N_s = 5 \times 10^{11} \text{ cm}^{-2}$. The *open circles* show the expected Fourier transform peak positions $(2\pi\hbar/e)N_{\pm}$ according to the calculated spin subband densities N_{\pm} at $B = 0$. Taken from [23]. © (2002) by the American Physical Society

above, assuming a 2D electron system in a 100 Å wide GaAs–Al_{0.5}Ga_{0.5}As QW grown in the crystallographic direction [113] with a constant total density $N_s = N_+ + N_- = 5 \times 10^{11} \text{ cm}^{-2}$ and a varying \mathcal{E}_z . For comparison, the circles mark the peak positions which one would expect according to (9.2) for the spin subband densities N_{\pm} calculated quantum mechanically at $B = 0$. The Fourier spectra in Fig. 9.13a,b are in strikingly good agreement. On the other hand, the peak positions deviate substantially from the positions expected according to the $B = 0$ spin splitting. In particular, the semiclassical analysis based on (9.16) reproduces the central peak, which is not predicted by (9.2). The asymmetry in Fig. 9.13 with respect to positive and negative values of \mathcal{E}_z reflects the low-symmetry growth direction [113] (Ref. [22]).

Adiabatic and Nonadiabatic Motion. An analysis of the classical spin precession along the cyclotron orbit reveals the origin of the anomalous magneto-oscillations. The spin-split states at $B = 0$ correspond to fixing the direction of the spin parallel and antiparallel to the effective field $\mathbf{B}(\mathbf{p})$ along the cyclotron orbit. However, in general, the precessing spin cannot adiabatically follow the momentary field $\mathbf{B}(\mathbf{p})$. This can be seen in Fig. 9.11, where we have plotted the momentary field $\mathbf{B}(\mathbf{p})$ and the precessing spin \mathbf{s} along a cyclotron orbit. Both the direction and the magnitude of \mathbf{B} change along the orbit. In particular, the Dresselhaus term reverses the direction of \mathbf{B} when $|\mathbf{B}|$ has a minimum. A spin vector that is no longer parallel or antiparallel to \mathbf{B} implies that the system is in a superposition of states from

both spin subbands, so that the magneto-oscillations are not directly related to the $B = 0$ spin splitting.

For the spin, in order to be able to follow the momentary field $\mathbf{B}(\mathbf{p})$ adiabatically, the orbital motion must be slow compared with the motion of the precessing spin, i.e. we must have $(e/m_0)B \ll |\mathbf{B}(\mathbf{p})|$ for all points \mathbf{p} along the cyclotron orbit. Therefore, it is the smallest value $B_{\min} = \min |\mathbf{B}(\mathbf{p})|$ along the cyclotron orbit which determines whether or not the spin evolves adiabatically. This is illustrated in Fig. 9.11, where the parameters were chosen such that initially the spin is parallel to the effective field \mathbf{B} . First \mathbf{s} can follow \mathbf{B} , but after a quarter period of the cyclotron orbit the effective field \mathbf{B} reaches its minimum B_{\min} and \mathbf{s} starts to “escape” from \mathbf{B} . Subsequently, the spin vector \mathbf{s} is no longer parallel to \mathbf{B} , even in those regions where B becomes large again. For comparison, a completely adiabatic motion is shown in Fig. 9.12. We remark that adiabatic spin precession does not imply $\rho = 0$, but only that the rotation axis \mathbf{n} is approximately parallel to the initial (and final) direction of the effective field \mathbf{B} . At $t = 0$ and $t = T$, a trihedron attached to \mathbf{s} can be oriented differently.

We noted in Sect. 9.3.1 that for many years, anomalous magneto-oscillations have been explained by means of magnetic breakdown [42, 30]. Underlying this approach is a rather different semiclassical picture, where each spin-split subband is associated with an energy surface with separate classical dynamics. In the present treatment, on the other hand, there is only one energy surface, complemented by the dynamics of a classical spin vector. It is the essential idea within the concept of magnetic breakdown that, in a sufficiently strong external magnetic field B , electrons can tunnel from a cyclotron orbit on the energy surface of one band to an orbit on the energy surface of a neighboring band separated from the first one by a small energy gap. For spin-split bands, the separation of these bands is proportional to the effective field B , i.e. magnetic breakdown is most likely to occur in regions of a small effective field B . This approach implies that the anomalous magneto-oscillations are essentially determined by the breakdown regions only. (These breakdown regions can be identified with mode-conversion points [35].) Here the present approach differs fundamentally from these earlier models: in the present ansatz, the spin precesses continuously along the cyclotron orbit, i.e. the angle ρ in (9.16) is affected by the nonadiabatic motion of \mathbf{s} in the regions of both small and large B (see Fig. 9.11).

In the adiabatic regime, where the spin precession is fast compared with the orbital motion, we can readily evaluate the angle ρ . First we shall derive two-component vectors $\psi(t)$ that are adiabatic solutions of

$$i\dot{\psi}(t) = \boldsymbol{\sigma} \cdot \mathbf{B} \psi(t) . \quad (9.17)$$

Then we shall combine the vectors $\psi(t)$ to form a matrix $d(t)$ that is an adiabatic solution of (9.9). We write \mathbf{B} using polar coordinates θ and ϕ :

$$\mathbf{B} = |\mathbf{B}| \begin{pmatrix} \sin \theta \cos \phi \\ \sin \theta \sin \phi \\ \cos \theta \end{pmatrix}. \quad (9.18)$$

The momentary eigenvalues λ_{\pm} and eigenvectors χ_{\pm} of $\boldsymbol{\sigma} \cdot \mathbf{B}$ are

$$\lambda_+ = |\mathbf{B}| : \quad \chi_+ = \begin{pmatrix} \cos(\theta/2) \\ e^{i\phi} \sin(\theta/2) \end{pmatrix}, \quad (9.19a)$$

$$\lambda_- = -|\mathbf{B}| : \quad \chi_- = \begin{pmatrix} -e^{-i\phi} \sin(\theta/2) \\ \cos(\theta/2) \end{pmatrix}. \quad (9.19b)$$

In the adiabatic limit, we can use the ansatz

$$\psi_{\pm}(t) = \exp \left[\mp i \int_0^t |\mathbf{B}(t')| dt' + i\gamma_{\pm}(t) \right] \chi_{\pm}(t), \quad (9.20)$$

i.e. we assume that the solutions $\psi_{\pm}(t)$ of (9.17) stay in the subspaces defined by $\chi_{\pm}(t)$. By inserting (9.20) into (9.17), we find that the Berry phase $\gamma_{\pm}(t)$ amounts to

$$\gamma_{\pm}(t) = \mp \frac{1}{2} \int_0^t [1 - \cos \theta(t')] \dot{\phi}(t') dt'. \quad (9.21)$$

Finally, we use $\psi_{\pm}(t)$ to construct an adiabatic solution $d(t)$ of (9.9),

$$d(t) = \begin{pmatrix} \psi_+^{\dagger}(0) \\ \psi_-^{\dagger}(0) \end{pmatrix} \begin{pmatrix} \psi_+(t) \\ \psi_-(t) \end{pmatrix}, \quad (9.22)$$

which obeys the correct boundary condition $d(0) = \mathbf{1}$. Evaluating the trace yields $\text{tr } d(T) = 2 \cos(\rho/2)$, where

$$\rho/2 = \int_0^T |\mathbf{B}(t')| dt' + \frac{1}{2} \int_0^T [1 - \cos \theta(t')] \dot{\phi}(t') dt' \quad (9.23)$$

and $T = 2\pi/\omega_c^*$ is the period of the cyclotron motion.

In the limit of small external fields ($B \rightarrow 0$), the Berry phase in (9.23) converges towards a constant. In addition, the integrand $|\mathbf{B}(t')|$ can be expanded with respect to a small Zeeman term, i.e. $|\mathbf{B}| \approx \mathcal{B}_0 + \mathcal{B}_1 B$, where the coefficients \mathcal{B}_0 and \mathcal{B}_1 are T -periodic in time. Note that neither the Dresselhaus nor the Rashba term depends explicitly on the external field B . Thus, in the limit of small external fields, we obtain $\rho(B) \approx \rho_0/B + \rho_1$ where ρ_0 and ρ_1 are constants, independent of B . Inserting the last relation into (9.16), we obtain

$$\delta D_{\text{ad}}(E) \propto \frac{1}{2} \sum_{\pm} \cos \left[\left(\frac{2\pi m^* E_F}{e\hbar} \pm \frac{\rho_0}{2} \right) \frac{1}{B} \pm \frac{\rho_1}{2} \right], \quad (9.24)$$

i.e. only in the limit of adiabatic spin precession are magneto-oscillations directly related to the $B = 0$ spin splitting.

By varying the crystallographic growth direction of the QW, it is possible to tune the value of \mathcal{B}_{\min} . In particular, for a QW grown in the crystallographic direction [110], the Dresselhaus term vanishes when \mathbf{p} is parallel to the in-plane directions [001] and [00 $\bar{1}$]; see Fig. 6.20. Thus, for a symmetric QW without Rashba SO coupling, we have $|\mathcal{B}(\mathbf{p})| = (e/m_0)B$ for these values of \mathbf{p} , which implies that there is no adiabatic regime and one always observes anomalous magneto-oscillations.

Analytical Treatment of the Rashba Model. For a system with Rashba SO coupling but no Dresselhaus term, we can estimate the accuracy of the approximate semiclassical approach by comparing with the exact eigenvalue spectrum (8.16). Using the Poisson summation formula, we obtain from (8.16) the exact trace formula [43]

$$\begin{aligned} \delta D_{\text{SC}}(E) = \frac{2G}{\hbar\omega_c^*} \sum_{\pm} \left[1 \pm \Xi / \sqrt{\frac{1}{4} \left(1 - \frac{g^*}{2} \frac{m^*}{m_0} \right)^2 + \frac{2E}{\hbar\omega_c^*} \Xi + \Xi^2} \right] \\ \times \sum_{k=1}^{\infty} \cos \left[2k\pi \left(\frac{E}{\hbar\omega_c^*} + \Xi \pm \sqrt{\frac{1}{4} \left(1 - \frac{g^*}{2} \frac{m^*}{m_0} \right)^2 + \frac{2E}{\hbar\omega_c^*} \Xi + \Xi^2} \right) \right], \end{aligned} \quad (9.25)$$

where

$$\Xi \equiv \frac{\alpha^2}{\hbar\omega_c^*} \frac{m^*}{\hbar^2}. \quad (9.26)$$

On the other hand, we can also evaluate analytically the spin transport equation (9.9), which yields

$$\text{tr } d(kT) = (-1)^k 2 \cos \left[2k\pi \sqrt{\frac{1}{4} \left(1 - \frac{g^*}{2} \frac{m^*}{m_0} \right)^2 + \frac{2E}{\hbar\omega_c^*} \Xi} \right]. \quad (9.27)$$

Using (9.10), we then obtain the following for the oscillating part of the DOS:

$$\delta D_{\text{SC}}(E) = \frac{2G}{\hbar\omega_c^*} \sum_{\pm} \sum_{k=1}^{\infty} \cos \left[2k\pi \left(\frac{E}{\hbar\omega_c^*} \pm \sqrt{\frac{1}{4} \left(1 - \frac{g^*}{2} \frac{m^*}{m_0} \right)^2 + \frac{2E}{\hbar\omega_c^*} \Xi} \right) \right]. \quad (9.28)$$

Equation (9.28) is a good approximation to (9.25) if

$$\frac{E}{\hbar\omega_c^*} \gg \Xi. \quad (9.29)$$

In an SdH experiment, we have $E \simeq \hbar^2 k_F^2 / (2m^*)$, where $k_F^2 = 2\pi N_s$. Thus (9.29) is equivalent to

$$N_s \gg N_m, \quad (9.30)$$

where N_m is the “quantum density” (6.15) below which only the lower spin subband is occupied at $B = 0$. We have seen in Sect. 5 that for realistic parameter values (9.30) is always fulfilled in quasi-2D systems. This justifies the approach based on (9.9) which in the present context of an \hbar expansion corresponds to the regime of weak SO coupling.⁵ For $k = 1$, and using the above approximate expression for E_F , (9.28) yields the SdH frequencies

$$f_{\pm}^{\text{SdH}} = \frac{2\pi\hbar}{e} \left(\frac{N_s}{2} \pm \frac{\alpha}{4\pi} \frac{2m^*}{\hbar^2} \sqrt{2\pi N_s} \right), \quad (9.31)$$

which represent the leading order in α of the exact $B = 0$ spin subband densities (6.18). We remark that a similar calculation based on the $k = 1$ component of the exact level density (9.25) and using the exact Fermi energy (6.17) yields the exact $B = 0$ spin subband densities (6.18). The above analysis also illustrates that Onsager’s interpretation of SdH oscillations is not affected by Zeeman splitting.

Other Systems. We note that the concepts developed here are rather general and, in particular, are not restricted to spin-1/2 systems. Indeed, an analogous semiclassical analysis can be carried out for any system with (nearly) degenerate subbands. These bands can be identified with a single band with an SO coupling acting on an effective spin degree of freedom, similarly to Lipari and Baldareschi’s treatment [44] of the multiply degenerate valence band edge in a semiconductor with a diamond or zinc blende structure. In particular, we expect that the present approach can be applied to the interpretation of de Haas–van Alphen experiments on ultrahigh-purity samples [45] that had called into question the established concepts of magnetic breakdown.

9.4 Outlook

Few approaches allow realistic, fully quantum mechanical calculations of magneto-oscillations that can be compared with band structure calculations at $B = 0$. This is due to the fact that, unlike the $\mathbf{k} \cdot \mathbf{p}$ method and the envelope function approximation, other methods for band structure calculations are often unsuitable for taking a quantizing magnetic field into account. In particular, the semiclassical concept of magnetic breakdown introduced in the early 1960s in order to explain anomalous SdH oscillations in metals, in spite of its wide use, has rarely been compared with fully quantum mechanical calculations. More recent experiments with metal samples of extremely high purity revealed unresolved discrepancies between these semiclassical concepts

⁵ A semiclassical treatment of the Rashba model in the limit of strong SO coupling has been given in [43].

and experimental data [45]. Later, the experiments and the semiclassical concepts were critically assessed by Pippard [46]. We expect that the present surprising results on anomalous magneto-oscillations in 2D electron and hole systems represent merely a starting point for more detailed investigations of these questions.

References

1. W. Shubnikov, W.J. de Haas: Proc. Netherlands Roy. Acad. Sci. **33**, 130 (1930) [171](#)
2. W.J. de Haas, P.M. van Alphen: Proc. Netherlands Roy. Acad. Sci. **33**, 1106 (1930) [171](#)
3. D. Shoenberg: *Magnetic Oscillations in Metals* (Cambridge University Press, Cambridge, 1984) [171](#), [175](#), [182](#)
4. L. Onsager: Philos. Mag. **43**, 1006–1008 (1952) [171](#), [173](#), [182](#), [183](#)
5. G. Landwehr: “Quantum transport in silicon inversion layers”, in *Advances in Solid State Physics*, ed. by H.J. Queisser, Vol. 15 (Pergamon-Vieweg, Braunschweig, 1975), p. 49 [171](#)
6. H.L. Störmer, Z. Schlesinger, A. Chang, D.C. Tsui, A.C. Gossard, W. Wiegmann: Phys. Rev. Lett. **51**, 126 (1983) [6](#), [122](#), [171](#), [172](#)
7. J.P. Eisenstein, H.L. Störmer, V. Narayanamurti, A.C. Gossard, D. Wiegmann: Phys. Rev. Lett. **53**(27), 2579–2582 (1984) [70](#), [122](#), [171](#), [172](#), [181](#)
8. J. Luo, H. Munekata, F.F. Fang, P.J. Stiles: Phys. Rev. B **38**(14), 10 142–10 145 (1988) [80](#), [122](#), [171](#), [172](#)
9. R. Wollrab, R. Sizmann, F. Koch, J. Ziegler, H. Maier: Semicond. Sci. Technol. **4**, 491 (1989) [80](#), [122](#), [171](#), [172](#)
10. B. Das, D.C. Miller, S. Datta, R. Reifenberger, W.P. Hong, P.K. Bhattacharya, J. Singh, M. Jaffe: Phys. Rev. B **39**(2), 1411–1414 (1989) [80](#), [122](#), [171](#), [172](#), [174](#)
11. J. Luo, H. Munekata, F.F. Fang, P.J. Stiles: Phys. Rev. B **41**, 7685 (1990) [80](#), [122](#), [171](#), [172](#)
12. M. Schultz, F. Heinrichs, U. Merkt, T. Collin, T. Skauli, S. Løvold: Semicond. Sci. Technol. **11**, 1168–1172 (1996) [80](#), [122](#), [171](#), [172](#)
13. G. Engels, J. Lange, T. Schäpers, H. Lüth: Phys. Rev. B **55**(4), R1958–R1961 (1997) [80](#), [122](#), [171](#), [172](#)
14. J.P. Heida, B.J. van Wees, J.J. Kuipers, T.M. Klapwijk, G. Borghs: Phys. Rev. B **57**(19), 11 911–11 914 (1998) [70](#), [80](#), [122](#), [171](#), [172](#)
15. J.P. Lu, J.B. Yau, S.P. Shukla, M. Shayegan, L. Wissinger, U. Rössler, R. Winkler: Phys. Rev. Lett. **81**, 1282 (1998) [122](#), [171](#), [172](#), [174](#), [179](#)
16. S.J. Papadakis, E.P. De Poortere, H.C. Manoharan, M. Shayegan, R. Winkler: Science **283**, 2056 (1999) [3](#), [6](#), [77](#), [100](#), [104](#), [109](#), [143](#), [171](#), [172](#), [174](#), [177](#), [178](#)
17. S. Brosig, K. Ensslin, R.J. Warburton, C. Nguyen, R. Brar, M. Thomas, H. Kroemer: Phys. Rev. B **60**(20), R13 989–R13 992 (1999) [80](#), [122](#), [171](#), [172](#)
18. D. Grundler: Phys. Rev. Lett. **84**(26), 6074–6077 (2000) [80](#), [122](#), [171](#), [172](#)
19. T. Matsuyama, R. Kürsten, C. Meissner, U. Merkt: Phys. Rev. B **61**(23), 15 588–15 591 (2000) [80](#), [122](#), [171](#), [172](#)

20. X.C. Zhang, A. Pfeuffer-Jeschke, K. Ortner, V. Hock, H. Buhmann, C.R. Becker, G. Landwehr: Phys. Rev. B **63**, 245 305 (2001) [122](#), [171](#), [172](#)
21. J. Nitta, T. Akazaki, H. Takayanagi, T. Enoki: Phys. Rev. Lett. **78**(7), 1335–1338 (1997) [70](#), [77](#), [100](#), [109](#), [121](#), [122](#), [171](#), [174](#)
22. R. Winkler, S.J. Papadakis, E.P. De Poortere, M. Shayegan: Phys. Rev. Lett. **84**, 713 (2000) [6](#), [172](#), [177](#), [180](#), [182](#), [188](#)
23. S. Keppeler, R. Winkler: Phys. Rev. Lett. **88**, 046 401 (2002) [6](#), [172](#), [183](#), [186](#), [188](#)
24. N.W. Ashcroft, N.D. Mermin: *Solid State Physics* (Holt, Rinehart, Winston, Philadelphia, 1976) [173](#)
25. H. Mayer, U. Rössler: Phys. Rev. B **44**, 9048 (1991) [21](#), [24](#), [37](#), [74](#), [212](#), [213](#), [214](#), [220](#), [174](#)
26. O. Madelung (Ed.): *Semiconductors*, Vol. 17a of Landolt-Börnstein, New Series III (Springer, Berlin, Heidelberg, 1982) [15](#), [74](#), [219](#), [220](#), [221](#), [222](#), [174](#)
27. T. Ando, Y. Uemura: J. Phys. Soc. Jpn. **36**(4), 959–967 (1974) [175](#), [178](#)
28. R. Winkler, S.J. Papadakis, E.P. De Poortere, J.P. Lu, M. Shayegan: Physica B **298**, 13–17 (2001) [179](#), [181](#)
29. U. Rössler, F. Malcher, G. Lommer: “Spin splitting in structured semiconductors”, in *High Magnetic Fields in Semiconductor Physics II*, ed. by G. Landwehr (Springer, Berlin, Heidelberg, 1989), Vol. 87 of Solid-State Sciences, p. 376 [77](#), [78](#), [83](#), [166](#), [181](#)
30. E.A. de Andrada e Silva, G.C. La Rocca, F. Bassani: Phys. Rev. B **50**(12), 8523–8533 (1994) [78](#), [83](#), [182](#), [189](#)
31. R.G. Littlejohn, W.G. Flynn: Phys. Rev. A **45**, 7697 (1992) [183](#)
32. H. Frisk, T. Guhr: Ann. Phys. (N.Y.) **221**, 229–257 (1993) [183](#)
33. J. Bolte, S. Keppeler: Phys. Rev. Lett. **81**, 1987–1991 (1998) [183](#), [184](#), [185](#)
34. J. Bolte, S. Keppeler: Ann. Phys. (N.Y.) **274**, 125–162 (1999) [183](#), [184](#), [185](#)
35. R.G. Littlejohn, W.G. Flynn: Phys. Rev. A **44**, 5239–5256 (1991) [183](#), [189](#)
36. C. Emmrich, A. Weinstein: Commun. Math. Phys. **176**, 701–711 (1996) [183](#)
37. M.C. Gutzwiller: *Chaos in Classical and Quantum Mechanics* (Springer, New York, 1990) [183](#)
38. M. Brack, R.K. Bhaduri: *Semiclassical Physics* (Addison-Wesley, Reading, MA, 1997) [183](#), [184](#)
39. K. Richter: *Semiclassical Theory of Mesoscopic Quantum Systems*, No. 161 in Springer Tracts in Modern Physics (Springer, Berlin, 2000) [184](#)
40. M.V. Berry: Proc. R. Soc. Lond. A **392**, 45–57 (1984) [185](#)
41. J.J. Sakurai: *Modern Quantum Mechanics*, revised edn. (Addison-Wesley, Redwood City, 1994) [31](#), [83](#), [151](#), [152](#), [204](#), [208](#), [185](#)
42. M.H. Cohen, L.M. Falicov: Phys. Rev. Lett. **7**, 231–233 (1961) [189](#)
43. C. Amann, M. Brack: J. Phys. A: Math. Gen. **35**, 6009–6032 (2002) [191](#), [192](#)
44. N.O. Lipari, A. Baldereschi: Phys. Rev. Lett. **25**(24), 1660–1664 (1970) [29](#), [30](#), [32](#), [192](#)
45. J.W. Eddy, Jr., R.W. Stark: Phys. Rev. Lett. **48**(4), 275–278 (1982) [192](#), [193](#)
46. A.B. Pippard: *Magnetoresistance in Metals* (Cambridge University Press, Cambridge, 1989) [193](#)